Universitat Autònoma de Barcelona

Transparent Conducting Oxides Based on Early Transition Metals: From Electrical and Optical Properties of Epitaxial Thin Films, to Integration in All-Oxide Photoabsorbing Heterostructures

Mathieu Mirjolet

Transparent Conducting Oxides Based on Early Transition Metals:

From Electrical and Optical Properties of Epitaxial Thin Films, to Integration in All-Oxide Photoabsorbing Heterostructures

A dissertation submitted for the degree of

DOCTOR OF PHILOSOPHY IN PHYSICS

by

Mathieu Mirjolet

Supervisor:
Prof. Josep Fontcuberta Griñó

Laboratory of Multifunctional Thin Films and Complex Structures
Institut de Ciència de Materials de Barcelona (ICMAB-CSIC)

Tutor: Prof. Javier Rodríguez Viejo
Doctorat en Física
Departament de Física - Facultat de Ciències
Universitat Autònoma de Barcelona

May 2021

Mathieu Mirjolet
ICMAB-CSIC
Campus de la UAB, Bellaterra, Barcelona, Spain
mathieu.mirjolet@gmail.com

May 2021

Memòria que porta per títol **"Transparent Conducting Oxides Based on Early Transition Metals: From Electrical and Optical Properties of Epitaxial Thin Films, to Integration in All-Oxide Photoabsorbing Heterostructures. "** i presentada per aspirar al Grau de Doctor en Física per **Mathieu Mirjolet**

Autor:
Mathieu Mirjolet, MSc.

amb el vist i plau de: **Prof. Josep Fontcuberta Griñó**, professor d'investigació del Institut de Ciències de Materials de Barcelona (ICMAB-CSIC) i **Prof. Javier Rodríguez Viejo**, catedràtic del Departament de Física de la Universitat Autònoma de Barcelona (UAB). I per a que així consti, signen el present certificat.

JAVIER RODRIGUEZ VIEJO - DNI 46620967J

Firmado digitalmente por JAVIER RODRIGUEZ VIEJO - DNI 46620967J
Fecha: 2021.05.13 19:41:36 +02'00'

Director:
Prof. Josep Fontcuberta Griñó

Tutor:
Prof. Javier Rodríguez Viejo

Barcelona, 13 de maig de 2021

Acknowledgements

Dear Colleagues and Friends,

When I look back at these past few years, I see an incredibly enriching experience that has only been possible thanks to your help and support. I would like to dedicate the following few words to all of you, the people who took part in this journey of mine.

My deepest gratitude goes to my supervisor and head of the MULFOX group, Prof. Josep Fontcuberta, who supported me throughout this PhD in numerous ways. Pep, your thirst for knowledge has been a great source of inspiration. Not only were you always available for discussions on materials science, but you also shared your curiosity and enthusiasm for science in general!

In the same vein, I would like to thank my colleagues and mentors who were the first actors of this enterprise, transferring me some of their knowledge and giving me precious advices: Dr. Gervasi Herranz, Dr. Florencio Sánchez, Dr. Ignasi Fina, Dr. Fanmao Liu, Dr. Matheus Gamino.
Gervasi, thank you very much for your precious help with scholarship, administrative details, and so on, before and during my arrival in Spain.

This thesis could not have been so diverse in content without the help of many collaborators. Their contribution, in term of measurements, discussions, advices... greatly contributed to the work presented here and to the publications that I have had the chance to co-author with them. For all of this, I want to acknowledge: Dr. Florencio Sánchez for his guidance on PLD growth of thin films; Dr. Hari Babu Vasili for his great contribution to X-ray absorption spectroscopy measurements; Prof. Roser Valentí, Dr. Vladislav Borisov and Adrian Valadkhani for providing first-principles calculations and their interpretation on the electronic properties of strontium vanadate; Dr. Gervasi Herranz, Dr. Mikko Kataja and Prof. Tommi K. Hakala for their polarization-dependent reflectance/transmittance measurements and their essential knowledge on plasmonics; Prof. Lambert Alff and Dr. Philipp Komissinskiy for their huge input on the growth of strontium niobate films; Dr. José Santiso for his expertise on X-ray diffraction; Dr. Francesca Peiró, Dr. Lluís López-Conesa and Dr. Sònia Estradé for the transmission electron measurements; Dr. Manuel Valvidares, Dr. Pierluigi gargiani, and Dr. Ibraheem Yousef for their contribution in the measurements carried at Alba synchrotron; Prof. Christian Bernhard and Dr. Premysl Marsik for the FIR ellipsometric measurements; Dr.

Mariona Coll and Pamela Machado for their help with the ellipsometry measurements carried at ICMAB; Dr. Francisco Rivadulla for the Seebeck measurements; Dr. Jordi Fraxedas and Dr. Guillaume Sauthier for their proficient contribution on X-ray photoemission measurements.

Naturally, I would like to thank my colleagues from the MULFOX group, with whom I shared numerous group meetings and scientific discussions: Dr. Fanmao Liu, Dr. Mateusz Ścigaj, Dr. Mengdi Qian, Dr. Nico Dix, Dr. Chen Yu, Dr. Jike Liu, Saul Estandia, Milena Sulzbach, and Yunwei Sheng.
Thanks to Dr. Jaume Gazquez, Dr. Carlos Frontera, Dr. Ferran Macià, Prof. Vassil Skumryev, and Prof. Vladimir Laukhin for their participation and input in group meetings. I am also grateful to the students I had the chance to supervise for giving me the opportunity to transmit some of modest knowledge: Anna Fritschen, Victor Serrano, Jordi San Mateo Sánchez and Clemens Lindermeir.

For the fruitful stay I have spent at the Institute of Materials Science of the Technische Universität Darmstadt, I would like to express my gratitude to Prof. Lambert Alff, head of the group, who gave me the opportunity of joining his team for few weeks. I am also grateful to Dr. Aldin Radetinac, Dr. Philipp Komissinskiy, Mahdad Mohammadi and the rest of the ATFT group for welcoming me so well, sharing their knowledge and facilities, and last but not least, for giving me a taste of the German culture.

I would also like to acknowledge the technical staff of ICMAB for their support. My first thoughts go to Raúl Solanas for his most-skilful operation of the PLD/sputtering setups. *Raúl, la manera en la que haces cantar esos instrumentos al unísono te hace merecer el título de gran director de coro. Gracias por tu ayuda y tu buen humor!* A big thanks to Dr. Mengdi Qian too, who later incorporated the team. I am also grateful for the help of: the XRD team, composed of Dr. Anna Crespi, Xavier Campos, and Joan Esquius, for their attentive operation of the diffraction setups and the many fruitful discussions; Dr. Bernat Bozzo and Dr. Ferran Vallès for the great support with the PPMS; the Nanoquim team with Luigi Morrone, Dr. Neus Romà, Marta Riba and Marta Gerbolés, for the introduction to the numerous techniques available in the cleanroom platform; Anna Esther and Judith Oró for their help with SEM; Maite Simón and Andrés Gómez for the AFM measurements; Vega Lloveras for her help with UV-Vis-NIR spectrophotometers; Roberta Ceravola for the TGA measurements; Mariona De Palau and Joshua Bailo for their assistance in Ceràmiques II chemical lab.
I would like to acknowledge the technical staff from ICN2, including: Dr. José Manuel Caicedo Roque for his advices on PLD target fabrication, Dr. Javier Saiz for the FTIR measurements, and Dr. Jessica Padilla for the XRD measurements.

Un grand merci Dr. Guillaume Sauthier pour ton aide avec les mesures de XPS, pour supporter mes innombrables questions (notamment au sujet de la fonction de travail de l'analyseur :D), et pour ta sympathie et bonne humeur!
Finally, thank you to Dr. Ignasi Villarroya from the Servei d'Anàlisi Química of UAB for his input on ICP-MS measurements.

I would like to acknowledge my PhD tutor, Prof. Javier Rodríguez; the coordinator of the PhD in Physics, Dr. Jordi Mompart; Francesc Poblet of the administration of the Department of Physics of UAB; and the doctorate school of UAB. From ICMAB, I want to thank Pietat Sierra, Sonia Roldán, and Marta Vendrell for helping me with bureaucratic matters.

The presented work was conducted at the Institut de Ciència de Materials de Barcelona (ICMAB-CSIC). I want to acknowledge the financial support that I received from the Ministerio de Economía y Competitividad del Gobierno de España (ayuda para contratos predoctorales con referencia BES-2015-075223), and from the COST Association (Action MP1308).

Now some more personal lines to my friends and family, who accompanied me with their love and support all along this journey.

Juri, we basically made this journey together you and me. Thanks for all the good moments, for your help on many aspects, for sometimes pushing me out of my comfort zone, for all the pizza, and for all the morning brainstorming sessions.
Artur, you took a little bit longer to get *on board*, yet you quickly became *Mon Frère*. Among all the good times together, the surf trips with you guys were a real revelation, so that they became a delightful and painful ritual. I sincerely hope they will be many more. But meanwhile I can just close my eyes and think of La Perla...
As a wise man once said: Thank you. 🫵

Alejandro (« ¡Tío! »), Tato, Pamela, Nico, Lavinia, Fran, thank you so much for all the nice activities we had in Barcelona and surroundings!

To all my office mates and other friends at ICMAB: Francesco, Jordi, Pengmei, Yunwei, Ma, Huan, Xiao, Ferran... Thank you all for the good vibe at ICMAB.

Barcelona is a city where I have had the chance to meet amazing people who, even if they are far from my eyes, will never be far from my heart.
Eric, je me sens chanceux que nos chemins se soient croisés au Carrer d'En Roig

24. Je suis souvent nostalgique de toutes les aventures qu'on a eu ensemble à Barcelone ou lors de nos voyages; mais je sens qu'il y en aura beaucoup d'autres! Je te souhaite plein de réussite avec ton doctorat et tes futurs projets, car tu le mérites Frérot!
Federico, hermano mío... Mi llegada a Barcelona no podría haber sido tan memorable sin tu encuentro. Cuando recuerdo nuestros momentos en Casa Barceló, siento tanta emoción que las palabras me fallan, así que solo añadiré una: ¡Seven!
Artemis, merci pour ta gentillesse! Bien que nos chemins se soient peu croisés, j'espère qu'on se reverra bientôt.

Ben, Benji, Luc et Tom, mes chers Bisons... Par où commencer?! Vous m'accompagnez déjà depuis une paire d'années, et chaque fois que l'on se voit, même après des mois entiers loin de vous, c'est comme si l'on ne s'était jamais quittés. Notre histoire est pavée de souvenirs impérissables et intarissables de tous les délires que l'on ait pu avoir ou les conneries que l'on ait pu faire ensemble. De ces dernières années, je garderai à jamais un tendre souvenir de nos petites escapades à Varsovie, Budapest, Madrid ou simplement à la Villa... Bien que ceux qui sont encore à venir pourraient bien être encore plus grandioses!

Ma chère famille. Merci pour votre amour inconditionnel et votre soutien durant toutes ces années. Maman, Papa, si je suis ce que je suis aujourd'hui c'est grâce à vous et aux valeurs que vous nous avez inculquées. Guillaume, je te souhaite plein de bonheur avec les filles. Je me réjouis que Marine et toi m'ayez choisi comme parrain de Charlie et vous félicite pour la venue de la petite Romy.
J'espère que vous comprenez que malgré la distance vous êtes toujours dans mon cœur, ce monde est seulement tellement vaste et plein de surprises que je ne peux tout bonnement pas rester bien longtemps à la maison sans vouloir repartir à l'aventure.
Parce-qu'ils le méritent aussi je dédie une pensée à mes chers Buddy et Jojo tout simplement pour rendre nos vies plus paisibles, et à ma chère Nina, qui m'a fait découvrir que les liens entre animaux et humains sont si précieux. Ton ronronnement restera à jamais gravé dans ma mémoire.

Abstract

Transparent conducting oxides (TCOs) are key elements to many technological devices. Their ability to combine high electrical conductivity and high optical transparency to visible light, make them particularly useful in a myriad of devices such as displays, solar cells, smart windows, etc.

Indium tin oxide (ITO) is so far the most widespread TCOs. By Sn-doping, this wide band gap In_2O_3 semiconductor can reach low resistivity (only about two orders of magnitude above conventional metals) while preserving its transparency. A major drawback of ITO is its high cost as indium, its main component, is a scarce material. Moreover, due to its nature of doped-semiconductor, some physical limits impose that its properties cannot be further improved.

On the other hand, some intrinsic metallic oxides composed of early transition metals also turn out to be transparent. In these materials, the partially filled narrow d band is responsible for high density of free carriers with increased effective mass, thus bringing the reflection edge down to the near-IR region.

In this thesis, we were interested in exploring the properties of metallic oxide thin films grown by pulsed laser deposition (PLD), namely $SrVO_3$ (SVO; $3d^1$) and $SrNbO_3$ (SNO; $4d^1$).

As high epitaxial quality is essential to obtain good functional properties, the first step consisted in optimizing the growth parameters for single phase and flat SVO/SNO films, displaying high crystallinity, conductivity and transparency. As anticipated, films need to be grown in ultra-high vacuum (UHV) to stabilize the 4+ oxidation state of V/Nb and using a high substrate temperature (700-800°C) to allow good mobility of the species on the substrate. However, the deposition in UHV and its subsequent highly energetic PLD plasma plume lead to a high concentration of point defects. We have solved this issue by using an inert background gas. Finally, we have studied the impact of epitaxial strain on the electrical conductivity and optical transparency window. All in all, it turned out that optimal films display larger conductivity than ITO, for a similar transparency.

Conventional wisdom would suggest that a low plasma frequency would be due to the electron-electron correlations within the narrow nd^1 band. In a systematic analysis of SVO transport data (temperature-dependent resistivity, etc.), we have concluded that the Fermi liquid theory alone cannot account for the carrier mass

enhancement. Instead, we have suggested that the 2D-like Fermi surface and the electron-phonon coupling play a major role. In addition, we have shown that the classical rigid band picture, of one free electron evolving in a $3d$-t_{2g} band is only a rough approximation, as attested by the observed hybridization of the V $3d$ and O $2p$ orbitals. Moreover, strain affects this hybridization by modifying the orbital hierarchy and covalency which could be responsible for the observed strain-dependent resistivity and effective mass.

By appropriate optical measurements, we have also discussed the nature of the plasmonic excitations at plasma frequency in SNO and SVO films. Interestingly, the possibility of exciting volume plasmons in these TCOs gives a glimpse on their potential applications in the field of plasmonics.

Finally, we have tested the suitability of SVO as electrode in photoabsorbing all-oxide heterostructures. In particular, we have successfully observed a photovoltaic effect in $LaFeO_3$-based capacitors and disclosed the important role of the electrode work function on the device performances. As outlook, we have concluded that SVO and SNO, by having distinct work functions, could allow to tune any device properties.

This work demonstrates the suitability and high potential of this whole new category of TCOs as electrode material in all-oxide devices. We are convinced that it opens the way to a plethora of possible devices, photovoltaic-wise or other.

Contents

Chapter 1

Introduction

1.1 The advent of modern electronics

The story of electronics began with the electron, isolated by Thompson and his cathode ray experiment in 1897.[1] Few years later, the vacuum tube was one of the first applications of the electron discovery, that was used in radio telecommunications to manipulate (amplify, transmit) small electrical signals, and constituted the building block of the electronics of the 50s. Although leaving a great legacy behind, such as the cathode-ray tube (CRT) television, the vacuum tube era eventually came to an end initiated by the invention, in 1947, of the first transistor. This solid-state version of the vacuum tube is also capable of amplifying and switching on-and-off electric signals. However, the major milestone of the history of electronics is the invention of the metal–oxide–semiconductor field-effect transistor, or in short *MOSFET*, by Atalla and Kahng in 1959. As early as the 60s, several transistors were fabricated onto the first *integrated circuits* (ICs),[2] which led Moore to make his surprisingly accurate prediction, known as *Moore's law* (1975), when affirming that the number of transistors per unit space will double every two years. His prediction turned out to be true and we are still living in the Moore's law era. Although according to Moore's law the ultimate transistor size could be the size of an atom, some physical limits (e.g. quantum tunneling, which provokes high leakage current in the source-to-drain channel) impede researchers to further downscale transistor to its actual size ($\approx$ 3-5 nm).

The example of the transistor clearly illustrates the fast developments of technologies and the necessity for highly efficient materials. Nowadays, apart from Si-based transistors and ICs, semiconductors in general (GaAs, Ge alloys, etc.) are widely

[1] Thompson even determined the mass of this particle to be 1800 times smaller than the one of the smallest particle known at the time, the hydrogen atom (later identified as the proton), and of opposite (thus negative) charge. Later on the electron mass was refined to 1/1836 times the proton mass.

[2] Nowaday, transistors are made using the complementary metal–oxide–semiconductor (CMOS) structure, a type of MOSFET fabrication process, used to fabricate ICs.

used in solid-state electronic devices: diodes, LEDs, lasers, solar cells... Another typical example is in photovoltaics, where the efficiency of (crystalline Si-based) single *p*-*n* junction solar cells is bounded by the Shockley–Queisser limit. The current limitations of semiconductors and the increasing needs for more powerful electronics have been the main driving forces to push research toward new type of devices, including new materials. Complex oxides appear as a promising alternative class of materials. They can either be combined with the existing semiconductors or be used to design all-oxide devices. Their complex electronic structure and subsequent properties are strong assets for the technologies of the future.

1.2 Complex oxides

As mentioned above, silicon is the base component of most technological devices, which in addition of showing some interesting properties as semiconductor, is very abundant, However, most of silicon on Earth is not present as pure element but in oxidized form, as silicates. As a matter of fact, almost all elements of the periodic table exist in the form of oxides in the Earth crust [1], where they can be found under a multitude of different crystalline structures such as rock-salt, wurtzite, spinel, perovskite, fluorite, etc. [2].

Transition metal oxides (TMOs) are particularly interesting, due to their partially filled narrow *d* shell. In TMOs, the complex interplay between charge, spin, lattice and orbital degrees of freedom is at the origin of a myriad of properties: multiferrocity, superconductivity, colossal magnetoresistance, metal-insulator transition, high-κ dielectrics, transparent conducting oxides, and so on. This leads to a tremendous amount of possible applications: ferroelectric memories, superconducting magnets, sensors, oxide FETs, photovoltaics and displays, etc.

In the laboratory, the various forms that can be given to oxides (bulk crystals, films, nanoparticles, nanowires, quantum dots, heterostructures) offer an additional way to further tune their physicochemical properties and design new devices. In particular, the possibility to design heterostructures of thin films opens the way to a multitude of applications [2–5]. This was made possible by the developments of thin-film deposition techniques such as pulsed laser deposition (PLD), sputter deposition, molecular beam epitaxy (MBE)...

Nonetheless, the interest for oxides remained pretty dormant until 1986,[3] year of the discovery of high-temperature superconductivity (HTS) in cuprate-perovskite

[3] Explaining that the current technologies do not involve much oxides (yet). In fact, over centuries, oxides were usually reduced to pure elements (as silicon, iron, copper, etc.). Which can sometimes involve a complex process of purification (depending on the targeted application). A good

ceramics [6].[4] Nowadays, not only the research on high-T_c superconductors is still a very active field, but there is a whole field of research focused on the applications of oxides for nanotechnologies and the concept of *oxide electronics* emerged few decades ago [5, 7].

1.2.1 Perovskites

The discovery of HTS brought a renewed attention to TMOs with the ABO_3 perovskite structure (Figure 1.1), which can be seen as a simple cubic structure composed of a cation A in its center, which is usually an alkaline earth or rare-earth element, and a transition metal B in its corners, surrounded by an octahedral oxygen cage. The perovskite structure offers many degrees of freedom for tuning its properties via chemical substitution of the A/B cations. However, depending on the cationic radii of A/B, the structure can vary from perfectly cubic to orthorhombic, hexagonal, etc. as a result of tilting or rotation of the oxygen octahedra. The change of structure with ionic radii is well-described by the well-known Goldschmidt tolerance factor.

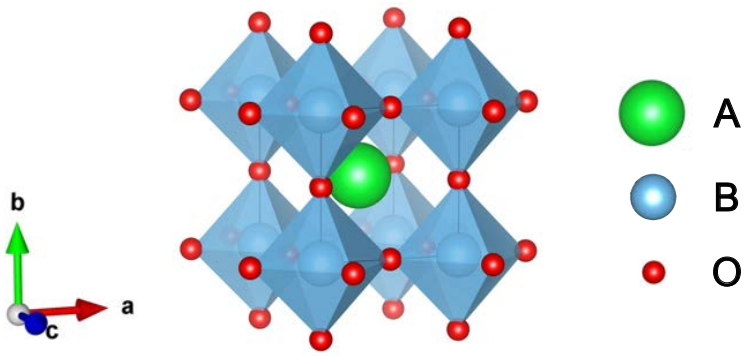

FIGURE 1.1: Sketch of perovskite unit cell with ABO_3 chemical formula.

In addition of the change in ionic radii, the valency of A/B has an impact on the electronic properties of the perovskite crystal. Oxygen, with its 4 valence shell electrons ($2p^4$), is highly electronegative and thus tends to "capture" 2 electrons from its surrounding elements to fill the empty valence states. On the other hand,

example is monocrystalline silicon wafers used in semiconductor industry, which have a purity of > 99.9999999 %.

[4] Although the first mineral with perovskite structure, calcium titanate ($CaTiO_3$), was discovered in 1839 by the Russian mineralogist Lev Perovski.

A and B are rather electropositive (they are situated on the left of the periodic table) and tend to "give electrons away" to form stable cations in the lattice. As A is the most electropositive and have usually one stable valence state, it gives away easily its electrons and have nearly one prevalent oxidation state in the ABO_3 structure (Sr^{2+}, Ca^{2+}, La^{3+}, etc.). On the other side, the B cation, usually a transition metal with multiple valence states gives 4 electrons away to the surrounding oxygen atoms. Depending on the choice of A/B cations, the material can be insulating, semiconducting or metallic. For instance, $Sr^{2+}Ti^{4+}O_3^{6-}$ is insulating, as Ti^{4+} has closed shell, and $3d^0$ electronic configuration. On the other hand $Sr^{2+}V^{4+}O_3^{6-}$ is metallic, with $3d^1$ electronic configuration, as V^{4+} has one electron in his d shell.

On another hand, the bond between the B cations and the oxygen anions has a crucial influence on the electronic properties of the perovskite. The hybridization of O p and B cation d orbitals is sensitive to the B-O-B bond angle. Primarily, the d orbitals are split by the crystal-field of the oxygen ligands into t_{2g} and e_g orbitals, but further breaking of the orbital degeneracy can occur through distortion of the lattice. The hybridization between O p and B cation d orbitals is therefore sensitive to the lattice and distortions of the latter provoke changes of the electronic properties, and phenomena such as metal-insulator transitions may be triggered. In the case of thin films for instance, these distortions may be tuned by substrate-induced strain.

1.3 Transparent conducting oxides

The name speaks for itself, transparent conducting oxides (TCOs) are materials combining high electrical conductivity and high transparency to visible light. TCOs serve a wide range applications as transparent electrodes in displays, touchscreens, solar cells, LEDs/OLEDs, smart windows, defrosting windows, flexible electronics and transparent electronics in general [8–14].

A typical TCO material has an electrical conductivity $\sigma > 10^3\,\mathrm{S\,cm^{-1}}$ (to avoid significant resistive power loss) and optical transmittance $T > 80\,\%$ over the visible range. Some other important criteria and/or requirements (functional or technological) to take into account when evaluating the suitability of a material as TCO include [8, 9]:

- High carrier concentration and mobility
- Raw material availability and costs (including manufacturing cost)
- Green materials and processing
- Stability and ease of integration (growth conditions)
- Suitability of the material work function [15]

So far, indium tin oxide (ITO) has been dominating the TCO market, as it is the best compromise fulfilling the above-mentioned criteria. However, the major drawback of ITO is its price due to the scarcity of indium.[5]

In the following, a brief description of the fundamental concepts, as well as the different types of TCOs, are given.

1.3.1 General definition

A transparent conductor (TC) is a material that combine high electrical conductivity and high transparency. These two properties are intrinsically connected as, in a metal, the free electron gas is at the origin of its high electrical conductivity but also its reflectivity of light. While this feature is thus responsible of the high sheen of conventional metals (such as Au, Ag, Al, etc.),[6] TCs have the particularity to reflect a smaller portion of light (up to the NIR only), which allows light of higher frequency to be either transmitted or absorbed (Figure 1.2).

The Drude free electron model gives a straightforward picture of the properties of metals. According to the model, the electrical conductivity σ of a metal is defined as:

$$\sigma = e\, n\, \mu = e^2\, \tau \frac{n}{m^*} \tag{1.1}$$

where e is the elementary charge, n the carrier density, μ the carrier mobility, τ the scattering time, and m^* the carrier effective mass.
The electrical resistivity is defined as the inverse of the conductivity:

$$\rho = \sigma^{-1} \tag{1.2}$$

The plasma energy E_{ω_p}, setting the position of the reflection edge, is defined as:

$$E_{\omega_p} = \frac{\hbar\, e}{\sqrt{\varepsilon_0\, \varepsilon_r}} \sqrt{\frac{n}{m^*}} \tag{1.3}$$

[5] See refs. [8, 14, 16–19] for more details on ITO and the applications of TCOs.

[6] In conventional metals, the free electrons reflect light in the IR-Vis-UV range [17, 20–22]. As a result, metals exhibit a high sheen, and polished metals are perfect mirrors. However, a very thin film of any metal can be transparent if its thickness is below the skin depth of the metal. In that case, the evanescent light waves will cross the material without interaction [23]. Nonetheless, a metal typically needs to be few nanometers thick ($\approx$ 5 nm) to reach a transparency of $\approx$ 50 % (the film is thus referred as *semi-transparent*) and such a harsh scaling down as strong repercussions on the film conductivity, as its thickness is close to the electron mean free path. Moreover, the deposition of homogeneous metallic ultrathin films may be challenging.

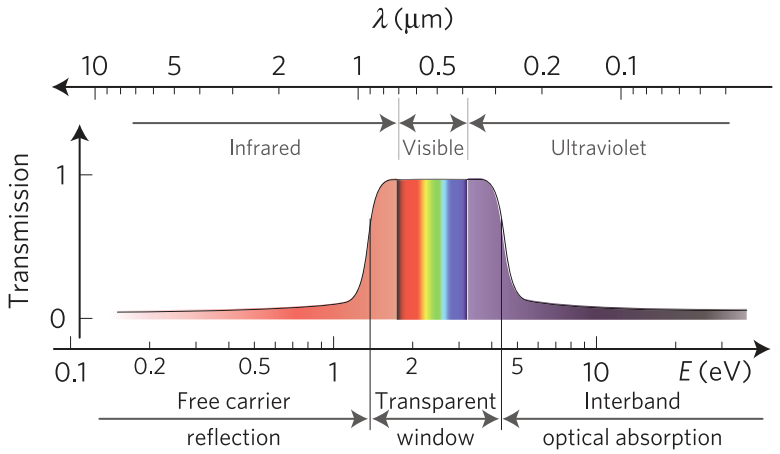

FIGURE 1.2: Sketch illustrating the transparency window of a transparent conductor. The free carrier reflection edge is in the NIR region, below 1.8 eV, which allows visible light to be transmitted. In the UV range, light is absorbed due to interband electronic transitions. Figure taken from [18].

where ε_0, ε_r are the vacuum and material relative permittivity, respectively. A transparent material is expected to have a screened plasma energy $E^*_{\omega_p} < 1.8$ eV.

In Equations 1.1 and 1.3, one can observe that the ratio n/m^* governs both the screened plasma energy $E^*_{\omega_p}$ and the conductivity σ. Indeed, the highest n/m^*, the highest the conductivity σ but also the screened plasma energy $E^*_{\omega_p}$, so that n/m^* has to be low enough for $E^*_{\omega_p}$ to be in the NIR range, and thus the material to be transparent. Hence, the necessity to preserve n/m^* ratio below some threshold value (no matter the values of n and m^* apart).

1.3.2 Doped wide band gap semiconductors

There are several ways of obtaining a transparent and conducting material, which all consist in tuning the n/m^* ratio. The most common approach is by doping a wide gap semiconductor (SC). In an undoped SC, the Fermi energy E_F lies in the middle of the bandgap. When sufficiently (degenerately) doped with electrons, the material's Fermi level is shifted up inside the conduction band (CB). As a consequence, the introduction of free electrons by doping (increase of n) provokes an increase of the material conductivity, plasma energy, and also optical band gap (i.e.

increases the minimum energy that photons need to be absorbed[7]). The example of ITO is shown in Figure 1.3.

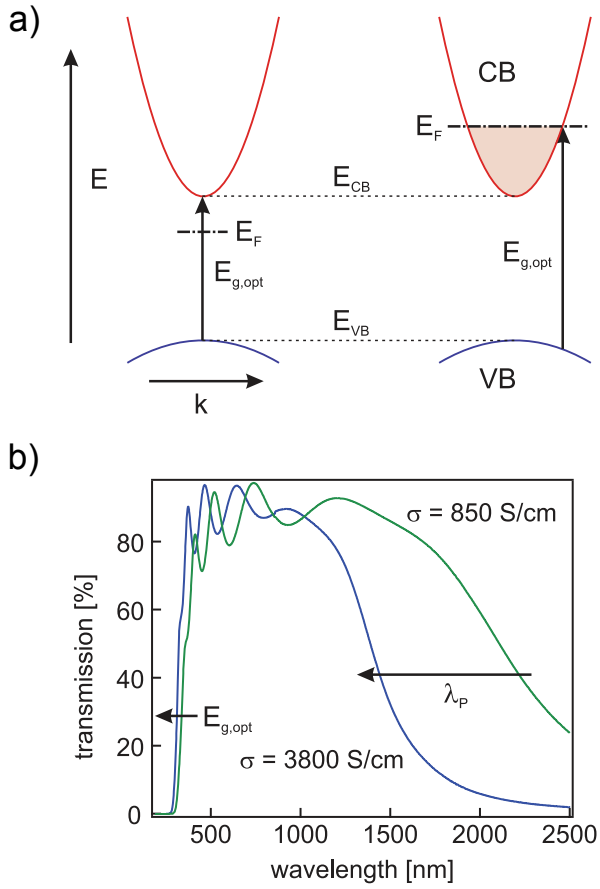

FIGURE 1.3: a) Schematic band structure of undoped (left), and *n*-type doped (right) semiconductors. b) Transmission spectra of two ITO films with different doping (also indicated by the conductivity). Figure taken from [15].

This approach was successfully applied and, as a matter of fact, nearly all of the TCOs on the market are degenerately doped semiconductors. The most famous are ITO, F-doped SnO_2 (FTO), doped ZnO (by In, Al or Gd), etc. More recently, La-doped $BaSnO_3$ (BLSO) also showed some promising properties [8, 24, 25].

[7] The optical band gap of a doped SC is the distance between the top of the valence band (VB) and the Fermi level (E_F). It is different than its intrinsic band gap, which is the distance between the VB and the CB.

However, these materials present some limitations. For instance, the maximum carrier concentration, limited by effects such as dopant solubility and self-compensation [17, 18, 26], prevent for further improvement of their conductivity.

1.3.3 Intrinsic metallic oxides with perovskite structure

Many perovskite oxides are intrinsically metallic due to their partially filled conduction band. They are mostly used as electrode in all-oxide heterostructures such as ferroelectric capacitors, etc. as they show good compatibility with other functional oxides such as ferroelectric (Ba,Sr)TiO_3 (BST), Pb(Zr,Ti)O_3(PZT), to mention a few.[8]
Among them, $LaNiO_3$ (LNO; $3d^7$) or $SrRuO_3$ (SRO; $4d^4$) are commonly used.[9] [28] More recently, attention was driven to $SrMoO_3$ (SMO; $4d^2$), which is the most conducting perovskite oxide ever reported (with RT-resistivity of $\rho \approx 5\,\mu\Omega\,cm$ observed in the bulk material [29], and $\rho \approx 20\,\mu\Omega\,cm$ in thin films) [30]. However, none of these materials is highly transparent, unless if reducing their thickness, which in turn may hamper their electrical conductivity. Figure 1.4 summarizes the room-temperature resistivity of the most popular metallic oxides used as electrode in all-oxide heterostructures, together with their bulk cell parameter to emphasize compatibility with other funcional oxides (some are indicated by the dashed lines).

Recently, Zhang et al. reported on $CaVO_3$ (CVO) and $SrVO_3$ (SVO) thin films with the best figure-of-merit (FOM) as transparent conductors [18],[10] and these materials attracted a lot of attention as serious rivals to ITO.[11] CVO and SVO are intrinsic metallic oxides were the electrical conduction stem from the $3d^1$ band filling. It is commonly argued that the electron-electron (*e-e*) correlations within the narrow $3d$ band are responsible for the large effective mass m^* of carriers. This latter is higher than in conventional metals and doped-SCs, and high enough to bring the plasma energy down to the NIR region in spite of the high carrier concentration n. In fact, SVO owe the lowest resistivity ($\rho \approx 28\,\mu\Omega\,cm$) with plasma energy below the visible (as illustrated in Figure 1.5).
Finally, another promising metallic oxide is $SrNbO_3$ (SNO). The lowest RT-resistivity was reported a resistivity of ($\rho \approx 28.5\,\mu\Omega\,cm$) by Oka et al. but films has

[8] Bottom electrodes made of conventional metals, such as Pt, can be detrimental for the device properties [27]. On the other hand, the possibility of growing oxide electrodes with flat interfaces and high crystalline quality opens the way to better functional properties in all-oxide devices.

[9] Another common perovskite bottom electrode is based on the degenerately doped $La_{1-x}Sr_xMnO_3$ *p*-type semiconductor, where $0.2 < x < 0.5$.

[10] The figure-of-merit (FOM) is criteria used for quantitatively comparing the performance of TCs. It is based on the material's optical transmittance T and the sheet resistance R_S, and was first introduced by Haacke in 1976 [37].

[11] https://www.futurity.org/correlated-metals-screens-1071452-2/

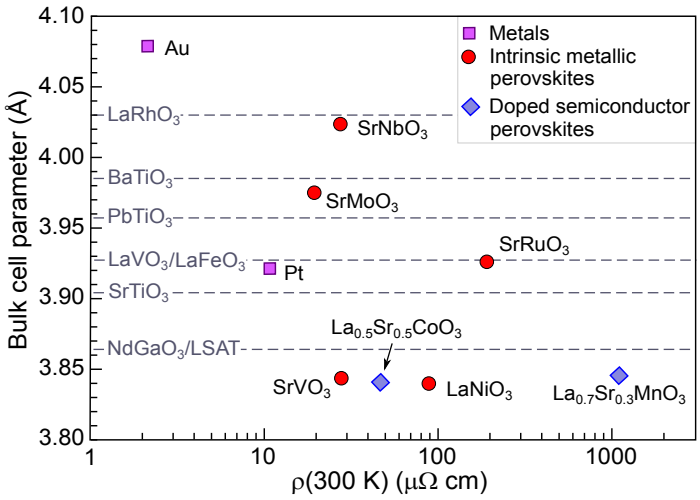

FIGURE 1.4: Compilation of popular metallic oxides used as electrode in all-oxide heterostructures. Data taken from [18, 28, 30–35]. The (pseudo)cubic bulk cell parameters of some typical perovskite oxides (substrates or films) are also indicated. Figure adapted from [36].

poor transparency, revealed broad absorption in both the visible and NIR regions of the absorption coefficient spectrum [31]. More recently Park et al. reported more transparent SNO films. With a RT-resistivity $\rho \approx 38\,\mu\Omega\,\text{cm}$ and a screened plasma energy $E^*_{\omega_p} \approx 2\,\text{eV}$ (although slightly in the visible), the resulting SNO films had similar FOM to vanadates [38].[12]

In conclusion, early transition metal oxides ($3d$, $4d$), such as CVO, SVO, SNO and SMO, are amongst the most conducting oxides that have been discovered so far. While SMO is the most conducting one, it is not as transparent as the others. On the contrary SVO and SNO show the best compromise between high conductivity and transparency, better than ITO and any other wide band gap doped-SC.

Other applications

Taking advantage of their high conductivity (alone), TCOs can also be used as highly conducting electrode to improve the performance of many devices, such as: high-frequency devices [39–42], solid oxide fuel cell (SOFC) [43–45], as photo-catalyst for water-splitting [46], or even in plasmonics [47] and spintronics.

[12] Moreover, the FOM of SNO in the UV range (260–320 nm) was much greater to SVO, due to the higher optical band gap of SNO compared to that of SVO.

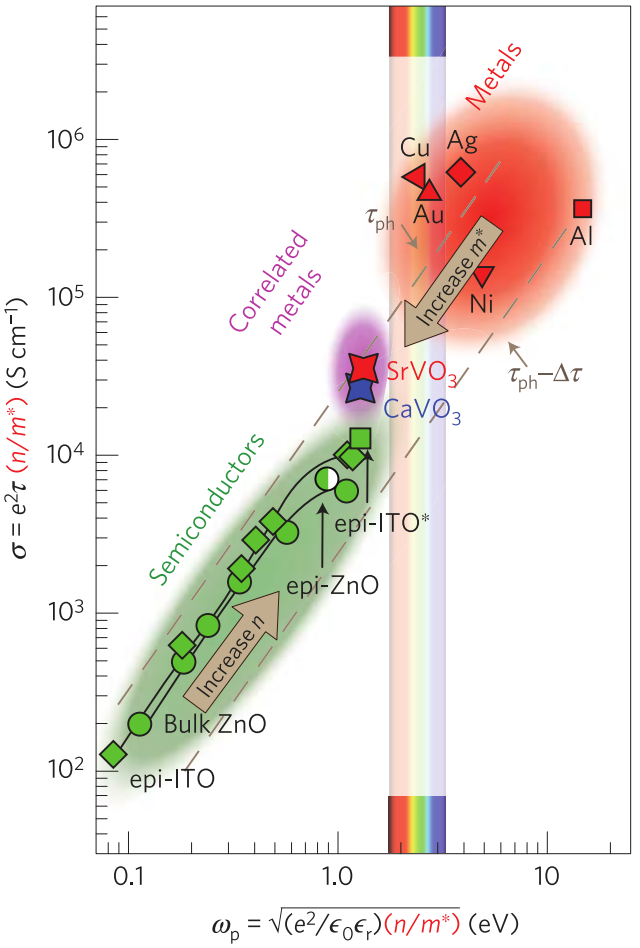

FIGURE 1.5: Compilation of conductivity (σ) vs plasma energy (annotated ω_p) for various transparent conducting oxides and conventional metals. Among transparent materials, $CaVO_3$ and $SrVO_3$ have the highest conductivity. Figure taken from [18].

1.4 Main objectives and thesis outline

Motivated by the need for TCOs with higher performances and cheaper than ITO, this work is focused on exploring the electrical and optical properties of some complex oxides based on early transition metals, as well as their suitability as transparent electrode for photovoltaics. More precisely, we aim at investigating the properties of two strongly correlated oxides, $SrVO_3$ (SVO) and $SrNbO_3$ (SNO), and

test their suitably in all-oxide heterostructures using centrosymmetric photoabsorbing oxides: $LaVO_3$ (LVO) and $LaFeO_3$ (LFO).[13]

In order to achieve the main objective of this thesis, studying the photoresponse in all-oxide heterostructures, growth optimization of different functional layers, acting as photoabsorber or transparent electrode, is first needed. Therefore, this work has been decomposed in the following steps:

- Optimising the epitaxial growth of various functional oxides as single layers. It includes the growth optimization of SVO and SNO as TCO thin films, and the one of LVO and LFO as potential photoabsorbers.
- Studying the electrical and optical properties of these materials as single layers. In particular, we want to ensure that the chosen TCOs have high conductivity and transparency. In the case of photoabsorbing layers, we are interested in measuring their absorption in the visible light.
- Incorporating the above-mentioned materials in a solar-cell-like all-oxide heterostructure and studying their photoresponse.

Most of the chapters (2 to 7) report on results on transparent conducting oxides, from growth-related aspects to a deeper focus on their functional properties and, in the last chapter (8), the fabrication and study of all-oxide heterostructures are addressed. The thesis outline is organized as follows:

- Chapter 2 describes the experimental methodology used throughout this work, from sample production to measurement techniques.

- Chapter 3 is the first chapter dedicated to the growth optimization of epitaxial $SrVO_3$ thin films. As it will be explained in details, highly crystalline thin films of this oxide are difficult to stabilize, especially by PLD. This is mainly due to the multivalent character of vanadium. After determining an optimal (PO_2, Temp.) growth window, it will be shown that the plasma frequency of our films is at the near-IF and its value can be tuned by carrier concentration, while conductivity can be finely tuned by epitaxial strain.

- Chapter 4 addresses an issue often encountered in the growth of $SrVO_3$ thin films by PLD: the presence of growth kinetics induced defects. In chapter 3, the determination of a growth window for single-phase $SrVO_3$ thin films disclosed the deposition in UHV to avoid formation of spurious phases, that tend to form if O_2 is used as a background gas (as for many oxide depositions). Here, we will show an approach considerably helping at reducing the

[13] $LaVO_3$ (Mott insulator) and $LaFeO_3$ (charge-transfer insulator) are both low band gap materials which show pronounced photoresponse. More details on their properties will be introduced in Chapter 8.

defects engendered by such growth process and with which we are able to grow by PLD SVO films having a record conductivity.

- Chapter 5 digs deeper into the electronic properties of $SrVO_3$ films. In particular, we will see how strong is the hybridization of O $2p$ and V $3d$ orbitals, usually neglected. $SrVO_3$ is indeed often described as a $3d^1$ metallic oxide. However, O $2p$ and V $3d$ bands slightly overlap and the amplitude of the overlapping can have direct consequences on the functional properties of the films. It will also be seen how the strain induced by the substrate can modify the crystal-field splitting of the perovskite structure, thus affecting the metal-oxygen hybridization, the orbital ordering and its electronic occupation.

- Chapter 6 focuses on the electrical transport in $SrVO_3$ films in order to account for properties such as the high effective mass of the charge carriers, responsible of the much-coveted material transparency to the visible light. The common belief is that the mass enhancement of the carriers is due to high electronic correlations, which is the so-called *Fermi liquid* theory. However, some experimental observations cannot be explained by this theory. In this chapter, we will argue that different aspects, usually omitted, of the electronic properties of $SrVO_3$, such as the shape of its Fermi surface and the electron-phonon interactions, play a relevant role on the effective mass enhancement and the temperature dependence of the resistivity.

- Chapter 7 explores the properties of another TCO: strontium niobate ($SrNbO_3$). With a $4d^1$ electronic configuration, $SrNbO_3$ is also metallic and transparent. Although the broader character of the $4d$ band in comparison to the $3d$ of $SrVO_3$ presumes of a smaller effective carrier mass. Here, we will show that thin $SrNbO_3$ films reach properties competing with the ones of $SrVO_3$. Moreover, we will explore in detail the nature of the plasma frequency and we will argue that it corresponds to excitations of bulk longitudinal plasmons by light. A comparison between $SrVO_3$ and $SrNbO_3$ will be made.

- Chapter 8 undertakes the fabrication and the photoresponse measurements of all-oxide heterostructures. With a first task of growing single-layers of $LaVO_3$ and $LaFeO_3$ films (which are both believed to be good photoabsorbers considering their small bandgap), the materials will then be integrated in capacitor-like structures using different transparent top electrodes. It will be shown that the electrical properties ($I-V$ curved in dark and under illumination) of the different heterostructures, as well as the observation of a photovoltaic effect, strongly depend on the built-in potential, itself dictated by the work function of the electrodes. After concluding on the suitability of the TCOs investigated in the thesis, we will propose alternative devices that could lead to higher photoresponse in these all-oxide heterostructures.

- Chapter 9 will give general conclusions over the work achieved in this thesis and some outlook on the topic.

Chapter 2

Experimental methodology

In this chapter, a description of all experimental techniques used in this thesis is given. The sample growth and preparation techniques are introduced in the Section 2.1; while their characterization techniques are explained in the Sections 2.2 – 2.7. It will be seen that diverse characterization techniques have been used, going from X-ray diffraction techniques for the structural characterization to electrical and optical measurements for the functional properties, to surface sensitive techniques, and so on. In Section 2.8, a brief description of first-principles calculations is given.

2.1 Sample preparation: from single layers to heterostructures

2.1.1 Pulsed laser deposition of oxide thin films

In the field of thin film research, various physical and chemical deposition techniques exist. For instance, sputtering, molecular beam epitaxy (MBE), pulsed laser deposition (PLD), chemical solution deposition (CSD) or even atomic layer deposition (ALD) are amongst the most common techniques [48].

PLD is a physical vapor technique in which a pulsed laser beam ablates a ceramic target of similar cationic composition than the thin film to be deposited. This latter forms onto a substrate material (placed few centimeters in front of the target, see sketch in Figure 2.1). One usually wishes to grow monocrystalline films, in order to reach optimal functional properties for instance. This may be achieved by epitaxial growth, where a single-crystal substrate with similar structure than the one expected for the film imposes its crystalline order to the incoming atoms during deposition. However, the way the film grows is largely affected by other parameters such as the growth conditions related to the PLD chamber, the laser, the substrate temperature, etc. as described hereafter.

When the laser energy is sufficiently high, the ablation causes congruent emission of atoms. It usually operates at a wavelength of $\lambda = 248\,\text{nm}$ (which corresponds to a photon energy of $E_{\text{ph}} = 5\,\text{eV}$) and is focused on a small spot ($\approx$ 1-2 mm²), so that the energy density (or fluence) is typically around $1-3\,\text{J}\,\text{cm}^{-2}$. The high energies involved provoke the formation of a plasma between target and substrate, and the whole process is thus far from equilibrium. The deposition takes place in a vacuum chamber to prevent any other species to soil the in-formation thin film. Only an eventual additional gas (composed of pure O_2, N_2, H_2, Ar, or even a mixture of several of them) is sometimes injected into the chamber in order to be incorporated in the film lattice and/or to reduce the kinetic energy of the ablated species coming from the target.

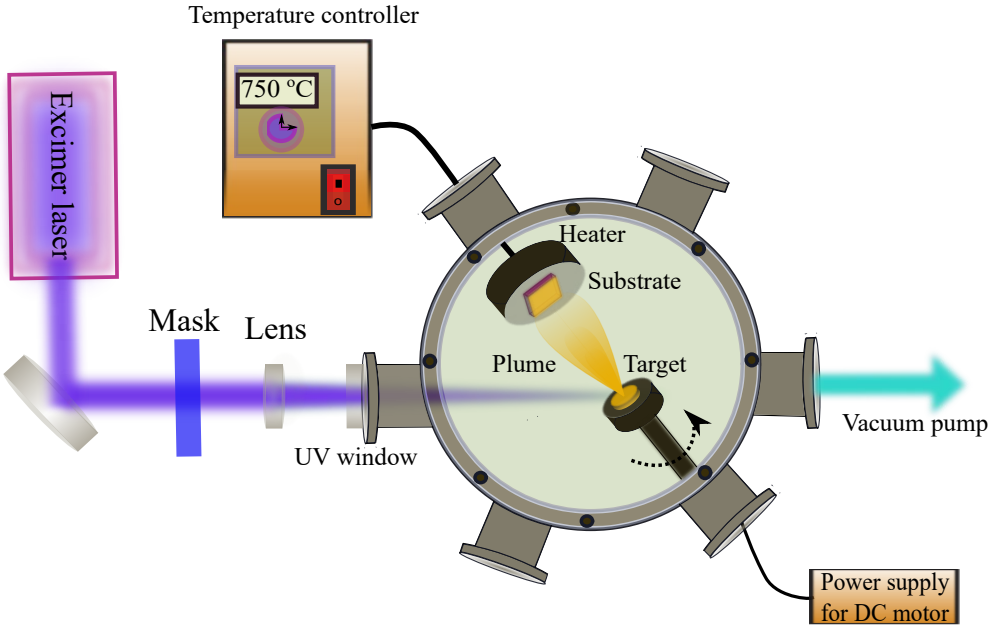

FIGURE 2.1: Sketch illustrating the PLD setup at ICMAB, operating an excimer KrF laser (248 nm). Courtesy of Dr. Mengdi Qian.

When the atoms reach the substrate surface they can undergo adsorption, desorption, diffusion, nucleation... (as depicted in Figure 2.2a). These mechanisms, and subsequently the growth mode, are crucially influenced by the substrate temperature, which is typically brought to several hundreds of degrees to facilitate the atoms mobility, and some other parameters such as the laser frequency (typically $1-10\,\text{Hz}$) and so on.

In short, a thin film can grow in several manners (see sketch Figure 2.2b):

- Layer-by-layer growth. In this 2D growth mode, adatoms first form small islands, until the surface has a critical density of islands and they start coalescing and cover the whole surface.
- Island growth, which is 3D growth mode where the attraction between adatoms is stronger that their attraction to the substrate atoms. As a consequence, they tend to form islands and this growth mode usually leads to higher film roughness and more defects.
- A mixture of the two previous ones (2D-3D), where the growth starts 2D but later on forms islands.
- Step-flow growth. Another 2D growth mode, this one is related to the miscut of the substrate. Because the single-crystal substrates are not perfectly cut along a crystallographic plan, their surface possesses atomically flat terraces separated by atomic steps. When the 2D growth is step-flow-like the adatoms diffuse on a terraces until they reach an edge (a step to the next terrace).

The deposition parameters of the PLD setup have a major role on the thin film deposition as they affect the growth conditions such as: kinetic energy of the incoming atoms, film growth rate and growth mode, etc. It is therefore necessary to adjust them until finding the growth window allowing optimal film quality. These parameters are:

- Substrate temperature
- Distance between target and substrate
- Choice of gas (O_2, Ar...) and pressure
- Laser parameters: laser fluence, pulse repetition rate (frequency), etc.
- Temperature ramping rates, post-annealing...

The PLD technique offers other advantages such as the possibility to grow in-situ heterostructures, by means of a carousel carrying up to six targets. Patterned films can also be grown by using a shadow mask (as shown in 2.3.3).
All in all, PLD is a versatile technique which allow the deposition of nanometric films of high crystallinity due to the many parameters allowing to tune the growth fashion.
In this work, two PLD setups have been used. One is located at the Thin Films Laboratory of ICMAB operated by Raúl Solanas and supervised by Dr. Florencio Sánchez. The second one at the Institute of Materials Science of the Technische Universität Darmstadt, in collaboration with the group of Prof. Lambert Alff.

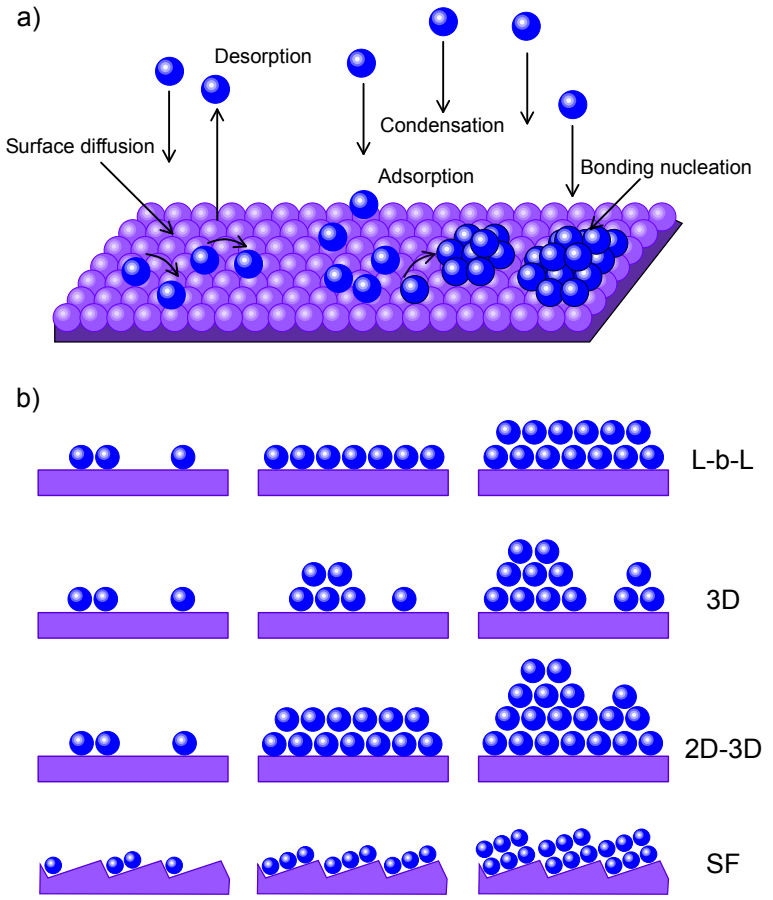

FIGURE 2.2: a) Sketch of the different mechanisms undergone by atoms reaching the substrate surface. b) Different possible growth modes.

2.1.2 Sputter deposition of metals

Sputter deposition (or sputtering) is another well-known PVD technique. Its principle is similar to PLD in the sense that a target material is ablated and the products of the ablation are deposited onto a substrate material. The difference resides in how the target's material is extracted. While in PLD, the ablation is done by a laser, for sputtering an inert gas (typically argon) is first introduced in the chamber and then ionised by high electromagnetic fields, thus forming a plasma. The plasma is then confined near the target material (the cathode) and its particles bombard the latter, thus provoking its "erosion". The target material eroded during this process is deposited onto the substrate (the anode), which is placed in front of the target.
The setup used at ICMAB is a radio frequency (RF) magnetron sputtering system (with a RF voltage of 13.56 MHz). The magnetron generates magnetic fields to

confine the plasma closer to the target. The particularity of RF sputtering being that the electrical field between target and substrate is AC. Such AC voltage allows to avoid accumulation of charges at the target material if the latter is insulating. Therefore, the advantage of this technique is to be able to sputter both conducting and insulating targets.

In this thesis, Pt sputtering was performed at room temperature. An argon pressure of 5×10^{-3} mbar was introduced in the sputtering vacuum chamber where a base pressure of $\approx 10^{-6}$ Torr was reached beforehand. The target to substrate distance is ≈ 5 cm and the sputtering power was of 10 W. Under these conditions the Pt growth rate was ≈ 0.36 Å/s (i.e. about 1 nm in 28 s).
As further explained in Chapter 8, Pt electrodes were deposited ex-situ on top of some oxides (namely $LaVO_3$ and $LaFeO_3$) to study their electrical properties (photoresponse, etc.) in a multilayer fashion. A 300 mesh TEM grid was used as shadow mask allowing to deposit about 400 electrodes (60 µm × 60 µm, 15 µm apart). On the other hand, when the deposition of a continuous Pt layer was necessary, the sample was transferred in situ from the PLD chamber to the sputtering chamber, without breaking the vacuum.

2.2 X-ray diffraction techniques

Throughout this thesis, X-ray diffraction (XRD) techniques have been used to characterize the crystalline quality of thin films. Typical informations that XRD techniques allow to have an insight on include: film thickness, film texture, preferred orientation, epitaxial quality, presence of defects, presence and identification of secondary phases, etc. In addition, XRD measurements were used for phase identification in polycrystalline powder samples measured during the fabrication process of PLD targets (detailed in Appendix A). Hereafter, a brief introduction to the fundamentals of XRD and the scanning geometries are given. For more details, the reader can refer to [49–52].

The XRD phenomenom is based on the elastic scattering of X-ray waves by the atoms in a lattice. When the incident X-rays hit a particular family of parallel crystallographic plans of atoms, constructive interferences between scattered X-rays may occur if the Bragg condition holds. This latter is defined by the Bragg's law:

$$n\lambda = 2\, d_{hkl} \sin\theta \tag{2.1}$$

where $n\lambda$ is the optical path difference between incident and diffracted X-rays (n being positive integer and λ the wavelenghth of the incident X-rays), θ the angle between the sample surface and the incident beam (see Figure 2.3). d_{hkl} is the interplanar distance between crystallographic planes of atoms with Miller indices (hkl) which, in orthorhombic systems (such as the perovskite structure), is defined as:

$$\frac{1}{d_{\text{hkl}}^2} = \frac{h^2}{a^2} + \frac{k^2}{b^2} + \frac{l^2}{c^2} \tag{2.2}$$

where (a, b, c) are the unit cell parameters and (h, k, l) the Miller indices corresponding to the $[hkl]$ the crystallographic direction.

Typically, the diffraction conditions are expressed in term of *reciprocal* space, which is a Fourier transformation of the *real* space (the lattice of atoms).[1] One can define the reciprocal space vector $\vec{Q}_{\text{hkl}}$, perpendicular to the planes with Miller indices hkl, as a function of d_{hkl}:[2]

$$d_{\text{hkl}} = \frac{2\pi}{|\vec{Q}_{\text{hkl}}|} \tag{2.3}$$

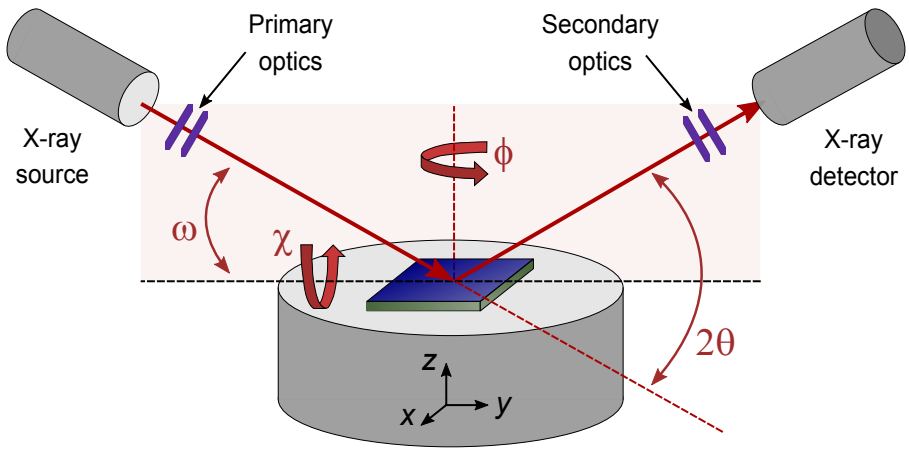

FIGURE 2.3: Sketch of typical XRD measurement setup, illustrating the main components and different angles that can be adjusted.

[1] For more details, one can refer to [50] for instance.
[2] Nothe that, depending on the convention used, the factor 2π may disappear [50].

A typical XRD measurement setups usually contains the following components: a X-ray source and detector, eventually equipped with some optics to ensure the beam is monochromatic and parallel, and a sample stage, usually a goniometer that allows sample rotation; all elements being within the same plane as depicted in Figure 2.3. The angle ω is defined as the angle between the incident beam and the sample surface, while 2θ is the angle between the incident and reflected beams; the sample can be rotated via the angles ϕ and χ. In this work, several diffractometers (summarized in Table 2.1), using different optics and detectors, were used to probe the film quality.

Setups (location)	**Measurement configurations**	**Measured materials**
Bruker D8 Discover (ICMAB)	$\theta-2\theta$, ω-scans, XRR	SVO (chap. 4–6), SNO (series B), BLSO, LFO
PANanalytical X'Pert MRD (ICN2)	$\theta-2\theta$, ω-scans, RSM	SVO (chap. 3–5)
Rigaku Smartlab (T. U. Darmstadt)	$\theta-2\theta$, ω-scans, XRR	SNO (series D)
Siemens D5000 (ICMAB)	$\theta-2\theta$, ω-scans, XRR. $\theta-2\theta$	LVO. Powders (appx. A)
Bruker AXS D8 Advance with GADDS 2D detector (ICMAB)	2θ–χ, RSM	SVO, SNO (series B), BLSO, LFO, LVO

TABLE 2.1: Description of the different diffractometers used in this work, together with measurement configurations and measured materials. All setups operate with a copper source that has three characteristic emission lines: Cu-K_{α_1} ($\lambda = 1.5406$ Å), Cu-K_{α_2} ($\lambda = 1.5418$ Å) and Cu-K_{β} ($\lambda = 1.3922$ Å). The three first diffractometers have the highest resolution, as the K_{α_2} and K_{β} radiations are filtered out by the primary optics.[3]

2.2.1 Texture quality and *c*-axis determination

In a diffraction experiment, the scattering vector $\vec{S}$, is defined as:

$$\vec{S} = \vec{k}' - \vec{k} \tag{2.4}$$

where $\vec{k}$ and $\vec{k}'$ are the wave vectors of the incident and diffracted beam, respectively. The direction and norm of $\vec{S}$ can be tuned by varying ω and 2θ, and its coordinates can be calculated in reciprocal lattice units as [50]:

$$\vec{S}_x = \frac{2\pi}{\lambda}[\cos(2\theta - \omega) - \cos(\omega)] \tag{2.5}$$

$$\vec{S}_z = \frac{2\pi}{\lambda}[\sin(2\theta - \omega) + \sin(\omega)] \tag{2.6}$$

Using the reciprocal space notations, one can then rewrite Bragg's law as:

$$\vec{S} = \vec{Q}_{hkl} \tag{2.7}$$

which indicates that the Bragg condition is fulfilled when the probing vector $\vec{S}$ coincides with a vector $\vec{Q}_{hkl}$ of the reciprocal space (as defined in Equation 2.3).

The out-of-plane crystallinity of the sample can be probed by doing a θ–2θ scan, which consists in keeping $\omega = \theta$ and thus $\vec{S}_x = 0$ and $\vec{S}_z$ is along $\vec{q}_{001}$ (see Fig. 2.4a). In other words, to perform such scan the source and the detector are moved in a symmetric way. The probing direction of the reciprocal space being out-of-plane, the interplanar distances d_{00l} (between crystallographic planes parallel to the sample surface) can be obtained from the corresponding $(00l)$ diffraction peaks; which in turn allow to retrieve the out-of-plane lattice constant, or *c-axis*, of the sample (typically a [001]-oriented film) by using Equations 2.1-2.2.[4]

It should also be added that a broadening of $(00l)$ diffraction peaks in a θ–2θ scan may be observed if there is a variation of *c-axis* (due to strain relaxation, etc.).

[3] In Chapter 4, the presence of other spurious emission lines is envisaged (when measurements were performed with the Bruker D8 Discover).

[4] In the thesis, most of the *c*-axis values was extracted from the position of the (002) diffraction peak. In Chapter 6, they were calculated by using the Nelson-Riley method to minimize some systematic errors due to the instruments, sample curvature and misalignment, etc. [53]. In this latter, all $(00l)$ (l = 1,2,3,4) peaks are used to extrapolate the *c*-axis (see for instance [54] for more details on the procedure.

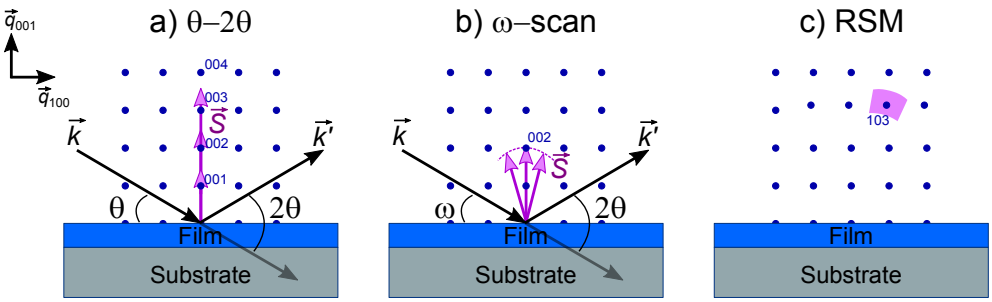

FIGURE 2.4: Sketches illustrating the different scanning geometries used for XRD measurements.

Assessment of crystallite tilting by ω-scan

Once a $\theta-2\theta$ scan has been performed and the $(00l)$ film reflections have been observed, one can performed an asymmetric ω-scan (also called *rocking curve*). This latter consists in keeping the angle 2θ fixed at a position where a diffraction peak was observed in the $\theta-2\theta$ scan,[5] and varying ("rocking") ω around the value of θ. A sketch of the measurement is shown in Figure 2.4b.
By doing so, one can measure an eventual elongation of the reciprocal space point (as indicated by the dashed line in Fig. 2.4b) that would result from diffracting planes slightly tilted compared to the substrate surface (tilted crystallites). Such planes with tilted c-axis would create tilted diffraction points, that would result in a continuous broadening of the main (hkl) spots.

PLD target crystallinity

The measurements on powder samples measured during the PLD target preparation (Appendix A) were also done in $\theta-2\theta$ scanning geometry. A typical powder sample is polycrystalline, with crystallites oriented in all directions. Therefore, while performing a $\theta-2\theta$ scan, all families of crystallographic planes $[hkl]$ produce diffraction peaks. As each compound has a specific set of Bragg diffraction peaks (varying in position and intensity), by analysing a powder diffraction spectrum one can thus identify which phases are present in the powder sample.[6]

[5] In perovskite samples, the diffraction peak corresponding to the (002) reflection of the reciprocal space is often chosen, as it usually displays the highest intensity.

[6] Here, the analysis of powder diffraction spectra was done with SIeve+ software from the International Centre for Diffraction Data (`www.icdd.com/pdf-4-support-software/`).

2.2.2 Reciprocal space maps and *a*-axis determination

A more visual picture of a portion of the reciprocal space around a particular point can also be obtained by combining the two previous measurements. If a series of $\theta-2\theta$ scans with different ω angle is performed around a point of the reciprocal space (typically (103) in perovskite, as depicted in Fig. 2.4c), one can reconstruct an image, a *map*, of the diffracting intensity versus q_{001} (or q_x) and q_{100} (or q_z) directions.[7] Equivalently, the mapping can consist of several ω-scans changing the 2θ angle.

The acquisition of a *reciprocal space map* (or RSM) is often performed in order to determine the in-plane strain state and thus calculate the in-plane lattice parameter (or *a*-axis) of the film. Nonetheless, if the system is not cubic or if one suspects any in-plane anisotropy, one can measure other spots of the reciprocal space. For instance, in addition of the (103) spot, one could measure the $(\bar{1}03)$ or even the one (013) and $(0\bar{1}3)$ after rotating the sample of 90° in-plane (ϕ angle).[8]
In the case of the (103) diffraction spot, using Equations 2.2-2.3,[9] one gets:

$$|\vec{Q}_{103}|^2 = \frac{1}{a^2} + \frac{9}{c^2} \tag{2.8}$$

which is equivalent to:

$$|\vec{Q}_{100}|^2 + |\vec{Q}_{003}|^2 = \frac{1}{a^2} + \frac{9}{c^2} \tag{2.9}$$

and can be decomposed and reformulated to access the (a, c) lattice constants, as:

$$a = \frac{1}{|\vec{Q}_{100}|} \quad \text{and} \quad c = \frac{3}{|\vec{Q}_{003}|} \tag{2.10}$$

2.2.3 Detection of secondary phases

The detection of secondary was done using a diffractometer equipped with a 2D detector (a Bruker D8 Advance equipped with a General Area Detector Diffraction Systems, shortened GADDS, detector, see Table 2.1). This latter can detect photons with a wide angular range (up to 30° in 2θ and 60° in χ), which is particularly useful to quickly access the texture quality of films, detect and identify secondary phases, etc. The typical measurement (called 2θ–χ frame in the thesis) is similar to a $\theta-2\theta$ scan. The advantage of these measurements is the possibility to access crystallites that are tilted regarding the χ angle (see Figure 2.3). These crystallinites

[7] By converting the ω and θ angles to q_x and q_z, respectively, using Equations 2.5-2.6.

[8] Other types of measurements such as ϕ-scan and pole figures, although not used in this work, can be done to confirm for instance that a film was grown epitaxially onto a substrate.

[9] Note that the factor 2π was removed for the sake of simplicity.

can be made of the main phase (in that case the sample is single-phase but polycristalline) or of secondary phases. For instance, in the case of $SrVO_3$ films, the presence of the spurious $Sr_3V_2O_8$ phase (which formation depend on the growth conditions) resulted in the observation of diffraction spots out of the diffraction plane perpendicular to the sample surface (that was probed in the classical $\theta-2\theta$ geometry, where $\chi = 0$). This is further discussed in Chapters 3-4.

2.2.4 Thickness determination

In this thesis, the film thickness was determined either by fitting of Laue oscillations or by X-Ray reflectometry (XRR).

Laue fringes are a typical feature resulting from the constructive interference of the diffracted X-rays, usually visible when the film as high crystalline quality and displays flat surface and interface with the substrate. Subsequently, oscillations may accompany the diffraction peaks in a $\theta-2\theta$ scan, and can be fitted to extract the film thickness using the formula:

$$I(\vec{Q}) = \frac{\sin^2\left(\frac{1}{2}\vec{Q}Nc\right)}{\sin^2\left(\frac{1}{2}\vec{Q}c\right)} \tag{2.11}$$

where N is the number of unit cells along the $[00l]$ direction, c is the out-of-plane lattice constant, and $\vec{Q}$ is the reciprocal lattice vector, defined as $\vec{Q} = 4\pi\sin(\omega)/\lambda$, where λ is the incident X-ray wavelength. Subsequently, one can extract the thickness $t = Nc$.[10]

On the other hand, XRR was also used to determine the film thickness. XRR is based on the specular reflection of incident light (here X-rays) between two media with different refractive indices. In addition to the film thickness this technique can give us information on the film density, and the roughness of the substrate/film and film/air (surface) interfaces. The measurement consists in a $\theta-2\theta$ but at grazing incidence (with very low incident angle, typically $0° < 2\theta < 6°$). Below a critical angle θ_c (usually around 0.2-0.5°), the X-rays are fully reflected by the surface, but when $\theta > \theta_c$, they start being being refracted and the specularly reflected intensity decreases proportionally with θ^4: this is the so-called Fresnel reflectivity. Superimposed to this decreasing *enveloppe*, an interference pattern (sometimes called *Kiessig fringes*) may be visible, emerging from the scattering at the different above-mentioned interfaces.

[10] As shown in Chapter 4, another more complex fit including the substrate contribution can also be attempted, using the script developped by Pesquera et al. [55].

The condition for constructive interference is given by the following relation [50]:

$$\frac{m_i^2 \lambda^2}{(2t)^2} = (\theta_i^2 - \theta_c^2) = (\sin^2\theta_i - \sin^2\theta_c) \tag{2.12}$$

where t is the film thickness, λ is the incident X-ray wavelength, and θ_i is the angle of an oscillation maximum i of order m_i. Therefore, by plotting $\sin^2\theta_i$ vs m_i^2 for all the successive maxima visible, one should expect a linear scatter plot with slope equal to $\lambda^2/(2t)^2$, from which the film thickness t can be extracted. In this thesis, the film thickness was either extracted by this method or by a fitting of the XRR spectrum using GenX software [56].

2.3 Electrical measurements

Transport measurements have been an important part in the characterization of metallic single layers. Indeed, as we mentioned before, a considerable part of the growth optimization of TCO thin films consists in maxing out their electrical conductivity. However, in order to have a deeper insight into their properties, one also needs to investigate the nature of the carriers, their mobility, their effective mass, etc. The measurements techniques allowing us to access these properties are described in the following sections 2.3.1 to 2.3.2. Finally, in the section 2.3.3, details of the electrical measurements performed to study the photoresponse in all-oxide or oxides/metal multilayers are given.

2.3.1 Resistivity, Hall effect and magnetoresistance measurements by Van der Pauw method

The Van der Pauw method is a technique used to measure the resistivity and Hall coefficient of samples with an arbitrary 2D shape (e.g. a thin film with square, rectangular, spherical, or some more random shape). However, the sample has to be homogeneous in thickness and composition, and present no holes [57, 58]. Such technique uses four contacts which is necessary to measure samples with low resistivity. Two contacts inject a current while two others measure a voltage. In this way, one can avoid the parasitic contact and lead resistance. In the Van der Pauw geometry, the contacts have to be placed at the circumferences of the sample. In our case, we use 5×5 mm² square samples and contacts were placed in each corner (see Figure 2.5). Ohmic contacts were made by applying conductive silver paint, making sure that they had a relative small size ($\approx 500\times500\,\mu$m²) compare to the sample size, or by sputtering Au contacts with a shadow mask (for SNO films grown and characterized at TU Darmstadt).

All temperature-dependent measurements were performed in a Physical Properties Measurement System (PPMS) from Quantum Design. The accessible range of temperature is 2-400 K, and the magnet delivers a magnetic field up to ± 9 T. A Lakeshore EMPX-HF probe station connected to a Keithley 2611B System SourceMeter was also used to perform RT-resistivity measurements. Both PPMS and Lakeshore setup gave same RT-resistivity values for a given sample.

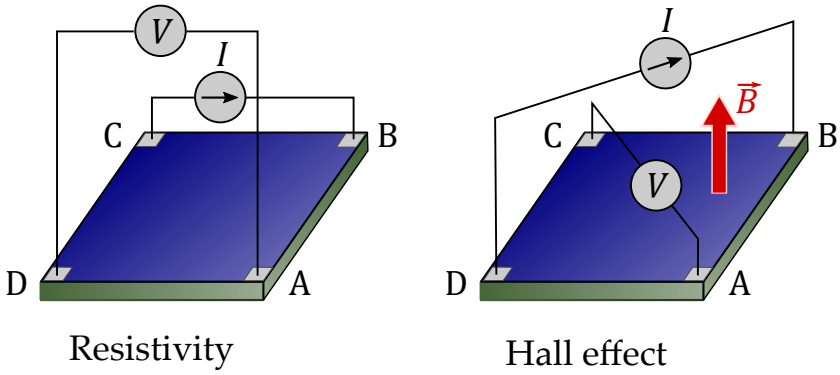

FIGURE 2.5: Sketches of a sample with electrical contacts and wired for Van der Pauw measurements of resistivity (left) or Hall effect (right).

Electrical resistivity

Van der Pauw demonstrated that the resistivity ρ of a sample of thickness t is given by the following expression:

$$\exp\left[\frac{-\pi t}{\rho}R_{\mathrm{AB,CD}}\right]+\exp\left[\frac{-\pi t}{\rho}R_{\mathrm{BC,DA}}\right]=1 \tag{2.13}$$

where $R_{\mathrm{AB,CD}} = V_{\mathrm{CD}}/I_{\mathrm{AB}}$ and $R_{\mathrm{BC,DA}} = V_{\mathrm{DA}}/I_{\mathrm{BC}}$ (as sketched in Figure 2.5). In order to facilitate the calculation of the resistivity ρ, Van der Pauw reformulated Equation 2.13 as follows:

$$\rho=\frac{\pi t}{\ln 2}\frac{(R_{\mathrm{AB,CD}}+R_{\mathrm{BC,DA}})}{2}f(R_{\mathrm{AB,CD}},R_{\mathrm{BC,DA}}) \tag{2.14}$$

where $f(R_{\mathrm{AB,CD}},R_{\mathrm{BC,DA}})$ is a function of the ratio $R_{\mathrm{AB,CD}}/R_{\mathrm{BC,DA}}$ (assuming that $R_{\mathrm{AB,CD}} \geq R_{\mathrm{BC,DA}}$) defined as:

$$\frac{R_{\mathrm{AB,CD}}-R_{\mathrm{BC,DA}}}{R_{\mathrm{AB,CD}}+R_{\mathrm{BC,DA}}}=f\,\mathrm{arccosh}\left[\frac{\exp(\ln 2/f)}{2}\right] \tag{2.15}$$

Equation 2.15 has been plotted in Figure 2.6. One can notice that $f = 1$ in the particular case that $R_{AB,CD}/R_{BC,DA} = 1$, which is the case for a perfectly square sample.

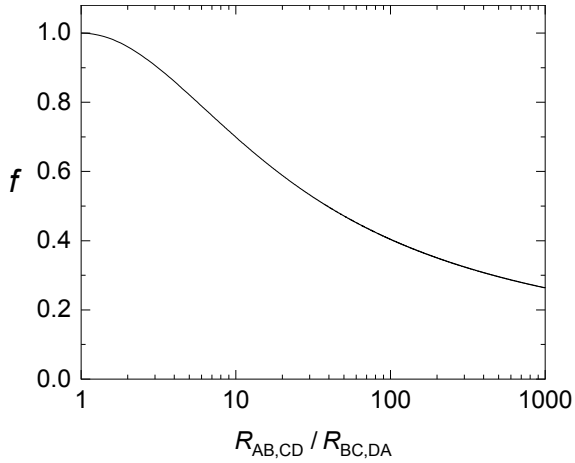

FIGURE 2.6: Function f computed for different values of $R_{AB,CD}/R_{BC,DA}$ from Equation 2.15.

Note that the resistances $R_{AB,CD}$ and $R_{BC,DA}$ should remain identical upon changing the current polarity which is systematically verified when performing measurements (also in the Hall effect configuration explained below).

Hall effect

The Hall effect occurs when a current I of charge carriers (of charge q) flowing through a sample, along a direction represented by their velocity vector $\vec{v}$, is deflected by an external magnetic field $\vec{B}$ as a result of the Lorentz force $\vec{F}_L$:

$$\vec{F}_L = q(\vec{E} + \vec{v} \times \vec{B}) \tag{2.16}$$

The charges are indeed deflected according to the right hand rule, i.e. in a direction perpendicular to their initial direction of propagation (i.e. perpendicular to $\vec{v}$), and also perpendicular to the magnetic field $\vec{B}$. This anisotropy of charge creates an electric field $\vec{E}$ parallel to the direction of charge migration which will at some point prevent further migration and lead to an equilibrium state in which the Lorentz force is cancelled out ($\vec{F}_L = 0$). Assuming one type of carriers (e.g. electrons, $q = -|e|$). By solving Equation 2.16 at this equilibrium condition, and assuming one

type of carriers (e.g. electrons, $q = -|e|$), it can be rewritten as:

$$V_H = \frac{R_H I B}{t} \tag{2.17}$$

where V_H is called Hall voltage, I is the injected current, B is the intensity of the applied magnetic field, t is the sample thickness and R_H is the Hall resistance, defined as:

$$R_H = \frac{-1}{n_H |e|} \tag{2.18}$$

n_H the Hall charge carrier density and e the elementary charge.

In practice, one measures the resistance $\tilde{R} = V_H / I$ (where I is an alternating current) as a function of applied magnetic field B. Similarly to the resistivity measurements explained above, the Hall measurements are performed in two contact configurations: $R_{BD,AC} = V_{AC} / I_{BD}$ and $R_{AC,BD} = V_{BD} / I_{AC}$ (as depicted in Fig. 2.5), that are then averaged out, so that: $\tilde{R} = (R_{BD,AC} + R_{AC,BD})/2$.
The slope R_H / t of the $\tilde{R} = (R_H / t)B$ is extracted from a linear fit, according to Eq. 2.17. Then n_H can be calculated by using Eq. 2.18 and the film thickness t measured beforehand (see Section 2.2.4).

Magnetoresistance

The magnetoresistance (MR) is the change of resistivity (longitudinal resistance) of a material observed under application of an external magnetic field, perpendicular to the current flow direction.
While the MR of a free gas of electrons is expected to be zero, it is common to observe a small positive MR in metallic samples [59]. This is due to the contribution of different types of carriers to the charge transport.

It this work, the MR was measured in the same configuration than the resistivity, as described above, but under an external magnetic field applied out-of-plane (see Figure 2.7) and varied between ± 9 T.

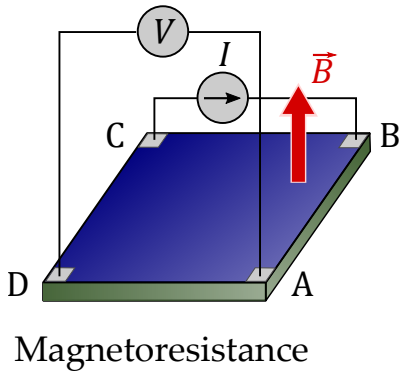

FIGURE 2.7: Sketch of a sample with electrical contacts and wired for magnetoresistance measurements using Van der Pauw method.

2.3.2 Seebeck coefficient measurements

In this work, the measurements of Seebeck coefficient were performed by Dr. Francisco Rivadulla, from Universidad de Santiago de Compostela (Spain).

The Seebeck effect is a thermoelectric effect in which an electrical potential difference ΔV appears across two regions of a material as a response to the application of a temperature gradient ΔT between these two points. The resulting Seebeck coefficient is defined as:

$$S = -\frac{\Delta V}{\Delta T} \tag{2.19}$$

This phenomenon is the basis of operation of devices such as thermocouples (temperature sensors). As the Seebeck coefficient is directly related to the carriers transport in metallic thin films, it can also be used to access the effective mass of carriers in metallic thin films such as the TCOs studied in this thesis.

For the measurements of the Seebeck coefficient, two Cr/Pt (5/50 nm) lines with four contacts (1 mm × 50 mm, 2 mm apart) were deposited by optical lithography on top of the film (see illustrative sample Figure 2.8). After deposition, a current of 1 mA was driven through the Pt lines at room temperature during 5 min to favor the recrystallization of Pt. The temperature dependence of the resistivity of each Pt line was measured in several cooling/heating ramps, until obtaining a reproducible result. The Pt resistivity was finally recorded on a heating ramp at 0.5 K/min and the recorded values were used as local thermometers. Two voltage contacts were also deposited at the vicinity of the thermometers (see Figure 2.8). Finally, a heater of the same composition was simultaneously deposited apart from the thermometers and voltage contacts, and isolated by cutting the thin film with a diamond tip glass cutter, to make sure that the current flowing through

the heater does not leak to the temperature/voltage probes. To generate heat, the resistance R of the heater is first measured. Then a constant current I is driven through it, dissipating a power $W = I^2 \times R$, and a thermal gradient is generated between the temperature/voltage probes. This gradient is expected to vary linearly with W. By checking this linearity, one can therefore make sure of measuring a purely thermoelectric effect, with no current leakage through the film.

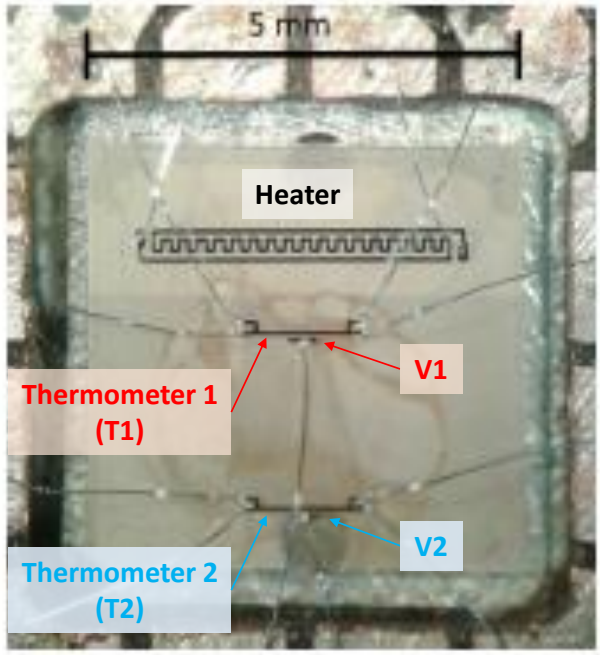

FIGURE 2.8: Micrography of a $SrVO_3$ sample prepared for Seebeck measurements. The patterns on top of the film were deposited by lithography as described in the text.

Before each Seebeck measurement, the sample was stabilized at the base temperature for at least 15 min to ensure the absence of spurious thermal gradients that could influence the determination of the intrinsic Seebeck voltage. Different currents were injected through the heater until a constant temperature difference between the Pt thermometers was achieved. The voltage between the Pt lines is measured at the same position with a switch. Fitting the voltage vs temperature difference provides an accurate measurement of the Seebeck coefficient (see Figure 2.9).

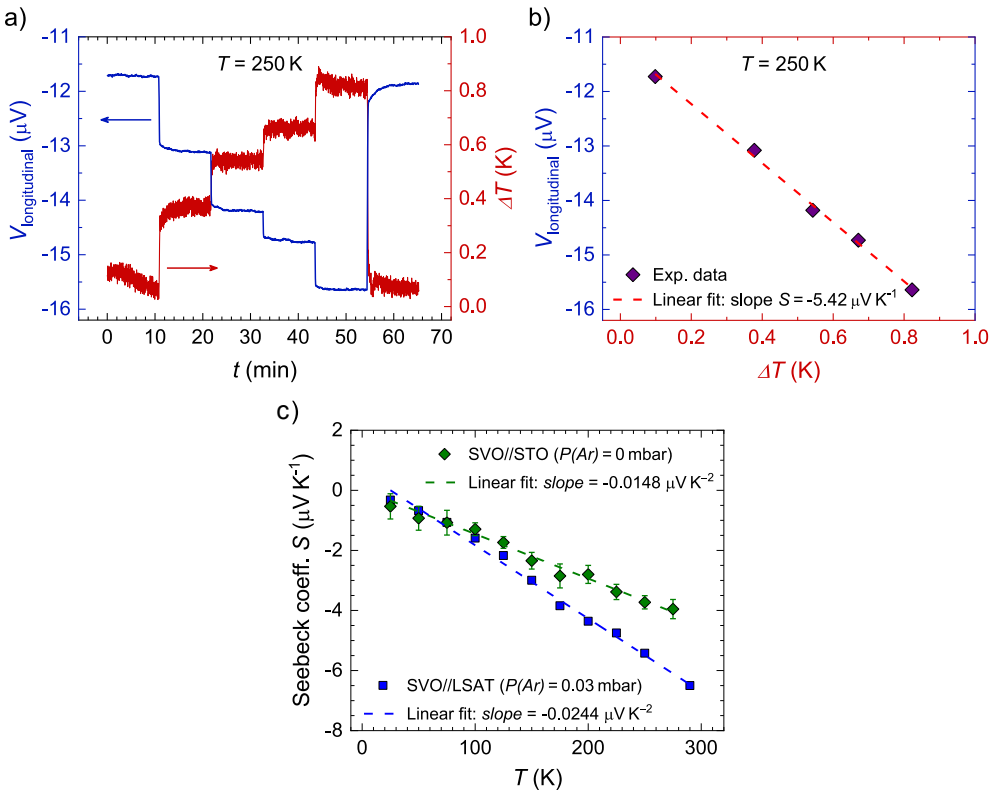

FIGURE 2.9: a) Steps of temperature difference between the Pt resistances and the corresponding longitudinal thermoelectric voltages, at a base temperature of 250 K, for one illustrative SVO sample. b) Linear fit of the longitudinal voltage vs temperature difference. The accuracy of the method allows a good measurement of the Seebeck coefficient without increasing much the temperature difference (always lower than 1.5 K), ensuring the reversibility of the process. In this example a Seebeck coefficient of $S = -5.52\,\mu V\,K^{-1}$ at $T = 250$ K was extracted. c) Temperature dependence of the Seebeck coefficient S measured on illustrative SVO films ($t \approx 70$ nm thick), deposited on LSAT and STO substrates, having different carrier density $n = 2.13\text{x}10^{22}$ cm^{-3} and $n = 2.56\text{x}10^{22}$ cm^{-3}, respectively.

2.3.3 I-V characteristics and photoresponse in metal-insulator-metal multilayers

One of the main goals of this thesis has been to build and characterize all-oxide metal-insulator-metal (MIM) heterostructures, in which the insulator is photoabsorbing and therefore a photoresponse is expected (a sketch of the device structure is shown in Figure 2.10). Such MIM device behaves as a capacitor and thus $I-V$

characteristics are expected to be more complex that the linear $I-V$ behavior of a simple (ohmic) resistor for instance. In fact, the shape of the dark $I-V$ curves can give crucial information on the electronic structure of the whole structure (rectifying behavior and presence of built-in potential V_{BI}, etc.). Moreover, in order to investigate the potential of oxide-based heterostructures as photovoltaic cells, one is usually interested in measuring typical values - which are key indicators of the solar cell yield - such as the open-circuit voltage V_{OC}, the short-circuit photo-current J_{SC}, fill-factor FF, etc. extracted from measurements of $I-V$ characteristics under illumination.

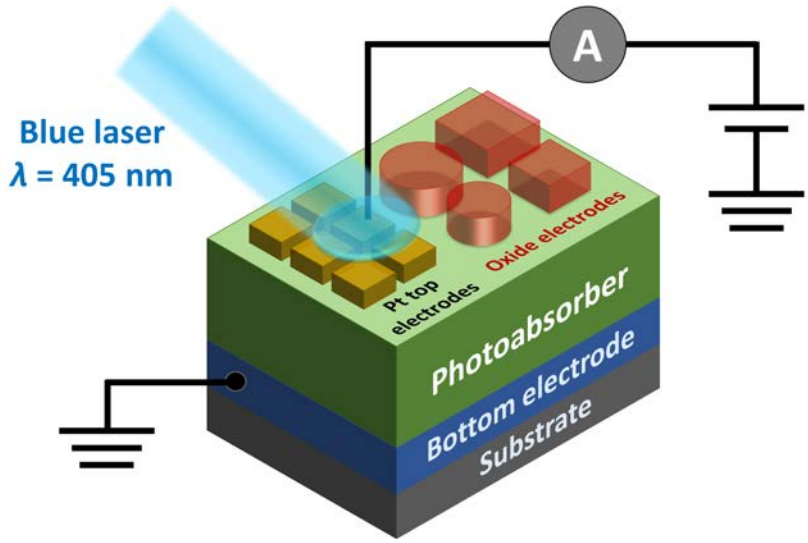

FIGURE 2.10: Sketch of typical device to measure photoresponse in MIM heterostructures. The bottom electrode and photoabsorbing layer are complete layers covering the whole substrate while the top electrodes are obtained by patterning via shadow mask. For electrical measurements, the bottom electrode is usually connected to the ground, and the top contacts are connected to the setup electronics. During photoresponse measurements the top contact is shinned by a laser beam (with cross-section area greater than the contact area).

The MIM heterostructures were prepared as follow: bottom electrode and photoabsorber layers were first deposited in a single step. Then the samples were removed from the PLD chamber, where a shadow mask (either for Pt or oxide electrodes) was mounted ex situ. Then the sample was either loaded to the sputtering chamber for Pt deposition (see Section 2.1.2 for details on sputtering parameters),

or back to the PLD chamber for deposition of a TCO material as top electrode (Figure 2.11).

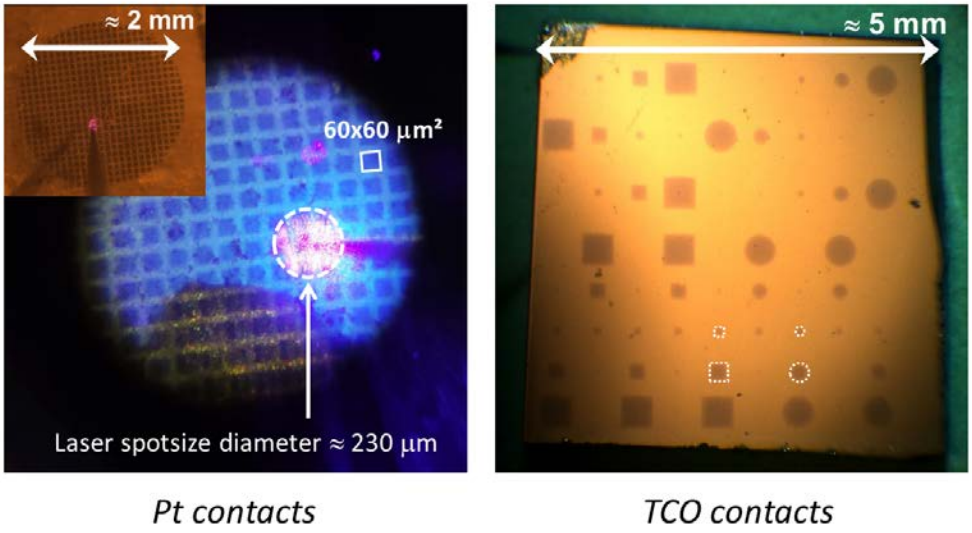

FIGURE 2.11: Electrical contacts deposited on top on the bottom electrode/photoabsorber stack, using a shadow mask. Left: micrography of sputtered semi-transparent Pt electrodes for electrical characterization. Right: micrography of PLD-deposited TCO contacts. "Useful" contacts are circled in white.

Here, the two-point-measured $I-V$ characteristics, with or without illumination, were performed in top-bottom configuration (Fig. 2.10), using gold-plated tungsten probe tips with a tip radius of 10 µm. A Keithley 6517B Electrometer/High Resistance Meter was used to apply a bias voltage V (usually performing a loop between −1 V and +1 V) and measure the resulting current I flowing through the MIM structure. The illumination was done using a monochromatic blue laser ($\lambda = 405$ nm, $E = 3.06$ eV) operating with a power of ≈ 20 mW (as priorly measured with a photoresistor). Considering the approximate diameter of the laser spot (≈ 230 µm), the corresponding power density was estimated to be $\approx 0.55\,\mathrm{W\,cm^{-2}}$. The Pt contact size is $60\times60\,\mu\mathrm{m}^2$. For TCO, the measured electrodes were either $100\times100\,\mu\mathrm{m}^2$, $200\times200\,\mu\mathrm{m}^2$ squares or round shapes with diameter of 100/200 µm. Bigger electrodes were not considered as the laser beam had an approximate diameter of ≈ 230 µm (as visible on the left picture of Fig. 2.11). When measuring TCO contacts, a similar current density was measured for no matter the contact area, indicating the absence of microcracks or pinholes in the contact. Typical $I-V$ characteristics in a $LaFeO_3$-based multilayer before and after illumination are shown

in Figure 2.12. The raw current I is indicated on the right y-axis and the current density J (equal to the I divided by the contact area) is shown on the left y-axis.

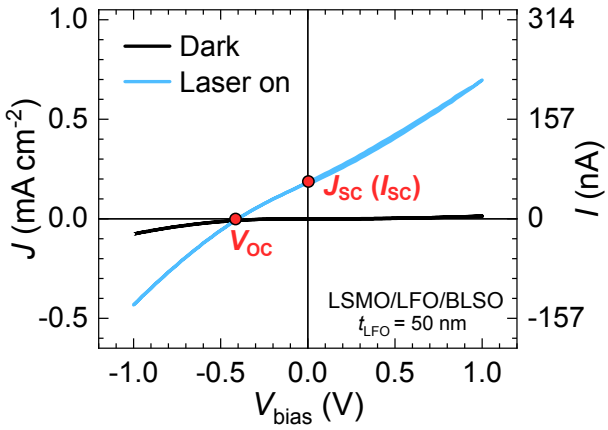

FIGURE 2.12: Example of $I-V$ characteristics measured in a MIM multilayer before and after illumination. Here the top contact (BLSO) diameter was 200 µm. Under illumination, the curve does not cross the origin anymore and the intercept with x- and y-axis are indicated as the open-circuit voltage V_{OC} and short-circuit photocurrent density J_{SC}, respectively.

2.4 Optical spectroscopy techniques

In this work, optical spectroscopy techniques were mostly used to quantify the transparency of single layers of transparent conducting oxides ($SrVO_3$, $SrNbO_3$ and $Ba_{0.95}La_{0.05}SnO_3$). The transparency of these materials is manifested by the onset of high transmittance to the visible light starting above the plasma frequency ω_p and below the band gap energy E_G. Therefore, the following techniques were used either to quantify the percentage of light transmitted in the visible range, or to determine the values of the plasma energy E_{ω_p} and E_G. On the other hand, in photoabsorbing layers ($LaVO_3$, $LaFeO_3$), they were used to extract their absorbance α and also to determine their bandgap E_G.

2.4.1 UV-Vis-NIR spectroscopy

In this work, ultraviolet-visible-near infrared (UV-Vis-NIR) spectroscopy was used to quantify the optical transparency of TCO samples by measuring their transmittance spectrum.

When light interacts with matter, it can be reflected, scattered, absorbed and/or transmitted (as schematized in Figure 2.13). The intensity of light must be conserved through the process, so that the sum of the light intensities of the enumerated processes equals the incident light intensity:

$$I_0 = I_R + I_S + I_A + I_T \tag{2.20}$$

As the experimental setup does not allow to obtain the scattering (diffused) term, we shall neglect this term in the following such that Equation 2.20 becomes:

$$I_0 = I_R + I_A + I_T \tag{2.21}$$

and by dividing on each side by I_0, one obtains the common expression:

$$1 = R + A + T \tag{2.22}$$

where R, A and T stand for reflectance, absorbance and transmittance, respectively.

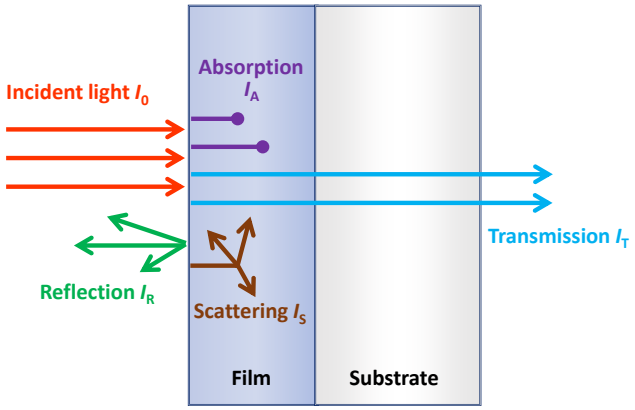

FIGURE 2.13: Light-matter interactions in a system composed of a thin film onto a transparent substrate. Light incidence is normal to the sample surface as in a UV-Vis-NIR experiment. Note that for the sake of clarity the reflection at film-substrate and substrate-air interfaces was omitted in the sketch.

Here, transmittance spectra were measured with either a Jasco V-780 (in the 190-1600 nm range) or with a Agilent Cary 5 (in the 200-800 nm range) spectrometers. Films were deposited on double-side polished substrates (5 mm × 5 mm × 0.5 mm

in size) to maximize substrate transmittance. Prior to film measurement, a reference spectrum, of either an empty sample holder or a pristine substrate, was acquired as background. Then the sample [film + substrate] was measured and the background subtracted, resulting in the transmittance spectrum of either the [film + substrate] system or the "free-standing" film, respectively. The nature of "free standing film" or "[film + substrate]" spectra will be indicated for each measurement.

2.4.2 Spectroscopic ellipsometry

Spectroscopic ellipsometry (SE) is a powerful non-invasive technique to study the optical properties of a material, namely its dielectric function ε. In thin films, it is a particularly useful technique for determining the optical constants and/or film thickness.
In Chapters 3-4-6, spectroscopic ellipsometry was primarily used to determine the plasma energy $E_{\omega_p} = \hbar\omega_p$ of TCO thin films (supposedly in the NIR). In metals, the plasma energy indicates the threshold between reflection of light by the metal (by the cloud of free electrons) and the onset of light penetration into the material, which might then be absorbed or simply transmitted. From the knowledge of the plasma energy and the optical bandgap values, one can therefore determine if the material is transparent to the visible light. Moreover, by combining plasma energy and dc electrical conductivity one can extrapolate the effective mass of the carriers, which can be useful to explain the electrical properties of the material.
As further discussed in Chapter 7, in metallic oxides the origin of the plasmon resonance is sometimes not well understood; and one might want to study the propagation of light of specific polarization (p or s) to answer these questions. In that case, the measured optical constants can also be used to calculate the p- and s-polarized transmittance/reflectance of a film [20].
More generally, SE allows the measure the absorption coefficient α of a material (proportional to the absorption constant κ). In the case of photoabsorbing materials, as those studied in Chapter 8 for instance, α allows to quantify the photoabsorption and to extract the bandgap value via Tauc plots.

Propagation of light through a medium

When an electromagnetic wave carrying electric field **E** and magnetic field **B** interacts with a material, it causes a redistribution of charge and currents in the latter, and its electric and magnetic states are modified as follows:

$$\mathbf{D} = \varepsilon\varepsilon_0\mathbf{E} = \varepsilon_0\mathbf{E} + \mathbf{P} \tag{2.23}$$

$$\mathbf{B} = \mu\mu_0\mathbf{H} = \mu_0\mathbf{H} + \mathbf{M} \tag{2.24}$$

where **P** and **M** are the spontaneous electric and magnetic polarizations of the material, and **D** and **H** are the electric displacement and magnetic induction. Here, two physical quantities have been introduced: the relative permittivity ε and the permeability μ of the material [20]. If we consider a non-magnetic material $\mu = 1$,[11] the relevant information about the propagation of light through the medium is contained in the dielectric constant ε,[12] which is a complex number such that:

$$\varepsilon = \varepsilon_r + \mathrm{i}\varepsilon_i = N^2 = (n + \mathrm{i}\kappa)^2 \tag{2.25}$$

where N is the complex refractive index of the medium; n is the refractive index defined as $n = c/v$ with c the speed of light in vacuum and v the phase velocity of light in the medium; and κ is the absorption constant.

Principle of ellipsometry

Light can be described by plane waves and any ray of light can be expressed a sum of orthogonally polarized plane waves. When light interacts with a medium separated from the air by a planar surface, a common and convenient coordinate frame consists in decomposing the electric field of light **E** in a component parallel $\boldsymbol{E}_\mathrm{p}$ and a component perpendicular $\boldsymbol{E}_\mathrm{s}$ to the plane of incidence.[13]
In general, the $\boldsymbol{E}_\mathrm{p}$ and $\boldsymbol{E}_\mathrm{s}$ components of light propagate differently through a medium and one can define the Fresnel's coefficients as the portion of reflected and transmitted light as:

$$r_{\mathrm{s,p}} = \left(\frac{E_\mathrm{r}}{E_\mathrm{i}}\right)_{\mathrm{s,p}} \tag{2.26}$$

$$t_{\mathrm{s,p}} = \left(\frac{E_\mathrm{t}}{E_\mathrm{i}}\right)_{\mathrm{s,p}} \tag{2.27}$$

where the different E components are depicted in Figure 2.14. (r_p, r_s, t_p, t_s) can be expressed as a function of the real refraction indexes (n) of the two media and the angles of incident, transmitted and reflected beams (see e.g. ref. [20] for the whole expressions).

[11] In ellipsometry for example, the magnetic state of the sample is not affected by light as its magnetic moments are too slow to react to the rapid optical oscillations. Therefore the important quantity is the electric field **E** [60].

[12] The electromagnetic wave equations, derived from Maxwell's equations, describe the propagation of electromagnetic waves through a medium. Their solution is the dispersion relation, which itself depends on the dielectric constant ε

[13] This convention is very convenient as a *p*-polarized (resp. *s*-polarized) component will be reflected/transmitted in a *p*-polarized (resp. *s*-polarized). For this reason those vectors are sometimes called *eigenpolarizations* [61].

Spectroscopic ellipsometry is based on the change of light polarization upon reflection by a medium with optical constants different than air ($n = 1$). The linearly polarized incident light has both p and s components (in phase). Upon reflection both components endure a different change of amplitude and a different phase shift. It results that the reflected light has elliptical polarization (as depicted in Figure 2.14), hence the name *ellipsometry*.
Ellipsometry measures both changes in the form of the complex reflectance ratio [60]:

$$\rho = \frac{r_p}{r_s} = \tan(\Psi)e^{i\Delta} \tag{2.28}$$

where $\tan(\Psi)$ is the difference of intensity, and Δ is the phase shift (see Figure 2.14). r_p and r_s are the reflection coefficients of p- and s-polarized components respectively, as described above, and depend on the optical constants of the material measured.
The asset of ellipsometry is therefore to measure these two values instead of just measuring the change of light intensity upon reflection, as in reflectometry for instance.[14]

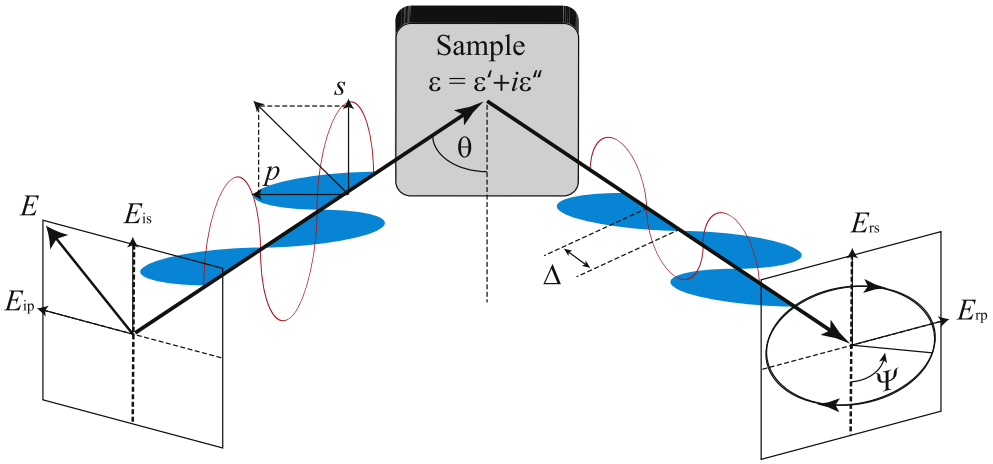

FIGURE 2.14: Sketch of the ellipsometry measurements configuration, adapted from [20]. The p-polarized (in blue) component of both incident and reflected light is in the plane of incidence (perpendicular to the sample surface), while their s-component is perpendicular to that plane.

[14] As explained in details by Oates et al. [20], to determine the dielectric function ε of a material one can either use a combination of reflection and transmission measurement techniques, or ellipsometry. While the first approach requires two different measurements to determine precisely the dielectric function, ellipsometry can give the same information by exploiting the changes in p and s polarized light upon reflection.

In the case of a single interface between air and a bulk isotropic material, the dielectric constant ε can be easily extracted from the measurement of ρ:

$$\varepsilon = \varepsilon_0 \sin^2\theta + \frac{(1-\rho)^2(\sin^2\theta)(\tan^2\theta)}{(1+\rho)^2} \tag{2.29}$$

where ε_0 is the ambient dielectric function ($\varepsilon_0 \approx 1$ for air) and θ is the angle of incidence (see Figure 2.14).
Here, this method was used to determine the pseudodielectric[15] function of our bulk single-crystal substrates.

In the case of a multilayer system, the problem is more difficult as reflection occurs at each interface, thus creating interferences. Here some transfer matrix methods are usually necessary to solve it and extract the optical constants of each layer [20]. However, in the simple case of a single isotropic layer deposited onto a bulk substrate, and where only the surface and the film/substrate interface reflect light, the problem is easier. If the film thickness is known and the substrate optical constants are known (as in our typical film/substrate systems[16]), only the optical constants of the film are unknown. This can be solved by some mathematical inversion as detailed in Ref. [62]. On the other hand, some more extensive data analysis consisting in modeling the dielectric function of the thin film by assuming that its dielectric response follows some specific laws (Drude response, Cauchy law, Tauc-Lorentz model...) can be done.

Measurement procedure and comparison between ellipsometers in the case of $SrVO_3$

Three ellipsometers have been used in this thesis (listed in Table 2.2), either for the sake of reproducibility of the results, to explore a different energy range, or both. Most of measurements were done at the Nanoquim facility at ICMAB, using a Sopralab GES5E Variable-Angle Spectroscopic Ellipsometer (VASE). The data treatment was done by WinElli II software.

All measurements were performed in reflection mode at ambient conditions. The microspot option was used to rule out any eventual backside reflection from the substrate. The measurement procedure was as follow: the ellipsometric angles

[15] In that case we rather refer to the *pseudodielectric* function of the bulk material because any surface layer or roughness has been omitted.

[16] Where we neglect the roughness of the film surface and film/substrate interface, usually in the order of few angstroms (*rms* roughness). Also the substrate backside reflection is considered negligible.

(Δ, Ψ) of "film//substrate" samples and "pristine substrate"[17] were first measured at different incident angles θ_i in the 60-75° range. Optimized conditions were found to be $\theta_i = 65°$ for LAO, LSAT, and NGO and $\theta_i = 68°$ for STO. The pseudodielectric/optical constants of the substrate were first extracted by direct inversion. Then, using the structure air/film/bulk-substrate, dielectric and optical coefficients ($\varepsilon = \varepsilon_1 + i\,\varepsilon_2$ and $N = n + i\,\kappa$) of the films were obtained (assuming isotropic ε) by mathematical inversion (as mentioned above). The extraction was done using WinElli II software. Films thickness was previously determined by XRR and inserted in the structure.

Setups	**Sopralab GES5E (ICMAB)**	**Nanofilm EP4 (Accurion GmbH)**	**Woollam VASE + IR spectrometer**
Energy range (eV)	1.22 – 5.44 (IR–UV)	1.55 – 3.1 (IR–UV)	0.01 – 6.2 (FIR–MIR–UV)
Sample type	SVO//LSAT	SVO//LSAT	SVO//LSAT
Sample geometry	Continuous (5x5 mm²)	Patterned (Hall bars)	Continuous (5x5 mm²)
Growth conditions	$P(Ar) = 0 - 0.1$ mbar	$P(Ar) = 0$ mbar	$P(Ar) = 0.1$ mbar
$E^*_{\omega_p}$ (eV)	1.23 – 1.28	1.20	1.21
Other materials	SVO (chap. 3,5,7) SNO, BLSO, LVO, LFO	SVO (chap. 4)	SVO (chap. 6)

TABLE 2.2: Description of the different ellipsometers used in this work. To emphasize the measurements (including data treatment) reproducibility between the different setups, the screened plasma energy $E^*_{\omega_p}$ of some illustrative SVO films are shown. On the last row, all materials investigated by SE in this work are indicated (most of measurements were performed at ICMAB).

As shown in Chapter 4, some patterned SVO films were measured in a Nanofilm EP4 from Accurion GmbH by Sebastian Funke. Measurements shown in Chapter 6 were done by Dr. Premsyl Marsik (Department of physics, University of Fribourg).

[17] Both pristine substrates and some annealed ones (following the PLD-deposition temperature ramp and in vacuum) were measured, but the data were identical.

They were performed in the far-infrared (FIR) and mid-infrared (MIR) using an IR spectroscopic ellipsometer, based on Bruker Vertex 70v FTIR spectrometer, similar to one described in Ref. [63], while the near-infrared to UV part of the spectrum was determined with Woollam VASE.

2.4.3 Polarization-dependent transmittance measurements

Polarization-dependent measurements of the transmittance were carried out by illuminating the samples with *p*- or *s*-polarized light from a halogen lamp via a small pinhole which ensured that only the sample was under illumination. The sample was placed to an angle of 30° with respect the incoming light beam and the transmitted light was collected and analyzed with a spectrometer. The spectrum of the transmitted light was normalized to the lamp spectrum, yielding the transmission spectrum of the multilayer system consisting on the oxide film and its substrate.
Measurements were performed by Dr. Mikko Kataja at the Institute of Photonics of the University of Eastern Finland.

2.4.4 Fourier-transform infrared spectroscopy

Fourier-transform infrared (FTIR) spectroscopy was used to measured the optical reflectivity of SVO thin films in order to determine their plasma frequency, signalled by a drop in reflectivity (discussed in Chapter 3).
The FTIR measurements were performed using a Vertex 80 spectrometer coupled with a Hyperion 2000 microscope (Bruker). Measurements were carried out by Dr. Javier Saiz at the Institut Català de Nanociència i Nanotecnologia (ICN2).

2.5 X-ray photoelectron spectroscopy

X-ray photoelectron spectroscopy (XPS) is a surface sensitive technique which consists in extracting core level electrons out of a material by exciting them with a high-energy X-ray beam; this is the so-called photoelectric effect. As the incident X-ray radiation is monochromatic, measuring the kinetic energy E_{kin} of the escaping electrons allows to retrieve their former binding energy E_{B} inside the solid. This binding energy gives precise information about the material's surface such as: which elements are present, their chemical states, their chemical environment, etc. Moreover, it may give some insight about the material homogeneity, contamination... Hereafter, a brief introduction to the measurement technique is given. For further reading, one can refer to ref. [64, 65].

A sketch of a typical XPS setup is shown in Figure 2.15. It uses a hemispherical electron analyzer (one type of electron energy spectrometer) to measure the electron kinetic energy. Typical XPS setup are equipped with various photon sources that can be used to probe different energy ranges. An Al K_α X-ray radiation of energy $h\nu = 1486.74\,\text{eV}$ (XPS measurement configuration) and a He I UV radiation of energy $h\nu = 21.2\,\text{eV}$ (in that case we refer to it as UPS measurements) are the most common. Whereas UPS excites electrons from the valence band, XPS excites electrons from the valence band and the core levels.[18] In the following, we shall focus on the XPS measurement configuration.

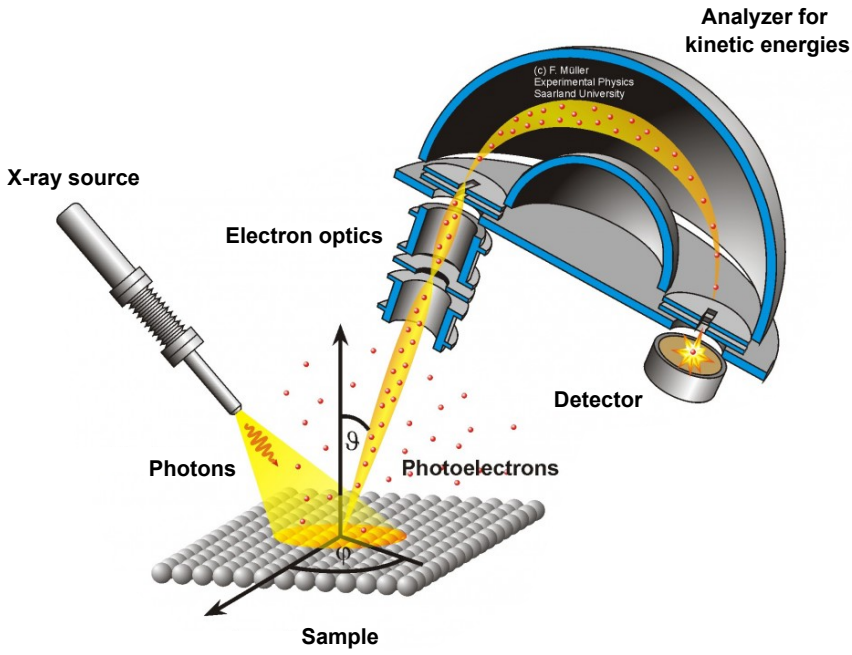

FIGURE 2.15: Sketch of a typical XPS setup.[19]

In this work, all XPS measurements were performed with a Phoibos 150 electron analyzer (SPECS GmbH) in ultra-high vacuum conditions (base pressure of 4×10^{-10} mbar). XPS measurements were performed with a monochromatic Al K_α X-ray source (1486.74 eV), irradiating a sample surface of about $0.5 \times 3.5\,\text{mm}^2$. The XPS resolution of $\approx 0.62\,\text{eV}$ was determined from the Gaussian FWHM of the Ag

[18] However, UPS allows measurements of the valence band with a higher resolution, and is more surface sensitive (the photon penetration depth depending on the photon energy).

[19] Figure adapted from: https://jacobs.physik.uni-saarland.de/home/index.php?page=forschung/home_cms_ausstattungdet14-1&navi=forschung. Accessed Date: 19/03/2021. Figure's credits: Dr. Frank Müller.

$3d_{5/2}$ peak of a clean polycrystalline silver foil. All measurements were done at a take-off angle $\theta = 0°$ (angle between the sample normal and the detector, see Fig. 2.15). After deposition, the sample was exposed to air for transferring from the deposition chamber to the XPS one. Inside the XPS chamber, it was attached to the sample holder by metallic screws, also ensuring an electrical contact between the sample surface and the ground, thus avoiding sample charging. Data analysis was performed by the CasaXPS processing software. For quantification, XPS peaks were integrated after subtraction of a Shirley background.
Measurements were carried out by Dr. Guillaume Sauthier at the Institut Català de Nanociència i Nanotecnologia (ICN2).

2.5.1 Principle of the technique

The photoemission process consists in photoionizing the material from an initial states (with N electrons) to a final state (with N-1 electrons and 1 hole).
The process of electron photoemission is often described by the three-step model [66, 67]:

i. Photoexcitation of a core level or valence band electron to an empty state above the Fermi level. This step is limited by the cross section (probability of photoionization) of the system.
ii. Transportation towards the surface. This process is affected by scattering and only the electrons not undergoing inelastic collisions can give information of their former binding energy. Here, the inelastic mean free path λ defines the distance that a (primary) electron can travel before collision, and is thus a limiting factor to the probing depth ($\approx$ 5-10 nm).
iii. Emission. In this step, electrons have to overcome the material's work function ϕ_s to be able to exit it (their kinetic energy must be higher than ϕ_s).

The relation between the kinetic energy E_{kin} of an electron leaving the material and its former binding energy E_B in the solid is:

$$E_B = h\nu - E_{kin} - \phi \tag{2.30}$$

where $h\nu$ is the energy of the incident radiation, and ϕ contains both contributions of the sample's work function ϕ_s (barrier to cross to exit the sample surface) and the analyzer's work function ϕ_a (barrier to overcome to reach the analyzer). In practice, the Fermi levels of the sample and the analyzer are equalled by establishing an electrical contact between them. It follows that:

$$E_B = h\nu - E_{kin} - \phi_s + (\phi_s - \phi_a) = h\nu - E_{kin} - \phi_a \tag{2.31}$$

The remaining ϕ_a is determined via a calibration and compensated in a way that the software gives the following simplified relation:

$$E_B = h\nu - E_{kin} \tag{2.32}$$

By doing so, one can directly access E_B by the knowledge of E_{kin} and $h\nu$.

In a typical XPS spectrum, the primary electrons (those that escaped the material without inelastic scattering) will create pronounced peaks which position depends on the type of atom and core level they originate from. Therefore, they are particularly useful to identify the species present in the sample, as well as their oxidation state. Moreover, as the binding energy of an electron around its nucleus is affected by the neighbouring atoms, several peaks can appear for the same core level if an atom is present with different oxidation states in the solid. As this difference of oxidation states affects the electron E_B by only few eV at most, information on the atom oxidation states usually requires to measure the region of the spectrum with longer acquisition time to improve the measurement resolution. An example of survey spectrum and zoom on core levels and valence band are shown on Figure 2.16.
The secondary electrons (those that did escape the material but underwent inelastic scattering on their way), on the contrary, will rather contribute to the background of the spectrum, not creating any peak.
Finally, the XPS spectrum also contains a variety of secondary peaks such as Auger, plasmons, and multiplet peaks, which emerge from the interaction of the excited electrons with the ionized system (in its final state). See for example ref. [68] for more details on the interpretation of the XPS spectra.

2.5.2 Stoichiometry quantization

In addition of identifying elements and their oxidation states, XPS measurements can be used to access the stoichiometry of the film surface. In that case the concentration of an atom i per volume unit is calculated as:

$$n_i = \frac{I_i}{S_i} \tag{2.33}$$

where I_i is the area under the peak of the element i after background subtraction, and S_i is a the atomic sensitivity factor (that takes into account some aspects such as the element cross section σ_i). The concentration of the same element i relative

to a selection of elements j present in the sample is defined as:

$$C_{\mathrm{i}} = \frac{n_{\mathrm{i}}}{\sum_j n_{\mathrm{j}}} \tag{2.34}$$

The surface composition of $SrVO_3$ films by XPS is discussed in Chapter 4 Section 4.3.1. There, it is strength that this method is focused on the surface composition and might not reflect the composition of the whole film if this latter is not homogeneous (for instance because of the presence of spurious phases at the film surface, cation segregation, or other effects).

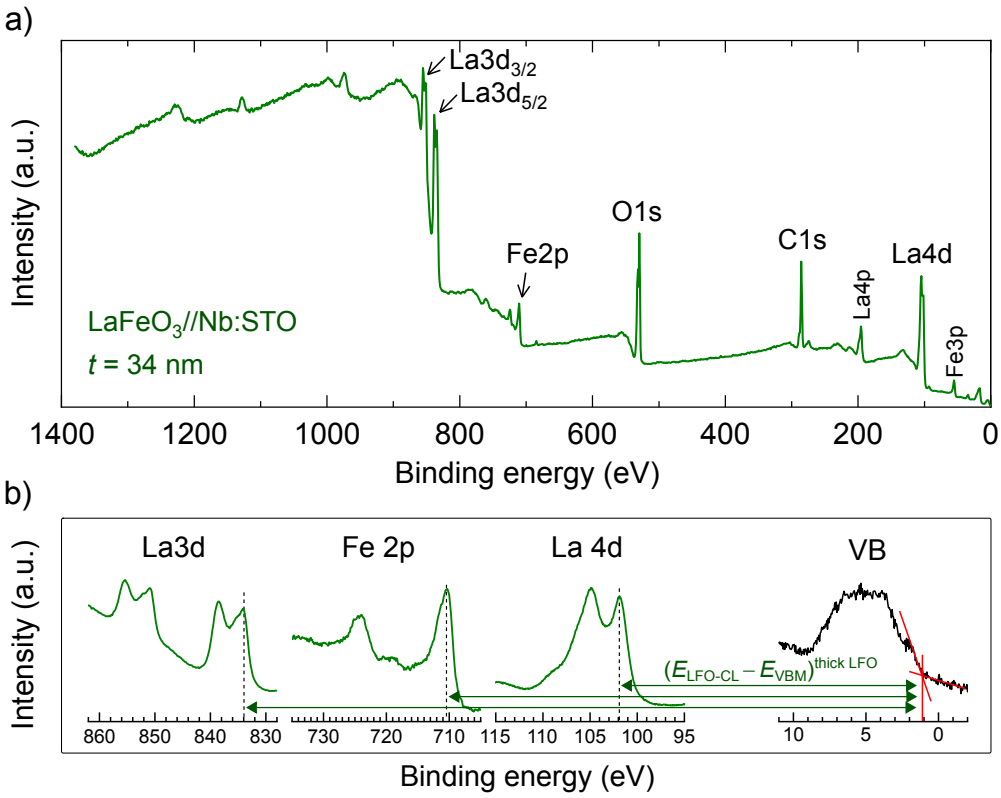

FIGURE 2.16: Illustrative XPS measurements of a $LaFeO_3$ film (34 nm thick). a) Survey spectrum. The main peaks are identified. b) Zoom of some core levels and valence band.

2.5.3 Measurements of the band alignment in heterojunctions

In heterostructures such as thin-film solar cells, the band alignment (alignment of the valence and conduction bands) of the different layers is a crucial element to take into account for the good operation of the solar cell. The most famous example is the pn-junction, where the photoexcited electron-hole pairs are transported to their respective electrodes as a result of the presence of a built-in electric field in the heterojunction. This built-in electric field is a consequence of the band alignment between the p-type and n-type layers (which have different work functions). In Chapter 8, we study similar devices as solar cells, comprising a photoabsorbing layer "sandwiched" between two metallic electrodes having different functions, thus creating a built-in potential through the heterostructure. Those are referred as metal-insulator-metal (or MIM) heterostructures (where I is the insulating photoabsorbing layer); and the knowledge of the band alignment at both interfaces (MI for the bottom interface and IM for the top one) can give information on the total built-in potential in the whole MIM structure.

In this work, the band alignment at the metal-insulator (or insulator-metal) interfaces were determined by XPS and spectroscopic ellipsometry (measurements of the bandgap). The XPS measurements allow to determine the valence band offset (VBO) between two semiconductors (SC-SC interface) or between a semiconductor and a metal (SC-M). interface[20] The position of the conduction band is extrapolated from the knowledge of each material's bandgap measured by ellipsometry.
As previously explained, XPS allows to access the information on the position of core levels and valence band. When measuring a bilayer, XPS can access the position of CLs on both layers (at the condition that the top layer does not exceed 5-10 nm in thickness, depending on the inelastic mean free path (IMFP) of the probed CLs). However, the valence band of both materials are likely to overlap in the measured spectrum and one can therefore not retrieve the valence band maximum (VBM) of each layer and their position relative to each other (see Figure 2.17b). This is starting point of the method first introduced in the 80s by Kraut, Waldrop et al. [69–71] and then largely used to determine the VBO at oxide-oxide interfaces (Chambers et al. [72–75], Klein et al. [41, 76, 77]) or the Schottky barrier height for hole injection (ϕ_p) at oxide-metal interfaces[20] (Klein et al. [27, 78, 79]).
This technique aims at exploiting the invariance of the distance between CLs and VBM within a given material, either as single layer or in a heterostructure (Figure 2.17). In a heterojunction, although the VB of both materials overlap (as sketched in Fig. 2.17b), there might an apparent shift of the CLs of the topmost

[20] In that second case, what is measured is the distance between the valence band maximum of the SC and the Fermi level of the metal, also called Schottky barrier for holes (ϕ_p).

layer B compared to those of the buried layer A. Therefore, one can use this information to retrieve the shift of the VB of layer B with respect to the one of layer A.
First of all, the distance between a given CL and the maximum of the valence band (VBM) in a thick layer (acting as a reference) is measured, for each material: $(E_{\text{CL-a}} - E_{\text{VBM}})_{\text{A}}$ in material A, and $(E_{\text{CL-b}} - E_{\text{VBM}})_{\text{B}}$ in material B (as shown for the illustrative measurement in Fig. 2.16 and also depicted in Fig. 2.17a). Then, the distance $(E_{\text{CL-b}} - E_{\text{CL-a}})_{\text{HJ}}$ between CL-a and CL-b is measured in the heterojunction (see Fig. 2.17b). Finally, the VBO ΔE_{VBM} at the heterojunction is calculated as:[21]

$$\Delta E_{\text{VBM}} = (E_{\text{CL-b}} - E_{\text{VBM}})_{\text{B}} - (E_{\text{CL-a}} - E_{\text{VBM}})_{\text{A}} - (E_{\text{CL-b}} - E_{\text{CL-a}})_{\text{HJ}} \tag{2.35}$$

The same procedure can be repeated for several CLs of A or B in order to verify that the shift of CLs of B regarding those of A is parallel.[22]
This method allows to determine the VBO with an uncertainty of $\approx 0.1\,\text{eV}$, even tough the typical XPS resolution if $\approx 0.6\,\text{eV}$ [69–71].

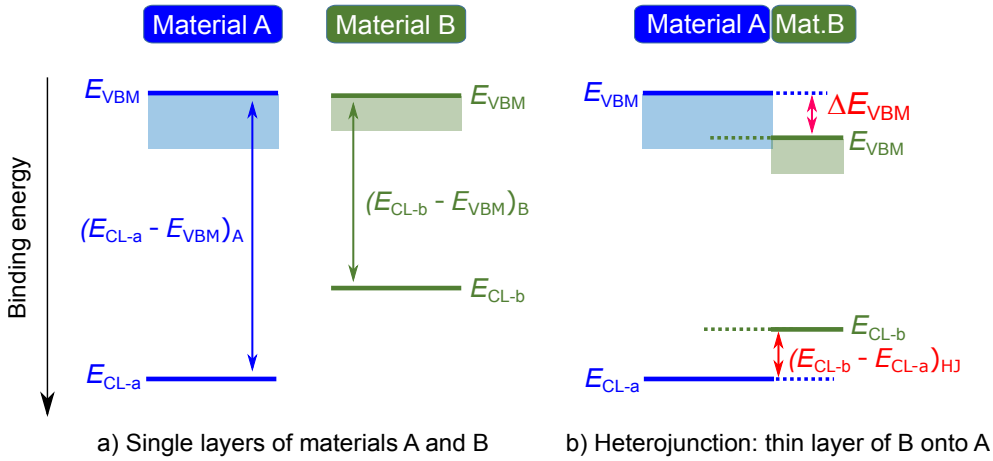

FIGURE 2.17: Sketch illustrating the measurements of VBO. a) In the thick A and B single layers, the distances between CLs and valence band maximum (VBM) are measured. b) In the heterojunction (thin layer of B deposited onto on a thick layer of A) only the distance between CLs is measured. The equation below the figure summarizes how the VBO is calculated from one pair of CLs.

[21] Also shown at the bottom of Fig. 2.17 with a color code indicating the origin of each term.
[22] A nonparallel shift of CLs of the topmost layer compared to those of the buried layer can occur in case of some interface reaction, sample charging, etc.

2.6 Soft X-ray absorption spectroscopy techniques

In transition metal oxides with cubic perovskite structure, the crystal field breaks the degeneracy of the d orbitals into 2 energy levels: the t_{2g} orbitals (d_{xy}, d_{xz}, d_{yz}) at lower energy, and the e_g orbitals (d_{z^2}, $d_{x^2-y^2}$) at higher energy. This separation, equal to the crystal field splitting energy $\Delta = 10\,\mathrm{Dq}$, arises from the different electrostatic field exerted by the ligands (the octahedral cage of oxygen anions) on the central metal cation orbitals (d_{xy}, d_{xz}, d_{yz}, and, d_{z^2}, $d_{x^2-y^2}$), as these have different shape and thus spatial distribution. Therefore, the ground state of cubic $SrVO_3$ ($3d^1$), for instance, corresponds to one free electron occupying a triply-degenerated t_{2g} orbital. However, if the lattice is distorted one may observe a further symmetry-breaking and a re-ordering of the t_{2g} and e_g orbitals. In perovskite thin films of late transition metal oxides, for instance, it has been shown that this symmetry breaking can be triggered by tetragonal distortions induced by strain originating from the mismatch between substrate and bulk film lattice constants [80–82]. In Chapters 3–5, we are studying the effects of strain on the orbital occupancy in $SrVO_3$ thin films, and its impact on the electrical and optical properties, by means of soft X-ray absorption spectroscopy (XAS) techniques.

In the following, a brief description of the principle of X-ray absorption spectroscopy (XAS) and X-ray linear dichroism (XLD) measurements will be given. For more details on these techniques as well as a description of the other measurements configurations (such as X-ray circular dichroism, etc.) one can refer to ref. [83–87].
All the X-ray absorption experiments shown in this thesis have been performed at the BOREAS beamline [88] of ALBA-CELLS synchrotron radiation source (Barcelona, Spain), by Dr. Hari Babu Vasili, Dr. Pierluigi Gargiani and Dr. Manuel Valvidares, who also contributed to the scientific discussions of the results.

2.6.1 X-ray absorption spectroscopy

X-ray absorption spectroscopy (XAS) is a spectroscopy technique allowing to access the electronic structure and local environment of atoms in matter. It usually operates a synchrotron radiation source of high intensity X-rays consisting in a tunable monochromatic X-ray beam with energy varying from $0.1 - 100\,\mathrm{keV}$ ($< 5\,\mathrm{keV}$ in the soft X-ray regime, as it is the case here). This technique shows many assets such as: its high resolution due to precise control of the photon energy, the possibility to tune the light polarization, a high intensity beam (fast acquisition time) and the possibility of using a micrometric spot size.

When the beam shines the sample, electrons from core level states are excited to empty states of the valence shell. Consequently, the measured XAS spectrum is marked by a strong absorption peak (resonant effect) at the photon energy corresponding to this transition; and the absorption intensity is proportional to the amount of available empty valence states. Moreover, in addition of the discrete transitions of electrons from core levels to the valence shell, some core electrons are excited to the continuum which manifest by a jump in absorption at the same energy, constituting the background of the XAS spectrum.
The intensity of the absorption peaks is proportional to the transition probability for one electron to be the excited from an initial state $|i\rangle$ (a core level) to a final state $|f\rangle$ (an empty state of the valence shell), which is given by the Fermi's golden rule:

$$\Gamma_{\mathrm{i}\to\mathrm{f}} \propto |\,\langle f|\, A_0\,\vec{\varepsilon}\,\mathrm{e}^{-\mathrm{i}(\vec{k}\vec{r}-\omega t)}\,|i\rangle\,|^2\,\rho(E_\mathrm{f}) \tag{2.36}$$

where A_0, $\vec{\varepsilon}$, $\vec{k}$, ω are the wave amplitude, polarization, wave vector and frequency of the incident electromagnetic field, and $\rho(E_\mathrm{f})$ is the density of states at the energy E_f of the final states. Dipole allowed transitions shall naturally give higher intensities. For instance here, in the case of a transition metal oxide such as $SrVO_3$, the common transitions measured are the $2p \to 3d$ at the vanadium site, which are manifested by a double peak (related to spin-orbit coupling) also known as V $L_{2,3}$-edge.[23] The electronic transitions at the oxygen ligands can also be useful. These are typically the $1s \to 2p$ transitions, forming the O K-edge.[24]

The electrons that have been excited to empty states of the valence shell de-excite emitting photons, Auger and secondary electrons, from which different modes of detection emerge. The most common modes of detection are fluorescent yield (FY) that detects the emitted photons, or total-electron yield (TEY) that measures the secondary electrons. Whereas the first one has the advantage of having a high probing depth, it can be affected by saturation and self-absorption effects. Thus, it can be preferable to use the TEY mode, as done in this work, although the probing depth is limited to 2-5 nm due to low electron escape depth [83, 89].

So far we have considered unpolarized incident light. However, the XAS signal can be sensitive to polarization of light due to peculiar orbital ordering of TMOs or their magnetization. If the sample is magnetic, circularly polarized light will have different absorption depending on the magnetic state of the system and it can result a

[23] The spin-orbit coupling splits the p orbitals in $p_{1/2}$ and $p_{3/2}$, which give rise to two distinct absorption peaks: the L_2- and L_3-edges, respectively.

[24] The existence of an O K-edge is necessarily due to the presence of holes in the p orbitals, which appears in TMOs due to hybridization between oxygen p-orbitals and metal d-orbitals. This point is further discussed in Chapter 5.

x-ray magnetic circular dichroism (XMCD). On the other hand, the charge distribution at the core and valence shells can also affect the absorption of light with linearly polarized light. This latter phenomenon give rise to a x-ray linear dichroism (XLD). In the following, we shall focus on XLD, as in $SrVO_3$ (Pauli paramagnet) no XMCD signal is expected.

2.6.2 X-ray linear dichroism

In TMOs, the valence shell is composed of partially-filled d orbitals which are nonspherical. It results an anisotropic charge distribution around the atoms. Therefore, the X-ray absorption should also depend on the polarization of the electric field of the incident X-ray waves, giving rise to the XLD signal. For instance, in the case of $2p \rightarrow 3d$ transitions, the light with vertical polarization (along the sample normal, i.e. the z-direction) will promote electron excitations from core level to the empty orbital having a z-component (xz, yz or z^2). On the other hand, the light with horizontal polarization (along the sample plane, i.e. within the (x, y) plane) will promote the electron excitations to orbitals having x- and/or y-expansion (xy or $x^2 - y^2$).

The case of $La_{1.85}Sr_{0.15}CuO_4$ ($3d^9$ perovskite oxide) is a simple example because the empty orbital is purely $x^2 - y^2$ and has no z component. As shown in Figure 2.18, light with in-plane polarization has a high absorption, while the one with out-of-plane polarization is nearly null as the z^2 orbitals are already occupied.

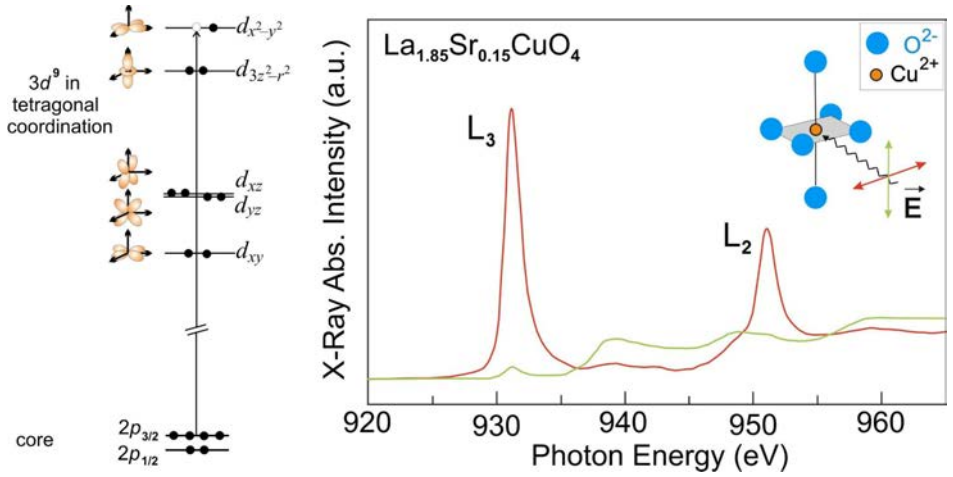

FIGURE 2.18: Example of XLD manifestation in $La_{1.85}Sr_{0.15}CuO_4$ ($3d^9$). The X-ray absorption at Cu $L_{2,3}$-edge with linear in-plane polarization (red) and out-of-plane (green) are shown. Figure taken from [83] (adapted from [90]).

As explained above, in $SrVO_3$ ($3d^1$) the XAS intensity at V L-edge occurs because of transitions between occupied $2p$ core levels to empty valence $3d$ states (which contain only 1 electron among 10 possible states). Therefore the XLD signal at V L-edge observed in SVO is due to the breaking of degeneracy of the empty orbitals. This is further explored in Chapter 5.

2.6.3 Measurements description

In this work, we measured the XAS spectra of $SrVO_3$ thin films at the V $L_{2,3}$ and O K-edges at 300 K and 2 K, using horizontally (H) or vertically (V) linearly polarized light and probing the XLD as the difference between the two light polarizations (see sketch of the measurement configuration in Figure 2.19a). The X-ray absorption was collected with V ($\boldsymbol{E} \parallel ab$, $\boldsymbol{E}_{ab}$) and H ($\boldsymbol{E} \parallel bc$, $\boldsymbol{E}_c$) polarizations, where ab and bc indicate the planes defined by the (a, b, c) crystallographic axes of the sample. For the $3d$ orbitals, the H-polarized XAS spectrum can be different for a grazing incidence ($\boldsymbol{E} \parallel c$) and the normal incidence ($\boldsymbol{E} \parallel b$) while the V-polarized spectrum ($\boldsymbol{E} \parallel a$) remains unchanged except the probing depth. Due to geometrical constraints and following common practice, most of the spectra were collected in the so-called grazing incidence with the X-ray incidence direction $\boldsymbol{k}$ at an angle $\theta = 30°$ with respect to the sample surface. Henceforth, we mention the electric field vectors of $\boldsymbol{E} \parallel c$ and $\boldsymbol{E} \parallel ab$ for the H- and V-polarized lights, respectively. The photocurrent was measured in the total electron yield (TEY) mode. XAS data in

TEY mode can be robustly collected from 300 K to 2 K, confirming the metallic nature of the SVO films in this temperature range. Average XAS spectra I_0 were obtained by averaging the XAS intensities collected for both linear polarizations, i.e. $I_0 = [I(\boldsymbol{E}_c) + I(\boldsymbol{E}_{ab})]/2$. The XLD signal is defined as: $XLD = I(\boldsymbol{E}_c) - I(\boldsymbol{E}_{ab})$.

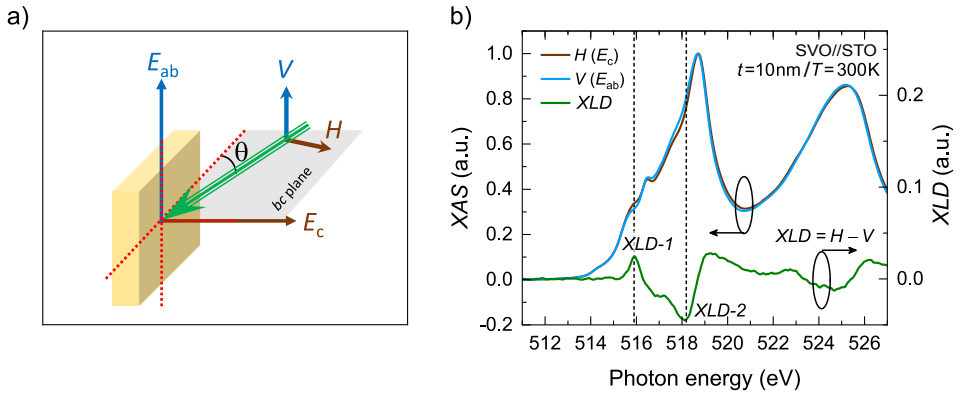

FIGURE 2.19: a) XAS/XLD measurement configuration. b) Example of XAS/XLD measurements around the V $L_{2,3}$ edge for a $SrVO_3$ thin film.

2.7 Other experimental techniques

2.7.1 Atomic force microscopy

Atomic force microscopy (AFM) is a type of scanning probe microscopy (SPM) technique in which a tip scans the sample surface to reveal its topography. The tip placed at the end of a cantilever is held above the sample surface, and while scanning it, any deflection of the cantilever provoked by variation of height is recorded. To do so, a laser is pointed at the cantilever head which reflects it, and thus the monitored reflected beam is sensitive to the cantilever deflection. The tip radius of curvature is of the order of the nanometer, and can record height variations of few angstroms [91, 92]. AFM therefore is powerful tool for thin film characterization, where the film morphology and roughness can give us information on the growth mode (2D or 3D). It can also helps at detecting the presence and nature of secondary phases.

Topographic images of thin films are usually performed in dynamic tapping mode, where the tip is maintained slightly (10-100 Å) above the sample surface, in order to avoid some deterioration of the sample surface or of the tip itself by friction or adhesion between them, or even due to surface contamination, that usually occurs in contact mode. The cantilever is then oscillated by means of a piezoelectric element. When the tip is approached near the surface, any dip or bum creates a

fluctuation of its oscillation amplitude and frequency, which is recorded to reconstruct the topographic image of the surface. Moreover, a phase shift between the initial sine wave and the cantilever response is also observed. A variation of this phase shift can be observed if the tip crosses an area of different composition (with different mechanical properties). Therefore the generated phase image can give useful information on the film surface composition.
In this work, AFM topographic images were recorded in dynamic mode in Keysight 5100 AFM or Keysight 5500 LS AFM setups. Measurements were performed at the Scanning Probe Microscopy Laboratory of ICMAB, by Maite Simón and Andrés Gómez. Images were analyzed using the software WSxM 5.0, from Nanotec Electronica S.L. [93].

2.7.2 Scanning electron microscopy and electron dispersive X-ray spectroscopy

Scanning electron microscopy (SEM) is a surface-sensitive technique using a high-energy electron beam to scan the sample surface. It can reach a nanometric resolution.
When electrons interact with a solid, they endure a variety of different processes. They can be elastically scattered, as in the case of back-scattered electrons (BSE), or inelastically scattered thus producing emission of secondary electrons (SE) and X-rays. In SEM measurements, BSE and SE are usually detected and provide information about the surface morphology. On the other hand, the SEM setup is usually coupled with a X-ray detector allowing to access the material chemical composition. In that case, the technique is called: electron dispersive X-ray spectroscopy (or EDX). Here, SEM measurements were performed on a Quanta 200 FEG-ESEM from FEI, equipped with an Energy Dispersive X-ray (EDX) system for chemical analysis.

2.7.3 Transmission electron microscopy

In Chapter 3, SVO thin films deposited on different substrates were measured by transmission electron microscopy (TEM), in order to get an insight on the effects of substrate-induced strain on the film microstructure.
TEM is a microscopy technique in which an electron beam crosses the sample and the interactions between beam and sample allow to reconstruct an image of the sample microstructure. The sample needs to be thin enough ($\approx 100\,\text{nm}$) so that electrons can go through it and exit without being absorbed or scattered inside the solid. This technique can reach atomic resolution (high-resolution TEM), thousands of times better than any light microscope, due to the smaller De Broglie wavelength of electrons compared to visible light photons.

Here, SVO specimens for TEM observation were prepared in cross section geometry by focused ion beam (FIB) using the lift-out technique. TEM images were acquired using JEOL J2100 as well as JEOL J2010F microscopes, both operated at an accelerating voltage of 200 kV.
TEM measurements were carried out by Dr. LLuís López-Conesa, Dr. Sònia Estradé and Prof. Francesca Peiró, from the University of Barcelona (UB).

2.7.4 Inductively coupled plasma mass spectrometry

Inductively coupled plasma mass spectrometry (ICP-MS) is a mass spectroscopy technique used to determine the composition and quantify the elements present in a sample. In the case of materials (thin films or PLD targets) with ABO_3, ABO_4 or $A_2B_2O_7$ chemical composition, ICP-MS is particularly useful to determine the A/B cationic ratio (thus expected to be equal to 1). In the case of PLD deposited thin films, it can be used to explore the stoichiometry transfer from target to film for instance. When measuring thin films though, one needs to make sure that the substrate does not contain any of the same A/B elements than in the film. This technique is destructive as it requires to dissolve the sample. This latter indeed needs to be in the liquid form, then it can be sprayed and ionized by an inductively coupled plasma. Once the plasma is formed, the ions are extracted and transported to a mass spectrometer. More details about the technique and setup can be found in ref. [94].
In this work, samples measured by ICP-MS were dissolved in aqua regia (for samples containing Sr and V) or in a mixture of aqua regia and hydrofluoric acid (for samples containing Sr and Nb). After dissolution, the samples were measured in a Agilent 7500ce ICP-MS, by the Servei d'Anàlisi Química of the Universitat Autònoma de Barcelona (SAQ-UAB), in collaboration with Dr. Ignasi Villarroya.

2.7.5 Thermogravimetric analysis

Thermogravimetric analysis (TGA) aims at measuring the mass variations of a sample as its temperature is varied. It provides information on the eventual chemical reactions, phase transitions, contaminants evaporation, oxidation/reduction reactions, etc. that can occur upon heating the sample (e.g. a powder). The measurements can be performed in oxygen, nitrogen, hydrogen, argon, or air. Other techniques, such as the differential scanning calorimetry (DSC), can be used simultaneously with TGA. DSC monitors the difference of amount of heat needed to increase the sample temperature as a function of temperature. It gives complementary sample information (thermal decomposition, phase transition, etc.).
In this thesis, some powder materials were measured by TGA-DSC (see Appendix A.2.1). The purpose was to define a sufficiently high drying temperature (but not too high to avoid thermal decomposition) to insure that the powders were

free of water contamination before their use for PLD target fabrication. Water contamination could indeed result in a weighting error and thus an error of cation stoichiometry in the final target.
The measurements were carried out at the Thermal Analysis Service of ICMAB, by Roberta Ceravola. The sample was maintained in a N_2/O_2 atmosphere and the temperature was varied from RT to 1400°C (except for V_2O_5 where the maximum temperature was set to 600°C, i.e. below the melting point).

2.8 First principles calculations

First principles calculations presented here were done in collaboration with the group of Prof. Roser Valentí of the Institut für Theoretische Physik, Goethe-Universität Frankfurt am Main. Calculations were performed by Dr. Vladislav Borisov and Adrian Valadkhani. All results presented in Chapters 5,6 were thoroughly discussed with them.

2.8.1 Description of the calculations performed in Chapter 5

The electronic properties of $SrVO_3$ were calculated using density functional theory (DFT) within the generalized-gradient approximation, as available in the all-electron full-potential localized orbitals (FPLO) basis set code [95, 96], and the generalized gradient approximation as exchange-correlation functional [97]. The integration in the Brillouin zone was performed using the trapezoidal method and a (20x20x20) $\boldsymbol{k}$-mesh, in the -10 eV to 0 eV (corresponding to E_F) interval. The contributions of different orbitals to the density of states were determined based on the Wannier analysis which includes the vandadium $3d$ and oxygen $2p$ states around the Fermi level. The lattice parameters were taken from our measurements of $SrVO_3$ films grown on different substrates ($t = 10$ nm, $P(Ar) = 0.03$ mbar).

2.8.2 Description of the calculations performed in Chapter 6

The electronic structure of bulk $SrVO_3$ was calculated using density functional theory [98, 99], as available in the all-electron full-potential localized orbitals (FPLO) basis set code [95]. The generalized-gradient approximation [100] was chosen for the exchange-correlation energy and the summation in the Brillouin zone was performed on the (20x20x20) $\boldsymbol{k}$-mesh. The Fermi surface was determined based on the band energies calculated on the (50x50x50) $\boldsymbol{k}$-mesh. The structural parameters of bulk $SrVO_3$ were taken from reported data for the bulk material (lattice parameter of 3.842 Å) and the measured (a,c) parameters of the films were used when appropriate.
In order to calculate the phonon properties, the density functional perturbation

theory was used, as available in the Quantum Espresso package [101]. In the first step, the electronic structure was determined self-consistently using the density functional theory [98] within the PBE parametrization of the generalized-gradient approximation. The electronic wavefunctions were represented by plane waves with an energy cutoff of 80 Ry. For the electronic density, larger cutoff of 320 Ry was used. The smearing for the electronic occupations was set to 0.02 Ry and the integration in the Brillouin zone was done on the Gamma-centered (10x10x10) $\boldsymbol{k}$-mesh. The calculation of the electron-phonon interaction was based on a denser (20x20x20) $\boldsymbol{k}$-mesh and the phonon modes at the Gamma point were determined with the threshold 10^{-16}.

Chapter 3

Independent tuning of optical transparency window and electrical properties of epitaxial $SrVO_3$ thin films by substrate mismatch

In this chapter, we present the growth optimization of $SrVO_3$ thin films. In particular, after establishing the optimal (PO_2, T) parameters leading to single-phase and metallic $SrVO_3$ films, we will show how the strain induced by the substrate can affect both electrical and optical properties. The work presented in this chapter was published with DOI: 10.1002/adfm.201904238 (see also the list of publications).

3.1 Introduction

Transition metal oxides are among the most studied materials due to the tremendous variety of properties they may display, such as superconductivity, metal–insulator transition, or multiferroicity [102]. High electrical conductivity and carrier mobility are critical requirements for the implementation of these materials in some advanced electronic components [103]. However, the room-temperature carrier mobility (μ) of the much explored $SrTiO_3$ n-type semiconductor, for instance, in which the conduction band derives from rather localized 3d orbitals, is only $\approx 10\ cm^2\ V^{-1}\ s^{-1}$. Similarly, the much larger carrier mobility discovered in $LaAlO_3/SrTiO_3$ and related interfaces, is limited to low temperatures [104]. In a different approach, focus was directed toward semiconductors made out of late transition metals, such as $BaSnO_3$ (BSO). In BSO, the relatively broad conduction band derived from Sn-5s orbitals anticipates a larger carrier mobility. Indeed,

this has been experimentally observed by the breakthrough report of $\mu \approx 320$ $cm^2\,V^{-1}\,s^{-1}$ in La-doped $BaSnO_3$ (La-BSO) single crystals [105]. Unfortunately, in La-BSO thin films the carrier mobility was found to be substantially reduced [106, 107], although molecular beam epitaxy (MBE) growth technique and proper substrate selection [108] have allowed to partially recover ($\approx$ 150 $cm^2\,V^{-1}\,s^{-1}$) the single-crystal mobility value. Anyhow, in these semiconducting materials, metallicity is obtained via doping and, in consequence, optimal conductivity can only be achieved via the subtle balance between the doping concentration and mobility, that typically vary in the opposite direction upon doping [109]. In an essentially different approach, the attention has recently shifted toward intrinsically conducting oxides made of early transition metal elements such as: V, Nb, Mo, etc. In the case of $SrVO_3$ (SVO), for example, the partial occupation of the V-3d band ($3d^1$ electronic configuration) is responsible of the metallic conductivity. In this material the valence band is made out of O-2p orbitals lies well below the 3d band and a large optical band gap exists ($\approx$ 3 eV) which guarantees no photon absorption in the visible range [18]. Moreover, the intrinsically narrow V-3d band should lead to relatively strong electron–electron correlations and consequently to an enhanced effective mass. The large carrier concentration ($\approx$ 1 electron per unit cell) and large effective mass combine to produce a plasma frequency ($\omega_p{}^*$) near infrared and thus SVO is found to be metallic and transparent in the visible optical range [18]. In recent years, SVO thin films have been grown by a number of techniques, including hybrid-MBE [18, 42, 110, 111] and pulsed laser deposition (PLD) [112–121], and room-temperature resistivity (respectively mobility) values have been found to be ranging from 200 $\mu\Omega\,cm$ (resp. 0.8 $cm^2\,V^{-1}\,s^{-1}$) to 28 $\mu\Omega\,cm$ (resp. 10 $cm^2\,V^{-1}\,s^{-1}$) in best films.

The combination of large electrical conductivity and optical transparency in the visible range is a bonus of strong interest in photovoltaics, plasmonics [46, 47], or information technologies and not surprisingly, correlated transparent oxides are attracting much attention. A question then arises: which are the factors limiting the carrier mobility and the transparency window of SVO thin films?

In epitaxial films, several factors may come into play. First, epitaxial strain may break the degeneracy of the cubic environment of the metallic vanadium cation in SVO by splitting the V-3d-t_{2g} triplet (Figure 3.1a). As a consequence, the conduction band width (W) and the electron orbital occupancy of the t_{2g} orbitals can be modified, affecting electron–electron correlations [122] and carrier mobility. Interestingly, it was reported that chemical pressure in $Ca_{1-x}Sr_xVO_3$ induces a gradual deformation of the unit cell that tunes W and, subsequently, the electronic [123] and optical [124] properties. It is understood that shorter V−O−V bonds in $CaVO_3$ compared to those of $SrVO_3$ are established via bending of the V−O−V

bond angle θ away from the $\theta = 180°$ observed in SVO. This bending reduces W and increases the electron–electron correlations with a subsequent increase of the carrier effective mass (m^*) and reduction of the plasma frequency. However, a recent report on SVO films epitaxially grown on substrates having different structural mismatch suggests that the electrical and optical properties of the SVO films vary depending on the substrate used although the variation does not correlate with epitaxial strain [125]. Intriguingly, the reported plasma frequency $\omega_p{}^*$ ($\hbar\omega_p{}^* \approx 2.3$ eV) [125] is substantially larger than that early measured in bulk and epitaxial films (≈ 1.3 eV) [18, 123]. Second, during growth, point defects, associated to nonstoichiometry or others, may arise compromising μ (Figure 3.1b) [42]. Third, structural mismatch between film and substrate produces a mechanical stress that can induce plastic deformations by strain relaxation in the film structure, which should also affect μ (Figure 3.1c). These latter effects have been found to be of relevance in La-BSO films and related materials [126]. Finally, in ultrathin SVO films, only few unit cells thick, quantum confinement may also give rise to selective orbital occupancy within the t_{2g} manifold [127], but this range of film thicknesses is beyond the present scope.

In this chapter, we aim at addressing these issues, with the general purpose of finding optimal conditions for highly conducting and transparent SVO films.

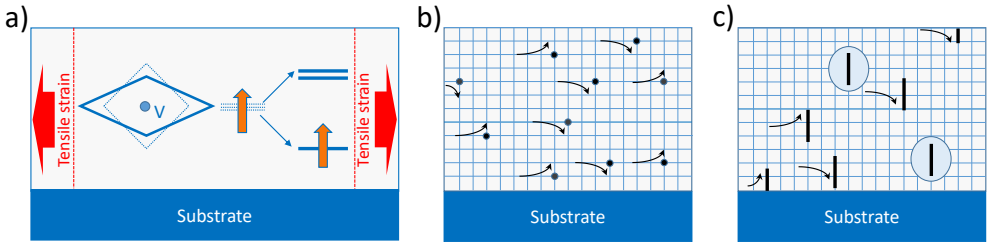

FIGURE 3.1: a) Sketch of the impact of (tensile) strain on the VO_6 polyhedron deformation and breaking of degeneracy of V 3d-t_{2g} (xy, xz, yz) orbitals. Electron occupancy is indicated by a vertical arrow. b) Carrier scattering (curved arrows) caused by point defects. c) Carrier scattering caused by extended defects, such as dislocations and cracks. Charge-screened defects are indicated by circles.

3.2 Sample preparation

SVO films were grown on cubic single crystalline perovskite substrates having different cell parameters: $SrTiO_3$ (STO, 3.905 Å), $(LaAlO_3)_{0.3}$-$(Sr_2AlTaO_6)_{0.7}$

(LSAT, 3.868 Å), $NdGaO_3$ (NGO, (pseudocubic) 3.863 Å), and $LaAlO_3$ (LAO, 3.791 Å). Bulk SVO is cubic with a_{SVO} = 3.842 Å. [111, 128] Therefore, the structural mismatch between SVO and the substrate, defined as $f = [a_S - a_{SVO}]/a_S$, where a_S is the cell parameter of the substrate was $f(\text{STO}) = +1.59\,\%$, $f(\text{LSAT}) = +0.65\,\%$, $f(\text{NGO}) = +0.52\,\%$, and $f(\text{LAO}) = -1.37\,\%$. Here, positive (resp. negative) f value signals that substrate imposes a tensile (resp. compressive) stress on the SVO film. As-received (001)-oriented single crystals (cubic and pseudocubic settings) were used as substrates. Films were grown by pulsed laser deposition (PLD) at a frequency of 5 Hz, a fluence of $\approx 2\,\text{J cm}^{-2}$, and the number of laser pulses was 2000. A $Sr_2V_2O_7$ target was prepared by solid state reaction of stoichiometric amounts of $SrCO_3$ and V_2O_5 (see Appendix A for details on the target preparation). The oxygen partial pressure (PO_2) inside the PLD chamber was varied from $PO_2 = 1\times10^{-4}$ mbar down to the base pressure at the growth temperature, corresponding roughly to $PO_2 \approx 4\times10^{-7}$ mbar. The temperature of deposition was varied between 700 and 800°C. After growth, films were cooled down to room temperature by switching off the heater of the sample holder, while keeping the same pressure as used for the growth.

3.3 Determination of optimal (PO_2, T) growth window

We first determined the growth window of SVO thin films in the PO_2 (4×10^{-7} to 1×10^{-4} mbar) and T (700 °C to 800 °C) ranges on (001) STO and (001) LSAT. The room-temperature resistivity (ρ) and crystalline phases (pure $SrVO_3$ films or coexistence of $SrVO_3$ and $Sr_3V_2O_8$ phases were obtained) are summarized in the (ρ, T, PO_2) diagram shown in Figure 3.2, where we include the room-temperature resistivity of the films on LSAT and STO versus the (T, PO_2) growth parameters. It can be appreciated that the main trends are common to both LSAT and STO substrates.

Data in Figure 3.2 show that single-phase and highly conducting SVO films are obtained at the lowest oxygen partial pressure ($PO_2 \approx 4\times10^{-7}$ mbar which corresponds to the base pressure of the growth chamber) whereas when increasing PO_2, films are multiphase ($SrVO_3$, $Sr_3V_2O_8$) and less conducting. Films grown at $PO_2 = 4\times10^{-7}$ mbar show only the (00l) reflections of the SVO perovskite indicating that the films are (001) textured, without traces (within the experimental sensitivity) of spurious phases. It can be appreciated in Figure 3.2 that films grown around 750−800 °C present the lowest resistivities. The roughness of the films increases with PO_2. AFM images are shown in Figure 3.3. Illustrative values of resistivity and roughness (rms) of films grown at 750 °C, are: $\rho \approx 82\,\mu\Omega\,\text{cm}$ and $rms \approx 0.41$ nm for the film deposited on LSAT and $\rho \approx 200\,\mu\Omega\,\text{cm}$ and $rms \approx 0.52$ nm for the film deposited on STO. The resistivity values compare well with those early reported for

thin films grown either by PLD (30−200 μΩ cm) [113, 114, 117] or hybrid-MBE (≈ 30−40 μΩ cm) [18, 42] as we shall analyze in detail below.

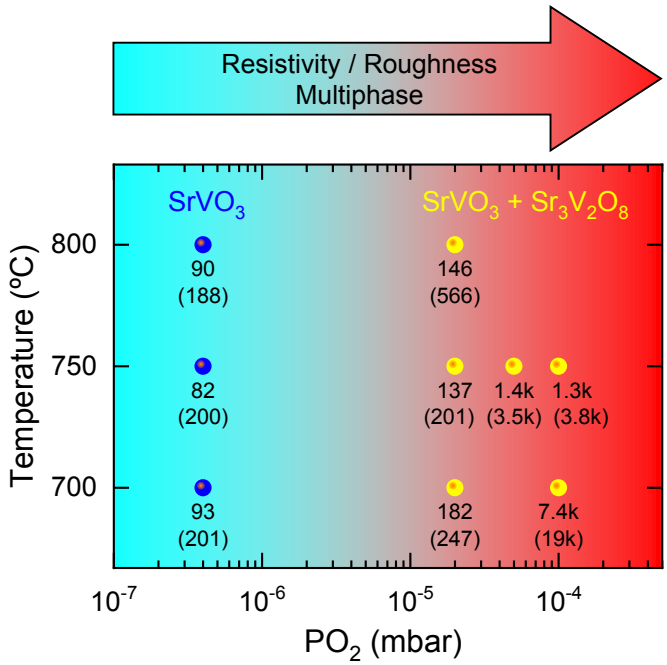

FIGURE 3.2: Growth window describing the crystalline phases and electrical properties of SVO films grown on (001) LSAT and (001) STO substrates, as a function of PO_2 and T during growth. The indicated numbers are the room-temperature resistivity data (in μΩ cm) for SVO on LSAT. Within parenthesis are the corresponding data for SVO films on STO. The color scale (from cyan to red) illustrates the increasing resistivity and roughness of the films.

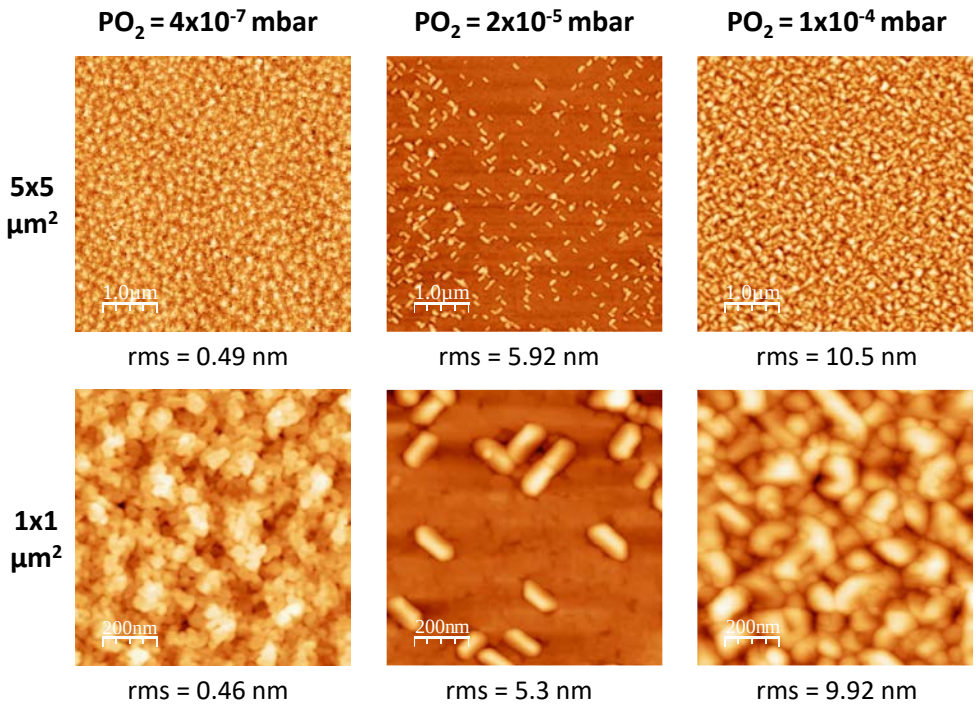

FIGURE 3.3: AFM topographic images, 5 µm×5 µm in size (top images), of SVO films grown on STO substrates at 750 °C and various PO_2 (as indicated). Bottom images are 1 µm×1 µm zooms emphasizing the outgrowths formed at film surface when deposition is performed at $PO_2 > 4\times10^{-7}$ mbar. The root-mean square (rms) roughness is indicated below each image.

3.4 Role of the substrate-induced epitaxial strain on the structural, electrical and optical properties

Interestingly, in Figure 3.2 it can be appreciated that in all cases, the resistivity values of SVO//LSAT films are significantly smaller than those of the SVO//STO films. As the structural mismatch of SVO on STO, f(STO) = +1.59 %, is larger than that of SVO on LSAT, f(LSAT) = +0.65 %, it may be hypothesized that f, and the associated elastic or plastic responses of the SVO lattice, may play an important role on carrier transport in SVO films. In the following, we shall use the optimal growth conditions determined above ($PO_2 \approx 4\times10^{-7}$ mbar, T = 750 °C) to explore in a systematic manner the role of structural mismatch between SVO and the substrates (STO, LSAT, NGO, and LAO), on the electrical, optical, spectroscopic properties and the microstructure of the films.

3.4.1 Surface morphology

Surface morphology analysis (topographic images are in Figure 3.4) shows that, irrespectively of the substrate, films grown under these conditions are remarkably flat, with $rms \approx 0.52$ nm (STO), 0.41 nm (LSAT), 0.46 nm (NGO), and 0.48 nm (LAO). In agreement with earlier findings [114], when increasing PO_2, SVO films display the gradual formation of outgrowths at their surface, related to the formation of spurious $Sr_3V_2O_8$ phase as evidenced by X-ray diffraction (XRD) data shown below.

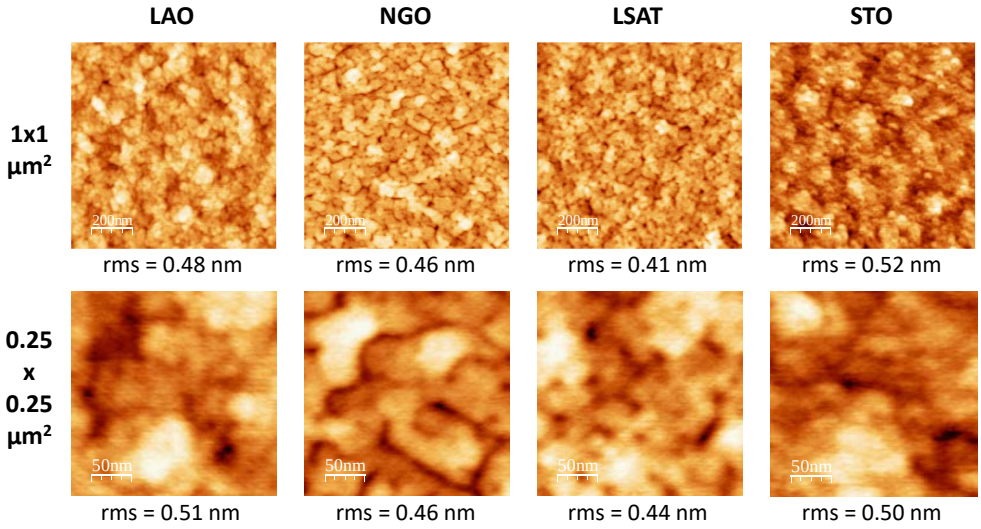

FIGURE 3.4: AFM topographic images, 1 µm×1 µm in size (top images), of SVO films grown at $PO_2 = 4\times10^{-7}$ mbar and $T = 750$ °C, on various substrates. Bottom images are 250 nm×250 nm zooms emphasizing the granularity of the films. The root-mean square (rms) roughness is indicated below each image.

3.4.2 Structural properties

The XRD $\theta-2\theta$ scans of films deposited under the optimal conditions (750 °C, 4×10^{-7} mbar) on all substrates, zoomed around the (002) reflection of the corresponding substrates, are shown in Figure 3.5a.

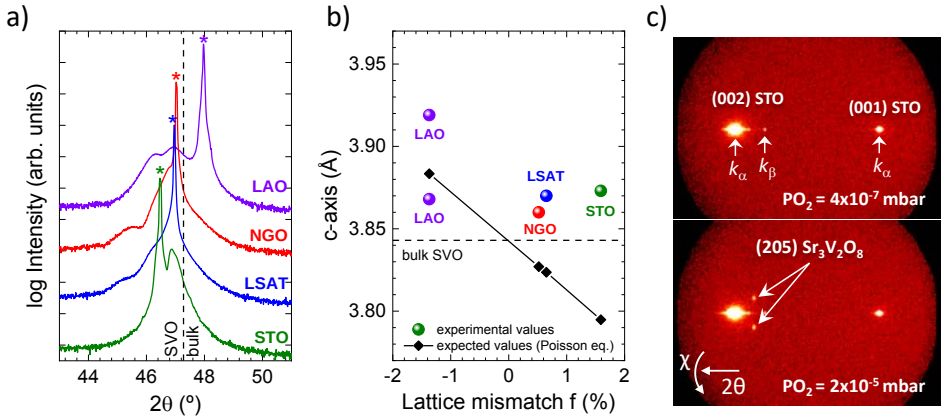

FIGURE 3.5: a) XRD $\theta-2\theta$ scans of films grown at $PO_2 = 4\times10^{-7}$ mbar and $T = 750$ °C on different substrates. The (002) reflection of the substrate is indicated by a star. The spectra are vertically shifted for clarity. b) Out-of-plane cell parameters (c-axis) of the films as a function of the lattice mismatch with the substrate (circles). Diamonds represent the expected c-axis values for fully strained films, evaluated using Poisson's equation and assuming unit cell volume conservation. c) 2θ–χ frames of SVO films on STO at $T = 750$ °C and $PO_2 = 4\times10^{-7}$ mbar (upper frame) and $PO_2 = 2\times10^{-5}$ mbar (lower frame).

We first focus on the SVO film on STO which has the largest tensile structural mismatch (f(STO) = +1.59 %). The (002) reflection of the SVO film (Figure 3.5a (green curve)), is located at the right of the (002) STO reflection, and attentive inspection reveals Laue fringes (see Figure 3.6). Interestingly, the (002) SVO reflection occurs at lower angle than that expected for bulk SVO (indicated by a vertical dashed line in Figure 3.5a), implying an expanded c-axis (c(SVO//STO) ≈ 3.873 Å). Therefore, the observed expansion of c-axis is not due to the stress (tensile) imposed by the substrate but is likely related to growth-induced defects, including nonstoichiometry, as commonly found in SVO films [42, 111, 115, 116]. The reciprocal space maps (Figure 3.7) show that the (002) SVO and (002) STO reflections are well aligned along [100] indicating that the in-plane cell parameter of SVO and STO are closely coincident and thus SVO is in-plane strained ($a \approx 3.905$ Å). Therefore, the VO_6 coordination polyhedron in SVO//STO has $c/a < 1$.

In the opposite limit, for SVO//LAO films where a large compressive mismatch exists (f(LAO) = -1.37 %), two broad (002) SVO reflections can be observed in the XRD pattern (top violet curve). One occurring at $(2\theta)_1 \approx 46.94°$, indicates an out-of-plane cell parameter c_1(SVO//LAO) ≈ 3.868 Å and the other, located at $(2\theta)_2 \approx 46.3°$, indicates a larger c-axis: c_2(SVO//LAO) ≈ 3.919 Å. These reflections

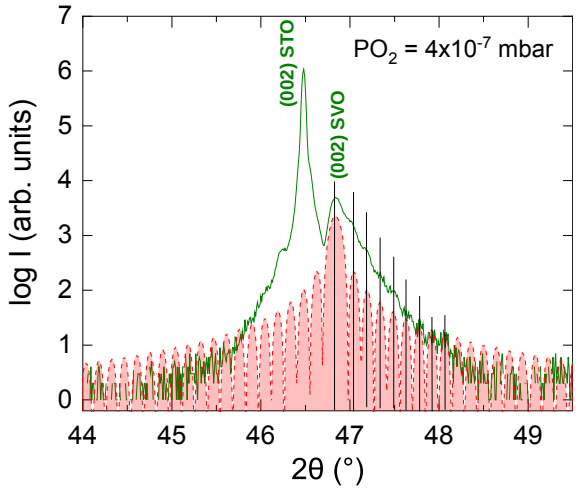

FIGURE 3.6: High resolution XRD $\theta-2\theta$ scan of SVO//STO film grown at $PO_2 = 4\times10^{-7}$ mbar and $T = 750$ °C. Laue fringes can be observed. The extracted thickness of 67 nm is in agreement with the one determined from X-ray reflectivity measurements (70 nm).

occur at smaller 2θ angles than bulk (002) SVO (vertical dashed line); hence both peaks correspond to larger c-axis than bulk SVO. Although this behavior could be expected if the negative mismatch of the LAO substrate on the film would induce a compressive epitaxial strain on the basal plane of SVO, the reciprocal space maps (Figure 3.7) indicate that the cell parameters of SVO are not clamped to those of the substrate but relaxed. Therefore, for SVO//LAO, the VO_6 coordination polyhedron has an enhanced tetragonality $c/a > 1$.

The X-ray reflections of SVO films on LSAT and NGO are hardly discernible from those of the substrate due to the close structural matching and a noticeable SVO line-broadening that, in accordance with topographic images (Figure 3.4), can be attributed to the limited size (grain size < 50 nm) of the coherently-diffracting volume, shrank by the presence of strain-induced defects (see Section 3.4.4). From the $\theta-2\theta$ and reciprocal space maps (Figure 3.7) we determine that the corresponding c-axis parameters are c(SVO//LSAT) ≈ 3.87 Å and c(SVO//NGO) ≈ 3.86 Å, while the in-plane parameters coincide with those of the corresponding substrates. Consistently with the results of the SVO//STO above, SVO films on NGO and LSAT films are epitaxially strained. Therefore, within the experimental resolution, for SVO//NGO and SVO//LSAT $c/a \approx 1$.

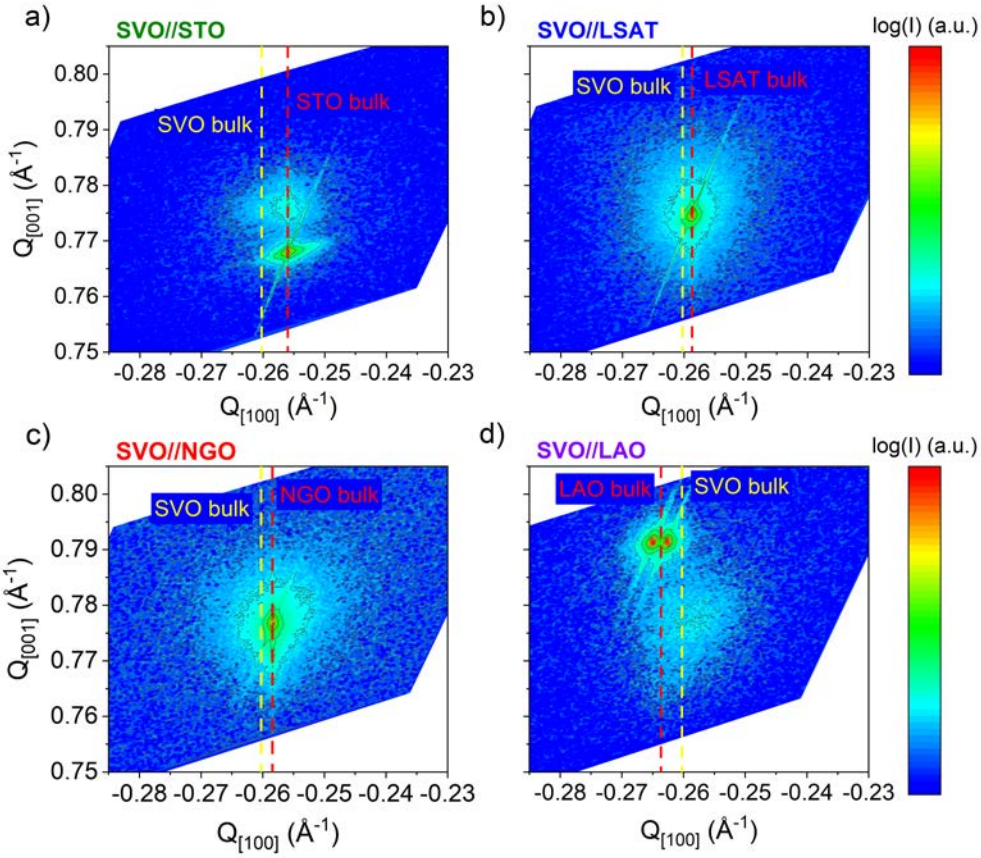

FIGURE 3.7: XRD reciprocal space maps around (-103) reflections of a) SVO//STO, b) SVO//LSAT, c) SVO//NGO, and d) SVO//LAO. Notice in a), b) and c) that the in-plane cell parameter of the film coincides with that of the substrate (vertical red dashed line). This is not the case in d) where the center (vertical white dashed line) of the relatively broad SVO reflection is clearly shifted with respect to that of the substrate.

In Figure 3.5b, we plot the c-axis parameters of all films. We also include the predicted cell parameter of epitaxial strained SVO films on the different substrates, calculated using the Poisson equation and assuming volume conservation [42]. It is clear that the c-axis values of the films, including c_2(SVO//LAO), are larger than that expected if a pure elastic compressive or tensile strain were acting on the SVO film. As mentioned above, a unit cell expansion is commonly observed in SVO films and attributed nonstoichiometric defects related to the extremely low PO_2 used during growth [42, 111, 115, 116]. Recently, it has been reported that using a nonreactive gas in the PLD growth process, this effect can be mitigated, probably

as a result of changing the Sr/V ratio or the oxidation state of species in the plume [112] (this is further explored in Chapter 4).

The symmetric X-ray diffraction $\theta-2\theta$ scans do not reveal the presence of spurious phases in none of films grown at low pressure ($PO_2 = 4\times10^{-7}$ mbar). However, as the corresponding reflections may not be visible in symmetric scans, we collected 2D maps of the reciprocal space along 2θ and χ angles. In Figure 3.5c (top panel) we show the 2θ–χ frame for SVO//STO samples. The intense (001) and (002) substrate reflections are well visible. The superimposed (001) and (002) SVO reflections are not distinguishable from those of the substrate, which is in agreement with the $\theta-2\theta$ scans (Figure 3.5a) and the lower resolution of the 2D detector. Importantly, no other reflections that could suggest the presence of spurious phases are visible in these films. We then conclude that films grown at the lowest pressure ($PO_2 = 4\times10^{-7}$ mbar) are single phase, as summarized in Figure 3.2. However, this is not the case for films grown at higher PO_2. In Figure 3.5c (bottom panel) we show a 2θ–χ frame of the SVO//STO sample grown at $PO_2 = 2\times10^{-5}$ mbar. In this map, additional spots that correspond to the (205) $Sr_3V_2O_8$ reflections are visible. Consistently, the AFM images of this SVO//STO sample (Figure 3.3) show outgrowths which are associated to the $Sr_3V_2O_8$ phase identified in the 2D maps [114]. Similar results are observed in films grown at high PO_2 on LSAT substrates.

3.4.3 Electrical transport properties

We turn now to the electrical transport properties of the films with the focus on its dependence on structural mismatch and the PO_2 used during growth. In Figure 3.8a we show the room-temperature resistivity $\rho(300\,K)$ of the SVO films grown on different substrates at $PO_2 = 4\times10^{-7}$ mbar (square symbols) and $PO_2 = 2\times10^{-5}$ mbar (circle symbols). The resistivity is minimal for the films grown on best-matched substrates (LSAT and NGO) and, for a given mismatch, the resistivity decreases when reducing PO_2. Accordingly, $\rho(300\,K)$ reaches its smallest value (at $PO_2 = 4\times10^{-7}$ mbar) for SVO//NGO films, where $f(\text{SVO//NGO}) = +0.52\,\%$. The resistivity value $\rho(300\,K, NGO) \approx 85\,\mu\Omega\,\text{cm}$ is comparable to the state-of-the-art resistivity values of films of similar thickness grown, under similar conditions, by PLD ($\approx 35-90\,\mu\Omega\,\text{cm}$ [112, 114, 116]) and only 3 times larger than that of films grown by hybrid-MBE ($\approx 30-40\,\mu\Omega\,\text{cm}$ [18, 42]). The same trend of $\rho(300\,K)$ with the lattice mismatch is also observed in the series of films grown at $PO_2 = 2\times10^{-5}$ mbar (circles). Therefore, data in Figure 3.8a indicates an important role of the film–substrate mismatch on the resistivity of SVO films.
The carrier concentration (n) and mobility (μ) values, extracted from resistivity and Hall effect measurements, of films grown at the lowest PO_2 (4×10^{-7} mbar) on different substrates, are shown in Fig. 3.8b (diamonds and squares, respectively).

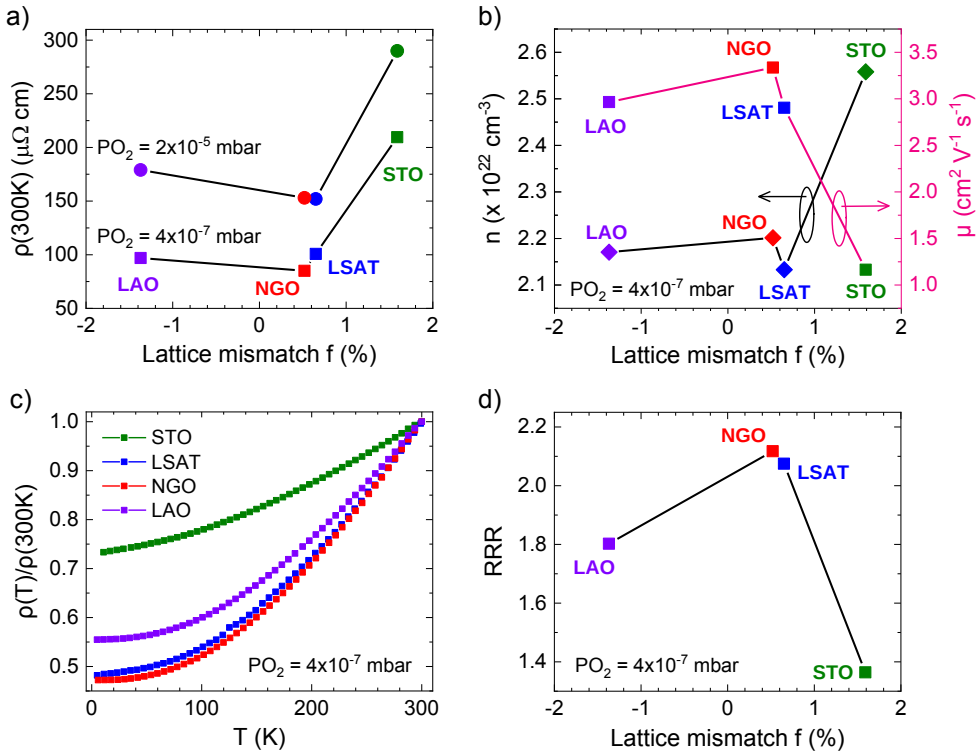

FIGURE 3.8: a) Room-temperature resistivity $\rho(300\,K)$ of films deposited on different substrates at $PO_2 = 4\times10^{-7}$ mbar (squares) and $PO_2 = 2\times10^{-5}$ mbar (circles). b) Carrier density (diamonds) and carrier mobility (squares) of the films grown at the lowest pressure ($PO_2 = 4\times10^{-7}$ mbar). c) Temperature dependence of the normalized resistivity $\rho(T)/\rho(300\,K)$ of the same films grown at the lowest pressure ($PO_2 = 4\times10^{-7}$ mbar); the corresponding structural mismatch is indicated. d) Residual resistivity ratio ($RRR = \rho(300\,K)/\rho(5\,K)$.)

We first note that n is almost constant ($n \approx 2.1 \times 10^{22}$ cm^{-3}) for films on LSAT, NGO, and LAO. This value is close to, but slightly larger than the value expected for stoichiometric SVO with V^{4+} ($3d^1$) ($n \approx 1.76 \times 10^{22}$ cm^{-3}). A perceptible 16% larger carrier concentration is observed for films grown on STO. We note that if the STO substrate would have opened a conducting parallel channel in the SVO//STO sample grown at the lowest pressure, then the measured carrier density would have been smaller but not larger. Therefore, a plausible reason is that the tensile strain imposed by the STO substrate favors a higher concentration of oxygen vacancies, that can provide additional carriers while reducing mobility [129].

The carrier mobility reaches its largest value ($\approx 3.3\ cm^2\,V^{-1}\,s^{-1}$) for SVO grown on the best matching NGO substrate, being marginally smaller in films on LSAT and LAO. A more pronounced reduction ($\approx 1.2\ cm^2\,V^{-1}\,s^{-1}$) is observed in SVO//STO, consistent with an increased strain-related nonstoichiometry, as indicated above.

The temperature dependence of the resistivity $\rho(T)$ and the residual resistivity ratio ($RRR = \rho(300\,K)/\rho(5\,K)$) of SVO films are also significantly different depending on the substrate used, as shown in Figure 3.8c,d, respectively. It can be appreciated that the SVO//NGO film displays the largest RRR ($RRR \approx 2.1$) (Figure 3.8d) and RRR gradually decreases in films on substrates having larger lattice mismatch. For instance, $RRR \approx 1.4$ for SVO//STO. Accordingly, the maximal RRR (minimal residual resistivity) is also obtained in films grown on well-matched substrates (Figure 3.8d). We note in passing that the largest RRR values reported for SVO films grown by PLD under standard PO_2 atmosphere were of only ≈ 1.7 [114, 116].

Overall, all data in Figure 3.8 strongly suggest that resistivity, carrier density, and mobility of SVO films grown under optimized conditions are primarily determined by the structural mismatch with substrates, maybe exacerbated by mismatch-controlled nonstoichiometry.

It is known that defects in solids, affecting carrier mobility, can be screened by carriers and therefore, the mobility is affected by the carrier density in an unconventional manner [17]. To explore this effect, we focus on SVO//LSAT and SVO//STO films as illustrative examples of well and poor matched substrates, respectively, and analyze the relationship between carrier density and mobility of SVO films. In Figure 3.9 we plot μ versus n for SVO//LSAT (squares) and SVO//STO (circles) films grown at the same temperature (750 °C) and varying PO_2. Data in Figure 3.9 reveal important trends. First, at any PO_2 the carrier mobility is larger for films grown on LSAT than on STO. Next, it is observed that for films on both substrates, an enhancement of mobility goes in parallel with an increase of carrier concentration ($\mu \propto n^b$, $b > 0$). The relevance of this observation is better appreciated by noticing that in conventional doped semiconductors, the opposite behavior is typically observed. Indeed, it is commonly found that μ decreases with increasing doping due to the enhanced scattering of carriers with dopant atoms. The reverse trend observed here bears some resemblance with properties of some strained semiconductors, such as $BaSnO_3$, where a similar $\mu \propto n^b$ (with $b > 0$) trend has been reported [107, 126]. It has been argued that this unusual increase of mobility when increasing the carrier density is due to the enhanced screening of extended defects, such as dislocations, by the carriers (Figure 3.1c) [17]. The confined and directional character of the relevant 3d orbitals forming the conduction band of SVO advances a strong sensitivity of carrier mobility to extended structural defects. Therefore, it

may not be a surprise that the carrier-induced screening can efficiently increase mobility.

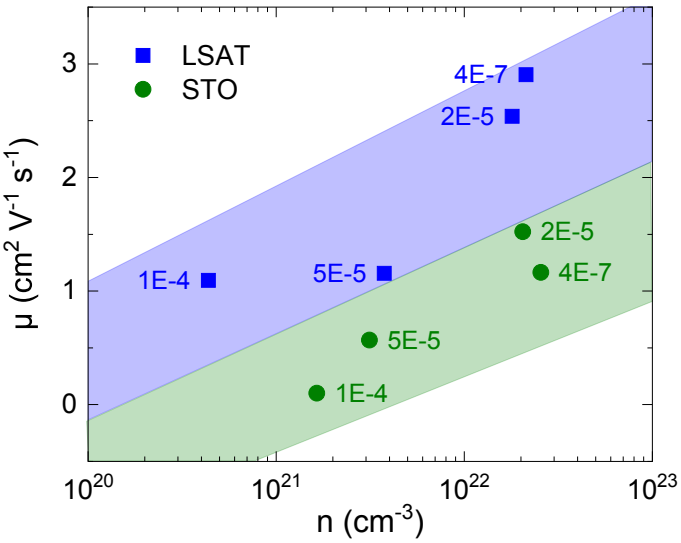

FIGURE 3.9: Carrier mobility versus carrier density for SVO//LSAT (squares) and SVO//STO (circles) films deposited at various PO_2.

3.4.4 Microstructure

The observations above suggest that extended defects associated to structural mismatch play a major role on charge scattering and trapping. To get insight on this, the microstructure of the films grown at $PO_2 = 4\times10^{-7}$ mbar and $T = 750\,°C$ were studied by transmission electron microscopy (TEM). Specimens from the SVO films grown on LAO, NGO, and STO were prepared in cross section geometry by focused ion beam (FIB) lift-out technique.

Figure 3.10a–c (main panels) shows bright field images of SVO//LAO, SVO//NGO, and SVO//STO, respectively. It can be appreciated that all films present a sharp interface (see horizontal solid lines) with the substrate, homogeneous thickness of ≈ 70 nm and a free surface with a roughness at the nanometer level. From these bright field images acquired in zone axis conditions, it can be seen that the films present an incoherent contrast, with obvious dissimilarities among them. In order to assess the density and nature of the crystal defects that may be responsible for the observed contrast, the crystals were oriented in two-beam conditions by tilting the specimen in the TEM. In opposition to zone axis condition, in which the crystal is oriented so that the Ewald sphere is tangent to a plane of nodes of the

reciprocal lattice of the crystal, in two-beam conditions the crystal is oriented in such a way that only a family of reflections is in Bragg condition (the second beam being the direct beam). By acquiring bright field images in this condition, defects in the direction given by the intersection of the Ewald sphere with the reciprocal lattice of the crystal are strongly highlighted.

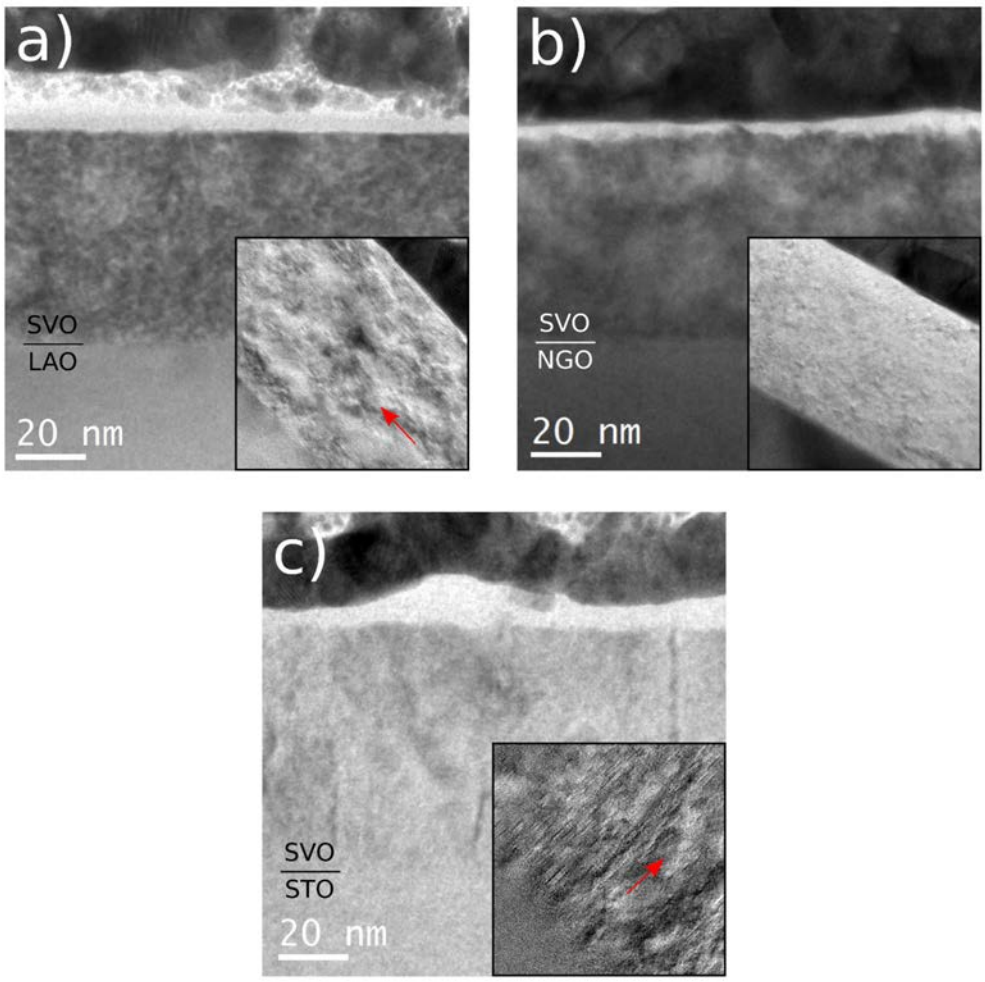

FIGURE 3.10: Cross-section of bright field TEM images of the SVO films grown on a) LAO, b) NGO, and c) STO substrates. Insets: bright field TEM images obtained by tilting the crystals to obtain two-beam conditions, highlighting the presence of defects in particular directions.

The bright field images acquired in two beam conditions described above, are shown in the insets of Figure 3.10a–c. Different two beam conditions were set for all the SVO films: one corresponding to the family of planes stacked in the growth direction and the other in the perpendicular direction. In Figure 3.10a (inset) we show an image collected for the SVO film grown on the LAO substrate, which we remind here is subjected to a compressive stress. The image reveals a microstructure of defects consisting on planar defects oriented parallel to the substrate (compressive stress, LAO) (Figure 3.10a (inset)). In contrast, planar defects oriented perpendicular to the substrate can be observed in SVO grown on substrates imposing a tensile stress (STO) (Figure 3.10c (inset)). The presence of oriented planar defects in thin films grown on mismatched substrates, has been reported in other perovskite thin films, such as $La_{0.5}Sr_{0.5}CoO_{3-x}$ [130–132] or $LaNiO_{3-x}$ [133] to name a few, and it is believed to be a signature of defects ordering (oxygen vacancies) to release epitaxial stress. More precisely, high resolution electron microscopy images of $La_{0.5}Sr_{0.5}CoO_{3-x}$ films grown on LAO and STO substrates, imposing -as in the present case- compressive and tensile stress respectively, clearly revealed a similar arrangement of planar defects [132]. In the present case, it cannot be excluded that planar defects could be related to the presence of $Sr_3V_2O_8$, as identified in some XRD data. However, the observation that in SVO film grown on NGO substrate (Figure 3.10b (inset)), with a very small lattice mismatch, a much smaller density of defects was observed in both crystal orientations seems to favor the former scenario. The presence of these extended planar defects should impact the electronic transport. Indeed, for SVO//STO where the array of defects is perpendicular to the interface, the carrier mobility should be much obstructed than in SVO//LAO where these defects lay parallel to the interface. This is indeed, the trend observed in Figure 3.8b.

3.4.5 Optical properties

Spectroscopic ellipsometry (SE) measurements were performed on SVO//(STO, LSAT, NGO, and LAO) films grown at $PO_2 = 4\times10^{-7}$ mbar and at $PO_2 = 2\times10^{-5}$ mbar. The real and imaginary parts of the dielectric constants ($\varepsilon = \varepsilon_1 + i\,\varepsilon_2$) and optical coefficients ($\tilde{n} = n + i\,\kappa$) were extracted from the SE data (see experimental section). Figure 3.11a,b shows the spectral dependence of ε_1 and ε_2 of some illustrative films.

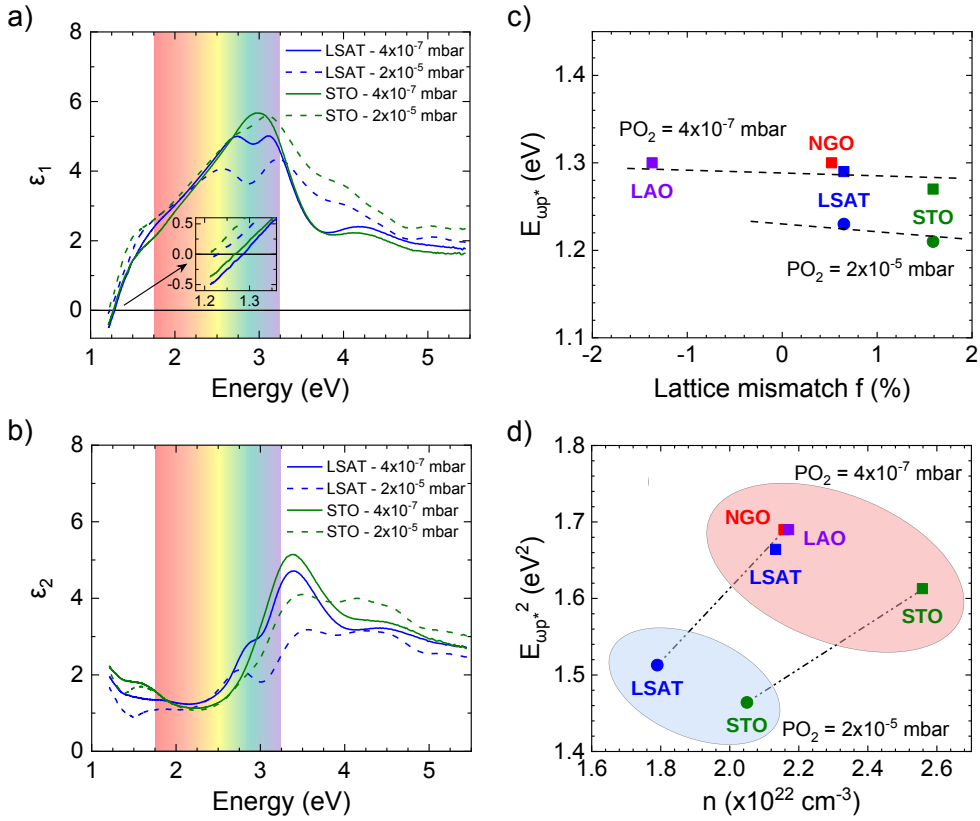

FIGURE 3.11: a,b) Complex permittivity $\varepsilon = \varepsilon_1 + i\,\varepsilon_2$ of SVO//LSAT and SVO//STO films grown at $PO_2 = 4\times10^{-7}$ mbar and $PO_2 = 2\times10^{-5}$ mbar, as indicated. c) Dependence of the measured screened plasma energy ($E_{\omega p}{}^* = \hbar\omega_p{}^*$) on the substrate mismatch f. The lines through the data are guides for the eye. d) Dependence of $E_{\omega p}{}^*$ versus carrier concentration n as derived from Hall measurements (Figure 3.8). The lines through the data allow visualizing the modulation of $(E_{\omega p}{}^*)^2$ *vs* n with growth conditions and the distinctive behavior of SVO//STO. Encircled samples were grown under the same PO_2.

The shape of both components of the complex permittivity ε are in good agreement with earlier reports [18]. From $\varepsilon_1(\omega)$ the screened plasma frequency $\omega_p{}^*$ can be determined by using the condition $\varepsilon_1(\omega_p{}^*) = 0$. Two salient features emerge from data in Figure 3.11a. First, $\omega_p{}^*$ increases when reducing PO_2 during growth and second, for a given growth PO_2, $\omega_p{}^*$ is reduced in SVO//STO compared to SVO//LSAT. These trends can be better visualized in Figure 3.11c where we plot $E_{\omega p}{}^*$ versus f values of these films. As seen, all $\hbar\omega_p{}^*$ values are around 1.2−1.3 eV, which is agreement

with earlier reports for SVO//LSAT [18]. To get a further insight on the implications of these observations, we recall that [123]:

$$(E^*_{\omega p})^2 = \frac{\hbar^2 e^2}{\varepsilon_0 \varepsilon_\infty} \frac{1}{m*} \times n \tag{3.1}$$

where ε_∞ is the high frequency relative permittivity of the medium, n is the free carrier density, m^* is the free carrier effective mass, and $\hbar$, e, and ε_0 stand for the reduced Planck constant, the electron charge and the free space permittivity, respectively. In Figure 3.11d we plot $({E_{\omega p}}^*)^2$ *versus* n (where n is the carrier density determined from Hall effect, see Figure 3.8). This plot allows to conclude that the plasma energy increases when reducing PO_2 because the carrier density increases. Moreover, the smaller slope of the ${E_{\omega p}}^{*\,2}$ (n) plot observed in SVO//STO anticipates a larger effective mass of carriers in comparison to SVO//LSAT. Using ε_∞ = 4, as determined in bulk SVO [123], the effective mass m^* can be computed from data in Figure 3.11d. For SVO//LSAT, we obtain m^*(LSAT) ≈ 4 irrespectively on the PO_2. For SVO//STO we obtain a significant larger mass m^*(STO) ≈ 5, which represents a 25 % enhancement. It is worth to recall that in $Ca_{1-x}Sr_xVO_3$ bulk materials, m^* was found to increase from 3.3 to about 4 when increasing x due to internal chemical pressure [123].

The complex refractive index of the film and substrate extracted from the ellipsometry measurements were used to calculate the sample reflectivity $R_{calc}(\omega)$, assuming a simple model consisting of a substrate and a SVO film, and to compare it with experimental data. Fourier transform infrared reflectometry (FTIR) measurements have been used to determine $R_{exp}(\omega)$ at normal incidence. The experimental $R_{exp}(\omega)$ and $R_{calc}(\omega)$ data for some illustrative films are shown in Figure 3.12).

Data reveal that both $R(\omega)$ display a minimum at around 600 nm (≈ 2 eV). This observation is in agreement with results from Boileau et al. [125] although we emphasize that the minimum of $R(\omega)$ cannot be taken as a measure of ${\omega_p}^*$, due to the substrate contribution to the reflectivity measurements. It is of the highest interest to notice that all samples, irrespectively of their DC conductivity, display a remarkably small $\varepsilon_2(\omega)$ in the visible range (Figure 3.11b), which is a signature of small absorption. It thus follows that, within the explored growth conditions range, although electrical conductivity and plasma frequency can be modulated, the optical absorption remains almost unperturbed.

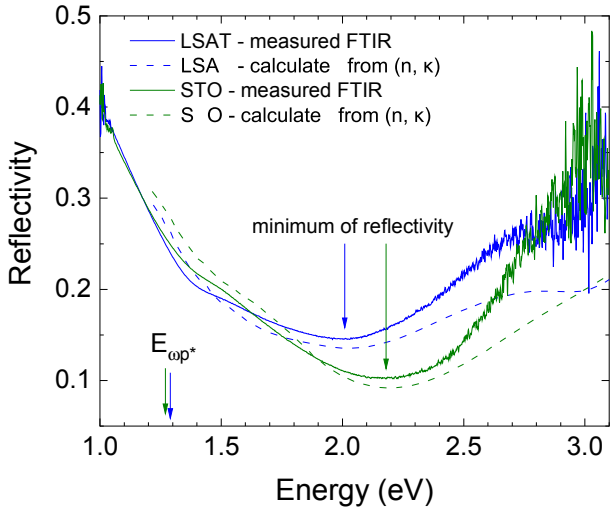

FIGURE 3.12: Calculated reflectivity and measured FTIR spectra at normal incidence, of SVO//LSAT and SVO//STO films grown at $PO_2 = 4\times10^{-7}$ mbar and $T = 750\,°C$. Reflectivity was calculated using a model consisting of a substrate (0.5 mm thick) and the corresponding SVO layer thickness. The optical parameters (n,κ) of film and substrate where obtained from the ellipsometry measurements as indicated.

The optical transmittance of SVO films (25 and 50 nm thick) deposited on LSAT has been measured and is shown in Figure 3.13. The measurement were performed using a pristine LSAT substrate (polished on both sides) for the baseline, so that the spectra showed here reflect the transmission coefficient of the SVO film only. The maximal transmittance in the visible range (after subtraction of the substrate contribution) of state-of-the-art reported SVO films (grown by h-MBE [18]) with similar thicknesses is indicated by the dashed lines. We can observe that our films display high transparency in the visible range, similar to the ones from ref. [18]. For a given thickness and at a given energy, our transmission coefficient is only few percent smaller than their value, which we attribute to the presence of point defects induced by the PLD growth.

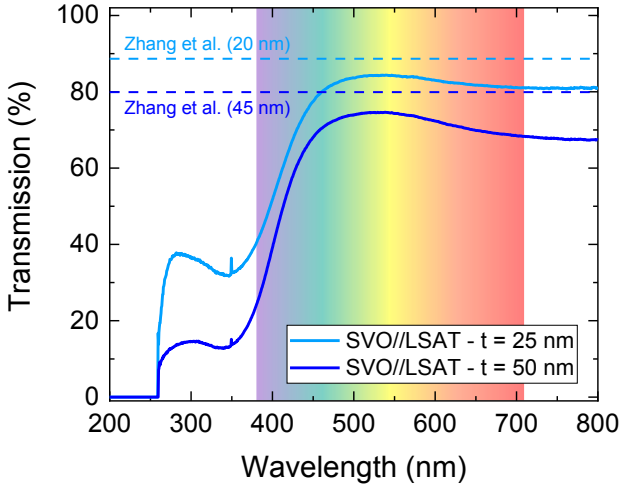

FIGURE 3.13: Optical transmittance of SVO films (25 and 50 nm thick, "free-standing" as explained in the main text), grown on double side polished LSAT substrates at $PO_2 = 4\times10^{-7}$ mbar and $T = 750$ °C. For reference, the maximal transmittance in the visible range (at $\approx$ 560 nm) of state-of-the-art SVO films of similar thicknesses grown on LSAT by hybrid-MBE [18] is included (dashed lines). The substrate contribution was also removed.

3.4.6 X-ray absorption and orbital occupancy

In section 3.4.5 we have shown that the effective mass of carriers in SVO films on STO is larger than that of SVO films on LAO, LSAT, and NGO substrates. As films on different substrates appear to be under different strain state, a natural question arises: Which is the role of strain on orbital occupancy and ultimately on bandwidth broadening? Indeed, it is well known that substrate-induced stress on epitaxial films of oxides breaks the orbital degeneracy and promotes a selective electron occupancy in well-defined orbitals, that affects transport properties [80]. The X-ray absorption (XAS) at metal $L_{2,3}$ edges in epitaxial metal oxide films, is sensitive to the relative orientation of the polarization direction of the incoming X-ray beam with respect to the film surface. This gives rise to an X-ray linear dichroism (XLD), defined as $XLD = I(E_{ab}) - I(E_c)$, different from zero if final states with different symmetry are not equally available [86]; $I(E_{ab})$ and $I(E_c)$ are the intensities of the absorption of light with the electric field (polarization) parallel to the film plane (E_{ab}) or perpendicular to it (E_c). For an epitaxial (001) SVO film, as in the present case, E_{ab} is probing electronic states with (xy) symmetry and (E_c) is probing electronic states with (xz, yz) symmetry. In the particular case of V-3d[1], if

the electron occupancy at the (xy) and (xz, yz) orbitals is not identical, a nonzero XLD should be apparent. XLD will be different depending if the lower lying state is (xy) or (xz, yz), that is depending on the sign of the energy difference $\Delta t_{2g} = E_{xz,yz} - E_{xy}$ where E_{xy} and $E_{xz,yz}$ are the corresponding energies. Notice that $\Delta t_{2g} > 0$ has to be found in presence of an in-plane expansion of the equatorial bonds in VO_6 and $\Delta t_{2g} < 0$ corresponds to an out-of-plane expansion of V−O−V bonds in VO_6.

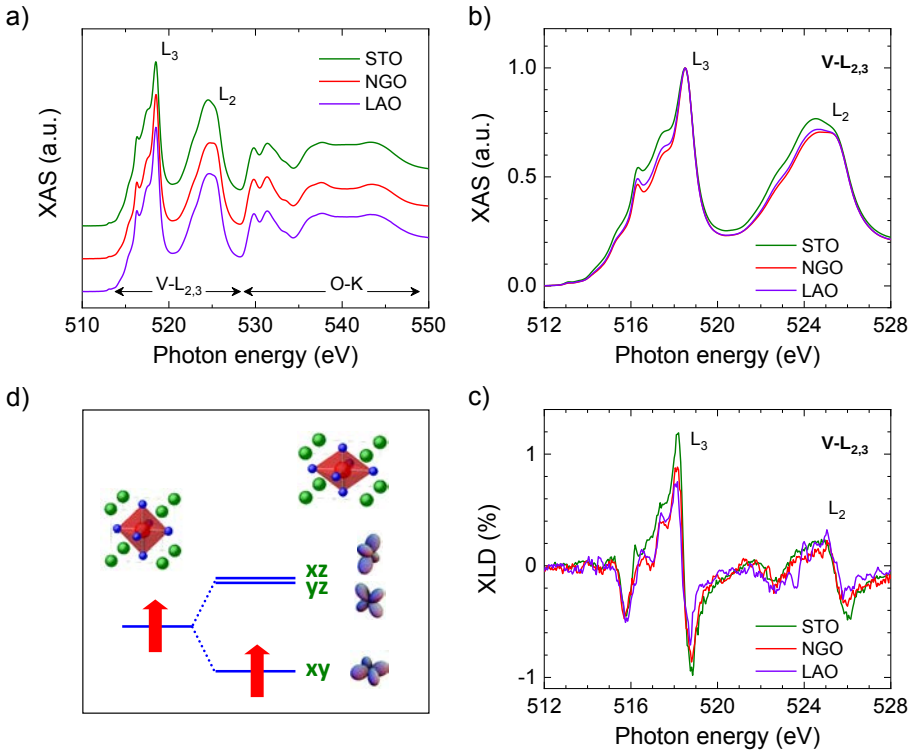

FIGURE 3.14: a) X-ray absorption (XAS) spectra at V-$L_{2,3}$ and O-K edges for SVO films (70−80 nm thick) grown on STO, NGO, and LAO substrates, as indicated. b) A zoom of the XAS spectra around the V-$L_{2,3}$ edges. c) Corresponding X-ray linear dichroism (XLD) (% of white line intensity) spectra of the same samples. d) Sketch of the V-3d-t_{2g} band splitting resulting from in-plane tensile strain of the VO_6 octahedron.

In Figure 3.14a we show the combined V-$L_{2,3}$ and O-K XAS spectra of the SVO films grown on STO, NGO and LAO substrates, selected because they display the maximal (STO tensile, LAO compressive) and minimal (NGO) mismatch. The V-L_3 and L_2 edges (at 519 and 524 eV) are signatures of the dipole transitions from

$2p_{3/2}$ to 3d and from $2p_{1/2}$ to 3d orbitals. The double peak (appearing at 530 eV) of the O-K prepeak is a fingerprint for the V^{4+} valence state. The relative intensity of the $L_{2,3}$ as well as the splitting of the O-K prepeak are characteristic of V^{4+} in an octahedral coordination [134, 135]. A detailed inspection of the low energy side of the L_3 peak (see Figure 3.14b) reveals a fine structure where three peaks can be identified. As shown by cluster calculations [135] the appearance of these peaks is prominent in tetragonally distorted VO_6 octahedra. In Figure 3.14b it can be appreciated that these features are more prominent in SVO//STO than in SVO//NGO and SVO//LAO, and according to the previous statement, we conclude that in SVO//STO, the VO_6 octahedra have a larger tetragonal distortion than in SVO//NGO and SVO//LAO.

A more direct evidence is provided by the XLD data shown in the following. In Figure 3.14c we present the $XLD = I(E_{ab}) - I(E_c)$ data of SVO//(STO, NGO, LAO) films. To appreciate the implications of the data in Figure 3.14c, we remind here that theoretical cluster calculations [135] of XLD for $\Delta t_{2g} > 0$ and $\Delta t_{2g} < 0$ predicts XLD spectra that are virtually opposite one another, and thus comparison with experimental data should allow to discern between $\Delta t_{2g} > 0$ and $\Delta t_{2g} < 0$. The XLD data in Figure 3.14c show that for SVO films, the overall trend is similar to the above predicted $\Delta t_{2g} > 0$ case [135]. Interestingly, as clearly shown by data in Figure 3.14c, the height of the most intense XLD peak, which is the most sensitive to the magnitude of Δt_{2g} is somewhat larger in SVO//STO than in SVO//(NGO, LAO). It has also been predicted that the features appearing at the low-energy side of L_3 are more sensitive to tetragonal distortion for $\Delta t_{2g} > 0$ than for $\Delta t_{2g} < 0$. In Figure 3.14b it can be appreciated that these features are more visible in SVO//STO than in SVO//NGO and SVO//LAO, and according to the previous statement, we conclude that in SVO//STO, Δt_{2g} is positive (> 0) and larger than in SVO//NGO and SVO//LAO. Therefore, the VO_6 octahedra in SVO// STO are under a larger tensile in-plane stress than in SVO//NGO and SVO//LAO. Although in principle Δt_{2g} could be deduced by comparing multiplet calculations with experimental spectra, we content ourselves here by using XLD to discern between tensile or compressive strain.

Overall, from both XAS and XLD data we conclude that: i) a tetragonal crystal field breaks the symmetry of the t_{2g} manifold into (xy) and (xz, yz) states; ii) as $\Delta t_{2g} > 0$, the $t_{2g}(xy)$ states lay lower in energy than $t_{2g}(xz, yz)$ and thus they have a higher electron occupancy (see Figure 3.14d for the unstrained and strained VO_6 octahedra and the t_{2g}-manifolds).

3.5 Conclusions

We have shown that $SrVO_3$ films grown under different oxygen pressure and on substrates having different structural mismatch, thus imposing different (tensile or compressive) epitaxial stress, clearly show distinct transport properties. The carrier mobility is found to be the largest in SVO films grown on matching substrates and lowering when films are grown on substrates imposing a large tensile or compressive strain. Although the film conductivity, carrier density and mobility are found to depend on the growth conditions (mainly the oxygen pressure) as expected in presence of growth-induced point defects (Figures 3.1b and 3.8) the dependence on these parameters on substrate mismatch is fully preserved, thus suggesting that the substrate plays a major role. Interestingly, the reduction of mobility is asymmetric, being more pronounced in case of tensile stress (SVO//STO) but only marginally larger in case of compressive stress (SVO//LAO).

Using first principle calculations Sclauzero et al. [136] have predicted that epitaxial strain on SVO has basically two effects. First, a crystal field of tetragonal symmetry breaks the degeneracy of the t_{2g} electronic triplet and, irrespectively of the sign of strain, the electronic correlations will be reinforced and approaching SVO to an insulator Mott regime. Second, stretching the M−O bonds should have a similar effect, whereas bond shortening should have the opposite effect, that is enhancing the hopping amplitude and thus promoting a more metallic character. Therefore, for tensile strain a more insulating character of SVO is expected whereas for a compressive strain, band narrowing and hopping-amplitude enhancement cancel out their contributions and only minor changes of carrier mobility are expected. Our XAS and XLD data provide clear evidence of the strain-induced breaking of symmetry and stabilization of the xy orbitals in STO compared to other substrates (Figures 3.1a and 3.14). This is consistent with the $c/a < 1$ distortion of the unit cell of SVO//STO, inferred from X-ray diffraction data. Charge redistribution enhances xy orbital occupancy, narrows the electronic bandwidth, and enhances the effective mass of carriers in films on STO compared to other substrates. This is precisely the result obtained from ellipsometry measurements, where m^*(SVO//STO) $\approx 1.25 \times m^*$(SVO//LSAT) (Figure 3.11). However, this 25 % enhancement of the effective mass of carriers in SVO//STO cannot account for the observed ≈ 200 % larger resistance in SVO//STO compared to SVO//LSAT (or other substrates) (Figure 3.8a). Therefore, other effects should play a bigger role on DC transport properties.

The TEM images have provided evidence of the existence of arrays of planar defects in SVO films grown on mismatched substrates and their orientation is compatible with the observed modification of mobility, more (less) pronounced in SVO films

on STO (LAO). This is the trend observed for the resistivity and carrier mobility of SVO films grown on different substrates (Figure 3.8a,b). Remarkably, it is found (Figure 3.9) that carrier mobility increases when increasing carrier concentration. This observation favors the view that electrical conductivity and mobility in these strained films, although affected by the heavier electron mass in tensile strained films, are primarily governed by microstructural effects, namely stress-induced planar defects (Figure 3.1c). Therefore, one could anticipate that avoiding strain relaxation, maybe by using thinner SVO films (as further explored in Chapter 5), the genuine effects of band reconstruction due to epitaxial strain will become more apparent on the DC electric transport properties. Otherwise, only optical conductivity (thus plasma frequency) is sensitive to these effects. From a practical point of view, it is remarkable that the optical transparency window remains in the visible range for all studied films irrespectively on the growth conditions and substrates, thus suggesting that the harsh conditions required to grow optimal SVO films may not be a limitation for future applications.

Chapter 4

Improvement of the electrical and optical properties of PLD-grown $SrVO_3$ thin films

In the experimental chapter, section 2.1, we have seen that PLD offers a very broad range of possibilities when tuning the deposition parameters. One can decide to change the nature and amount of background gas in the chamber, vary the substrate temperature or even play with the laser settings (fluence, frequency, etc.). As a matter a fact, any variation of one of these parameters can have a crucial impact on the film growth, and subsequently on its crystalline quality and thus functional properties. In this chapter, we describe an approach used to reduce defects engendered by the growth of $SrVO_3$ thin films in UHV. We show the structural and functional improvements resulting from growing $SrVO_3$ in an inert argon atmosphere. In Appendix B, we also describe other strategies (although less efficient) attempted to reduce growth-induced defects, by tuning other parameters of the PLD setup.
The work presented in this chapter was published with DOI: 10.1002/adfm.201808432 (see also the list of publications).

4.1 Introduction

As seen in Chapter 3, the epitaxial growth of SVO is intricate as stabilization of V^{4+} is challenging (V^{3+} and V^{5+} are competing valence states, leading to the formation of spurious insulating phases). For that reason, extremely low oxygen pressures ($PO_2 \approx 10^{-7}$ mbar) are required [114]. It is instructive to notice that, whereas the room-temperature resistivity values of optimal films are reported to be in the 30−120 μΩ cm range independently of the growth technique used, the residual resistivity ratio (RRR) ($RRR = \rho(300\,K)/\rho(5\,K)$) is typically of about 2 for films grown by PLD and PED [114–117, 137–140] but it is dramatically larger ($RRR \approx$

120−222) for hybrid-MBE grown films [18, 42, 111]. This observation implies that the growth process has a large effect on the carrier mobility (and hence the electrical conductivity), probably related to the presence of growth-induced defects in the film. Indeed, in PLD technique, the use of ultralow pressure ($\approx 10^{-7}$ mbar) during growth has important consequences on the spatial expansion and kinetic energy of the ablated species [141, 142] as well as on the self-sputtering and backscattering processes [143]. Probably the most obvious is that energetic species can impinge upon the substrate and the growing film, with subsequent creation of various defects including nonstoichiometry. Therefore, at first sight, the possible use of PLD (or any other hyperthermal technique) for deposition of materials requiring extremely low oxygen pressures may appear to be challenging.

In this chapter, aiming at understanding and controlling growth-induced defects in SVO films and monitoring their impact on their electronic properties, namely electrical resistivity, carrier density and mobility, and optical transmittance, we report on the properties of SVO films grown by PLD under nonreactive Ar atmosphere. The reason behind is that a nonreactive gas could contribute to plasma thermalization and consequently, reduce the kinetic energy of the species in the plume and their flux at the film surface, as demonstrated in the growth of high-temperature superconductor films [141]. It will be shown that using this strategy, the extension of the plume of laser-ablated species can be controlled (Figure 4.1a) and films grown under optimal Ar pressure display a remarkable reduction of their room-temperature resistivity down to $\approx 30\ \mu\Omega\,\text{cm}$, thus competing with the record values of hybrid-MBE films, and the residual resistivity ratio rises by about a factor five compared to reported SVO films grown by conventional PLD and PED, as summarized in Figure 4.1b. Importantly, the transparency of the films in the visible range is enhanced by the new growth process developed here and rivals that of the hybrid-MBE grown films [18]. These findings indicate that TCO films such as SVO, and probably other materials requiring ultralow oxygen pressure deposition conditions, can be grown with optimal properties by PLD or other more scalable techniques, as required for large scale applications. From a different perspective and beyond the scope of TCOs, SVO films have been explored in search of quantum confinement effects; indeed, orbital selective quantization and anomalous mass enhancement effects have been reported [127, 144] in PLD-grown films, and SVO is considered to be the *drosophila* model for strongly correlated physics [145]. Moreover, as emphasized by Backes et al. [145], the role of defects is pivotal for a microscopic description of the spectroscopic features. The improved properties of SVO films reported here may stimulate revisiting some scenarios.

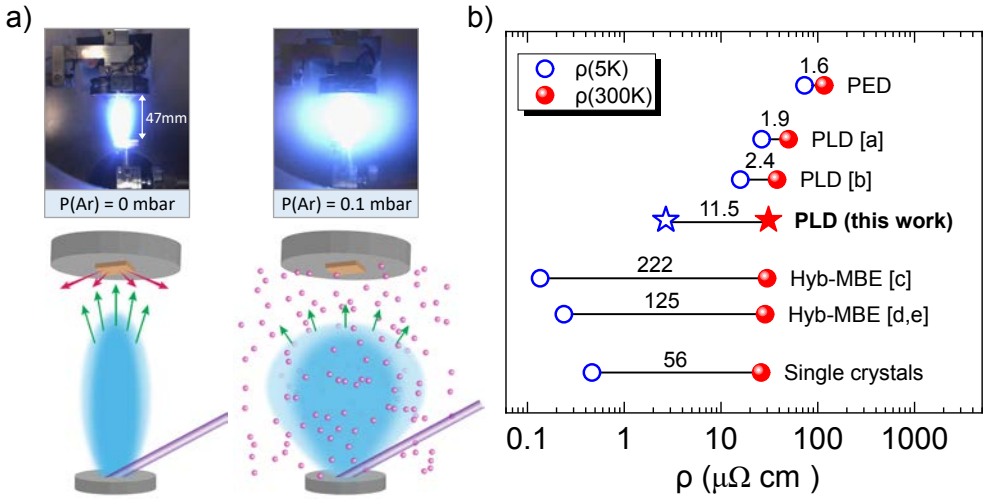

FIGURE 4.1: a) Pictures of the SVO plasma during PLD deposition in vacuum or under argon pressure of 0.1 mbar. To provide a suitable scale, the target-to-substrate distance (47 mm) is indicated. Sketches below each picture highlight the occurring phenomena. Green arrows length illustrates the kinetics of species reaching the substrate. In the case of the deposition in vacuum, red arrows represent resputtering process. b) State-of-the-art electrical resistivity values of SVO films at room-temperature (red solid circles) and at low temperature (5 K) (blue circles) grown by different techniques, as indicated. The number above each bar indicates the corresponding *RRR* value. Reference data were taken for PED [140], PLD (a [138], b [114]) and h-MBE (c [42], d [18], e [111]) grown films. Data for SVO single crystals [128] are also included. Data reported in this work are shown by stars.

4.2 Sample preparation

Here, SVO films were grown on single crystalline perovskite substrates: (001) LSAT and (001) NGO. Here NGO is indexed with a pseudocubic unit cell. The lattice mismatch, defined as $f = [a_S - a_{SVO}]/a_S$, where $a_{SVO} = 3.842$ Å is the cell parameter of bulk SVO [18, 128] and a_S is the cell parameter of the substrate (3.868 Å for LSAT, and 3.863 Å for NGO) is f(LSAT) = +0.65 % and f(NGO) = +0.52 %. Thus, an epitaxial growth would impose a tensile strain on the film in both cases. Films were grown by PLD using a laser frequency of 5 Hz and a fluence of $\approx 2\,J\,cm^{-2}$. A fixed number of 2000 pulses was used. Films were deposited at 750°C. The base pressure at the growth temperature is of about 2×10^{-6} mbar (corresponding to a residual oxygen partial pressure of roughly $PO_2 \approx 4 \times 10^{-7}$ mbar). A series of films was grown under argon pressure $P(Ar)$ ranging from $P(Ar) = 0 - 0.3$ mbar. After growth, films were

cooled to room temperature by switching off the substrate heater, while keeping the same pressure as used for the growth.

4.3 Structural characterization

In Figure 4.2a,b we show a zoom of the $\theta-2\theta$ X-ray diffraction (XRD) scans around the (002) reflection of SVO//LSAT and SVO//NGO films grown at different Ar pressure $P(Ar)$. We first note the presence of the (002) SVO reflections, whose position gradually shift with $P(Ar)$. Only (001) reflections are visible in broader angular scans (Figure 4.3), indicating a (001) textured growth. We note that the (002) SVO reflections of films grown on LSAT and NGO at $P(Ar) = 0$ mbar, that is at the base pressure of the chamber, can hardly be discernible from those of the substrate due to the close structural matching and a notorious SVO line-broadening associated to a limited size of the coherently-diffracting volume of SVO, as confirmed by atomic force microscopy (AFM) images (Figure 4.4). The asymmetric broadening around the substrate reflection, visible in Figure 4.2a,b, reflects the overlapping of a broad (002) SVO peak with the one of the substrate. The small intensity peak occurring at the left of the main substrate peak is a spurious signal from the substrates (Figure 4.5). Accordingly, the corresponding c-axis parameters would be c(SVO//LSAT) $\approx$ 3.92 Å and c(SVO//NGO) $\approx$ 3.90 Å). It is clear that these c-axis values are larger than that of bulk SVO (dotted line in Figure 4.2c) and also larger than those expected if a genuine substrate-induced epitaxial tensile stress f ($\approx$ +0.6 %) due to the structural mismatch (f(LSAT) = +0.65 %; f(NGO) = +0.52 %) was acting on the film. The expected strain-induced c-axis values calculated from the Poisson equation, that is assuming volume conservation [42, 48], are shown in Figure 4.2c (dashed lines). Therefore, the observed expansion of c-axis is not due to the epitaxial (tensile) stress imposed by the substrate but it is likely related to growth-induced nonstoichiometry, as commonly found in SVO films [42, 111, 115, 116, 146].

Reciprocal space maps (not shown here) of SVO//NGO films grown at various $P(Ar)$ indicate that all films are fully strained to the substrate ($a_{SVO} = a_{subs.}$), which was expectable considering to small lattice mismatch f between bulk SVO and NGO/LSAT substrates (as shown in Chapter 3 Section 3.4.2).

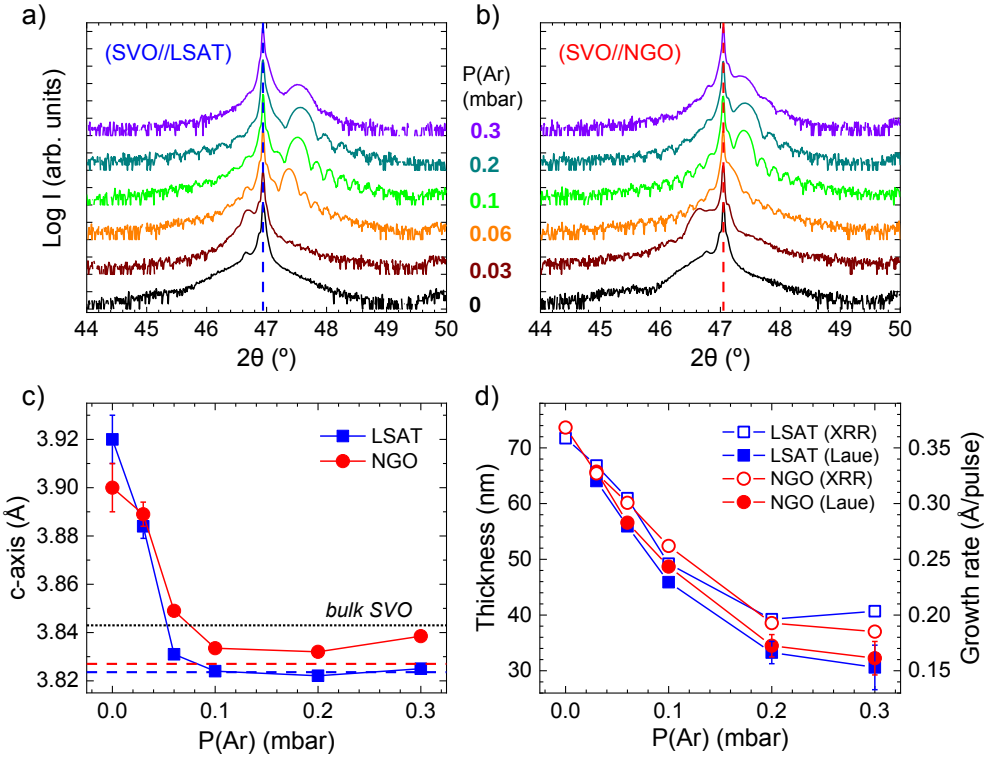

FIGURE 4.2: X-ray diffraction $\theta-2\theta$ scans, zoomed around the (002) SVO reflections of: a) SVO//LSAT, and b) SVO//NGO films grown at various $P(Ar)$. The number next to each scan indicates the corresponding $P(Ar)$ in mbar. The dashed line indicates the position of the substrate reflection. c) Out-of-plane cell parameters of SVO on LSAT (squares) and NGO (circles) films as a function of $P(Ar)$. The horizontal dotted line indicates the c-axis of SVO single crystal; the predicted c-axis lengths associated to the tensile epitaxial strain imposed by LSAT and NGO substrates, calculated assuming unit cell conservation, are shown by dashed lines: LSAT (blue, bottom) and NGO (red, top). d) SVO film thickness (left axis) and growth rate (right axis) dependence on $P(Ar)$ of films deposited on LSAT (squares) and NGO (circles). Filled symbols correspond to thickness values extracted from Laue fringes while empty symbols stand for XRR determined thickness. Error bars are indicated when they are larger than the symbol size.

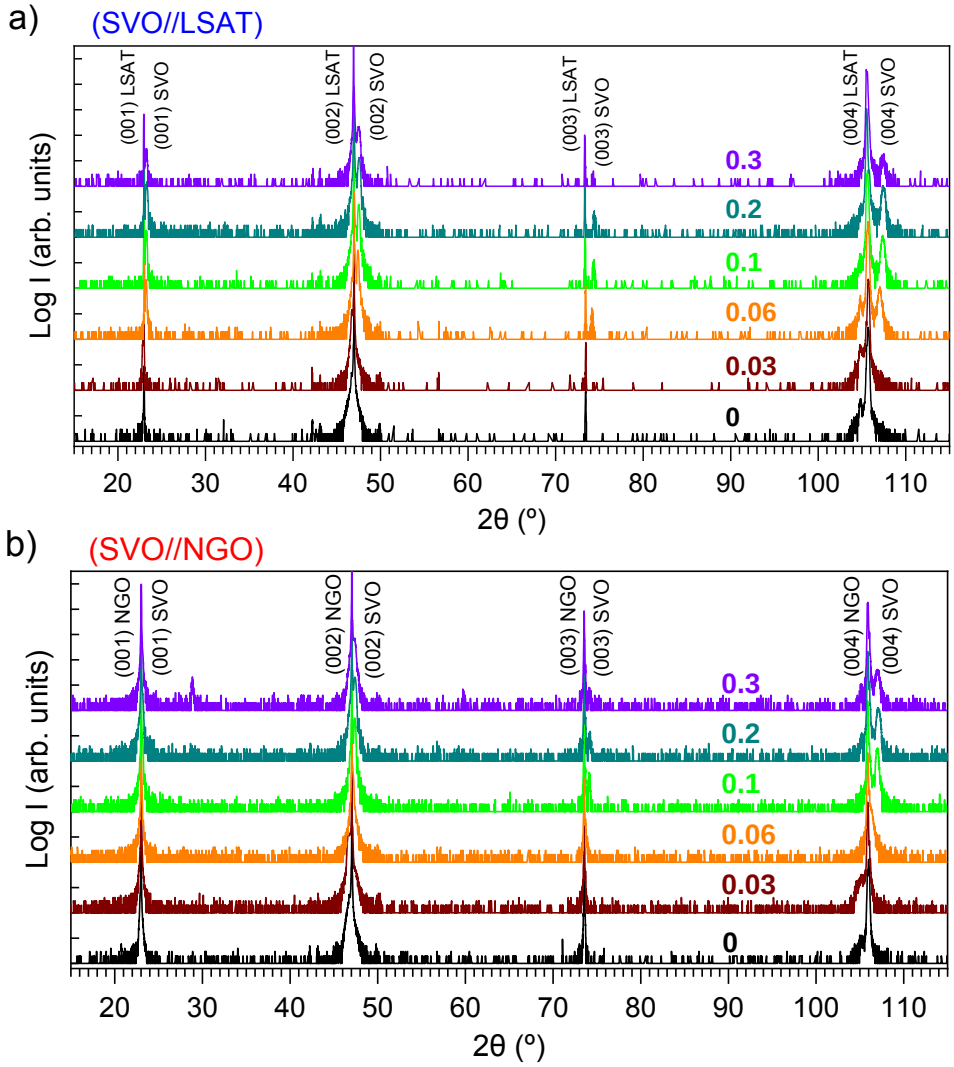

FIGURE 4.3: X-ray diffraction $\theta-2\theta$ scans of: a) SVO//LSAT and, b) SVO//NGO films grown at various $P(Ar)$. The number on top of each scan indicates the corresponding $P(Ar)$, in mbar.

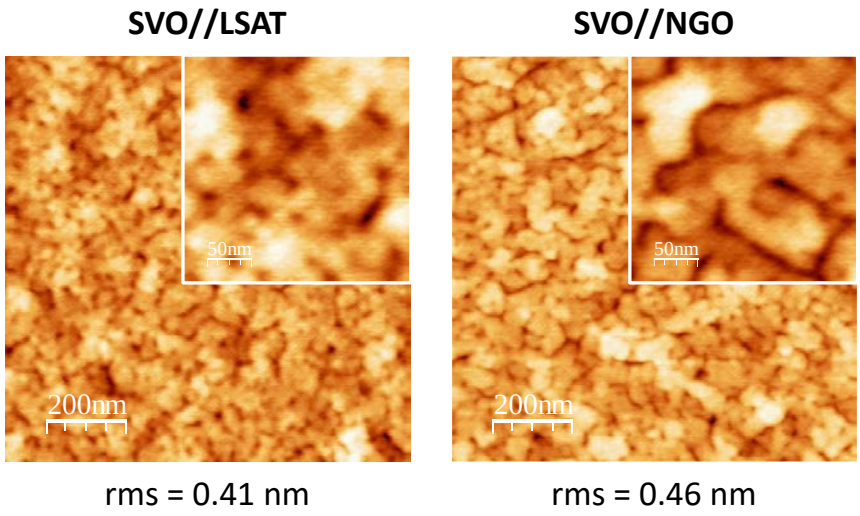

FIGURE 4.4: AFM topographic images (1 µm×1 µm) of SVO films on LSAT (left images) and on NGO (right images), grown at the lowest pressure corresponding to $P(Ar) = 0$ mbar. Insets are 250 nm×250 nm zooms. It can be appreciated that films have a granular structure, with typical lateral sizes below ≈ 50 nm.

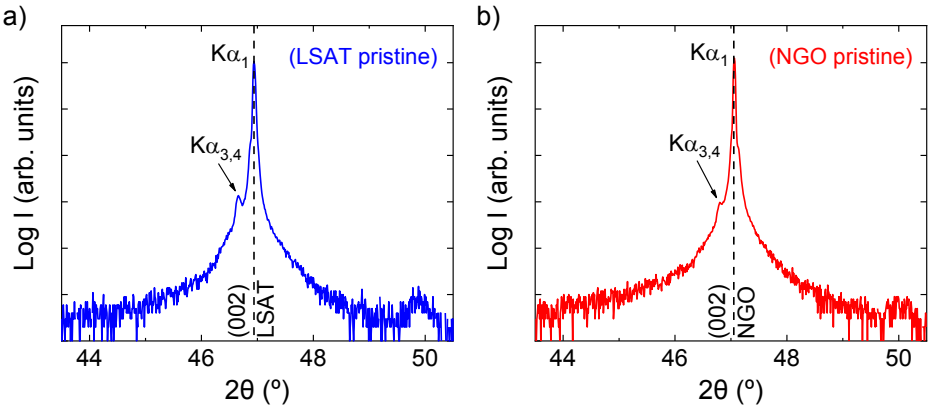

FIGURE 4.5: X-ray diffraction $\theta-2\theta$ scans around the (002) reflection of pristine (a) Cubic (001) LSAT, and (b) Pseudocubic (001) NGO substrates. The main (002) reflection peak associated to the Cu Kα_1 radiation is well defined, but accompanied by a satellite peak associated to the Cu K$\alpha_{3,4}$ radiation [147, 148], which can interfere in an accurate c-axis determination for some SVO films.

Of the highest interest is the observation in Figure 4.2a,b that when increasing the Ar pressure, the Laue fringes of the SVO films become clearly apparent indicating that their crystalline quality has largely improved. On the other hand, it can be appreciated that the (002) SVO reflection shifts toward larger angles, that is: smaller c-axis, when increasing $P(Ar)$. This can be better appreciated in Figure 4.2c where the out-of-plane lattice parameters, determined from the $\theta-2\theta$ XRD scans, for SVO//LSAT (squares) and SVO//NGO (circles), are plotted against the Ar pressure. It is clear that the c-axis shrinks, from the larger value obtained when $P(Ar)$ = 0 mbar, toward a value smaller that the bulk one and closely approaching the c-axis value calculated on the basis of Poisson law and assuming a fully strained film. This suggests that SVO is stoichiometric when grown under a substantial Ar pressure and its crystal lattice is fully tensely strained. Therefore, by using an inert Ar buffering atmosphere during growth, the stoichiometry and the crystalline quality of the films are both improved. This observation dramatically illustrates the role of the energy of the impinging species on the film's quality.

It is worth noticing that the atomic force microscopy images of samples grown using the $P(Ar)$ = 0.03 mbar are remarkably flatter ($rms \approx 0.22$ nm), with well visible terraces and steps (on LSAT), than surfaces of films grown at the base pressure ($P(Ar) = 0$) where $rms \approx 0.45-0.50$ nm (Figure 4.6). At higher $P(Ar)$, the surface becomes rougher and some crystallites are apparent. In agreement with earlier reports [114] and our X-ray 2D reciprocal space maps (Figure 4.7), these crystallites correspond to the spurious $Sr_3V_2O_8$ phase.

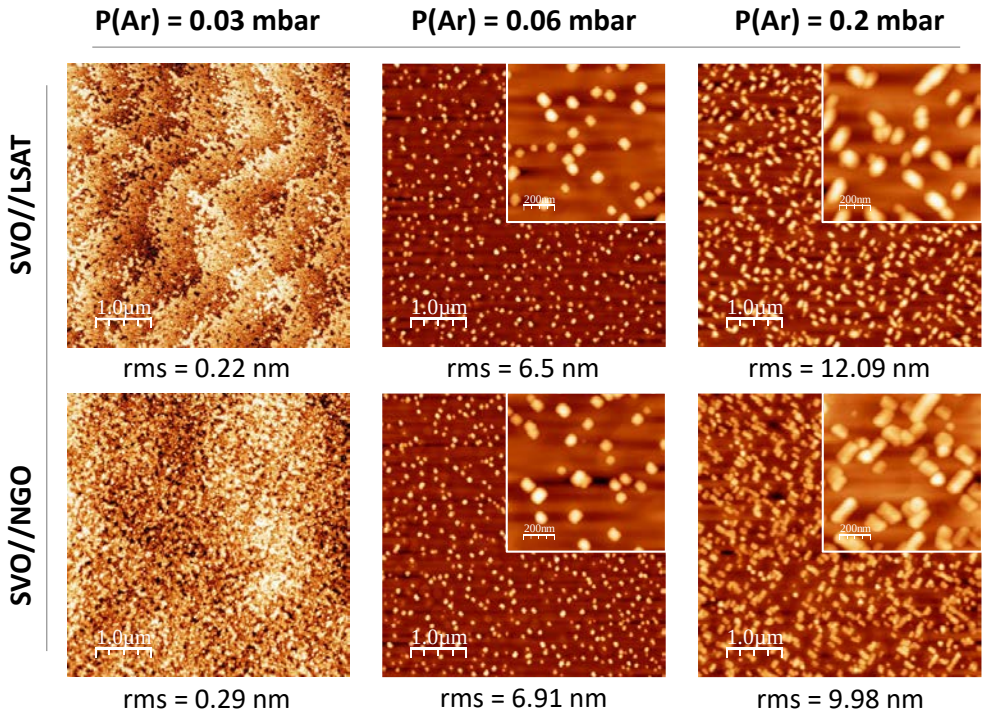

FIGURE 4.6: AFM topographic images, 5 µm×5 µm in size, of SVO films grown at various $P(Ar)$ on LSAT (top images) and NGO (bottom images). Insets in some images are 1 µm×1 µm images emphasizing the outgrowths formed at film surface when growth is performed at higher $P(Ar)$.

Naturally, when increasing the Ar pressure in the chamber, the plasma becomes broader and the growth rate decreases. As shown in Figure 4.2d, the growth rate lowers down from ≈ 0.37 to ≈ 0.15 Å per pulse and thus the film thickness, at the used number of pulses, is reduced from about ≈ 75 to ≈ 30 nm when increasing $P(Ar)$. In passing, we note that if resputtering would have been suppressed by the high $P(Ar)$ pressure, the growth rate in Figure 4.2d would show the opposite trend. Therefore, the nonobservation of this feature implies that, in the explored pressure range, resputtering does not affect significantly the growth rate. In Figure 4.2d, the thickness values depicted are deduced either from the X-ray reflectivity data (XRR) (empty circles) or Laue fringes (filled circles) with good agreement (more details are given in Figure 4.8).

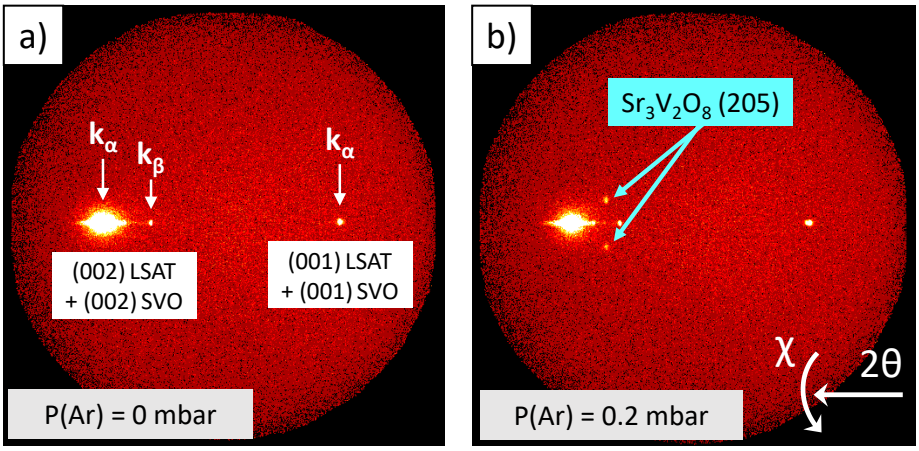

FIGURE 4.7: XRD 2θ–χ frames of SVO on LSAT films grown at: a) $P(Ar) = 0$ mbar and, b) $P(Ar) = 0.2$ mbar. Whereas only the LSAT reflections are visible in the left image (due to the limited resolution of the 2D detector), spots corresponding to (205) reflections of $Sr_3V_2O_8$ are visible in the right image.

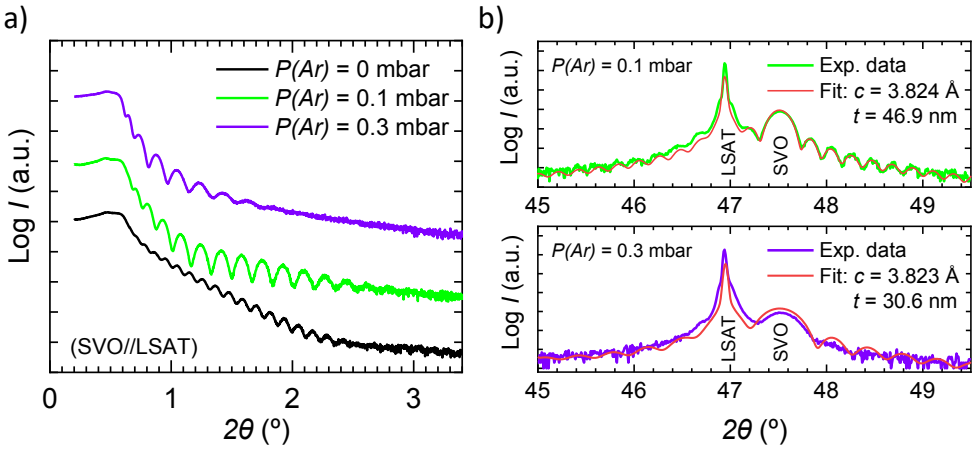

FIGURE 4.8: a) Examples of XRR data of SVO//LSAT grown under various $P(Ar)$. b) Illustrative examples of fitting of Laue fringes observed in the XRD θ–2θ scans. We determined a thickness of $t = 46.9$ nm (resp. $t = 30.6$ nm) and a c-axis of $c = 3.824$ Å (resp. $c = 3.823$ Å) for the film grown under $P(Ar) = 0.1$ mbar (resp. $P(Ar) = 0.3$ mbar). A description of the fitting method can be found in Pesquera et al. [55].

4.3.1 Films stoichiometry

It is worth to stress that whereas it is known that the $Sr_3V_2O_8$ phase is formed under relatively rich oxygen atmosphere [114], here its presence becomes more prominent at nominally the same oxygen pressure (residual vacuum) but under higher $P(Ar)$. A possible explanation could be that when increasing Ar pressure, scattering of plasma species increases, being more prominent for the lighter elements [142], and thus a deficient flux of vanadium adatoms should be expected at the film surface, eventually leading to the formation of a substoichiometric ([V/Sr] < 1) oxide, such as $Sr_3V_2O_8$. The [Sr/V] concentration ratio in the SVO film and its dependence on $P(Ar)$ has been explored by using energy dispersive X-ray spectroscopy (EDX) and X-ray photoemission spectroscopy (XPS) (Figure 4.9). The [Sr/V] composition of the target (see Appendix A.3 and of a single-phase film (SVO//NGO, deposited at $P(Ar) = 0$ mbar) have been measured by ICP-MS and both gave [Sr/V] = 0.95 (as indicated in Figure 4.9a).

Energy Dispersive X-ray spectroscopy (EDX) measurements have been done on SVO//NGO samples to extract an estimate of the film composition. Experiments have been performed with an electron energy of 15 keV and the Sr-L and V-K lines. We note that there is some overlapping of the V-K line with the Nd-L one (coming from the substrate) that may induce a systematic error in the calculated concentrations, and so we restrict to consider the [Sr/V] ratio trend rather than their absolute values. In Figure 4.9a above we include data taken on 5 different regions for each film. It can be appreciated that there is a dispersion of [Sr/V] of about 8 %, which is rather common in EDX analysis. One could also tentatively infer a slight tendency to enrich the Sr contents of the samples by about 7−9 % when $P(Ar)$ increases. However, as a phase segregation of $Sr_3V_2O_8$ occurs, at least at the film surface, the observed increase of [Sr/V] could be simply a result of the increasingly presence of $Sr_3V_2O_8$ phase, when $P(Ar)$ increases, rather than a change of the film composition itself.

We had also performed XPS measurements. Samples cannot be measured *in-situ* but transferred to the XPS chamber via ambient atmosphere exposure. On the other hand, it is obvious that samples grown at different conditions cannot be grown simultaneously. Therefore, when samples are XPS-measured they have been in contact with atmosphere during an avoidably different amount of time. Although Ar+ sputtering can be done to clean the surface, it is known that this process may result on alterations of the material's structure, so we prefer here to focus on fresh non-sputtered samples. In Figure 4.9b we show the relative change of the [Sr/V] ratio of samples grown at three different $P(Ar)$. Data have been evaluated from the integration of the XPS data taken in the appropriate spectral regions, after

removing the baseline by using standard protocol and CasaXPS software. Data have been collected at normal incidence. Two different sets of lines have been used for quantization. We first used Sr-3d and V-2p lines to evaluate [Sr/V] using the atomic sensitivity factors provided the CasaXPS. Results are included in Figure 4.9b (down green triangles). At first sight the data would suggest a reduction of the Sr/V ratio of about 6 % when increasing the $P(Ar)$. However, the extremely surface sensitive character of XPS precludes to strongly support the conclusion above. Indeed, if instead of the V-2p line one uses the V-3s line, which although having a smaller intensity and thus a relatively larger error bar, has a binding energy smaller and thus a kinetic escape energy of electrons larger and correspondingly is less sensitive to surface effects, the [Sr/V] ratio displays the opposite trend as shown in Figure 4.9b (up red triangles). The [Sr/V] ratio evaluated using the Sr-3d and V-3s lines, in spite of the larger error bar associated to the weak V-3s signal, suggest that it increases with $P(Ar)$. This conclusion is in qualitative agreement with that derived from the EDX data (Figure 4.9a).

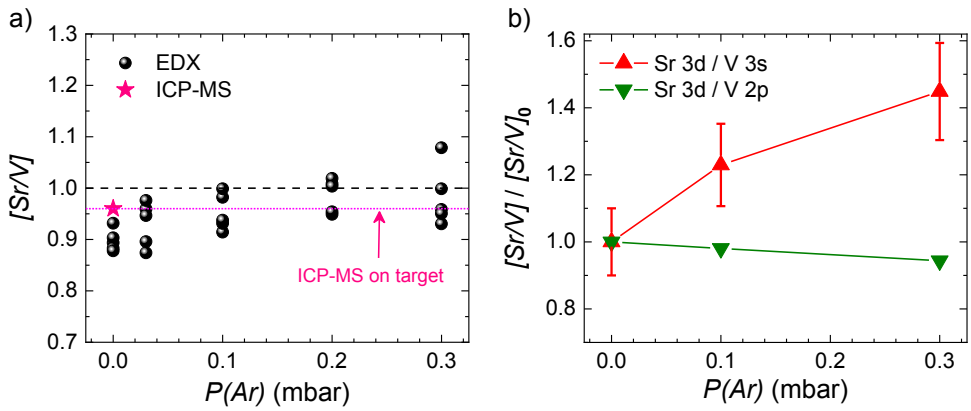

FIGURE 4.9: Dependence of the relative concentration of [Sr/V] as a function of the $P(Ar)$ used during film growth, deduced from: a) EDX, and b) XPS analysis. In a) the target composition measured by ICP-MS , as well as the one of a single-phase film, are also indicated.

In summary, the EDX and XPS data could be interpreted as providing some hint towards some slight enrichment of [Sr/V] with $P(Ar)$ in the SVO films. However, as X-ray diffraction and AFM clearly indicate the progressive formation of $Sr_3V_2O_8$ precipitates at the surface, the observed Sr enrichment does not necessarily reflect an actual Sr enrichment in the $SrVO_3$ structure, which could be fully stoichiometric. It thus follows that the impact of $P(Ar)$ on the actual composition of the film cannot be derived neither from EDX nor from XPS data.

4.3.2 About the vanadium valency

In $SrVO_3$ the valence state of V is expected to be 4+, implying a $3d^1$ occupation and a metallic character, as observed. The XPS data around the O-1s and V-2p peaks of films grown at different $P(Ar)$ are shown in Figure 4.10, where we also include for convenience the XPS data of the optimally oxidized SVO film reported by Lin et al. [149]. From their multiple peak analysis, they conclude that the V-$2p_{3/2}$ line can be decomposed into three components (as indicated in Figure 4.10c) having binding energies of 517.9, 516.2 and 514.5 eV which correspond to nominal d^0 (V^{5+}), d^1 (V^{4+}), and d^2 (V^{3+}) components, respectively. Their relative intensities vary with the oxidation state of the sample and the relative weight of final state effects. The XPS data of our $P(Ar)$ = 0 mbar sample (Figure 4.10a) is very similar to that of the optimally oxidized sample from Lin et al. although the V-$2p_{3/2}$ line in our case occurs at 517 eV, probably due to calibration differences. We strength that the films of Lin et al. were grown and measured *in-situ*. Therefore, the presence a similar d^0 component in our spectrum, accompanying the d^1 one, shall not be taken as a signature of over-oxidation but rather as a result of surface reconstruction and final state effects.

The XPS data of the film grown at $P(Ar)$ = 0.3 mbar (Figure 4.10b) shows an enhanced d^0 contribution that reflects a higher oxidation state at the surface. This is fully compatible with the experimental observation (X-ray diffraction and AFM) of the formation of $Sr_3V_2O_8$ crystallites at the film surface.

4.4 Transport properties

The room-temperature resistivity $\rho(300\,K)$ of all SVO films as a function of $P(Ar)$ is depicted in Figure 4.11. It is obvious that by increasing $P(Ar)$ a substantial reduction of $\rho(300\,K)$, of about 60 %, can be achieved in SVO films on both substrates. Further increase of $P(Ar)$ above 0.1 mbar, produces a subsequent increase of $\rho(300\,K)$. The lowest $\rho(300\,K)$ values: 31 μΩ cm (SVO//NGO) and 38 μΩ cm (SVO//LSAT), are similar than those obtained in hybrid-MBE grown SVO films (28 μΩ cm [18]) and are smaller than most of PLD grown SVO films of similar thickness (38 [114], 47 [116], and 120 μΩ cm [115]).
The temperature-dependence of the resistivity down to 5 K was measured and used to determine the RRR ($RRR = \rho(300\,K)/\rho(5\,K)$). In Figure 4.12a we show $\rho(T)/\rho(300\,K)$ of SVO//LSAT and SVO//NGO films grown at $P(Ar)$ = 0.2 mbar. For reference, we also include the corresponding data for films grown at the base pressure $P(Ar)$ = 0 mbar. It is clear in Figure 4.12a that using a suitable $P(Ar)$, the $\rho(T)/\rho(300\,K)$ data show a larger slope and correspondingly, not only the room-temperature resistivity is reduced by using $P(Ar)$ but the residual resistivity

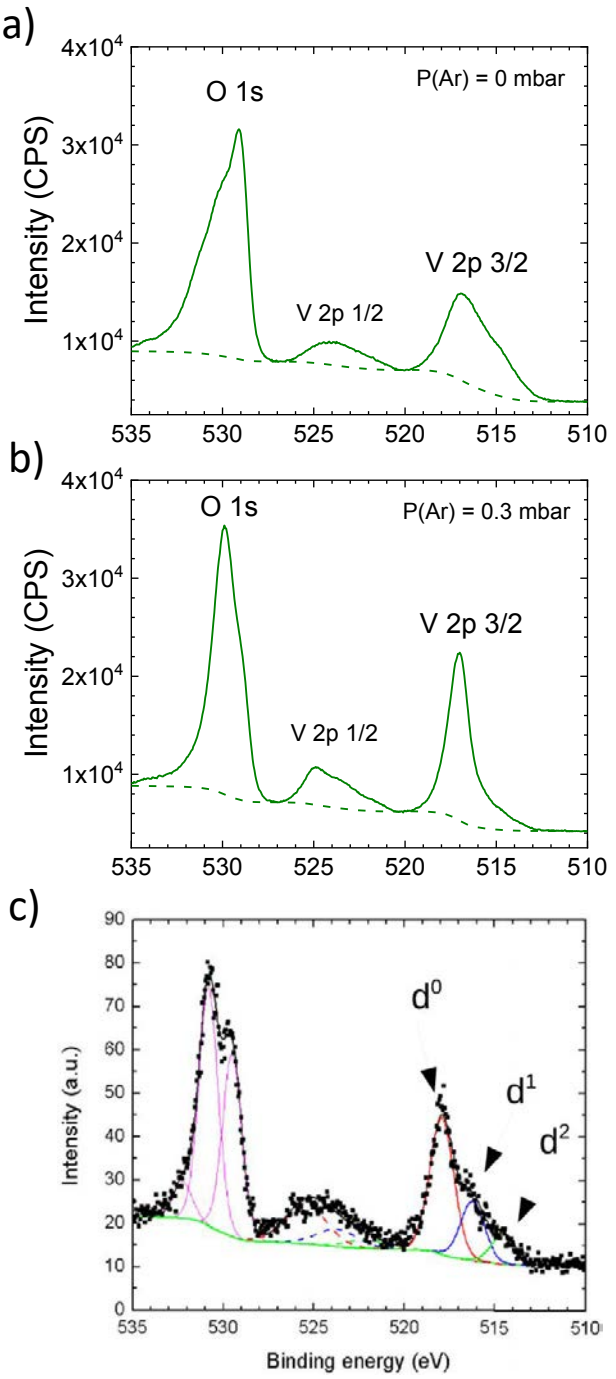

FIGURE 4.10: XPS V-2p spectra of SVO films grown at: a) $P(Ar) = 0$ mbar, and b) 0.3 mbar. In the panel c) we include the corresponding spectrum of an optimally oxidized film from Lin et al. [149]

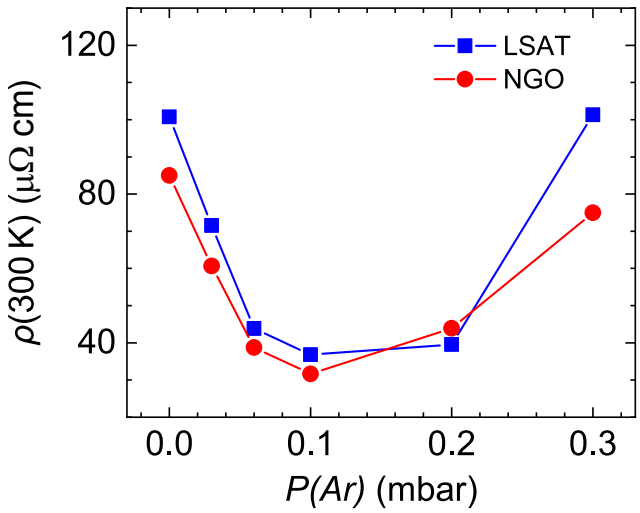

FIGURE 4.11: Room-temperature resistivity $\rho(300\,K)$ of SVO films grown on LSAT and NGO substrates under various $P(Ar)$.

decreases as well. This can be better appreciated in Figure 4.12b where we plot the RRR for all films. The RRR rises when increasing $P(Ar)$, from about 2 in films grown at $P(Ar)$ = 0 mbar, up to $RRR \approx 11.5$ in films grown on LSAT at $P(Ar)$ = 0.2 mbar. Further increase of $P(Ar)$ reduces again the RRR. According to data in Figure 4.12d, films grown at different pressures have thicknesses varying between $\approx 70-30$ nm. As in this thickness range the film resistivity does not depend significantly on the thickness (Figure 4.13), their comparison should not be affected by size effects.

The obtained largest RRR values (≈ 11.5 and ≈ 7.5, for SVO//LSAT and SVO//NGO, respectively) are definitely much larger, by roughly a factor five, than earlier reports of SVO films grown by PLD ($RRR \approx 1.7-2.4$ [114–116]) or by pulsed e-beam deposition ($RRR \approx 1.6$ [139, 140]), as summarized in Figure 4.1b.

The carrier density (up triangles) and mobility (down triangles) of SVO//LSAT (upper panel) and SVO//NGO films (lower panel) are plotted in Figure 4.14a. One first notices that SVO films grown on LSAT and NGO at $P(Ar)$ = 0 have a carrier density $n = 2.14 \times 10^{22}$ cm^{-3} and 2.2×10^{22} cm^{-3}, respectively. These values are very close to, although slightly larger, the value expected for stoichiometric SVO with V^{4+} ($3d^1$) ($\approx 1.76 \times 10^{22}$ cm^{-3}). We note that the XPS data of our SVO films grown at $P(Ar)$ = 0 mbar are coincident with those reported for MBE *in-situ* grown optimally oxidized SVO films [149] supporting a $3d^1$-V^{4+} valence state (Figure 4.10).

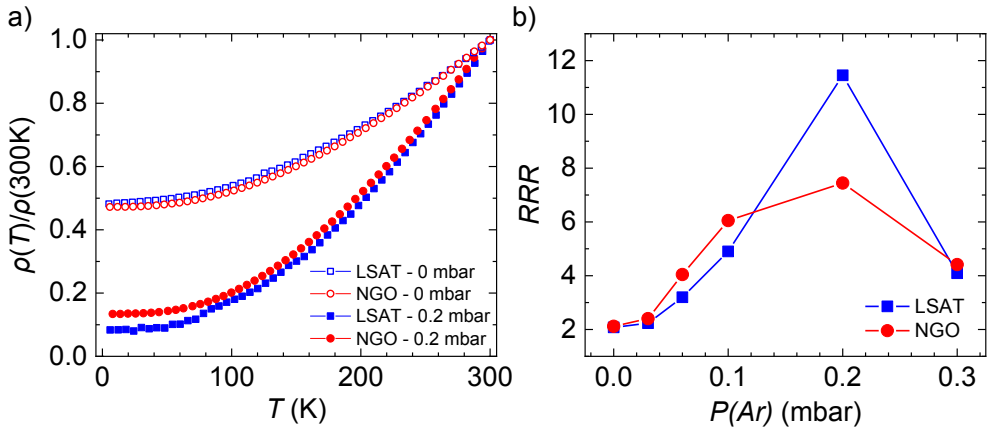

FIGURE 4.12: a) Temperature-dependence of the normalized resistivity $\rho(T)/\rho(300\,K)/$ for SVO films on LSAT and NGO substrates, grown under $P(Ar) = 0.2$ mbar. Data for similar films grown at the base pressure $P(Ar) = 0$ mbar are also included. b) Residual resistivity ratio ($RRR = \rho(300\,K)/\rho(5\,K)$) as a function of argon pressure for films grown on LSAT and NGO substrates.

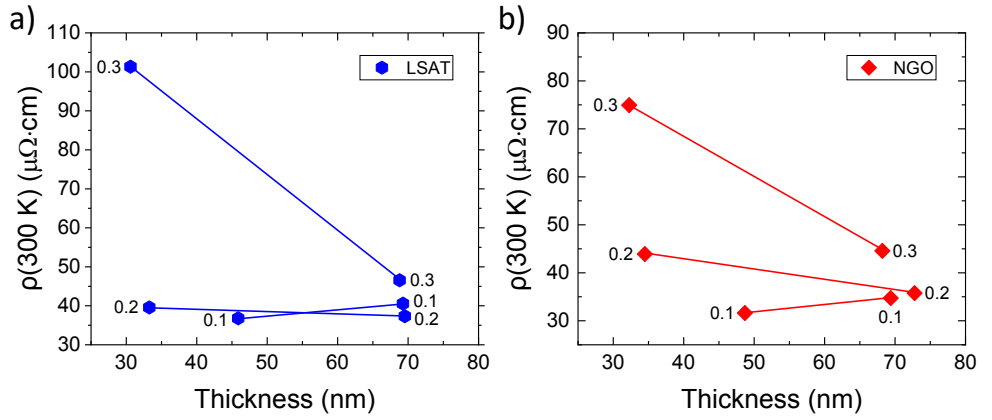

FIGURE 4.13: Thickness dependence of the resistivity of SVO films grown on LSAT and NGO at different $P(Ar)$ (as indicated by the labels (mbar)).

However formal assignment of the valence state of V to $3d^1$ configuration or others (i.e., $3d^0$, $3d^2$) is challenged by final state effects [149]. The carrier mobility is $\mu \approx 2.9$ cm^2 V^{-1} s^{-1} for SVO//LSAT and for 3.3 cm^2 V^{-1} s^{-1} for SVO//NGO. Data in Figure 4.14a shows that there is a very remarkable increase of carrier mobility and density when increasing $P(Ar)$ up to $\approx 0.1-0.2$ mbar and a subsequent decrease with further increase of $P(Ar)$. Indeed, the carrier mobility is increased by roughly a factor two, achieving $\mu \approx 8.3$ cm^2 V^{-1} s^{-1} for $n = 2.4 \times 10^{22}$ cm^{-3} (SVO//NGO) when introducing the nonreactive Ar gas during growth. We notice that mobility in early PLD-grown films was of ≈ 0.8 cm^2 V^{-1} s^{-1} [116] and $\approx 8-9$ cm^2 V^{-1} s^{-1} in hybrid-MBE films [18, 42].

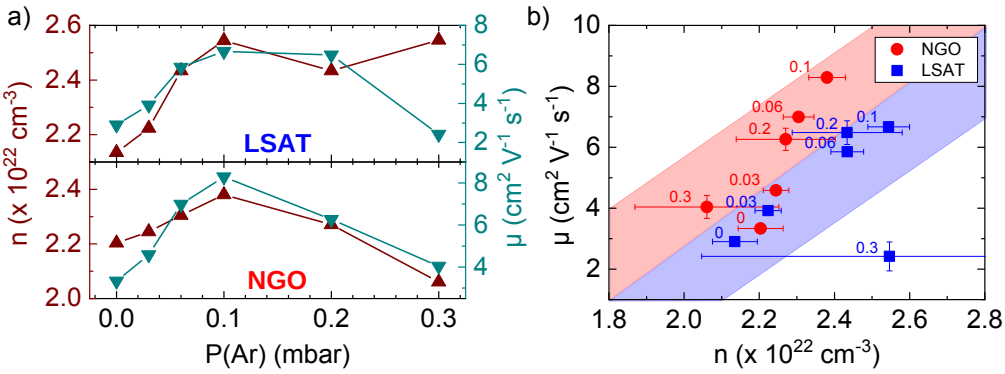

FIGURE 4.14: a) Carrier density (up triangles) and carrier mobility (down triangles) of SVO on LSAT (upper panel) and on NGO (lower panel) as a function of the deposition argon pressure $P(Ar)$. b) Relationship between carrier mobility and carrier density for SVO films grown on LSAT and on NGO, grown under different $P(Ar)$ (in mbar, indicated by the numbers next to the data points). Error bars, mainly affecting carrier density due to uncertainty in film thickness, are indicated.

Data in Figure 4.14a,b clearly reveal than an increase of carrier concentration goes in parallel with an enhanced mobility ($\mu \propto n^b$, $b > 0$). The relevance of this observation is better appreciated by noticing that in doped semiconductors the opposite behavior is typically observed. Commonly, μ decreases with increasing doping due to the enhanced scattering with dopant atoms. The reverse trend observed here bears some resemblance with properties of some strained semiconductors, such as (Ba,Sr)SnO_3 or even n-GaN [150] where a $\mu \propto n^b$ relation with $b \approx 1/2$ has been reported [106, 107, 151]. It has been argued that this unconventional increase of mobility when increasing carrier density is due to the enhanced screening of defects, such as dislocations or impurities, by the carriers (n). In a similar scenario, scattering by ionized impurities in degenerate semiconductors leads to $\mu \propto n^b / Z_i^2 N_i$

where (Z_i, N_i) are the charge and concentration of ionized impurities [17]. Therefore, as mentioned above, by using $P(Ar)$ the plume-induced nonstoichiometry is reduced and consequently, a concomitant enhancement of mobility is expected, as observed.

4.5 Optical properties

In Figure 4.15a we show the optical transmittance of the bare LSAT substrate together with that of SVO films, about 50 nm thick, grown using either the base pressure ($P(Ar)$ = 0) (red line) or an argon pressure $P(Ar)$ = 0.1 mbar (blue line). It is interesting to note that the films grown under Ar have a slightly larger transparency than those grown at the base pressure. This observation is consistent, as argued above, with a reduction of light-absorbing point defects in the films grown under Ar. Moreover, it can be appreciated that the transparency of Ar-grown films is similar to that reported for films of similar thickness (63 %) (indicated in Figure 4.15a by a dashed line) grown by hybrid-MBE [18]. The improved optical transmittance of the films is well visible in the picture shown in Figure 4.15b.

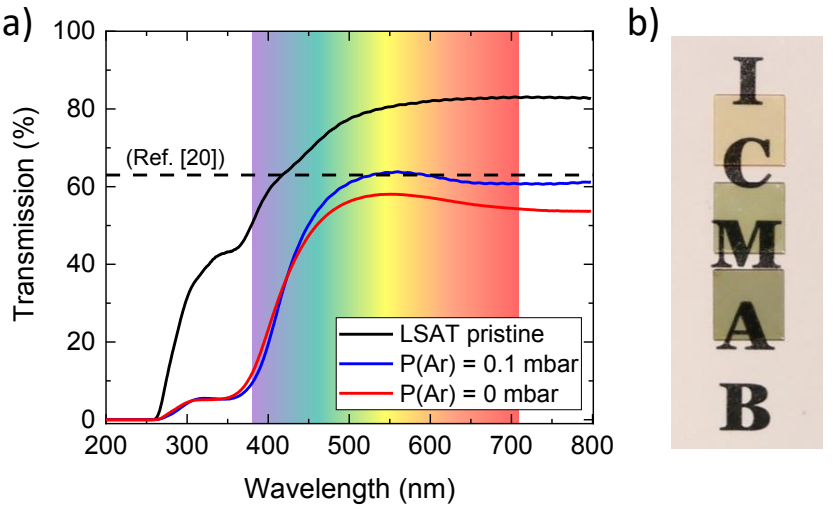

FIGURE 4.15: a) Optical transmittance of SVO films on LSAT, about 50 nm thick, deposited either at $P(Ar) = 0$ mbar (red) or at $P(Ar) = 0.1$ mbar (blue). Transmission spectrum of the pristine LSAT substrate is also included (black). For reference, the maximal transmittance in the visible range of state-of-the-art SVO films grown on LSAT by hybrid-MBE [18] is included (dashed line). b) Picture of the three samples displayed on a background and ordered as in the legend of fig. a).

Finally, the plasma energy of the SVO//LSAT film grown at $P(Ar) = 0$ mbar, can be roughly estimated from the zero-crossing of the real part of the permittivity, occurring at ≈ 1.2 eV (Figure 4.16). This value is very close to the screened plasma frequency (≈ 1.33 eV) reported for hybrid-MBE grown thin films [18] (Figure 4.16). To obtain the unscreened plasma frequency, necessary to compute the correlation-enhanced effective mass, a complete analysis of the optical conductivity is required, which is beyond the scope of this chapter. For hybrid-MBE SVO thin films [18], having a similar screened plasma frequency and similar conductivity values, the unscreened plasma energy $\hbar\omega_p$ was evaluated to be ≈ 2.1 eV; a similar value should be expected here. Using $n \approx 2 \times 10^{22}$ cm^{-3} this would indicate a correlation-renormalized effective mass of about $m^* \approx 3$, consistent with the 3d nature of the orbitals forming the conduction band of SVO.

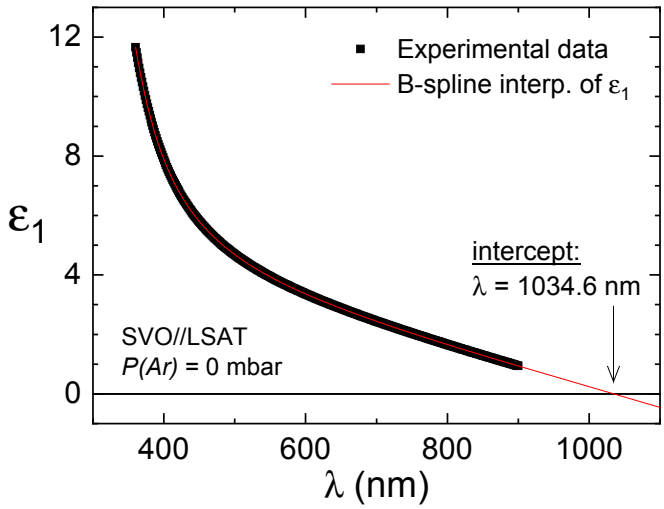

FIGURE 4.16: Real part ϵ_1 of the optical permittivity obtained by using spectroscopic ellipsometry measurements on a SVO film deposited on LSAT at $P(Ar) = 0$ mbar. The zero-crossing of ϵ_1 (obtained by b-spline interpolation of the experimental data) signals a screened energy plasma (defined as: $E_{\omega p}{}^* = hc/\lambda(\epsilon_1 = 0)$) of about 1.2 eV. These measurements were performed using an Imaging Ellipsometer Nanofilm EP4 from Accurion GmbH.

4.6 Conclusions

Overall, the data shown above indicate that the resistivity of SVO films on lattice matched substrates (LSAT and NGO) is critically determined by the harsh growth conditions, namely the extremely low pressure required in the growth chamber, and the concomitant presence of energetic species impinging the film and the subsequent creation of point defects in the latter. We have shown that, to some extent, increasing the pressure of a nonreactive gas during growth, allows to obtain SVO films with optimized properties (higher room-temperature electrical conductivity and carrier mobility). We claim that, as deduced from the structural data information, the improvement of the electrical quality factors of the films goes in parallel with a reduced density of plume-induced nonstoichiometry related defects in the films and a concomitant reduction of the unit cell volume. We argue that point defects, most likely nonstoichiometric defects, are the bottleneck to obtain optimally conducting films when growth requirements impose using low-oxygen process in the growth chamber. The use of a partial pressure of nonreactive gas appears as a simple way to optimize films properties. This unconventional approach to grow oxide thin films may pave the way toward the development and integration of transition metal TCOs in the latest technologies. Although here we have chosen to use a nonreactive gas to modulate the laser plume, other alternative strategies, such as tuning the laser fluence could be investigated for the search of similar effects.

Chapter 5

Orbital occupancy and hybridization in strained $SrVO_3$ epitaxial films

In this chapter, we study the electronic structure of $SrVO_3$ under different epitaxial strain by means of XAS/XLD measurements.[1]

5.1 Introduction

The interplay between orbital, charge and spin degrees of freedom in transition metal oxides (TMO) is at the heart of the myriad of different properties they display and it is responsible for their extreme responsivity to external stimuli. Electron density (n) and conduction bandwidth (W) are the knobs that allow fine tuning of the relative strength of these degrees of freedom. Early transition metal oxides, containing $3d^n$ cations, have been much explored due to the possibility of tuning and monitoring the strength of electron-electron (*e-e*) correlations by increasing n or reducing W. For instance, in the $3d^2$ compound V_2O_3, *e-e* correlations open a gap in the $3d$-derived conduction band upon cooling or under pressure, and the material displays a metal-insulator transition (MIT) from a paramagnetic metal into an antiferromagnetic insulator. Electrical properties of V_2O_3 are thus understood by the presence of a Mott-Hubbard MIT, where correlations are controlled by electronic bandwidth [152, 153]. However, it has also been observed that at the MIT, involving a change of symmetry, the hierarchy of electronic orbitals, their electronic occupation [154] and their bandwidth [155] change. This implies also changes in hybridization between V $3d$ and O $2p$ orbitals and thus the charge transfer may change significantly, implying that the electron counting at $3d^n$ is not preserved and a simple d-orbital Mott-Hubbard description may be insufficient [156]. Vanadium dioxide VO_2, having a single electron at $3d^1$ orbital (from the V^{4+}

[1] See measurement description in Section 2.6 of the methodology chapter.

oxidation state), may, at first sign, appear as a simple example to study *e-e* correlation effects. In VO_2, metallic ions occupy the center of an oxygen octahedral cage of edge-sharing octahedral chains along the rutile c_R-axis. The crystal field partially breaks the $3d$ fivefold degeneracy into a low energy t_{2g} triplet and an e_g doublet at higher energy. Common electron counting would predict a metallic behavior due to the partial occupation of the t_{2g} states. In fact, due to the existing orthorhombic distortion in VO_2, the degeneracy of the t_{2g} triplet is further broken into an a1g singlet, with orbitals along the axial c_R-axis, and a double degenerated e_g state with orbitals in the equatorial plane, giving rise to non-bonding $\pi(a_{1g})^{nb}$ and antibonding $\pi(e_g)^*$ orbitals respectively, which are broad enough to overlap and give rise to the observed high temperature metallic conduction. However, upon lowering the temperature, VO_2 displays a structural change at about $T_{MIT} \approx 340\,K$ that produces a dimerization along the rutile c_R-axis. The centric V^{4+} ions of edge-sharing oxygen octahedral cages move apart and importantly, reinforce the $d-p$ hybridization, thus pushing upwards the antibonding $\pi(e_g)*$ orbital. As a result, the overlap between $\pi(a_{1g})^{nb}$ and $\pi(e_g)^*$ is suppressed; the $\pi(a_{1g})^{nb}$ orbital becomes fully occupied, giving rise to a MIT. VO_2 exemplifies the dramatic role of hybridization on the properties of expectedly simplest $3d^1$ systems. It is worth noticing that in the rutile structure, the existence of edge-sharing VO_6 octahedra implies the presence of relatively short V-O distances that may exacerbate t_{2g}-t_{2g} interactions, making the system particularly sensitive to second order Jahn-Teller distortion, and subsequent charge rearrangement [155, 157]. Not surprisingly, the orbital filling and the MIT of VO_2 have been found to be sensitive to epitaxial strain [158].

The question that emerges is to elucidate the relevance of the octahedra packaging, that is: edge-sharing versus corner-connected octahedral network, on the sensitivity of metal-oxygen hybridization and orbital filling to strain. In contrast to the VO_2 case mentioned above, in the $SrVO_3$ (SVO) and $CaVO_3$ (CVO) perovskites, the VO_6 octahedra are corner-connected. The *e-e* correlations in these $3d^1$ metallic oxides are presumed to be weaker and the metallic character to be preserved to the lowest temperatures [128]. Whereas the large Sr^{2+} ion gives rise to a cubic SVO structure, the Ca^{2+} is too small to fit in its oxygen cage, forcing the tilting and rotation of the VO_6 octahedra to reduce the oxygen cage size. As a result, bulk SVO is cubic while bulk CVO is orthorhombic. Both materials remain metallic to the lowest temperatures, although the conduction bandwidth and effective masses slightly increases from SVO to CVO [124, 159]. It is worth to recall that a MIT has been observed in ultrathin (2-3 u.c.) SVO films, and it has been proposed to be due to confinement-induced reduced bandwidth [118, 160] and the resulting orbital-selective quantization effects [144]. MIT or charge localization and reduced dimensionality effects have also been reported to occur in thicker (≈ 7 nm) SVO

films [116, 140]. The observation of a MIT occurring at higher thickness in CVO [161, 162] than in SVO could be consistent with the narrower bandwidth of CVO; although, as discussed by Nekrasov et al. [159], thermodynamic data [124, 163] signal only a marginal effective electron mass enhancement in $Sr_{1-x}Ca_xVO_3$ with increasing x [162]. Finally, we remark that the existence of strong hybridization and crystal-field effects that imply charge redistributions are relevant in early transition metals [164–166], and may change with film thickness, thus challenging the simplest Mott-Hubbard model description in such cases.

SVO, owing to its simple electronic configuration, its cubic structure and a relatively broad bandwidth responsible for its high electrical conductivity (with room-temperature resistivity $\rho = 30$-$50\,\mu\Omega\,$cm, see e.g. ref. [18] or Chapter 4), has been the *drosophila* for research in correlated systems [145]. Here, we aim to settle if epitaxial strain acting on SVO films could induce a symmetry breaking of the t_{2g} (xy, xz, yz) orbitals of corner-connected VO_6 octahedra, modify the $2p$-$3d$ hybridization and promote a charge redistribution within the t_{2g} manifold.

Orbital occupancy can be explored by x-ray absorption spectroscopy (XAS), and particularly by the x-ray linear dichroism (XLD) at the V $L_{2,3}$ and O K absorption edges. As the XAS intensity is proportional to the available empty states (Fermi's golden rule), it would allow us to probe the V $3d$ orbital occupancy as well as the V-O hybridization. Photons with an energy larger than about 515 eV can be absorbed at V $2p_{3/2}$ and V $2p_{1/2}$ core levels and the intensity of the corresponding absorption lines (L_3 and L_2, respectively) is proportional to the available lowest energy V $3d$ final states (t_{2g} and e_g). Similarly, XAS absorption at O K-edge occurs when light is absorbed at O $1s$ core levels and electrons are excited to the lowest energy empty O $2p$ states. Observation of O K-edge absorption is a fingerprint of the existence of empty states at O $2p$ and thus of the covalence of the V-O bonds. The oxygen O K-edge occurs at about 530 eV which is only ≈ 15 eV above the V L_2-edge and thus the measured absorption intensity at >530 eV contains a tail of the V L_2 absorption [89].
To get access to the subtle differences in the orbital occupancy of t_{2g} (xy, yz/xz) or e_g (x^2-y^2, z^2) states, one can collect the x-ray absorption spectra (XAS) for $\boldsymbol{E} \parallel ab$ and for $\boldsymbol{E} \parallel c$ (later shortened as $\boldsymbol{E}_{ab}$ and $\boldsymbol{E}_c$, respectively), where ab and c indicate in-plane and out-of-plane x-ray electric-field $\boldsymbol{E}$ directions, respectively). The resulting dichroism ($XLD \approx I(\boldsymbol{E}_c) - I(\boldsymbol{E}_{ab})$) is therefore a measure of different empty states at orbitals with different in-plane (xy of t_{2g}; x^2-y^2 of e_g) or out-of-plane (yz/xz of t_{2g}; z^2 of e_g) symmetries. This technique has been successfully used in recent years to determine orbital occupancy within the different subsets of e_g and t_{2g} orbitals, in several transition metal oxides (Ti [167], V, Mn [80, 168], Fe,

Co [169], Ni [81, 170, 171], Cu [172, 173], etc.).

Moreover, the O K-edge may also display a remarkable slave dichroism if the covalently-mixed (p_x, p_y, p_z) − t_{2g} (xy, yz/xz) orbitals and (p_x, p_y, p_z) − e_g (x^2-y^2, z^2) orbitals are differently occupied. Indeed, XLD at O K-edge has been used to unravel electronic reconfigurations in manganite superlattices [174] or the nature of MIT in VO_2 [175].

Here, aiming at exploring and disentangling the effects of strain and covalency on the electronic redistributions in the corner-connected polyhedral network of SVO, films of different thicknesses have been grown on single crystalline perovskite substrates having different structural mismatch with SVO, to impose different stresses on the SVO film. The structural and electrical properties of the films have been inspected and their conduction band properties explored by XAS and XLD at V $L_{2,3}$ and O K-edges. It turns out that epitaxial strain promotes selective occupancy of V t_{2g} orbitals that, in spite of the relatively weaker strength of the $\pi^*(t_{2g})$ bonds, also modulates the electron occupancy of hybridized oxygen $2p$ orbitals, where hole occupancy is also affected. Implications of these findings on the understanding of some relevant properties of metallic oxides are discussed.

5.2 Sample description

SVO films of thickness t of 10, 20, and 70 nm were grown on LAO (compressive strain; $f_{LAO} = -1.37\%$), NGO (tensile strain; $f_{NGO} = +0.52\%$), and STO (tensile strain; $f_{STO} = +1.59\%$). The growth pressure was either $P(Ar) = 0$ mbar (base pressure) or $P(Ar) = 0.03$ mbar.[2] All film roughness was < 4 Å (see Appendix D.1).

5.3 Strain-induced tetragonal distortions

Illustrative XRD data for SVO (10 nm) films on different substrates are shown in Figure 5.1a (data for all films are shown in Appendix D.2). Laue fringes in the $\theta-2\theta$ patterns are well visible, thus assessing the film quality, allowing to confirm the film thickness and to extract the out-of-plane lattice parameters (c-axis) by simulating the XRD pattern. From the fitting of $\theta-2\theta$ scans and the analysis of the reciprocal space maps we deduced the cell parameters (a, c) and the tetragonality ratio c/a (Fig. 5.1b). It is observed that all films, except the 70 nm on LAO, have the in-plane cell parameters (a-axis) coinciding with those of substrates and thus these films are coherently strained on the corresponding substrates (Fig. 5.1a and Appendix

[2] More details on growth in UHV or argon are given in Chapters 3 and 4, respectively.

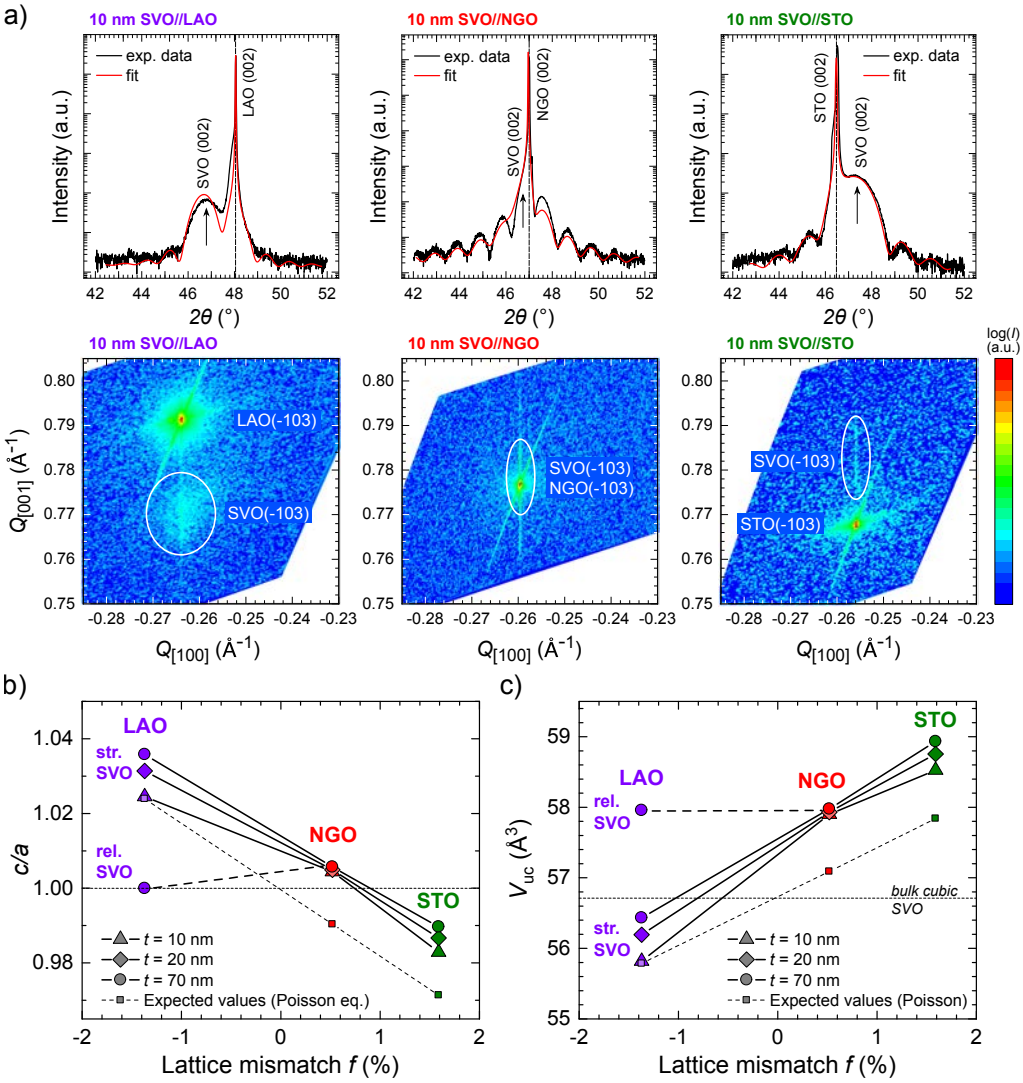

FIGURE 5.1: a) Top panel: $\theta-2\theta$ scans of SVO films (10 nm, $P(Ar) = 0.03$ mbar) grown on LAO, NGO and STO substrates. The continuous red lines are the results of the optimal simulation used to extract the c-axis and film thickness. Bottom panel: corresponding reciprocal space maps measured around the (-103) reflection. The SVO reflection is circled. b) Experimental c/a ratio for SVO films of various thicknesses (10, 20 and 70 nm), grown on LAO, NGO and STO, at BP (the $P(Ar) = 0.03$ mbar series is not shown here for sake of clarity). The dashed line indicates the expected c/a values for fully strained films ($a = a_{\text{sub}}$) where c is calculated using Poisson equation (with Poisson ratio $\nu = 0.28$). c) Measured unit cell volume V_{uc} as a function of structural mismatch f. The dashed line indicates the expected unit cell volume calculated using the indicated Poisson ratio. Dotted lines in b) and c) indicate the expected c/a ratio and V_{uc} of bulk SVO, respectively.

Fig. D.4). In contrast, the reciprocal space map of the (70 nm thick) SVO//LAO film reveals the coexistence of fully strained and partially relaxed regions (Fig. D.4).
Figure 5.1b depicts the tetragonality ratio c/a for all films evaluated from the extracted (a, c) cell parameters. It can be appreciated that the tetragonality increases from STO to NGO and to LAO. For SVO//STO films, $0.98 \leq c/a \leq 0.99$ (depending on thickness) would indicate a tensile stress compared to cubic SVO, whereas the SVO//LAO films, having $1.025 \leq c/a \leq 1.035$, would be consistent with a compressive stress. SVO//NGO films are marginally tensile stressed ($1.004 \leq c/a \leq 1.006$). Overall, this is the expected structural response of a SVO film to the tensile-to-compressive film/substrate mismatch variation. We also include in Figure 5.1b (solid squares, dashed line) the predicted tetragonality ratio of SVO//STO and SVO//NGO and SVO//LAO films calculated using the reported Poisson ratio for SVO ($\nu = 0.28$) [42] to account for the elastic response of the SVO lattice to in-plane epitaxial strain (ε). For coherently grown films $\varepsilon = f$. It can be appreciated that for all strained films, the measured c/a values display the expected dependence on epitaxial strain. However, the values of c/a are larger than the ones predicted using the Poisson ratio, which suggests an expansion of the c-axis that cannot be explained exclusively by an elastic deformation of the lattice. Observation of an anomalous expansion of out-of-plane c-axis in epitaxial oxide thin films, more noticeable in films on STO and NGO imposing a tensile strain, is a common finding and typically attributed to oxygen defects in the lattice, which are predicted to be more abundant in films under tensile strain [176]. SVO follows this rule. Consistent with the observed partial relaxation of the compressively stressed SVO//LAO, the experimental c/a values of the relaxed fraction of the film falls below the extrapolated fully-strain c/a values. As shown in Figure 5.1c, the measured unit cell volume (V_{uc}) of SVO films under tensile strain is larger than that of bulk SVO. There is a clear expansion of the unit cell with increasing tensile strain (i.e. reducing c/a), which indicates that point defects incorporation depends on strain, being more pronounced for tensile strain than for compressive one [176].

5.4 Thickness-dependent transport properties

All SVO films reported here, including the thinnest ones ($t = 10$ nm), are metallic (Figure 5.2a and Appendix D.3) with residual resistivity ratios RRR ($= \rho(300\,\text{K})/\rho(5\,\text{K})$) ranging from 1.4-1.7 for the thinnest films (10 nm) and increasing to 1.6-2.1 for the thicker films (70 nm). Therefore, the largest RRR is obtained in films on the best matching substrate (NGO) (as already shown in Chapter 3). As shown in Figure 5.2b, the resistivity of the films slightly decreases upon increasing thickness. In Figure 5.2c we show the carrier density (n) per unit volume ($1/\text{cm}^3$) (left axis) as extracted from room-temperature Hall measurements. Carrier density values are in the $(1.8\text{-}2.6)\times10^{22}$ cm^{-3} range which is within the range of reported

values for similar SVO films: 2.26×10^{22} cm^{-3} [18] and $(2.0\text{-}2.3)\times10^{22}$ cm^{-3} [125]. It is worth noticing that SVO films of similar thickness grown under the same nominal conditions, on LSAT and NGO, having both substrates similar mismatch, have also similar carrier concentration (2.14×10^{22} cm^{-3}) (Chapters 3,4). It can be appreciated in Figure 5.2c that n increases when increasing the tensile strain. This observation is in agreement with the observed expansion of the unit cell and the possible role of non-stoichiometric effects on this remarkable trend.

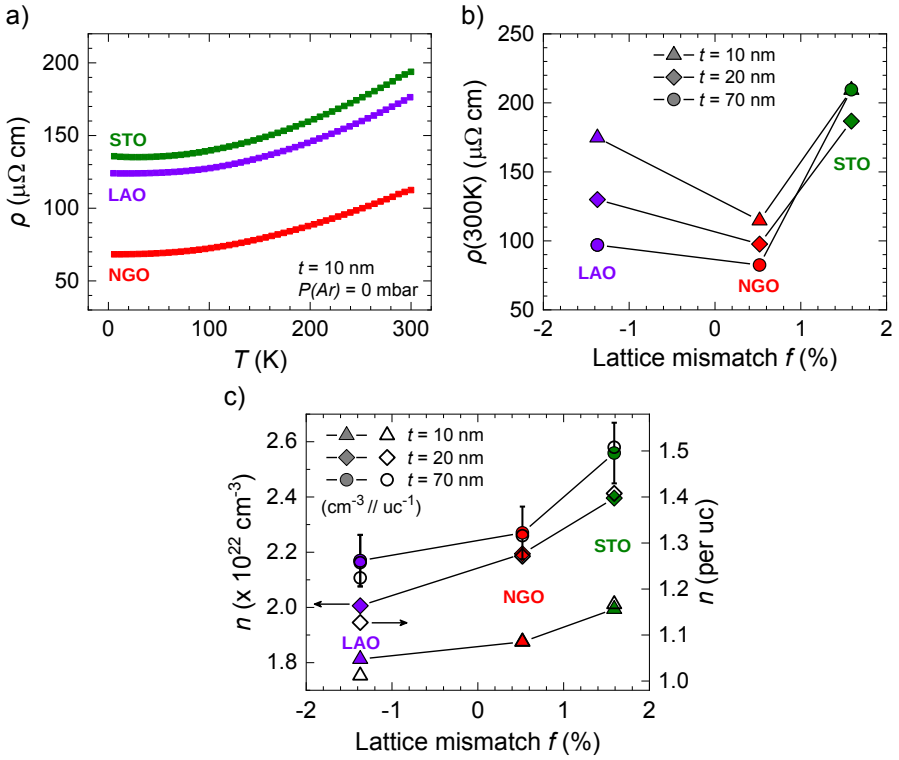

FIGURE 5.2: a) Temperature dependence of the resistivity of SVO (10 nm) films grown on various substrates. b) Dependence of the room-temperature resistivity of films of 10, 20 and 70 nm grown on substrates having different lattice mismatch (f) as indicated. c) Carrier concentration (n) per unit volume of film (cm^{-3}) (left axis) and per unit cell (right axis). Error bars (shown only for the 10 nm series for the sake of clarity) are calculated assuming a maximum error of 5% in thickness determination, and neglecting any possible contribution from the substrate.

5.5 Exploration of the orbital occupancy by X-ray absorption spectroscopy (XAS) and X-ray linear dichroism (XLD) measurements

In Figure 5.3a,b, we show the average XAS of SVO (10 nm and 70 nm) films recorded at grazing incidence, on LAO, NGO and STO substrates, in the energy range of 510-555 eV, where the V $L_{2,3}$ absorption edge is present and followed by the O K-edge. The V L_3 ($\approx$ 519 eV) and V L_2 ($\approx$ 525.5 eV) edges are well visible but the O K-edge pre-peak has a slight overlap with the V L_2-edge and extends to a wide energy region (530-550 eV). The V $L_{2,3}$-edge is expected to differ for different valence states of V^{m+} ions (e.g. V^{3+}, V^{4+}, V^{5+}), lowering in energy upon reducing of the valence sate, and its shape is further enriched by the presence of multiplet fine structure whose contribution largely depends on the local symmetry and the electron density [177, 178]. The chemical shifts in the XAS $L_{2,3}$ spectra of Figure 5.3a,b, are consistent with the V $3d^1$ electronic configuration. Moreover, the absence of a characteristic splitting occurring at the L_2 in V $3d^2$ systems [178], the absence of a distinctive peak at 515 eV [179] characteristic of V^{5+} and the overall agreement of the shape of the XAS spectra with that predicted for $SrVO_3$ [135], confirm that, within the depth probing sensitivity ($\approx$ 5 nm) of XAS in TEY mode, V^{4+} ($3d^1$) is the dominant formal state of the transition metal in our SVO films, regardless of the thickness or substrate. Moreover, the shape of the XAS spectra is extremely similar to that reported for isoelectronic $CaVO_3$ [180].

We now focus our attention to the XAS at O K-edge, associated to transitions between O $1s$ and O $2p$ orbitals, and particularly to the pre-peak doublet maxima appearing at M_1 ($\approx$ 529.5 eV) and M_2 ($\approx$ 531.5 eV) (indicated by arrows in 5.3a,b), which are known to be sensitive to oxygen contents [182]. The mere observation of the M_1 and M_2 peaks indicates that these transitions indeed occur and thus empty final states are available at O $2p$ orbitals. This doublet is a fingerprint for the hybridization between O $2p$ and metal $3d$-t_{2g} and between O $2p$ and $3d$-e_g states, respectively, which is reported to be strong in early transition metals. Correspondingly, the energy difference $\Delta M = M_2 - M_1 \approx 2$ eV, is a measure of the so-called ligand field energy splitting $\Delta E = E(e_g) - E_(t_{2g})$ [164, 181]. The relative intensity $I(M_1(t_{2g}))/I(M_2(e_g))$ is sensitive to the electronic occupancy at V $3d$ levels, which should vary according to the valence state of V^{m+} ions and hybridization. We note that an accurate determination of this ratio is challenged by the presence of the tail of the vanadium L_2-edge; therefore, we will restrict ourselves to a qualitative analysis. For the $t = 10$ nm SVO films of Figure 5.3a, the $I(M_1)/I(M_2)$ ratio is in excellent agreement with reference data for VO_2 oxide (as reproduced in the inset of Figure 5.3a) [181, 183]. Therefore, the $I(M_1)/I(M_2)$ ratio closely matches that

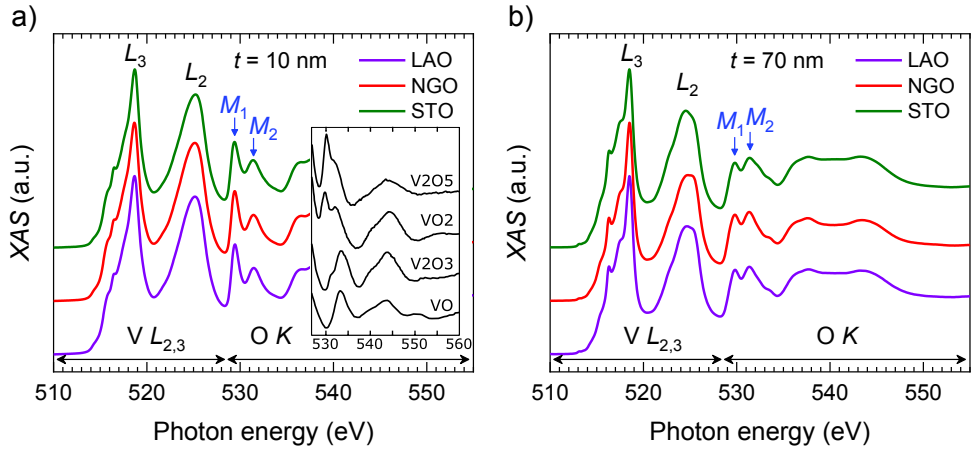

FIGURE 5.3: XAS of V $L_{2,3}$ and O K absorption edges of SVO films grown on STO, NGO and LAO, and for thicknesses of: a) 10 nm, and b) 70 nm. The energy ranges of V $L_{2,3}$ and O K-edges are indicated along the x-axis. Arrows of M_1 and M_2 at O K-edge pre-peak doublet represents the main absorption lines between O $1s$ and O $2p$ states, hybridized with $3d$-t_{2g} and $3d$-e_g states. Inset in a): illustrative O K XAS data for different VO_x oxides (experimental data adapted from Hébert et al. [181]).

reported for an average V d^1 configuration, without perceptible changes when changing the substrates. Liberati et al., reporting XAS of $CaVO_3$ films grown on different substrates, obtained similar spectra to those of Figure 5.3a and concluded that V^{4+} (d^1) oxidation state was prevalent in all films [180]. It is worth noticing that comparison of the XAS O K spectra recorded at normal and grazing incidence (Appendix D.4) does not reveal any discernible chemical shift – within the experimental resolution (< 10 meV) – suggesting that, within the sensitive penetration depth, the SVO films are electronically homogeneous.

The O K-edge of the $t = 70$ nm films on various substrates (Figure 5.3b) shows a reduction of the $I(M_1)/I(M_2)$ ratio, indicating that the density of $2p$ final states has changed either due to strain-related modification of hybridization and/or a change of the amount of electrons [180]. Indeed, if the formal charge of V^{4+} would reduce to V^{3+}, implying a higher density of electrons mostly at t_{2g} levels, then the available holes at $2p$ (hybridized with t_{2g}) would decrease and, correspondingly, the M_1 intensity would be reduced. Consistently, the Hall effect data (Figure 5.2c) signal an increase of carrier density of about 22-25%. A consistent increase of c/a with thickness is observed for films on LAO and STO, while thickness does not modify appreciably c/a in NGO (Figure 5.1c). As films on all substrates display a similar modification of the $I(M_1)/I(M_2)$ ratio, we conclude that carrier density

seems to contribute to the observed differences in O K XAS with film thickness, with little impact on the V $L_{2,3}$ features.

We next aim at addressing if the electron distribution within the $3d(t_{2g}, e_g)$ manifold is affected by substrate mismatch and film thickness. The XAS data in Figure 5.3a and 5.3b give a first but limited hint. Indeed, the fine structure of the V L_3-edge is related to final states available at t_{2g} and e_g orbitals. XAS features at the lower energy side of the L_3-edge were assigned to xy and xz/yz orbitals [184]. Recently, Wu et al. [135] used a configuration interaction approach to calculate XAS for V^{4+} in octahedral coordination and noticed that these multiplet-related features are very sensitive to tetragonal deformations of the coordination VO_6 polyhedra. The shape of L_3 in our spectra (Figure 5.3a,b) closely resembles those calculated for strained SVO films [135]; however, raw V L_3 XAS data do not allow to obtain a deeper insight into electron occupancy and its dependence on substrate.

Therefore, we turn now to exploit the sensitivity of XAS to the polarization direction of the incoming photons to deduce XLD, and identify the symmetry of occupied states. As already mentioned in the experimental section, the data were collected for the light incidence direction $\boldsymbol{k}$ at an angle θ with the sample surface, with the electric field vector pointing along two perpendicular directions: V ($\boldsymbol{E} \parallel ab$) and H ($\boldsymbol{E} \parallel bc$), where ab and bc indicate the planes defined by the (a, b, c) crystallographic axes of the sample (see Figure 5.4a). In these polarization-dependent experiments, the spectra were collected at various θ angles (8°, 30°, 60°, and 85°) with respect to the film surface (b-axis) from nearly in-plane (8°) to almost normal incidence (85°). At $\theta = 0°$, the electric field $\boldsymbol{E}$ of H polarized light is perpendicular to the sample surface, along the c-axis (and $\boldsymbol{E} = \boldsymbol{E}_c$); whereas, at $\theta = 90°$, E is parallel to it, along the b-axis ($\boldsymbol{E} = \boldsymbol{E}_b$).

Aetukuri et al. [158] showed that an insight into orbital occupation in V^{4+} can be safely achieved by restricting the XLD analysis to the lowest energy excitonic part of the V L_3 spectra (512-516 eV) range. On the other hand, extraction of V-3d related XLD values requires appropriate normalization of the raw XAS spectra collected for H and V polarizations. A partial overlapping between the V L_2 post-edge and O K-edge pre-peak is known to be an issue for V L-edge spectroscopy, and background subtraction is prone to introduce errors in quantitative analyses [178]. We have restricted ourselves to the excitonic region and we have normalized the spectra to ≈ 528 eV, just at the L_2 post-edge to minimize the impact of O K-edge to the absorption. The spectra were further normalized to the average intensity of the V L_3 peak in order to assess the quantitative data analysis at V L_3 XLD peak.

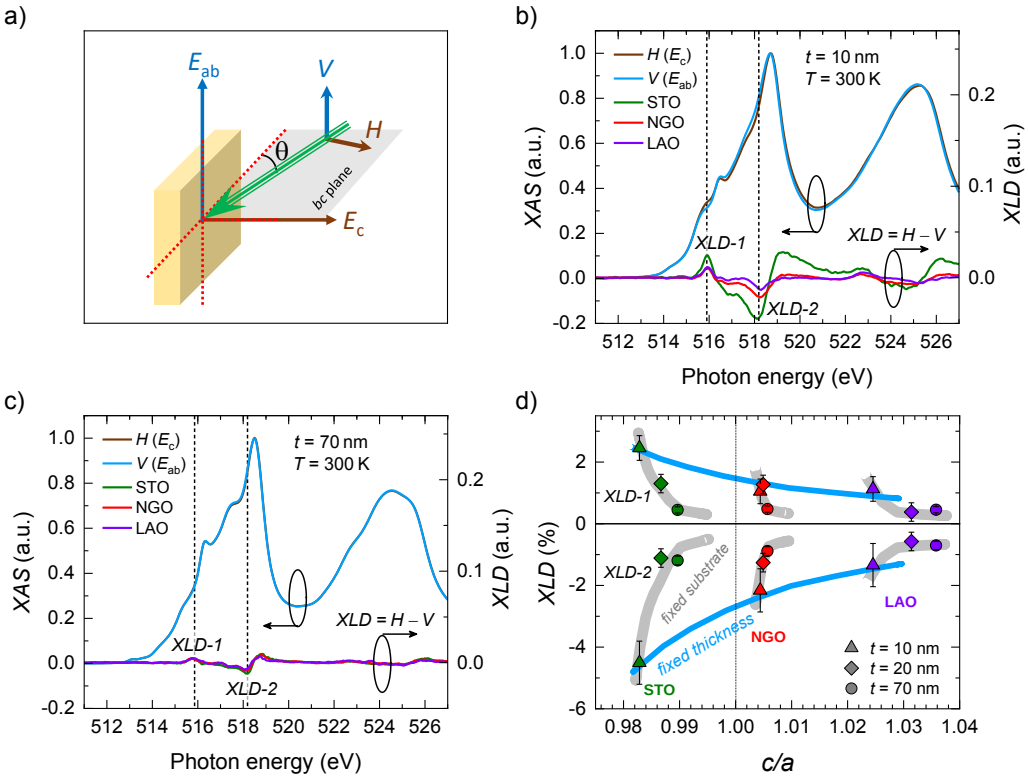

FIGURE 5.4: a) Experimental arrangement for XAS and XLD measurements. b-c) Illustrative H- and V-polarized XAS spectra (collected at RT and grazing indence $\theta = 30°$) of 10 and 70 nm SVO//STO film, respectively. Bottom spectra of the panels represent the XLD spectra (i.e. $I(\boldsymbol{E}_c) - I(\boldsymbol{E}_{ab})$) for each substrate (STO, NGO and LAO). Some reference energies, *XLD-1* and *XLD-2*, for maxima of positive and negative dichroism, respectively, are indicated by vertical dashed lines. d) Summary of the XLD maxima values of SVO films for various thicknesses (10, 20, and 70 nm) grown on STO, NGO and LAO substrates.

In Figure 5.4b we show XAS at the V $L_{2,3}$-edges of 10 nm thick SVO films grown on various substrates (STO, NGO, and LAO) recorded at room temperature and $\theta = 30°$, implying that the $\boldsymbol{E}$ of V-polarized spectra is parallel to the sample surface ($\boldsymbol{E}_a$, commonly written as $\boldsymbol{E}_{ab}$) and the $\boldsymbol{E}$ of H-polarized spectra is almost perpendicular to it ($\boldsymbol{E}_c$) (Figure 5.4a). Notable differences can be observed in the raw V L_3 XAS intensities, but they are better appreciated in the corresponding dichroic XLD signals shown in the bottom part of Figure 5.4b. Two different energies at V L_3 XLD signals are selected for the discussion, indicated by dashed vertical lines and labeled as *XLD-1* and *XLD-2*, where XLD displays well defined maxima for positive and negative dichroism. It is apparent that the amplitude of the corresponding *XLD-1* and *XLD-2* intensities are largest for the SVO films on STO, but reduces for the films on NGO and LAO. Data recorded at 2 K display a very similar trend (Appendix D.5). The XLD measurements have been done on the SVO films of 20 nm and 70 nm thicknesses in a similar manner. For instance, in Figure 5.4c, we show the data for 70 nm SVO films (data for the 20 nm films data in the Appendix D.6). It can be appreciated that XLD displays similar features as in the 10 nm films (Figure 5.4b) except the amplitudes at *XLD-1* and *XLD-2* are reduced with the increasing thickness. Figure 5.4d summarizes the XLD maxima values by displaying the amplitudes of *XLD-1* and *XLD-2* for each substrate (STO, NGO, and LAO) with different thicknesses (10, 20, and 70 nm), both parametrized by the corresponding c/a tetragonality ratio. Data show two main trends. First, the magnitude of *XLD-1* and *XLD-2* decreases from STO to LAO substrates, most noticeable in the thinnest films. Second, data also evidence than upon increasing film thickness and reducing the octahedral distortion $|1 - c/a|$, XLD progressively lowers, being the effect more remarkable in the most strained films (STO//SVO) and weaker in the partially relaxed films (SVO//LAO). Therefore, data in Figure 5.4d provides an insight on the impact of substrate and thickness on orbital occupancy in SVO films.

We next focus on the sign of the dichroic signal. To minimize multiplet-configuration mixing effects [135, 184, 185], we restrict ourselves to the dichroic signal observed at the lowest energy range. In Figure 5.4d it is apparent that the dichroic signal at *XLD-1* is positive implying that the XAS intensity recorded with $\boldsymbol{E}_{ab}$ is smaller than the $\boldsymbol{E}_c$. In the simplest electron-hole picture, this would indicate that xy orbitals are more occupied than xz/yz. Data show that this orbital polarization is gradually reduced from STO to NGO to LAO, although XLD (*XLD-1*) remains positive for all films ($t = 10$ nm). Accordingly, the xy orbitals are most favorably occupied in all films, irrespectively of $c/a > 1$ or $c/a < 1$. XLD measurements were recorded at different angles (8°, 30°, 60°, and 85°) for the thinnest films (10 nm), confirming the systematic variation of the XLD signal with substrate (Appendix D.7). Figure 5.4d also contains XLD data of the 20 nm and 70 nm SVO films on different substrates. The same trend as in the thinnest films

can be observed, with the amplitude of the XLD signal at *XLD-1* reducing when increasing thickness. However, we noticed above that in thicker films the XAS data at O K-edge and Hall data suggest some V^{4+} reduction to V^{3+}, that could signal a decrease in the oxygen contents in the film, thus changing not only the electronic distribution within the $3d$ orbitals but also its density. Therefore, we concentrate in the following on the data of the thinnest SVO (10 nm) films, where no traces of charge modification could be identified in XAS at V $L_{2,3}$ and O K-edges, as the most robust evidence of changing electron occupancy with substrate-induced stress. The XLD at *XLD-2* feature has its sign reversed (XLD < 0), with respect to *XLD-1*, and displays a mirror dependence on tetragonality ratio c/a and on film thickness. The presence of XLD features (*XLD-1* and *XLD-2*) of opposite sign differing by about 2.2 eV is fully consistent with calculations by Wu et al. [135].

As mentioned, electronic occupancy at metal t_{2g} orbitals should have its fingerprint on the O K-edge XAS and the XLD at O K-edge. Accordingly, XLD data at O K-edge has been determined as for V $L_{2,3}$. In Figure 5.5 we show the XAS spectra in the O K region of 10 nm SVO films grown on the different substrates, collected at the grazing incidence ($\theta = 30°$) with the $\boldsymbol{E}_c$ and $\boldsymbol{E}_{ab}$ polarizations as indicated.

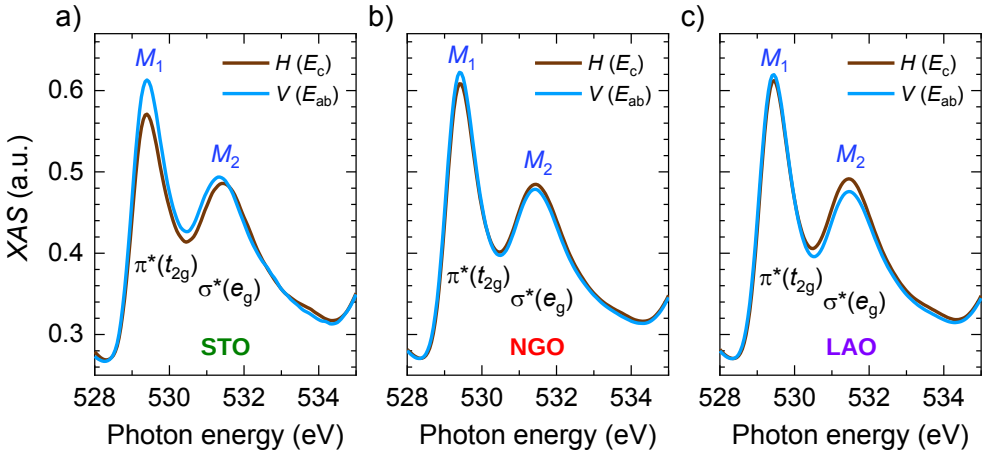

FIGURE 5.5: O K-edge XAS pre-peak of 10 nm SVO films grown on: a) STO, b) NGO, and c) LAO. A significantly larger dichroism at t_{2g} peak for STO than for NGO/LAO and the reverse at e_g peak reflect changes of hybridization with strain.

In order to analyze the XAS data in Figure 5.5 we recall that the M_1 and M_2 peaks correspond to available states at O $2p$ orbitals hybridized with ligand field split V $3d$ states, resulting in $\pi^*(t_{2g})$ and $\sigma^*(e_g)$ orbitals. The intensity of the

$\pi^*(t_{2g})$ absorption peak is considerably larger than the one of the $\sigma^*(e_g)$ peak: $I(\pi^*(t_{2g}))/I(\sigma^*(e_g)) \approx 1.25$ (Figure 5.6, right axis). This difference originates from the larger multiplicity of the t_{2g} orbitals compared to e_g ones (3/2 = 1.5) modulated by the distinct hybridization of $\pi^*(t_{2g})$ and $\sigma^*(e_g)$ orbitals. It can be also appreciated in Figure 5.5 that the energy difference between $\Delta E_{CF} = E(\sigma^*(e_g)) - E(\pi^*(t_{2g}))$ is of about 2.0 eV as commonly found for early transition metal oxides [164, 186], and virtually insensitive to the substrate. Next we focus on the O K XLD signal defined as the XAS intensity at the corresponding $I(\pi^*(t_{2g}))$ and $I(\sigma^*(e_g))$ maxima recorded using $I(\boldsymbol{E}_{ab})$ and $I(\boldsymbol{E}_c)$ ($XLD = I(\boldsymbol{E}_c) - I(\boldsymbol{E}_{ab})$). In Figure 5.6 (left axis) we show the XLD values for films on various substrates.

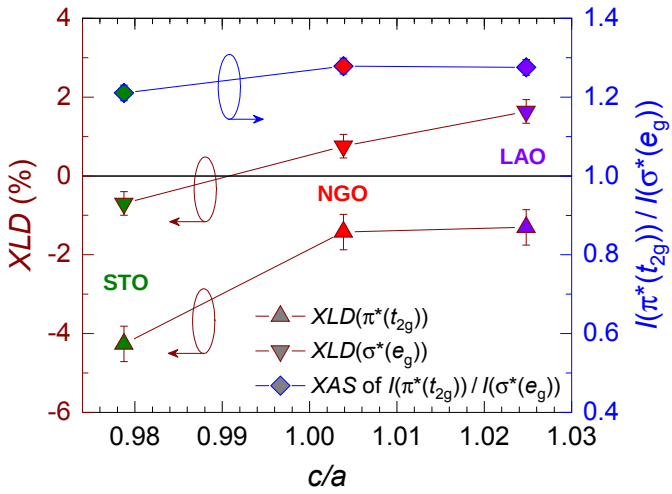

FIGURE 5.6: Left axis: XLD at O K-edge for SVO films (10 nm thick) on substrates imposing different tetragonality ratios (c/a). Square symbols indicate the XLD at $\pi^*(t_{2g})$ and $\sigma^*(e_g)$ absorption peaks, as indicated. Right axis: $I(\pi^*(t_{2g}))/I(\sigma^*(e_g))$ intensity ratios.

It is clear in Figure 5.6 (and data in Figure 5.5a) that for the tensile strained SVO//STO film (smallest c/a ratio), the XAS intensity $I(\pi^*(t_{2g}))$ is larger for $\boldsymbol{E}_{ab}$ than for $\boldsymbol{E}_c$, and accordingly XLD$(\pi^*(t_{2g})) < 0$. The observation that XLD$(\pi^*(t_{2g})) < 0$ indicates a higher concentration of holes at $(p_x + p_y)$ orbitals of the $(p_x + p_y)$-d_{xy} hybrid. In other words, strain modifies the $\pi^*(t_{2g})$ p-d hybridization, driving charge (for $c/a < 1$) from the $p_x + p_y$ orbitals towards the metal. An analogous reasoning accounts for the observed reduction of XLD$(\pi^*(t_{2g}))$ when increasing c/a. Similarly, the dependence of XLD$(\sigma^*(e_g))$ on c/a also reflects the corresponding changes of $\sigma^*(e_g)$ hybridization.

These observations can be rationalized on the basis of strain modification of $2p$-$3d$ hybridization and subsequent changes in the electron occupancy at $2p$-$3d$ hybridized orbitals. We notice that in an octahedral VO_6 environment, symmetry arguments dictate that, focusing on the VO_2 plane of SVO structure, d_{xy} hybridizes with $(p_x + p_y)$; d_{xz} hybridizes with $(p_x + p_z)$ and d_{yz} hybridizes with $(p_y + p_z)$, whereas $d_{x^2-y^2}$ hybridizes with $(p_x + p_y)$ and d_{z^2} with p_z, as illustrated in the Figure 5.7 (central panel) and Figure 5.7a-b.

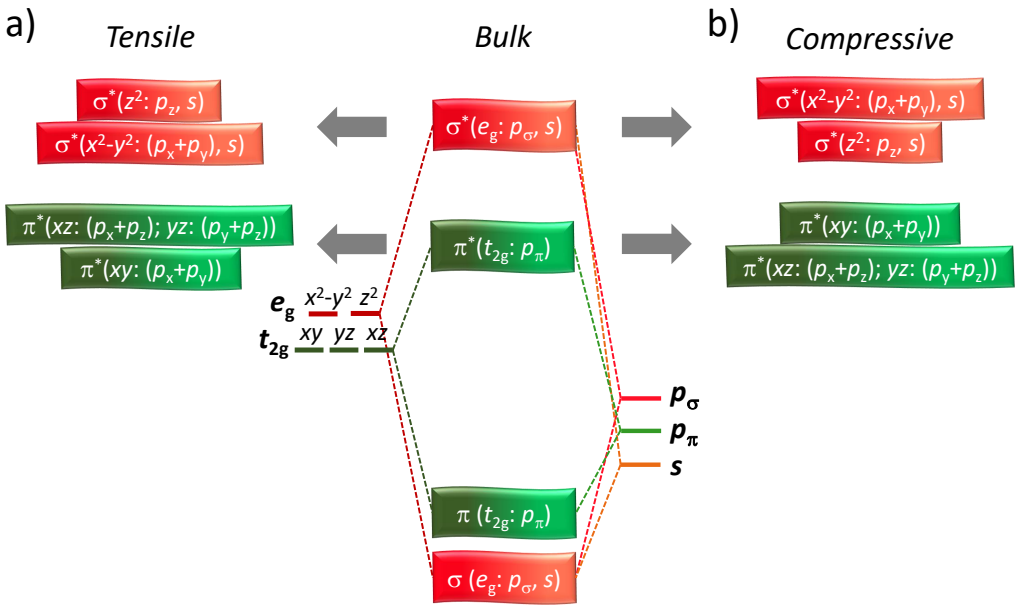

FIGURE 5.7: Central panel: Energy-band diagram for $SrVO_3$ thin films. The hybridized (σ, σ^*) and (π, π^*) orbitals, and their parentage, are indicated. The symmetry broken hybridized orbitals under the effect of: a) tensile strain, and b) compressive strain.

Under tensile strain (SVO//STO), d_{xy} orbitals are pushed down as observed by XLD(V $L_{2,3}$). Consequently, the hybridized orbital is shifted down (Figure 5.7a) and the (p_x, p_y) orbitals which are hybridized with d_{xy}, are electron-depleted by charge transfer to the metal. Accordingly, XAS at O K-edge should be larger for $\boldsymbol{E}_{ab}$ (more holes available) than for $\boldsymbol{E}_c$, and thus XLD($\pi^*(t_{2g})$) should be negative (<0), as we observed. Similarly, when SVO films are under compressive stress (SVO//LAO), $d_{xz,yz}$ orbitals are shifted down in energy as observed by XLD(V $L_{2,3}$). Therefore, the hybridization of these orbitals with the corresponding p_z orbitals (Figure 5.7b) implies that the p_z orbitals are electron-depleted (hole-rich) and the correspondingly XLD($\sigma^*(e_g)$) is positive (>0), as we experimentally observed

(Figure 5.6).

In order to analyze the role of tetragonal distortion on the electronic structure of SVO, we performed first principles DFT calculations. Of interest here is the integrated partial density of states (*IDOS*) associated to oxygen (p_x, p_y, p_z) and vanadium $3d$ (t_{2g}, e_g) orbitals and to disclose how their relative weight evolve with c/a.

In Figure 5.8a, we show the sum of the integrated density of states *IDOS* of in-plane (x^2-y^2, xy) and out-of-plane (z^2, xz, yz) orbitals of $3d$-e_g and $3d$-t_{2g} manifolds, as a function of the tetragonal distortion c/a determined in SVO films on STO, NGO and LAO ($c/a = 0.978$, 1.003, 1.024, respectively). We also include in Figure 5.8a the data for a cubic SVO of cell parameter $a = c = 3.86$ Å, corresponding to the unit cell parameter of an unstrained cubic SVO film of volume 57.5 Å^3 (Figure 5.1c). *IDOS* plots for every individual orbital are included in Appendix D.8. Data in Figure 5.8a clearly show that in-plane orbitals are stabilized under tensile strain ($c/a < 1$); the opposite trend is observed for out-of-plane orbitals. This is agreement with data in Figure 5.4d. The same trend can be appreciated in Figure 5.8b where we show *IDOS* of in-plane and out-of-plane $2p$ orbitals. Therefore, p-d hybridized in-plane orbitals move in unison under tetragonal cell distortion, and similarly the out-of-plane hybridized orbitals. However, the relative p/d relative weight in hybrid orbitals is not preserved when changing c/a, as clearly indicated by data in Figure 5.8c, where the *IDOS* ratios ($IDOS(p)/IDOS(d)$) for in-plane (left) and out-of-plane (right) orbitals are depicted. This implies a charge redistribution among V-O bonds under strain. Indeed, the $2p$ orbitals become progressively more occupied when increasing c/a. Oppositely, for $c/a < 1$, the ratio [$IDOS(p$, in-plane$)/IDOS(d$, in-plane$)$] lowers compared to its value for $c/a = 1$. This implies that the in-plane orbitals of $3d$ character are pushed down compared to the corresponding hybridized $2p$ orbitals, which thus have a relatively lower *IDOS*, as argued above. Correspondingly, the available states at $2p$ in-plane orbitals become larger. This accounts for the observed XLD($\pi^*(t_{2g})$) < 0 observed for $c/a < 1$ as shown in Figure 5.6. A similar reasoning accounts for the observed XLD variation for $c/a > 1$.

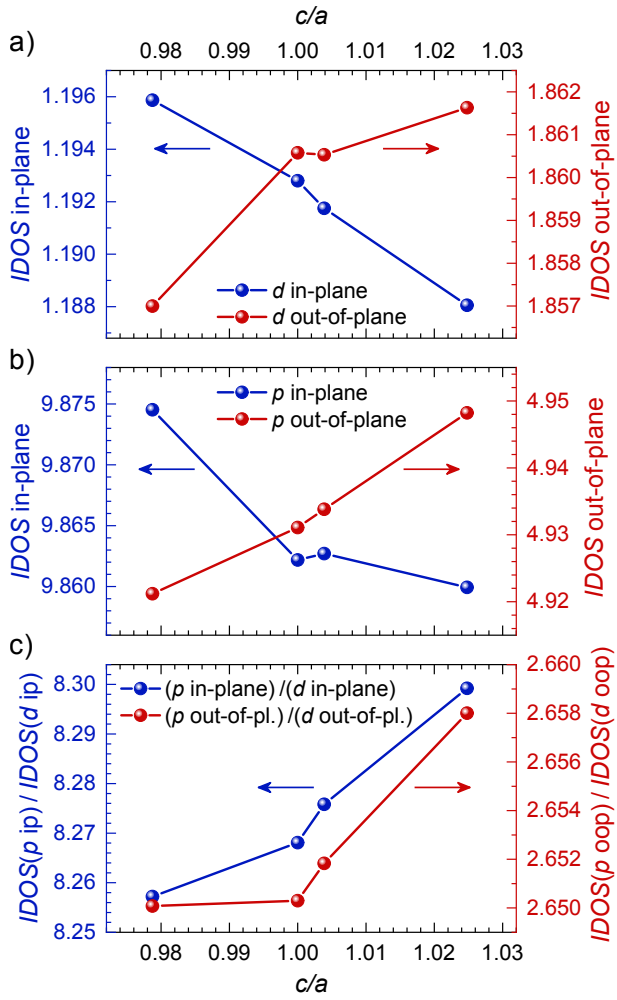

FIGURE 5.8: a) Sum of the integrated partial density of states (*IDOS*) of in-plane (left axis) and out-of-plane (right axis) $3d$ orbitals. b) Similar data for in-plane (left axis) and out-of-plane (right axis) $2p$ orbitals. c) Ratio between the total density of states of $2p$ and $3d$ character $IDOS(2p)/IDOS(3d)$ in-plane (left) and out-of-plane (right).

5.6 Summary and conclusions

In summary, bulk $SrVO_3$ is cubic, but when SVO films are grown on substrates having different structural mismatch with SVO, epitaxial growth imposes compressive or tensile strain on the film structure and its tetragonality ratio can be varied from $c/a > 1$ to $c/a < 1$ depending on the substrate used and the film thickness. XAS at V $L_{2,3}$ and O K-edges of the thinnest films (10 nm) display almost identical features fully consistent with the expected $3d^1$ V^{4+} electronic configuration of this oxide. XLD is well visible at $L_{2,3}$-edges, indicating that the $3d$-t_{2g} orbitals are not degenerate but signaling a clear hierarchy of (xy, xz, yz) orbitals that gradually varies with the epitaxial strain. In films having an in-plane tensile strain (SVO//STO), the in-plane xy orbitals are preferentially occupied by electrons, gradually levelling out in films under compressive strain. XAS at O K-edge provides a clear evidence of a relevant $2p$-$3d$ hybridization. XLD at O K-edge indicates that hybrid π^* orbitals in epitaxially tensile strained films, having an in-plane symmetry, have a hole-density that decreases in compressive strained films. The consistent variation of occupancy in $2p$ and $3d$ orbitals with strain shows that substrate-induced symmetry breaking modulates orbital occupancy at the metal site but also the metal-oxygen hybridization. It follows that charge density at the metal site is not preserved under strain but redistributes within the hybridized bonds. However, whereas in the case of edge-shared coordination polyhedral (VO_2 case) changes of hybridization with temperature or strain are strong enough to promote a metal-insulator transition, in the corner-connected octahedral networks, strain slightly modifies the electrical conductivity but SVO films (at least ≥ 10 nm) remain metallic. Still, the rigid band image of an electron redistribution restricted within the $3d$-t_{2g} manifold and dictated by strain does not hold in the simplest $3d^1$ perovskite, with corner-sharing octahedral network, but hybridization plays a relevant role.

Chapter 6

Electron-phonon coupling and electron-phonon scattering in $SrVO_3$ thin films

In this chapter, we present a thorough analysis of the transport properties of $SrVO_3$ thin films. In particular, we propose a different explanation than the Fermi liquid theory to account for phenomena such as the effective mass enhancement (responsible of the material's transparency).
The work presented in this chapter was published with DOI: 10.1002/advs.202004207 (see also the list of publications).

6.1 Introduction

Strong coulomb interactions characteristic of partially occupied narrow $3d$ bands renormalize the properties of charge carriers in *Fermi liquids* (FL), resulting, among other effects, in a large increase of their effective mass m^*_{ee}, with respect to the effective band mass m^*_{band}. Increasing further the carrier density (n) or reducing the conduction band width (W), may eventually give rise to an emerging insulating state (Mott transition) [187–190].
This framework has been used to rationalize the properties of correlated electronic systems. The case of transition metal oxide (TMO) perovskites ABO_3 (B is a transition metal) is particularly illustrative. The robustness of the perovskite scaffolding (a 3D network of octahedrally coordinated BO_6 polyhedra) allows multiple cation substitutions at A/B sites that modify the electron filling and B-O bond distances and angles, achieving in some cases a band-filling and bandwidth-driven Mott transition [191].

The complexity of the problem is schematized in the diagram below (Figure 6.1), where we take as example a TMO containing one single electron in a $3d^1$ band, e.g. $SrVO_3$. In a cubic BO_6 cage, the single electron of the transition metal M occupies the (d_{xy}, d_{xz}, d_{yz}) orbitals of $3d$-t_{2g} parentage. The resulting band (of width W), being partially occupied (1/6), will host a metallic conductivity (Figure 6.1, center). Within the FL picture, the carrier effective mass would be renormalized to m^*_{ee}, which will be larger than m^*_{band}. Modification of the bond topology and charge distribution within the t_{2g} band, may promote the opening of a Mott gap. Vanadium $3d^1$ oxides such as (Sr,Ca)VO_3 or VO_2 fit in this picture, as recently overviewed by Brahlek et al. [192]. According to that, the-shifted plasma frequency ($\omega^*_p \propto (n/m*)^{1/2}$) of (Sr,Ca)$VO_3$ can be attributed to a large effective mass m^* arising from $e-e$ correlations (i.e. $m^* = m^*_{ee}$) (Figure 6.1, bottom). In the same vein, an abrupt metal insulator transition occurs in VO_2 upon cooling due to the opening of a Mott gap (Figure 6.1, top). The properties of these materials are thus described within a purely electronic model including correlation effects (Figure 6.1, bottom-top).

Although the success of this approach has been tremendous, some properties of metallic oxides cannot be described within this framework. For instance it has been repeatedly reported that the resistivity (ρ) and the inverse carrier mobility (μ^{-1}) of $SrVO_3$ (SVO) follow a nearly T^2 temperature dependence [18, 116, 124, 140]. In fact, $\mu(T) \approx T^{-2}$ is commonly observed in doped Mott insulators, such as $LaTiO_3$ or $SmTiO_3$, but also in doped band insulators (e.g. $SrTiO_{3-x}$ and (Gd,La,Nb):$SrTiO_3$, as recently reviewed by Stemmer et al. [193]), some high-T_C superconductors (HTS), or oxyselenides [194]. It has been emphasized that although $\mu \approx T^{-2}$ may be consistent with the picture of $e-e$ scattering in a FL, the dependence of the amplitude of this scattering term on carrier density sharply contradicts expectations based on the FL description of interacting electron systems [193, 195]. Therefore, the whole scenario should be revisited.

In this regard, we suggest that the topology of the Fermi surface (FS) could be an important ingredient to this picture, previously overlooked. Along the Γ-X direction, only (d_{xy}, d_{xz}) orbitals overlap and therefore the FS consists of a 2D cylinder. A similar situation occurs along the orthogonal directions, and thus the FS is formed by three interpenetrated cylinders (Figure 6.1, right). The relevance of a quasi-2D FS on the carrier mobility is not minor: in anisotropic metals with quasi-cylindrical FS branches, $e-ph$ scattering promotes a distinctive $\approx T^{-2}$ temperature dependence of the carrier mobility, early described in great detail for Bi [196].
The second feature is that carriers in a $3d^1$ TMO move within an ionic lattice background. This implies that, even in the presence of screening, the lattice can be polarized around the moving charge. Carriers, in this scenario (Figure 6.1, left),

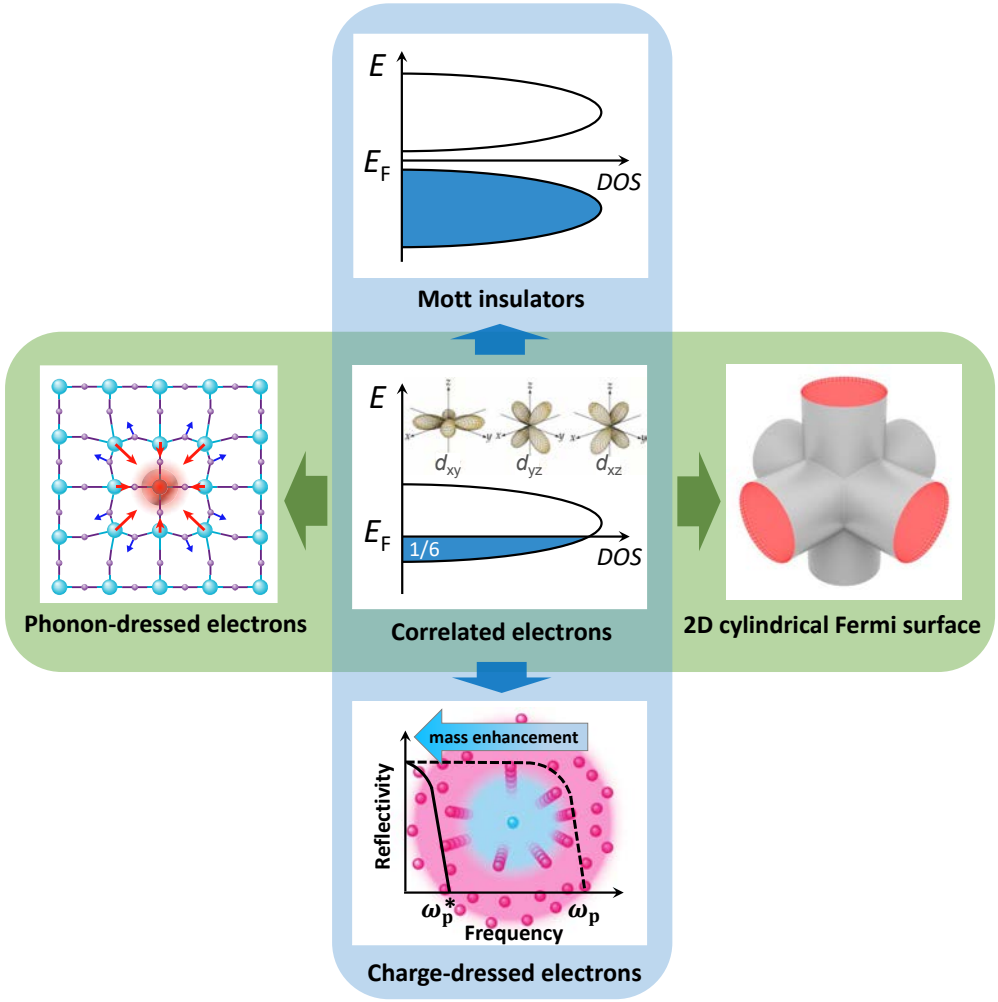

FIGURE 6.1: (Center) Partially occupied t_{2g} (d_{xy}, d_{xz}, d_{yz}) orbitals, (1/6) in the sketch, are responsible for metallic behaviour. Electron-electron correlations may increase carrier effective mass (m^*_{ee}) and, among other consequences, reduce the plasma frequency (bottom illustration) or, eventually, open a Mott gap (top illustration). In cubic metal-oxide surrounding, the symmetry of the (d_{xy}, d_{xz}, d_{yz}) orbitals produces a quasi 2D cylindrical Fermi surface (right). Charge carriers in an ionic lattice are dressed with a lattice polarization cloud (left illustration), enhancing also the effective mass ($m^*_{e\text{-}ph}$).

are dressed with a lattice distortion, that translates into an effective mass ($m^*_{\text{e-ph}}$) related to the coupling of electrons to the lattice ($e-ph$ coupling). In view of the two above-mentioned aspects, SVO is at the crossroad of $e-e$ correlations, $e-ph$ strong coupling and low dimensional FS (Figure 6.1), whose interplay requires renewed attention. An important general question is whether the quadratic temperature dependence of the resistivity is indeed an undisputable fingerprint of $e-e$ correlations, or if other scenarios should be envisaged.

In this chapter, we aim at revising some of these issues by reporting on electric transport data (resistivity, magnetoresistance, Hall and Seebeck coefficients) of a large set of $SrVO_3$ (SVO) epitaxial films deposited on suitable substrates and with different growth conditions, selected on purpose to modify the lattice distortions and, expectedly, the lattice dynamics.
It will be first shown that all films have $\mu(T) \approx T^{-2}$ and $\rho(T) \approx A\,T^2$, where A is a proportionality coefficient. These temperature dependences are consistent with earlier findings [18, 116, 124, 140]. In these references, A was identified as the coefficient corresponding to the temperature-dependent $e-e$ scattering rate (A_{ee}) in a FL, i.e. $A \equiv A_{\text{ee}}$ [197–199]. However, from the analysis of the magnitude of A and its carrier density dependence, we conclude that the temperature dependence of $\mu(T)$, in contrast to earlier views, may not originate from $e-e$ scattering in a FL. Instead, we show that $\rho(T)$ can be well described by a polaronic model (Figure 6.1, left panel), where the relevant phonon energies can be tuned ad-hoc by epitaxial strain and subsequent lattice distortion. We also show that $e-ph$ scattering in a cylindrical 2D FS (Figure 6.1, right panel) accounts for the observed $\mu(T) \approx T^{-2}$, the temperature-dependent Seebeck coefficient $S(T)$ and the observed magnetoresistance and its Kohler's scaling. We thus conclude that $e-e$ interactions and $e-ph$ coupling in $3d^1$ TMOs probably should be taken on an equal footing to account for the experimental mass renormalization, as found in other oxides [200, 201], and that the 2D character of the FS should be explicitly considered to build a comprehensive view of the carrier transport in these seemingly most simple metallic oxides.

6.2 Transport properties

6.2.1 Sample description

The SVO films presented in this chapter were already introduced in Chapters 3,5,4. In short (more specifications will be given when appropriate), those are SVO films of thickness 10-70 nm, grown on single crystalline STO, LSAT, NGO and LAO substrates, at $P(Ar) = 0$-0.3 mbar or $PO_2 = 4\times10^{-7}$-2×10^{-5} mbar. All films were grown

at substrate temperature $T = 750$°C. Depending on the growth conditions and substrates, the tetragonal distortion c/a is modulated.

6.2.2 Temperature dependence of the electrical resistivity

Figure 6.2 displays illustrative $\rho(T)$ data of SVO films. In Figure 6.2a we include data of films on different substrates, all having a thickness $t \approx 70$ nm and grown at $P(Ar) = 0$ mbar. The metallic character of all films is clear, and the $\rho(300\,\text{K}) \approx$ 85-100 μΩ cm for films grown on LSAT, NGO and LAO is similar to state-of-the-art literature data [18, 112, 114, 116, 140, 202]. The resistivity $\rho(T)$ of the SVO film on STO is vertically shifted due to the presence of planar defects associated to the large tensile mismatch of SVO with the STO substrate (as shown in Chapter 3), although its slope remains similar to the other films. In Figure 6.2b we show data of films grown on one of the substrates (NGO), all having same thickness ($t \approx 70$ nm), but grown at different Ar pressures. As mentioned, it can be appreciated that growth pressure has a major effect on $\rho(T)$ and optimal films are obtained for $P(Ar) = 0.2$–0.3 mbar. In Figure 6.2c, where we show $\rho(T)$ data of SVO films of different thicknesses on NGO, it can be appreciated that the resistivity of the films gradually increases as thickness reduces, as commonly found in SVO [18, 116,

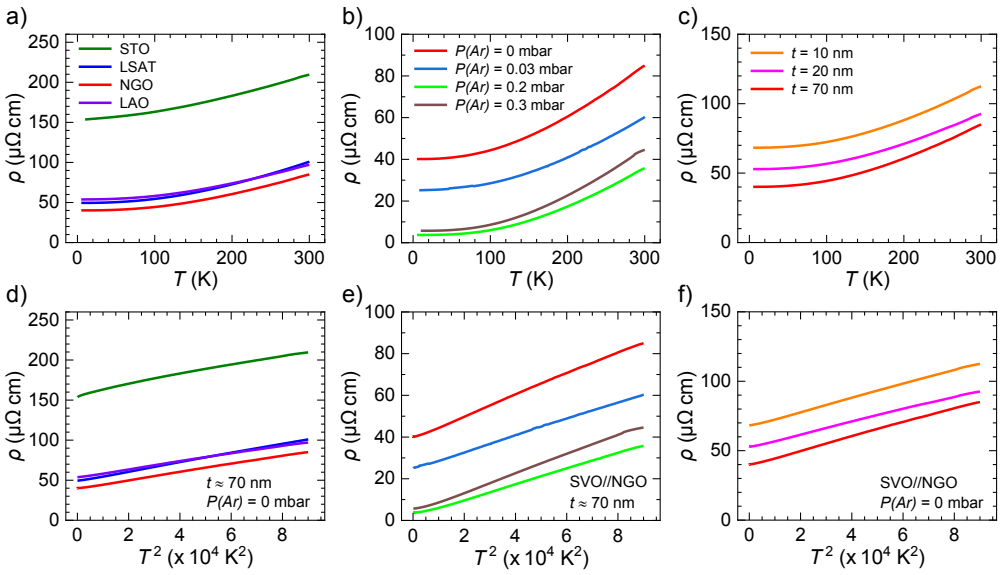

FIGURE 6.2: Temperature dependence of $\rho(T)$ of selected series of SVO samples, plotted vs T (a-c) and vs T^2 (d-f). The impact of substrate, growth conditions and thickness are illustrated in (a,d), (b,e) and (c,d) respectively.

140]. The RRR ratio has been determined for all films (reported in Chapters 3-5-4 and recalled in Appendix E.1). It turns out that RRR is as high as ≈ 12 in optimally grown films, and decreases down to $RRR \approx 2$ in films grown on poorly matched substrates and/or too-high or too-low $P(Ar)$. It is worth noticing that $RRR \approx 12$ are among the highest values ever reported for PLD-grown SVO films (see growth optimization in Chapter 4).[1]

All $\rho(T)$ data in Figure 6.2a-c display a characteristic non-linearity, ubiquitously found in all reported SVO films [18, 112, 116, 140, 202]. A first insight on the microscopic origin of the $\rho(T)$ dependence can be obtained by plotting $\rho(T)$ vs T^2, as shown in Figure 6.2d-f. It can be observed that $\rho(T)$ has an almost linear dependence on T^2 as commonly found in SVO films. The data can be roughly described as $\rho(T) = \rho_0 + AT^2$ and can be fitted to extract (ρ_0, A), as shown in Figure 6.5 and Appendix Section E.2. This $\rho(T) \approx T^2$ dependence is commonly interpreted as the fingerprint of $e-e$ scattering in strongly correlated systems.

In Figure 6.3a, we show the extracted A values for all samples as a function of the carrier concentration (n) determined from room-temperature Hall effect measurements. It can be appreciated that A varies within the $\approx (3 \times 10^{-10} - 4 \times 10^{-9})\,\Omega\,\mathrm{cm\,K^{-2}}$ range when the carrier density varies within the $\approx (3 \times 10^{21} - 2 \times 10^{22})\,\mathrm{cm^{-3}}$ range (see data in Appendices E.1-E.2). In Figure 6.3a we also include the A values reported in the literature for $Ca_{1-x}Sr_xVO_3$ polycrystalline samples ($4.2 \times 10^{-10} - 9.1 \times 10^{-10}\,\Omega\,\mathrm{cm\,K^{-2}}$) [124] as well as for SVO thin films ($2.5 \times 10^{-10} - 5 \times 10^{-10}\,\Omega\,\mathrm{cm\,K^{-2}}$) [18, 116, 140]. The close similarity of all available data is remarkable. To set in an appropriate context the large variation in magnitude of A, in Figure 6.3b we show the A values for SVO and related oxide materials. For that we have selected oxides where the conduction band is mainly formed by partially occupied $3d$-t_{2g} orbitals, either intrinsic (SVO case) or obtained by electron doping of Mott insulators (e.g. Sr:$GdTiO_3$) [203] or band insulators (La:$SrTiO_3$, Nb:$SrTiO_3$ or $SrTiO_{3-x}$) [195, 204, 205], as first summarized by Mikheev et al. [206] and Stemmer et al. [193]. It is remarkable that A can be varied by about five orders of magnitude when the carrier concentration changes by about five orders of magnitude; we conclude that $A \approx (1/n)$ over a very wide range of carrier concentration, as indicated by the dashed line in Figure 6.3a,b.

The temperature-dependent carrier mobility $\mu(T)$ ($\mu = 1/(\rho ne)$) was determined from $n(T)$ extracted from Hall effect measurements, and $\rho(T)$. Illustrative $n(T)$ and $\mu(T)$ data are depicted in Figure 6.4a. It can be appreciated that $n(300\,\mathrm{K}) \approx 2.5 \times 10^{22}\,\mathrm{cm^{-3}}$, reducing slightly ($\approx 12\,\%$) at 5 K. The mobility rapidly

[1] Let's recall that RRR is used in the following as a label for film quality [18, 42, 111, 202].

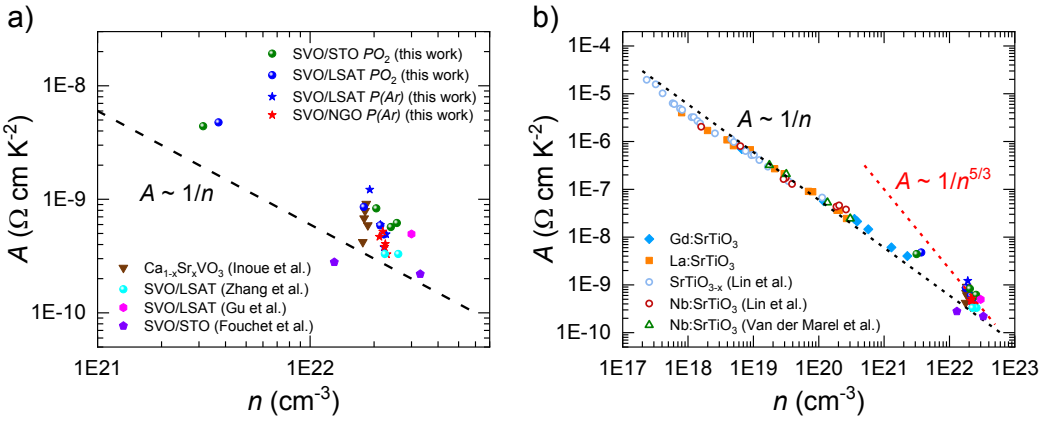

FIGURE 6.3: a) Coefficient A of $\rho(T) = \rho_0 + AT^2$ vs carrier density (n) as extracted from Hall measurements, for some SVO films. Data from literature references [18, 116, 124, 140] are also included. b) Comparison of present A values with available literature values for SVO films and related metallic oxides (figure adapted from Mikheev et al. [206] and Stemmer et al. [193], including data of Gd:$SrTiO_3$ from Moetakef et al. [203], La:$SrTiO_3$ from Cain et al. [205], Nb:$SrTiO_3$ from Van der Marel et al. [204], and $SrTiO_{3-x}$ and Nb:$SrTiO_3$ from Lin et al. [195]). Dashed lines indicate $A \approx n^{\alpha}$ power dependences with α = -1 and -5/3.

decays with increasing temperature. As shown in Figure 6.4b, $\mu^{-1}(T) \approx T^2$ which is similar to $\rho(T)$, implying that $\mu(T)$ governs $\rho(T)$. Therefore, in the following we indistinctly refer to the quadratic temperature dependence of $\rho(T)$ or $\mu^{-1}(T)$.

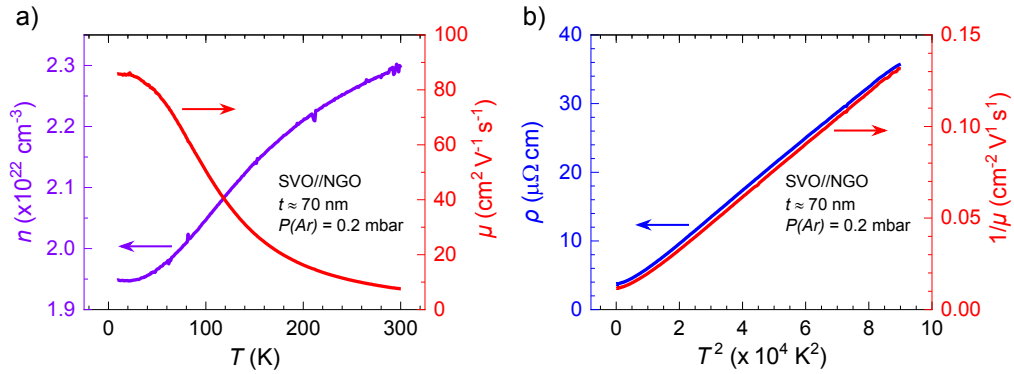

FIGURE 6.4: a) Temperature-dependent carrier concentration (left axis) and mobility (right axis) of an illustrative SVO film (70 nm thick, deposited on NGO at $P(Ar) = 0.2$ mbar). b) Resistivity (left axis) and inverse mobility (right axis) vs T^2 of the same film.

A detailed inspection of the data in Figure 6.2d-f reveals, however, that the T^2 dependence may only be a first approximation to the actual temperature dependence of $\rho(T)$. Finer details of $\rho(T)$ fits can be appreciated in Figure 6.5 where we show illustrative fits of $\rho(T)$ to $\rho(T) = \rho_0 + AT^2$ on samples having large $RRR = 9.6$ (Fig. 6.5a) and $RRR = 2.1$ (Fig. 6.5b). It is obvious in Figure 6.5a,b that $\rho(T)$ data show a clear departure from the functional T^2 dependence, most noticeable at $T \leq 180$ K (dashed vertical line). A similar trend is observed in all measured films, namely films with larger RRR (> 3) display departure from T^2 behavior at $T \leq 180$ K (more fits are shown in Appendix E.2). Importantly, the deviation from T^2 becomes lest perceptible in films with lower RRR (Figure 6.5b-e). Including a phonon-like T^5 term did not improve fits and did not affect the extracted A parameter. Fits to other samples, residual fit differences and fits including additional T^5 terms are shown in Appendix E.2.

To explore the origin of the departure of $\rho(T)$ from $\approx T^2$ observed in optimal films with the largest RRR, we consider that the dynamics of the d^1 electron, moving in the narrow $3d$-t_{2g} band within an ionic matrix ($O^{2-}/V^{4/5+}$), bear some similitude to polaronic motion. Indeed, it has been claimed that polaronic carrier motion could be of relevance in itinerant-electron systems approaching the localized edge, including $CaVO_3$ [207], weakly-doped Ln:STO (where Ln is a lanthanide), orthorhombic manganites $La_{1-x}Ca_xMnO_3$ [208, 209], $La_{0.7}Sr_{0.3}MnO_3$ [210] and $La_{2/3}(Ca_{1-x}Sr_x)_{1/3}MnO_3$ [191], or in doped $LaTiO_3$ and $NdTiO_3$ [211, 212]. Within this framework, the carrier mobility is determined by their coupling to some low energy phonons. The polaronic resistivity is given by the following expression [209, 213]:

$$\rho(T) = \rho_0 + \frac{\hbar^2}{ne^2a^2t_p} \times \frac{1}{\tau} \tag{6.1}$$

where t_p is the hopping amplitude for polarons, a the cell parameter, n the carrier density and ρ_0 is the residual resistivity. τ^{-1} is the polaron relaxation rate, which is dictated by the $e-ph$ coupling to some phonon modes. In the simplest assumption of polaron coherent motion, in which a single optical phonon mode ($\hbar\omega_0$) dominates the polaron relaxation rate, τ^{-1} is given by the expression [209]:

$$\frac{1}{\tau} = \frac{A_{\text{e-ph}} \cdot \omega_0}{\sinh^2\left(\frac{\hbar\omega_0}{2k_BT}\right)} \tag{6.2}$$

where $A_{\text{e-ph}}$ encapsulates the $e-ph$ coupling strength and the effective mass of the dressed electron ($m^*_{\text{e-ph}}$) and k_B is the Boltzmann constant.

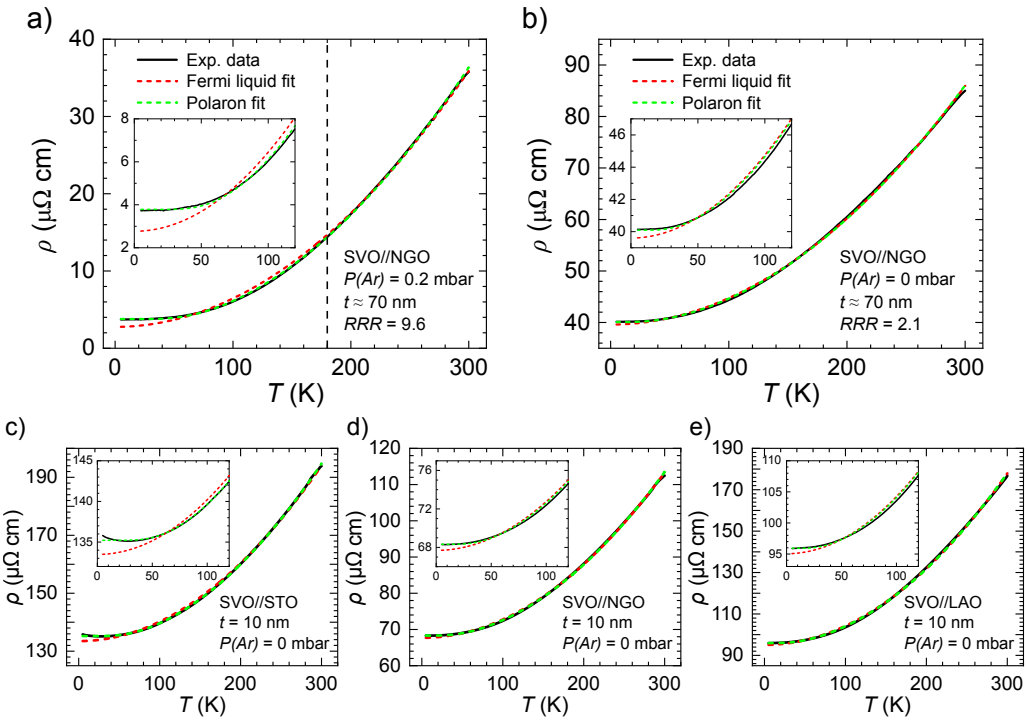

FIGURE 6.5: a,b) Illustrative $\rho(T)$ data of SVO films on NGO substrates (70 nm, grown at different $P(Ar)$) largely differing in RRR, as indicated. c,d,e) $\rho(T)$ data of SVO films (10 nm, $P(Ar) = 0$ mbar) grown on substrates imposing tensile (STO, NGO) or compressive strain (LAO) on SVO. The dashed red line is the fit to the T^2 dependence. Dashed vertical black lines indicate the temperature where noticeable departure from the quadratic T-dependence is observed. The dashed green line is the fit to the polaronic model. Insets are zooms of the low temperature region.

Assuming that $A_{\text{e-ph}}$ in Equation 6.2 is temperature independent, by combining all parameters, Equation 6.1 can be rewritten as:

$$\rho(T) = \rho_0 + \frac{A^*_{\text{e-ph}} \cdot \omega_0}{\sinh^2\left(\frac{\hbar\omega_0}{2k_B T}\right)} \tag{6.3}$$

where $A^*_{\text{e-ph}}$ is given by:

$$A^*_{\text{e-ph}} = \frac{\hbar^2}{ne^2a^2t_p} \cdot A_{\text{e-ph}} \tag{6.4}$$

In Figure 6.5a,b (dashed green lines), we include the fits of the $\rho(T)$ data using Equation 6.3, that allow to extract the phonon frequency ω_0. We observe that data are well reproduced in all temperature range (5-300 K), particularly in the low temperature region (< 180 K), where the quadratic fit failed. Similar excellent fits have been obtained for all samples with large RRR (> 3-4) (see Appendix E.2). Residual fit differences are reduced by about 90% compared to T^2 fits and similar excellent fits have been obtained for all samples, and fitted parameters are robustly obtained irrespectively of fitting procedures (Appendix E.2).

Aiming at exploring changes of the phonon frequency (ω_0) with lattice distortion, we first concentrate on fully strained films grown on substrates where epitaxial strain dictates different c/a ratios. One expects that phonons in SVO films are sensitive to tetragonal distortions of the VO_6 octahedra which can be quantified by the c/a ratio extracted from XRD. In Figure 6.5c-e we show the $\rho(T)$ data of SVO ($\approx$ 10 nm, $P(Ar) = 0$ mbar) films on STO, NGO and LAO. As observed, the polaronic model leads to excellent fits. The extracted $\hbar\omega_0$ values are around 20.6 meV (STO), 12.7 meV (NGO) and 10.7 meV (LAO), which indicates a clear softening under compressive distortion of the SVO lattice (from $c/a < 1$ to $c/a > 1$). Figure 6.6a (decorated sphere symbols) shows the observed $\hbar\omega_0$ and its variation with c/a. We also include in Figure 6.6a the phonon energy $\hbar\omega_0$ extracted from the fits of SVO films on optimally matched substrates (LSAT, NGO) grown at different pressures (0-0.3 mbar) and thicknesses (10-70 nm). For completeness, we have also included (light blue spheres) the $\hbar\omega_0$ data extracted from fits to digitized $\rho(T)$ data of films grown by hybrid-MBE (h-MBE) [18, 42], which nicely fall on top of our data (fits are shown in Appendix E.2c).

In Figure 6.6b (left axis, full spheres), we explore a possible correlation between the $e-ph$ coupling related $A^*_{\text{e-ph}}$ parameter and the phonon energy $\hbar\omega_0$. The data show that the $e-ph$ coupling strength increases with $\hbar\omega_0$. and we also include data from literature [18, 42] (light blue spheres) that follow the same $A^*_{\text{e-ph}}(\hbar\omega_0)$ trend. To get an insight into the possible implications of data in Figure 6.6b, it is convenient to evaluate $A_{\text{e-ph}}$ from $A^*_{\text{e-ph}}$ using Equation 6.4. A rough estimate of $A_{\text{e-ph}}$ can be obtained using $n \approx 2\times10^{22}$ cm^{-3}, $a \approx 4$ Å, and $t_p \approx 0.6$ eV[2] and a typical value of $A^*_{\text{e-ph}}$ from Figure 6.6b ($\approx 1\times10^{-20}\,\Omega$ m s). It turns out that $A_{\text{e-ph}} \approx 7$. In Figure 6.6b (right axis) we show the $A_{\text{e-ph}}$ values (empty circles) calculated using the actual n, the mean cell parameter $a = \sqrt[3]{V_{\text{uc}}}$ (V_{uc} is the measured unit cell volume) and the experimental $A^*_{\text{e-ph}}$ values of all samples. These data provide a transparent view of the variations of the strength of the $e-ph$ coupling and its dependence on the phonon frequency. Within the polaronic framework, $A_{\text{e-ph}}$ is proportional to the effective mass of phonon-dressed electrons and the data in Figure 6.6b indicate that it becomes larger when phonons harden.

[2] We use here the DFT calculated hopping integral for electrons (not polarons) in SVO [214]

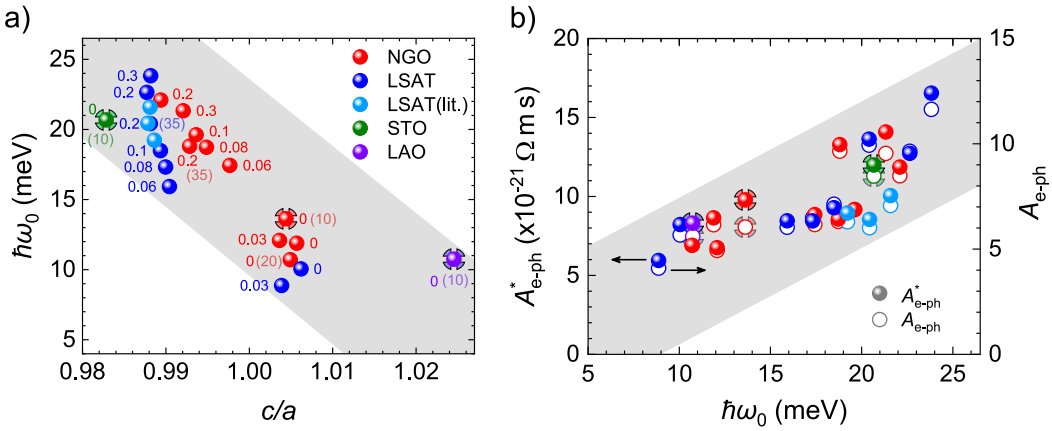

FIGURE 6.6: a) Dependence of the phonon energy ($\hbar\omega_0$) extracted from $\rho(T)$ using the polaronic model (Equation 6.3) of SVO films as a function of their tetragonal cell distortion (c/a). Films were grown on NGO (red spheres), LSAT (blue), STO (green) and LAO (violet), at different $P(Ar)$ (as indicated by the labels; units are mbar). All films are 70 nm, except some few as indicated by the additional label in parenthesis. b) Left axis (full spheres): Dependence of $A^*_{\text{e-ph}}$ on the phonon energy ($\hbar\omega_0$). Right axis (empty circles): Electron-phonon coupling parameter $A_{\text{e-ph}}$ calculated from the experimental $A^*_{\text{e-ph}}$ as described in the text (Equation 6.4). In (a,b) we also include (light blue spheres) the corresponding data points extracted from reported resistivity data of SVO films deposited on LSAT by h-MBE, by Zhang et al. (20 and 45 nm thick) [18] and by Moyer et al. (50 nm thick) [42]. Errors bars for fit-extracted ω_0 and $A^*_{\text{e-ph}}$ in (a,b) are smaller than the symbol size (see Appendix Tables E.1-E.2).

6.2.3 Temperature and magnetic field dependent magnetoresistance

In Figure 6.7a, we display the transverse magnetoresistance $MR(H) = [R(H) - R(H=0)]/R(H=0)$ of a representative SVO film (70 nm; NGO substrate; $P(Ar) = 0.2$ mbar), recorded at various temperatures. The resistance $R(H,T)$ is recorded with the magnetic field $\boldsymbol{H}$ perpendicular to the film plane and thus the current is transverse to $\boldsymbol{H}$. It can be observed that MR is positive, parabolic on $\boldsymbol{H}$ and rather small (< 2 % at 5 K) and decreases with increasing temperature. MR in a conventional metal is given by $MR \approx (\omega_c\tau)^2 = (\mu\mu_0 H)^2$, where ω_c and τ are the cyclotron frequency and scattering time respectively, and μ and μ_0 are the mobility and the vacuum permeability, respectively. Therefore, a fit of the parabolic $MR(H)$ dependence observed in Figure 6.7a allows to determine the carrier mobility. The mobility extracted from the fits is about $\mu \approx 30\,\text{cm}^2\text{V}^{-1}\text{s}^{-1}$ at 300 K and clearly increasing up to $\approx 160\,\text{cm}^2\text{V}^{-1}\text{s}^{-1}$ at 5 K (inset in Figure 6.7a).

This increase of mobility values upon cooling is consistent with that observed by Hall measurements (included also in inset in Figure 6.7a), although μ values are somewhat smaller in the latter, as often observed [215].

On the other hand, as stated by the Kohler's rule [216], $MR(H)$ data recorded at different temperatures should be a unique function $F(x)$, with $x = [\mu_0 H / R(H=0)]$. This scaling is shown in Figure 6.7b were it can be appreciated that data recorded at all temperatures collapse onto $F(x)$. The Kohler's rule is expected to hold irrespectively on the carrier nature (e.g. correlated electrons or polarons) and scattering mechanism [217].
Here it is relevant to emphasize that, in a non-magnetic system, MR is non-zero only if different carriers participate in the transport, and this has to happen if the FS is constituted by interpenetrated cylinders as in the present case.

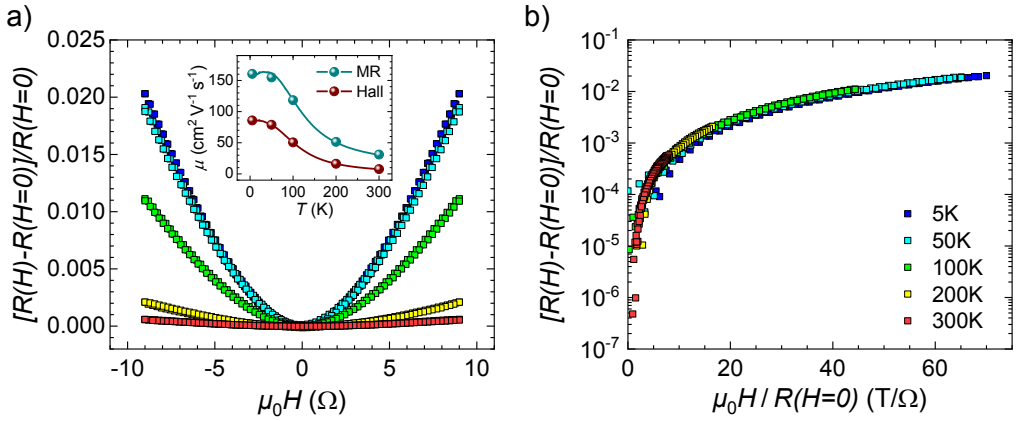

FIGURE 6.7: a) Magnetoresistance $MR = [R(H) - R(H=0)]/R(H)$ of SVO film (70 nm thick; deposited on NGO substrate; $P(Ar) = 0.2$ mbar) recorded with magnetic field perpendicular to the film surface, at various temperatures (5, 50, 100, 200 and 300 K). Data display a clear parabolic dependence $MR \approx H^2$. Inset: Carrier mobility extracted from Hall effect and magnetoresistance measurements as indicated. b) Kohler plot of $MR(H)$ measured at 5, 50, 100, 200 and 300 K, illustrating the expected collapsing.

Indeed, first principles calculations (DFT) of the electronic structure of bulk SVO clearly indicate that the Fermi surface has a multiband character and is dominated by the d_{xy}, d_{xz} and d_{yz} orbitals, although a non-vanishing contribution $\approx$ 20 % (in terms of the density of states) of the oxygen $2p$ states is apparent. Each of these three orbitals forms originally a cylinder along a perpendicular direction

(Figure 6.8), e.g. d_{xy} orbitals correspond to the cylinder along the $\boldsymbol{k}_z$ direction. Calculations were performed for bulk SVO, using the cell parameters of tensely and compressively strained (10 nm) SVO films. They indicate that the fine details of the covalent mixing are somehow modified, but the main features are fully preserved. Combination of three orbitals and the hybridization between the three FS sheets results in the obtained picture, where the outer sheet has a quasi-2D character and different carriers contribute to them, which can account for the observed magnetoresistance.

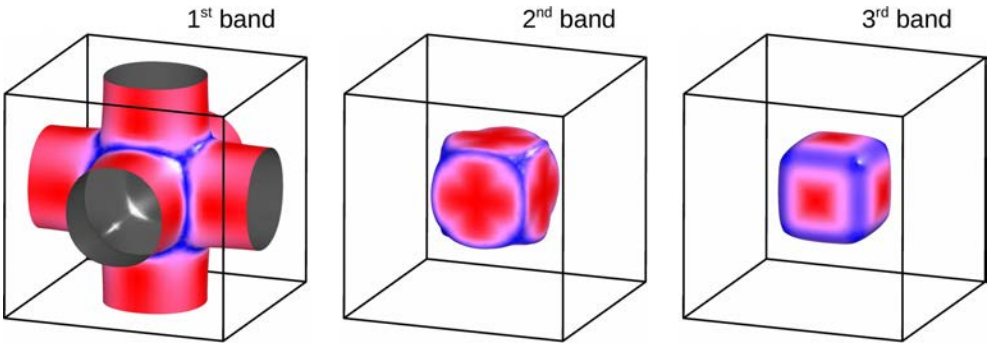

FIGURE 6.8: Fermi surface of cubic SVO determined from first principles. Three sheets of the Fermi surface are shown. The aspect ratio of the quasi-cylindrical 1st band is 1:2.1.

6.2.4 Seebeck coefficient

In Figure 6.9, we display the temperature dependence of the Seebeck coefficient $S(T)$ of an illustrative SVO film (70 nm; LSAT; $P(Ar) = 0.03$ mbar; similar data obtained for other samples are shown in methodology chapter Section 2.3.2).
$S(T)$ is negative and increases linearly (in modulus) when increasing temperature, as expected for band transport of electron carriers in which $S(T)$ is given by [197]:

$$S(T) = \frac{-\pi^2 k_B^2}{3e} T \left[\frac{g(E)}{n} + \frac{\partial}{\partial E} \ln[\tau(E)] \right]_{E=E_F} \tag{6.5}$$

where $g(E)$ is the density of states, n the carrier density and E_F the Fermi energy. $\tau(E)$ is an energy dependent scattering time, which in general can be written as $\tau \approx E^{\alpha}$ where α is related to the scattering mechanism. Within the simplest parabolic band approximation, for $\tau \approx E^{-1}$ ($\alpha = -1$), as deduced from optical measurements

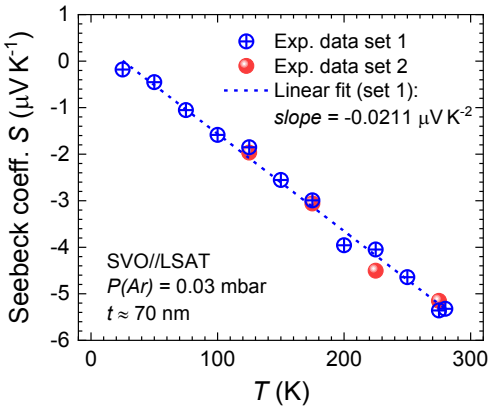

FIGURE 6.9: Temperature dependence of the Seebeck coefficient S measured on a SVO film (70 nm thick; deposited on LSAT). Open blue symbols (data set 1) are data measured when ramping the temperature. Solid red symbols (data set 2) are data determined in a different temperature run, by setting the temperature before measuring the Seebeck voltage.

by Makino et al. [123], $S(T)$ reduces to:

$$S(T) = \frac{-\pi^2 k_B^2}{6e} \frac{T}{E_F} \tag{6.6}$$

The slope $dS(T)/dT$ allows to extract E_F and, using the carrier density n deduced from Hall measurements ($n = 2.13 \times 10^{22}\,cm^{-3}$), the transport effective mass m^* can be determined. From Figure 6.9, $dS(T)/dT = -0.0211\,\mu V\,K^{-2}$ and using Equation 6.6 we obtain $E_F = 0.58\,eV$ and $m^* \approx 4.8 m_e$ (m_e is the free electron mass). ARPES measurements indicate a Fermi energy at about 0.5 eV [218] which is in excellent agreement with our Seebeck data. Therefore, we conclude that transport in SVO is ruled by carriers having a large effective mass. Within the scope of the Brinkman-Rice model [219], $m^* \approx 4.8 m_e$ would indicate that the system is close to the metal-insulator transition. More elaborate ab-initio calculations for bulk SVO including only electronic correlation effects within dynamical mean field theory also find a significant mass enhancement [220–222]. This scenario has been proposed to account for the observation of a metal-insulator transition in ultrathin SVO films [116, 118, 140] and in irradiated SVO films [223]. However, as we argue in the following, the mass enhancement can also be contributed by $e-ph$ coupling, as the polaronic fits suggest.

6.3 Discussion

We have first shown that the temperature-dependent $\rho(T)$ data of SVO films can be roughly described either by a quadratic T^2 dependence, that we recall is commonly taken as a signature of $e-e$ scattering in correlated electronic systems, or by a polaronic model involving phonon-dressed electrons. However, we have demonstrated that the quality of fits, performed in a wide temperature range (5-300 K), is significantly improved using a polaronic model. In the following, we carefully revise these findings.

6.3.1 The quadratic temperature dependence of the resistivity

The quadratic temperature dependence of $\rho(T)$ in metals is a common observation [224]. The $e-e$ scattering rate is given by $1/\tau = B_{ee}(k_B T)^2/(\hbar E_F)$, where B_{ee} is a dimensionless constant of order unity [197]. The electrical resistivity is given by $\rho = (m/ne^2)(1/\tau)$ and, if only the scattering time is temperature dependent, it follows that $\rho(T) \approx 1/\tau \approx T^2$. Accordingly, $\rho(T) \approx T^2$ can be viewed as a signature of FL.

For a spherical Fermi surface $E_F = (\hbar^2/2m)(3\pi^2 n)^{2/3}$ and therefore, $\rho(T) \approx (2m^2 k_B^2)/(e^2\hbar^3(3\pi^2)^{2/3}n^{5/3})T^2 \approx n^{-5/3}T^2$ [225]. Mobility data in Figure 6.4a,b as well as $\rho(T)$ in Figure 6.2d-f are roughly consistent with this T^2 dependence. However, the $A(n)$ data shown in Figure 6.3a is well described by $A \approx n^{-1}$ over a large range of carrier concentration, rather than $A \approx n^{-5/3}$ (dashed lines in Figure 6.3b). In the simplest view, $A \approx n^{-1}$ would imply that $1/\tau$ (and therefore $1/\mu$) would not depend on carrier density, which is at odds with expectations for a FL model. As recently emphasized [193, 206], this discrepancy holds for a large number of oxides at the verge of a metal-insulator transition. However, it is worth noticing here, that the expected $A \approx n^{-5/3}$ dependence for a FL had been observed in other systems, such as in the semimetallic TiS_2 [226]. It follows that the observation of $\rho(T) \approx T^2$ cannot be assigned univocally to $e-e$ scattering in a FL description, because data in Figure 6.3a would imply that scattering is independent on carrier density.

The magnitude of the A coefficient in $\rho(T) \approx AT^2$ signals another discrepancy. As shown in Figure 6.3a, for our SVO films we obtained $A \approx 1\times10^{-10} - 1\times10^{-9}\,\Omega\,\mathrm{cm\,K^{-2}}$ values, which are similar to those reported by Inoue et al. ($4.2\times10^{-10}\,\Omega\,\mathrm{cm\,K^{-2}}$) [124]. Within the $e-e$ scattering model, as introduced above, $A \equiv A_{ee}$ is given by:

$$A_{ee} = \frac{2m^2 k_B^2}{e^2\hbar^3(3\pi^2)^{2/3}n^{5/3}} \tag{6.7}$$

Using as typical parameters ($n = 2.13 \times 10^{22}\,\mathrm{cm}^{-3}$ and $m^*_{ee} \approx 4$) one gets: $A \approx 1 \times 10^{-11}\,\Omega\,\mathrm{cm\,K}^{-2}$, which is almost two orders of magnitude smaller than the measured values. A two orders of magnitude discrepancy would have also emerged if Inoue et al. [124] had compared their experimental values to predictions given by Equation 6.7.

Summarizing, the observation that $A \approx n^{-1}$, suggesting that μ does not depend on n, and the severe discrepancy of measured and expected A values questions the $e-e$ scattering in a FL scenario as the origin of the roughly quadratic temperature dependence of resistivity. Next, we investigate the role of the $e-ph$ scattering.

6.3.2 Electron-phonon scattering in cylindrical Fermi surfaces

We first notice that the temperature dependence of $1/\tau$ is primarily due to scattering events with phonons. At high temperature, all phonon branches are equally populated and the phonon number increases linearly with T, therefore $1/\tau \approx T$ and $\rho(T) \approx T$, as frequently observed.
However, at lower temperature the different phonon occupation of different phonon branches leads to a more complex situation, which becomes particularly remarkable for anisotropic Fermi surfaces. Indeed, it was long ago recognized that $e-ph$ scattering in metals with cylindrical Fermi surfaces (e.g. Bi [196]) leads to $1/\tau \approx \rho(T) \approx T^2$ in some temperature range. As recently emphasized by Snyder et al., the topological 2D feature of the FS in some metallic oxides can be at the origin of $1/\tau \approx \rho(T) \approx T^2$ [227, 228]. Indeed, a cylindrical Fermi surface of SVO has been observed by ARPES [127, 218, 229, 230]. The recent observation of a similar T^2-dependent resistivity in Bi_2O_2Se oxyselenides, where the Fermi surface is an elongated ellipsoid [231], may point to a common origin.

According to Kukkonen [196], the electrical resistivity of metals with cylindrical Fermi surface display a genuine T^2 temperature dependence in a temperature region bounded by $T_p < T < T_k$. The temperature limits T_p and T_k are determined by the dimensions of the Fermi surface through the relation $T_p = 2\hbar v_S p_F / k_B$ and $T_k = 2\hbar v_S k_F / k_B$ where p_F (respectively k_F) is the diameter (respectively the height) of the cylindrical Fermi surface and v_S the sound velocity [196, 232]. In the SVO case, by approximating the FS to a cylinder, using $p_F \approx 0.5(\pi/a)$ and $k_F \approx (\pi/a)$ as deduced from ARPES experiments [218], which is in excellent agreement with our calculations (Figure 6.8), and the experimental transverse sound velocity $v_S \approx 4000\,\mathrm{m\,s}^{-1}$ [233], we get $T_p \approx 239\,\mathrm{K}$ and $T_k \approx 478\,\mathrm{K}$. We notice that the estimated low-temperature limit ($\approx 239\,\mathrm{K}$) for $\rho \approx T^2$, is somewhat higher than the low temperature experimental bound for the quadratic T^2 term ($\approx$ 180-200 K), below which a clear departure from T^2 is observed (Figure 6.5a,c). To what extent

this discrepancy is related to limitations of the anisotropic scattering model of Kukkonen [196] (such as the assumption of a single band carriers and absence of phonon drag), or is linked to the present approximation of a (interpenetrated) cylindrical Fermi surface for SVO, remains to be solved.

Therefore, one could tentatively conclude that the $\rho(T) \approx T^2$ dependence may result from the $e-ph$ scattering in the quasi-2D cylindrical Fermi surface characteristic of $3d$-t_{2g} metal oxides. Seebeck and magnetoresistance data would be also compatible with this picture.

6.3.3 Polaronic transport

Landau first suggested the possibility for lattice distortions to trap electrons by means of an intrinsic modification of the lattice phonon-field induced by the electron itself. The resulting $e-ph$ quasiparticle (the *polaron*) is a coupled $e-ph$ system in which the polarization generated by the lattice distortions acts back on the electron, renormalizing its properties, for instance the effective mass.
At low temperature, (small) polarons may display a coherent band-like transport, where the phonon-mediated scattering rules their mobility [234, 235]. As the phonon number decreases with temperature, the resistivity decreases upon lowering temperature and small polarons behave as heavy particles with effective mass $m^*_{\text{e-ph}}$. In this regime, $\rho(T)$ is given by Equation 6.1-6.4. As shown, data can be well reproduced by these expressions. As emphasized by Van der Marel et al. [204], this $\rho(T)$ dependence is expected to hold for small polarons; but on the other hand, Devreese et al. [236] also signaled that, even in one of the most studied polaronic materials (Nb:$SrTiO_3$), the distinction between small and large polarons is not that sharp. We will not attempt to dig here into this distinction.

Instead, we note that in recent years, the small polaron scenario has been used to describe $\rho(T)$ of heavily doped manganites [209, 237] or doped Mott insulators $LaTiO_3$ [211, 212] and $NdTiO_3$ [212]. We focus now our attention on the relevant phonon energies ($\hbar\omega_0 \approx 5-25\,\text{meV} \approx 60-290\,\text{K}$) extracted from the fits of $\rho(T)$ of our films (Figure 6.5) and the observed variation with the tetragonal distortion c/a (Figure 6.6). Preliminary calculations in SVO (summarized in Appendix E.3) allow to identify phonons in this energy range that soften when increasing c/a as observed experimentally (Fig. 6.6a). Phonons within the same energy range were extracted from $\rho(T)$ data in manganites [191, 209, 238], $LaTiO_3$ [211], and $Ba_{1-x}K_xBiO_3$ [239, 240]. Therefore, we propose that similar phonons may govern the dynamics of *dressed* electrons in SVO films.

The $e-ph$ coupling implies an enhanced effective mass ($m^*_{\text{e-ph}}$). Therefore, following Zhao et al. [209], we identify in Equation 6.2, $A_{\text{e-ph}} \equiv \lambda$ where $\lambda = [(m^*_{\text{e-ph}}/m^*_{\text{band}}) - 1]$ [241, 242], and we use λ as a measure of $e-ph$ coupling. It follows from data in Figure 6.6b, that $5 < \lambda < 10$, and accordingly, $6 < m^*_{\text{e-ph}}/m^*_{\text{band}} < 11$, depending on the tetragonality ratio c/a of the SVO films. Therefore, there is a dramatic enhancement of the electron effective mass via $e-ph$ dressing. The large $m^*_{\text{e-ph}}/m^*_{\text{band}}$ effective mass derived from the polaronic fit is consistent with the large effective mass derived above from Seebeck data. Moreover, we notice that similar values have been reported in nickelate thin films ($m^*/m^*_{\text{band}} \approx 6-7$) [243].

Search for direct evidences of $e-ph$ coupling in cuprates was of paramount relevance in the quest for a microscopic mechanism for $e-e$ pairing. Lanzara et al. [241] used angle-resolved photoemission spectroscopy (ARPES) to show that, in some cuprated, electrons experience an abrupt change of its velocity and scattering rate at some well-defined energy (50-80 meV) that was interpreted as a fingerprint of $e-ph$ coupling. Interestingly, recent ARPES data in SVO [218, 229], showed similar features at $\approx$ 60 meV, that were also attributed to the coupling of electrons with these phonons. In principle, this conclusion would be in agreement with the polaronic model discussed here, although the significant difference on the energy of most relevant phonons for *dc* conductivity and ARPES remains to be elucidated.

Finally, we mention that we have reported ellipsometric measurements to deduce the effective mass of carriers in SVO films (Chapter 3), which is in agreement with earlier reports [123], and obtained $m^*/m_e \approx 3-5$ (depending on the substrates and growth conditions). Ellipsometric measurements have also been performed in some of the films of this chapter, to determine the plasma frequency and consistent $m^*/m_e \approx 4.1$ values have been obtained (shown in Appendix E.4). It is also enlightening to notice that m^*/m^*_{band} values extracted from specific heat coefficient (γ) and magnetic susceptibility (χ) data of ceramic SVO samples differ by about a factor $R_W \approx 1.6$ (Wilson ratio), which also suggests that $e-ph$ coupling to be relevant [124].
To gain some perspective, it may be useful to point out that it has been recently shown that bosonic modes largely contribute to effective mass renormalization in $SrRuO_3$ oxide. $SrRuO_3$ is a metallic and ferromagnetic (< 150 K) $4d$ system (Ru^{4+}: d^4: ($t_{2g}^{3\uparrow}$, $t_{2g}^{1\downarrow}$)) that had been commonly assumed to be a strongly correlated metallic system [244, 245]. However, detailed calculations [246] have lately suggested correlations to be weaker than expected and ARPES data have provided strong evidence of $e-ph$ coupling [200]. The fact that in both $SrVO_3$ and $SrRuO_3$, the itinerant electrons ($3d$-t_{2g}^1 and $4d$-($t_{2g}^{3\uparrow}$, $t_{2g}^{1\downarrow}$), respectively) reside in a quasi-degenerate

t_{2g} band may be instrumental on the enhanced relevance of $e-ph$ coupling.

We end by noticing that it has been recently reported that, beyond the original Kadowaki-Woods plot, there is a kind of universal link between the Fermi energy and the prefactor A of the T^2 resistivity, which persists across various Fermi liquids [194], that remain to be explained. Our data also nicely fall within this scaling (see Appendix E.5).

6.4 Conclusions

In summary, we have analysed transport properties of epitaxial $SrVO_3$ thin films, where V^{4+} ions have a single $3d^1$ electron in a t_{2g} orbital triplet. First, we have shown that $\rho(T)$ displays roughly a T^2 dependence ($\rho(T) \approx \rho_0 + AT^2$) which is in agreement with earlier findings. However, the fit quality is unsatisfactory; the observed dependence of $A(n)$ is not that expected in a Fermi liquid and the magnitude of the A coefficient differs by two orders of magnitude from expectations for $e-e$ scattering. This disconformity appears not only in SVO (intrinsic metal) but, as earlier pointed out, is shared by other conducting oxides (mainly doped semiconductors). We emphasize that this discrepancy is common to oxides having a low occupation of narrow $3d$-t_{2g} bands.

Two different scenarios are considered to account for the available experimental data. We first note that the Fermi surface of these $3d^x$ ($x \leq 1$) oxides is mostly formed by three interpenetrated cylinders oriented along the three principal axis and thus the Fermi surface has a 2D character. As argued, the extreme anisotropy of the Fermi surface has a profound impact on the temperature dependence of the electron-phonon scattering and a $\rho(T) \approx T^2$ dependence was predicted in some temperature range, which is roughly in agreement with observations in SVO. For a $3d^1$ TMO, the FS includes up to three sheets, implying multiband conduction, which is consistent with the observed magnetoresistance.
Secondly, a polaronic (or vibronic) scenario has been explored. It has been shown that, assuming a single phonon mode ($\hbar\omega_0$) to be relevant for the $e-ph$ coupling, $\rho(T)$ can be excellently fitted in all temperature range (5-300 K). It is observed that the frequency of the relevant phonon can be tuned by the tetragonal distortion in SVO imposed by epitaxial strain and growth conditions. Moreover, it is found that $\hbar\omega_0$ and the $e-ph$ coupling strength (λ) both systematically increase under a tensile deformation of the lattice ($c/a < 1$) and subsequently, the polaron effective mass, also increases.
In summary, the results indicate that $e-e$ scattering in a FL alone does not account the observed temperature dependence of resistivity, mobility and magnetoresistance in these transition metal oxides. Instead, other ingredients need to

be invoked. The cylindrical 2D-like nature of the Fermi surface of SVO and the $e-ph$ coupling giving rise to a polaronic transport, appear to be necessary ingredients to account for available transport, calorimetric and spectroscopic data. SVO and presumably other $3d^x$ ($x \leq 1$) oxides may share a similar $e-ph$ coupling that has remained largely unexplored. These findings may have some practical consequences. To mention one, in the search for transparent conducting oxides, where focus was on correlated systems, the present findings suggest that enhanced $e-ph$ coupling could be an efficient tool to bring the plasma frequency to the infrared region.

Chapter 7

Optical plasmon excitation in transparent conducting $SrVO_3$ and $SrNbO_3$ thin films

In this chapter, we first address the growth of $SrNbO_3$. In a second time, we explore the optical properties of $SrNbO_3$ and $SrVO_3$ films. In particular, we study the nature of the plasmon excitation at the plasma frequency.

7.1 Introduction

Oxide-based photocatalysts for water splitting have been extensively investigated towards efficient exploitation of sunlight for H_2 production. Sunlight photoabsorption in a semiconductor creates electron-hole (e-h) pairs that can migrate to the surface of the material, decomposing H_2O into H_2 and O_2. Whereas a key advantage of oxides is their inherent chemical robustness, a major drawback is that the bandgap of most oxides, most notably the so-called band-insulators (such as TiO_2 or $BaTiO_3$), is too large to absorb light. Bandgap engineering by chemical doping either at cationic or anionic sites of the structure allows increasing the absorption of visible photons, but typically at the cost of enhancing the e-h recombination rate and thus challenging efficiency. Alternatively, a possible way around this difficulty is to use light absorption in some metals, such as Au or Ag, which can excite plasmons that can be used to inject electrons in the conduction band of an embedded semiconductor and, therefore, can be used for hydrogen evolution reaction. Whereas the tandem system (metal-semiconductor) photocatalyst has shown promises of large efficiency, the required noble metal nanostructures challenges its cost-efficiency.

Recently, it has been reported that strontium-deficient powders of $Sr_{1-x}NbO_3$ are metallic and display a wonderful red color, which was taken as a fingerprint of

an optical absorption process. It has also been shown that these materials are able to sustain photo-oxidation without degradation and promote the oxidation of methylene blue and the oxidation and reduction of water [247, 248]. These results were intriguing in a number of aspects. For instance, what is the nature of the relatively narrow photo-absorption process, developing at about 1.9 eV, allegedly related to the well-defined color? Additionally, on basic grounds, it could be expected that the free carriers of a metallic system would screen any electric field thus precluding e-h separation, which is not in agreement with experimental observations. Addressing the first question, first-principles calculations showed that about 1.8 eV above the conduction band (CB) of $Sr_{1-x}NbO_3$ there is a large density of empty states of Nb-4d parentage (labelled band B_1). It was then proposed that the relevant absorption in the visible occurs between the CB and B_1 [247, 249, 250].

In this respect, Tauc plots of optical absorption in epitaxial SNO thin films [31] indicated an indirect band gap as well as the existence of a minimum at around 2 eV which both suggest an overlapping of absorption bands of different origin in the visible region. Along these lines, Wan et al. [46] reported a thorough investigation of the transport and optical properties of $SrNbO_{3+\delta}$ films grown on (001) $LaAlO_3$ (a_{LAO} = 3.791 Å; mismatch f_{LAO} = -5.77 %) single crystalline substrates, under different oxygen pressures. On the basis of the observed metallic character and the large carrier density and mobility of films grown at low enough oxygen pressures, Wan et al. [46] argued that any electric field inside the SNO film should vanish, thus leaving open the ultimate reason for the persistence of e-h pairs, and questioned the assignment of the optical absorption band at 1.8 eV to an interband CB-B_1 transition. Instead, from optical characterization (UV-visible-NIR transmission coefficients and spectroscopic ellipsometry data) Wan et al. inferred the existence of an indirect gap of about 4.1 eV, while from reflectance spectra they extracted a plasma frequency of $\hbar\omega_p \approx 1.65$ eV (750 nm). The permittivity $\varepsilon(\omega) = \varepsilon_1(\omega) + i\varepsilon_2(\omega)$, the complex refractive index (n, κ) and the loss function $LF(\omega) = -\mathrm{Im}[\varepsilon^{-1}(\omega)] = [\varepsilon_2(\omega)/(\varepsilon_1^2(\omega) + \varepsilon_2^2(\omega)]$ were calculated from ellipsometric data. It was found that the extinction coefficient $\kappa(\lambda)$ increases above 4.1 eV (indicating the bandgap), remains relatively flat in the 2-4.1 eV range and increases again below 2 eV where the Drude peak develops. Of the highest relevance for the forthcoming discussion is that the losses displayed a well-defined peak at about 1.8 eV (688 nm), and that was taken as a fingerprint of a plasmonic resonance in the SNO film. Wan et al. further elaborated that these intraband plasmon excitations are responsible for the catalytic activity [251] rather than the interband CB-B_1 transition picture. Nonetheless, the nature of these plasmons remains to be elucidated. Indeed, Wan et al. argued that they should be surface rather than bulk plasmons [46]. However, as also noted by these authors [252] conventional surface plasmons in metallic films typically require phase-matching mechanism

to be excited (such as structuring arrays or Otto and Kretschmann configurations).

From a broader perspective, it is important to explore the role of plasmon excitations in other transition metal oxides. Along these lines, a case of interest is that of $SrVO_3$ (SVO), which is also metallic and has a similar cubic perovskite structure. At variance with SNO, SVO has a narrower conduction band (due to the $3d$ parentage of electrons in the conduction band), which increases the effective mass trough electronic correlations [253] bringing the plasma resonance to lower energy than in SNO. In fact, it has been shown that in SVO films the plasma frequency deduced from optical transmission and ellipsometric measurements is below the visible and thus SVO is fully transparent to visible light (see Chapters 3-4 and [18, 125] for instance).

In this chapter, we aim at elucidating the nature of the optical excitations observed in isoelectronic SNO and SVO films. As recognized by Asmara et al. [252] the optical response of SNO films, including the nature of the plasmon-like excitations, can be largely affected by growth-associated defects. Consequently, we first address the growth optimization of SNO films and subsequently we discuss and compare the plasmon-like resonances of SNO and SVO films. It will be shown that suitably polarized light indeed can excite bulk plasmons in unpatterned thin films, without auxiliary $\boldsymbol{k}$-matching mechanism. Opportunities for engineering plasmonic resonance in thin films will be highlighted.

7.2 Determination of optimal growth conditions of $SrNbO_3$ films

7.2.1 Sample preparation

Epitaxial $SrNbO_3$ (SNO) films have been grown on single crystalline (pseudo)cubic (001)-oriented LSAT and $GdScO_3$ (GSO) substrates; with cell parameters $a_{LSAT} = 3.868$ Å, and $a_{GSO} = 3.967$ Å, respectively. It results a lattice mismatch $f = (a_{sub} - a_{SNO})/a_{sub}$ with bulk cubic SNO ($a_{SNO} = 4.023$ Å) of $f_{LSAT} = -4.01$ % and $f_{GSO} = -1.41$ %, respectively. We have used pulsed laser deposition (PLD) as deposition technique, varying the growth argon pressure $P(Ar)$ within the 0-0.3 mbar range, where zero indicates the ultimate base pressure of the chamber ($\approx 10^{-6}$ mbar). SNO films properties are extremely sensitive to growth conditions. For comparison purposes, two series of films have been grown with two different PLD systems. Series B was grown at ICMAB-CSIC and series D at the Institute of Materials Science of the Technische Universität Darmstadt. Series B (resp. D) was grown using a laser fluence of about 2 J cm^{-1} (resp. 0.9 J cm^{-1}) and frequency of 5 Hz (resp. 4 Hz). Substrate temperature (i.e. 700°C) and target-substrate distance

(of 45 mm) were identical in both cases. Right after deposition and still at deposition temperature, the argon mass flow was turned off and the vacuum pump valve kept closed, while the valve was kept open in the series D. Finally, in series B, at each $P(Ar)$, pairs of films on LSAT and GSO were grown simultaneously to minimize spurious growth differences. At each $P(Ar)$, ad-hoc calibration was performed by X-ray reflectometry to determine the growth rate. This resulted in films thickness of around 70 nm. Once the optimal $P(Ar)$ (i.e. 0.08 mbar) was determined, the film thickness was varied from 18 nm to 140 nm by varying the number of laser pulses (series B films). Epitaxial $SrVO_3$ (SVO) films were grown by PLD at ICMAB. Details on growth conditions and characterization have been described in Chapter 4 and their properties will be evoked when appropriate.

7.2.2 Structural characterization and surface morphology

The X-ray diffraction symmetric $\theta-2\theta$ scans (Figure 7.1a,c,d) were used to confirm the (001) texture of all samples, the absence of spurious phases, and to evaluate the out-of-plane cell parameters (c) (Figure 7.2). It turns out that the c-axis parameters depend on the $P(Ar)$ used, expanding when reducing the pressure, and are slightly different due to substrate-induced epitaxial strain. For instance, at $P(Ar) = 0.08$ mbar, c(SNO//GSO) = 4.076 Å and c(SNO//LSAT) = 4.058 Å. The observed c-axis of SNO//GSO, at this pressure, is close to the value expected due to epitaxial strain and assuming a Poisson ratio $\nu = 0.31$ [249]. In contrast the c(SNO//LSAT) value is smaller than expected, indicating that the film is partially relaxed due to their larger structural mismatch. Films grown at lower pressure display expanded c-parameters ($\approx$ 4.12 Å), as commonly observed in oxygen deficient films [254] or with cation off-stoichiometry [30]. Consistently, the rocking curves width increases from a minimum value of $\Delta\omega = 0.05°$ at 0.08 mbar to 0.42° at the lowest pressure (Figure 7.1b).

Reciprocal space maps around asymmetric $(103)_{pc}$ reflections (Figure 7.3) were used to determine the in-plane cell parameters of the films and to assess the coherent growth of SNO//GSO and the relaxation of SNO//LSAT. Indeed, the sharpest diffraction spots are observed for films grown at $P(Ar) = 0.08$ mbar, which have in-plane cell parameters either coinciding with the substrate (SNO//GSO) or shifted towards bulk values (SNO//LSAT). All in all, structural data suggest that SNO films can be optimally grown at around $P(Ar) = 0.08$ mbar, both in series B and series D.

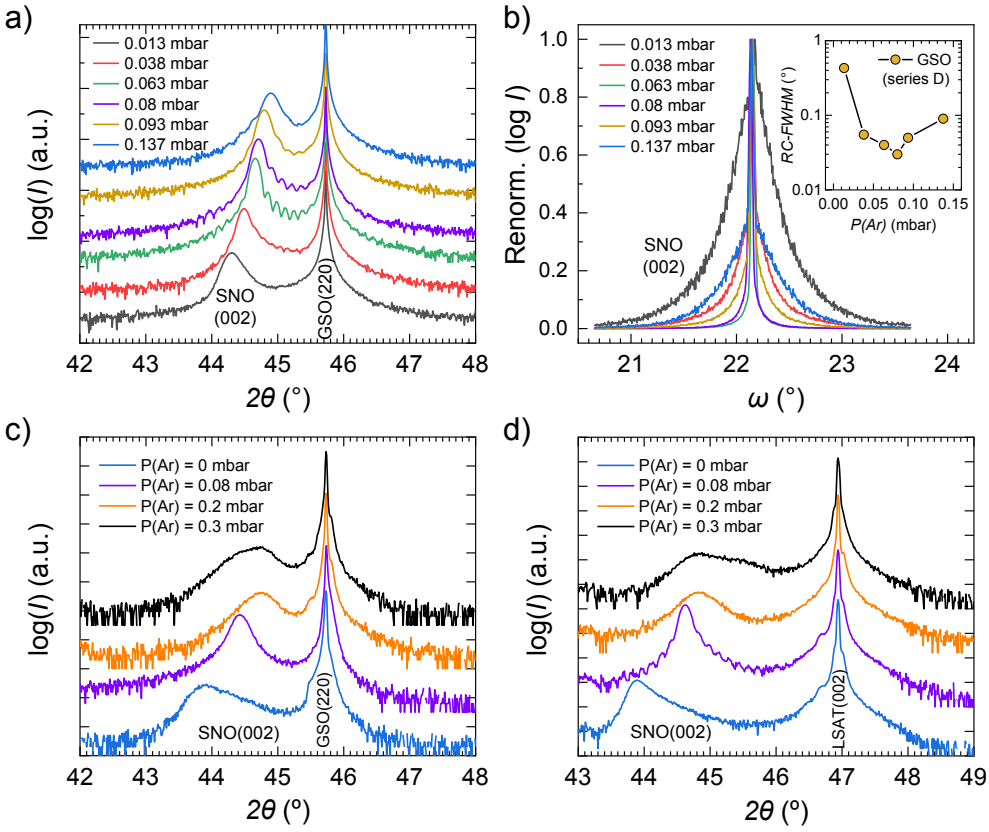

FIGURE 7.1: a) $\theta-2\theta$ scans of SNO//GSO of series D. b) Corresponding ω-scans ("rocking curves") of the same series of samples. c) $\theta-2\theta$ scans of SNO//GSO of series B. d) $\theta-2\theta$ scans of SNO//LSAT of series B. All in all, one can observe Laue fringes for the optimal argon pressure (i.e. $P(Ar) = 0.08$ mbar), and also narrowest rocking curves, for any series of films or substrate.

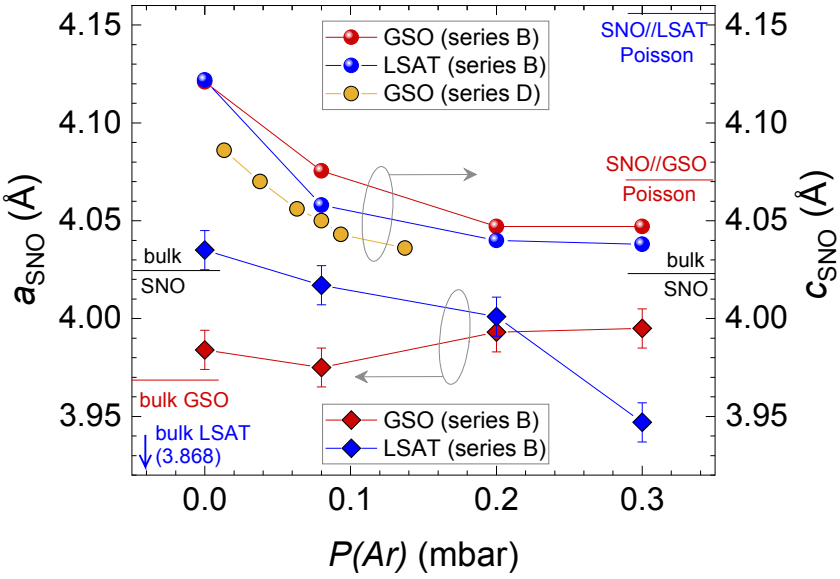

FIGURE 7.2: Summary of all (a, c) lattice constants of films of series B and D, deposited on GSO and LSAT substrates, as a function of $P(Ar)$.

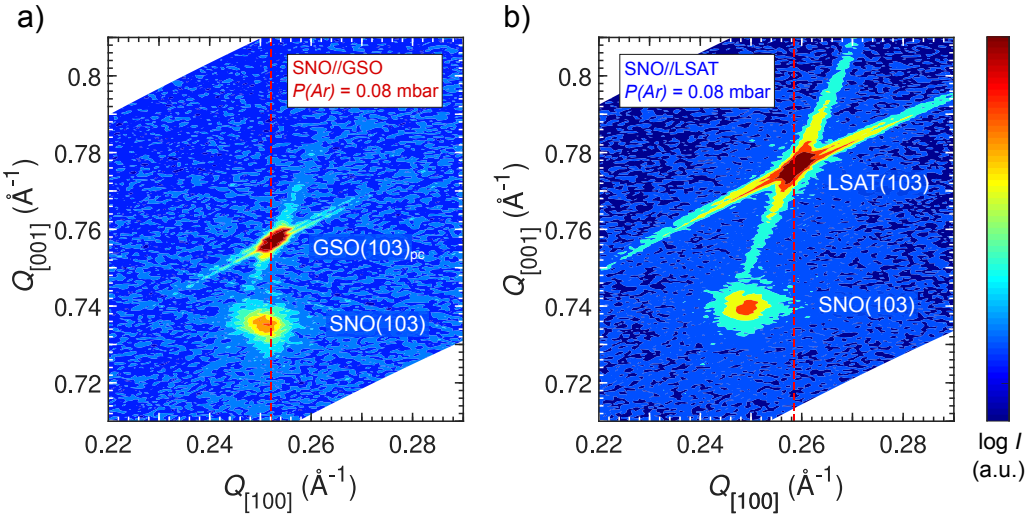

FIGURE 7.3: Reciprocal space maps around the (103) of two illustrative samples (of series B) deposited at optimal $P(Ar) = 0.08$ mbar, on GSO (left) and LSAT substrates (right). While SNO is nearly fully strained to the GSO substrate, it is highly relaxed on the LSAT substrate, as expected considering the higher lattice mismatch.

Atomic force microscopy images in Figure 7.4 show that the *rms* roughness is below one unit cell (u.c.) for the thinnest films (≈ 18 nm) increasing up to about 1.5 u.c. for the thickest ones (≈ 140 nm).

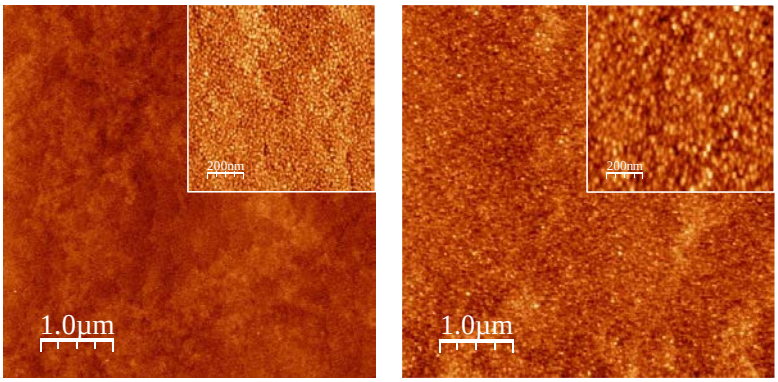

FIGURE 7.4: Atomic force microscopy images of the surface of two SNO//LSAT films (18 nm and 140 nm thick) deposited at optimal $P(Ar) = 0.08$ mbar.

7.2.3 Transport properties

In Figure 7.5a we show the temperature dependence of the electrical resistivity of SNO films (≈ 65 nm thick) grown at $P(Ar) = 0.08$ mbar on LSAT and GSO substrates (series B). Both films display a metallic character with a room temperature resistivity $\rho(300\,\text{K})$ of 80 µΩ cm and 70 µΩ cm, respectively. The smaller mismatch of SNO on GSO accounts for the higher conductivity of SNO films on GSO than on LSAT.

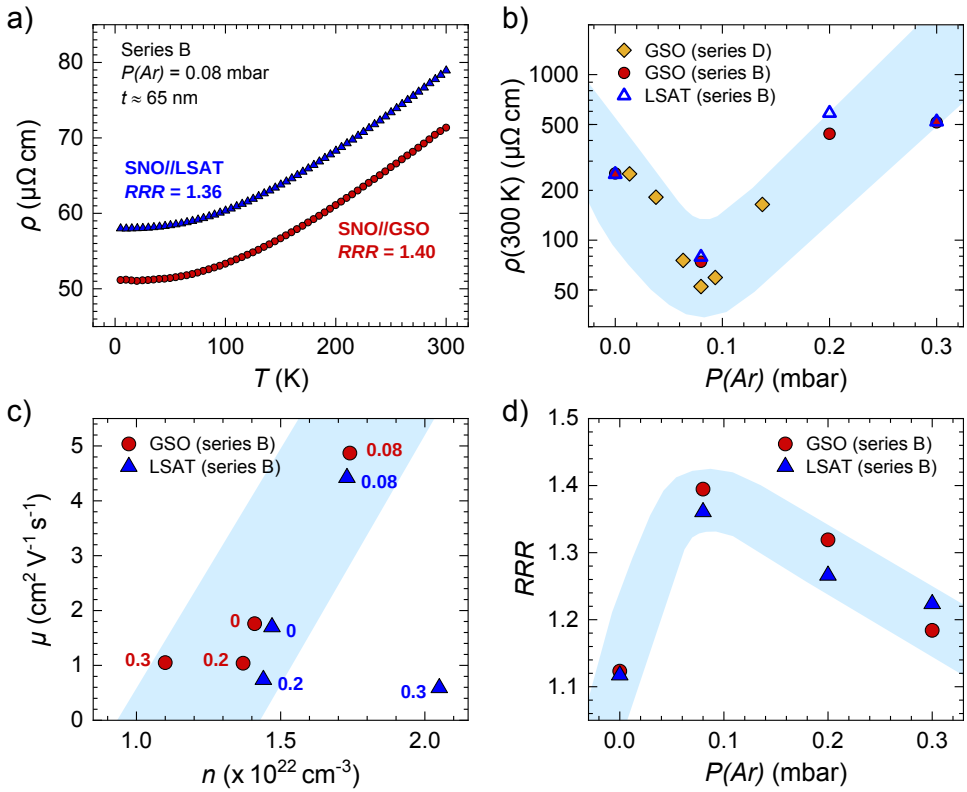

FIGURE 7.5: Transport properties of SNO films. a) Temperature-dependent metallic resistivity ρ in two illustrating films showing lowest RT-resistivity. b) Compilation of RT-resistivity $\rho(300\,K)$ of films of series B and D as a function of $P(Ar)$. c) Room-temperature carrier mobility μ vs carrier density n of films of series B. Labels indicate the growth $P(Ar)$, in mbar. d) Evolution of the residual resistivity ratio (RRR) as a function of $P(Ar)$.

The dependence of $\rho(300\,K)$ on the growth pressure, shown in Figure 7.5b, reflects the dramatic role of $P(Ar)$ on the conductivity of the films, that holds both for LSAT and GSO substrates. We include in Figure 7.5b data collected in films of series B and D to emphasize that an identical dependence of $\rho(300\,K)$ on $P(Ar)$ is observed in films of both series. It is observed that for any substrate, the minimal $\rho(300\,K)$ is obtained at $P(Ar) = 0.08$ mbar, and is slightly smaller in films of series D (50 μΩ cm) than in films of series B (70 μΩ cm), probably due to differences in fluence of the lasers. Observation of optimal properties for films grown at $P(Ar) = 0.08$ mbar is fully consistent with the structural data, namely the observation of sharp Laue fringes and narrowest rocking curves (Figure 7.1), obtained at this pressure. The residual resistivity ratio ($RRR = \rho(300\,K)/\rho(5\,K)$) of the films (Figure 7.5d), which is

primarily a fingerprint of defects density, and the corresponding carrier scattering, closely mimics the dependence $\rho(300\,\mathrm{K})$ on $P(Ar)$ (Figure 7.5b), and confirms the optimal pressure for SNO film growth. We notice that $\rho(300\,\mathrm{K})$ of our optimal films is smaller by more than an order of magnitude and have a larger RRR than films in Wan et al. [46] illustrating the higher quality of our films. Hall measurements indicate that optimal films also have the highest carrier density ($n \approx 1.7\times10^{22}\,\mathrm{cm}^{-3}$), which approaches the nominal one (1 e^-/uc, $n = 1.54\times10^{22}\,\mathrm{cm}^{-3}$) and the highest mobility $\mu \approx 5\,\mathrm{cm}^2\,\mathrm{V}^{-1}\,\mathrm{s}^{-1}$ (Figure 7.5c). It is worth recognizing in Figure 7.5c that the growth pressure rules carrier density in all films, grown simultaneously on different substrates, whereas μ and RRR are typically smaller on films grown on the substrate with the relatively larger mismatch (LSAT). It is found that when reducing the film thickness below 40-50 nm, the resistivity of all films increases significantly (see Figure 7.6).

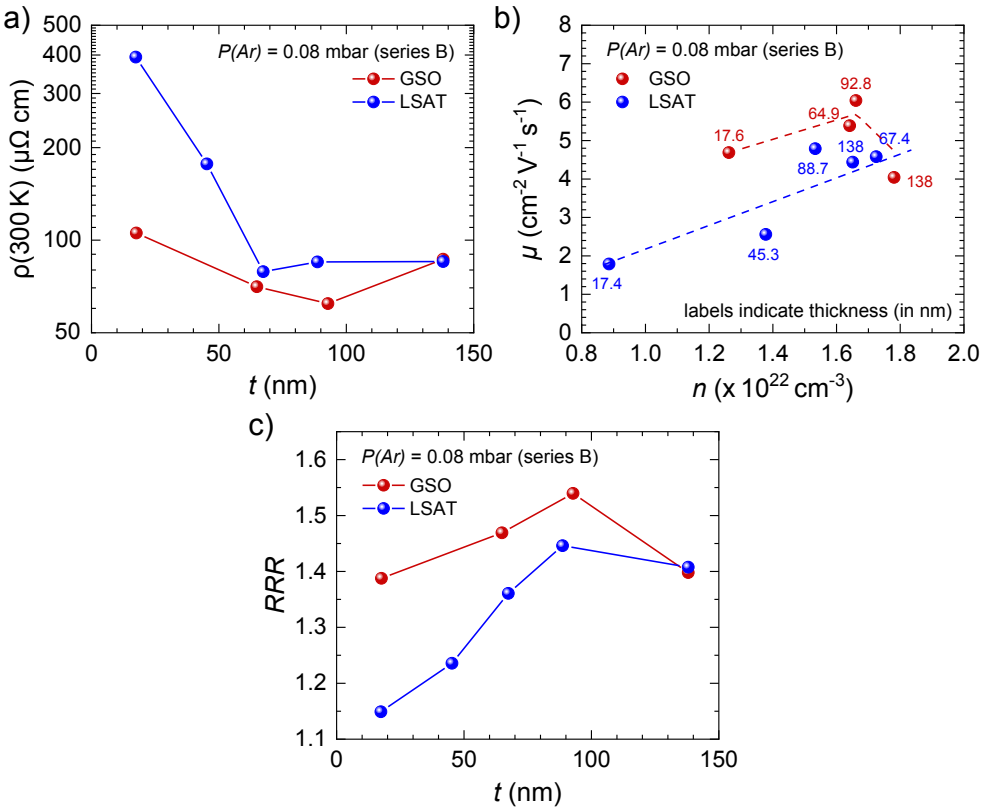

FIGURE 7.6: a) $\rho(300\,\mathrm{K})$ for various thicknesses of SNO films (series B), deposited on GSO and LSAT. b) Room-temperature carrier mobility μ vs carrier density n plot of the corresponding samples. c) Residual resistivity ratio ($RRR = \rho(300\,\mathrm{K})/\rho(5\,\mathrm{K})$) of the corresponding samples.

7.3 Optical transmittance

In Figure 7.7a, we show the optical transmittance (unpolarized light) $T(\lambda)$ of SNO//LSAT films of different thickness, grown at the optimal pressure ($P(Ar) = 0.08$ mbar). It can be appreciated that $T(\lambda)$ has a broad maximum at around 400-500 nm and a fast decay at $\lambda > 550$ nm which are in agreement with early reports [46]. As expected, the overall $T(\lambda)$ decreases when increasing thickness and the decay of $T(\lambda > 550\,\text{nm})$ becomes more apparent when increasing film thickness. This is consistent with previous results, which show an important absorption at $\lambda \approx 700$ nm, leaving a minimum in reflectance at $\lambda \approx 600$ nm [46].

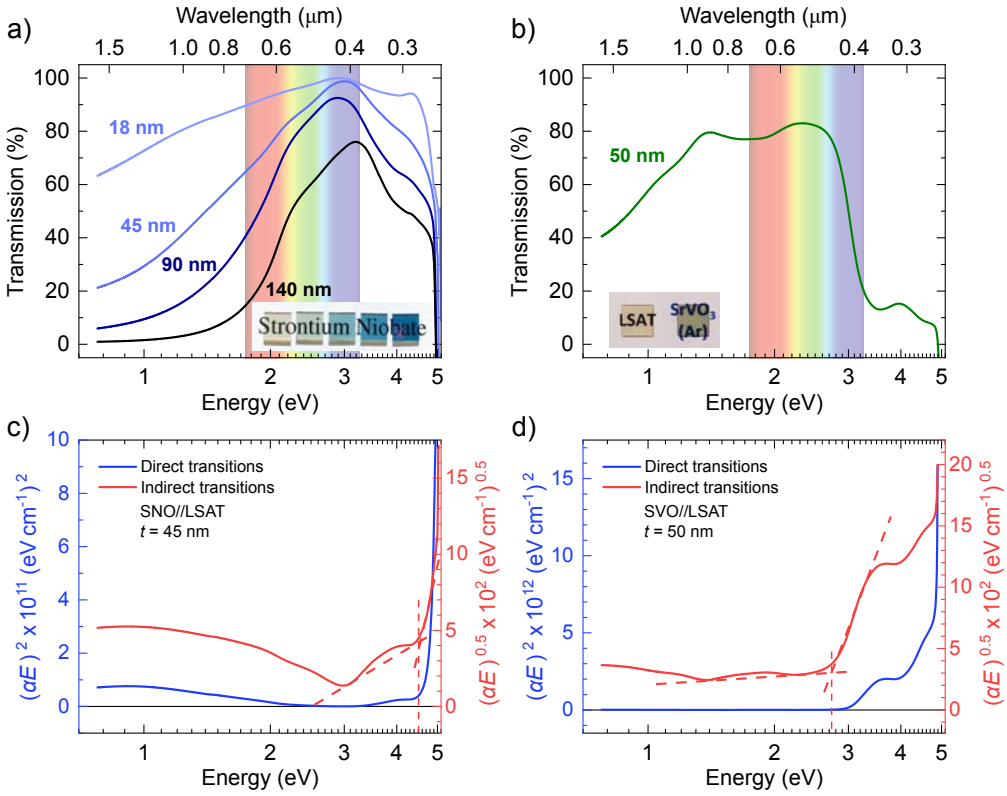

FIGURE 7.7: UV-vis-NIR transmittance data of: a) SNO films with thicknesses ranging from 18 nm to 140 nm, and b) SVO film of 50 nm. Bottom graphs represent Tauc plots of: c) 45 nm SNO film and, d) 50 nm SVO film, plotted for direct (left axis) and indirect (right axis) optical transitions. Dashed lines indicate a linear extrapolation of data at appropriate energy range.

The Tauc plot ($(\alpha h\nu)^{1/2}$ vs $h\nu$) of the of 45 nm SNO film is shown In Figure 7.7c. Assuming an indirect absorption (right axis), a bandgap of about 4.5 eV can be estimated (dashed line), which is in agreement with earlier estimates [31, 46]. We note that the presence of a dip at about 2.9 eV (427 nm), coinciding with the maximum of transmittance in Figure 7.7a, reflects the probable coexistence of different absorbing bands in the UV-visible region, as already noticed by Oka et al. [31]. It is also worth mentioning that DFT calculations by Paul et al. [255] predicted similar absorbance and indirect bandgap ($\approx$ 4.5 eV) (Appendix F.1).

At this point it is enlightening to show the corresponding data for a metallic SVO film ($\rho(300\,\mathrm{K}) \approx 40\,\mu\Omega\,\mathrm{cm}$) of similar thickness ($\approx$ 50 nm) grown under optimal $(T, P(Ar))$ conditions (as determined in Chapter 4). As shown in Figure 7.7b, the SVO film shows a flat large transmittance in the visible and thus it is a colorless transparent conductor. Instead, there is a dramatic drop of transmittance developing at $\approx$ 450 nm (2.7 eV), that DFT calculations associate to (allowed) transitions between the O $2p$ valence band and the empty V $3d$-t_{2g} states [18]. The corresponding Tauc plot (Figure 7.7d) provides an additional estimate of this energy gap. Of more relevance here is that the transmissivity is essentially constant up to about 900 nm ($\approx$ 1.38 eV) suggesting a full reflectivity at low energy and thus a plasma frequency at about 1.38 eV, i.e. in the NIR.

7.4 Plasma frequency and loss function

A deeper insight into the optical properties of these films can be obtained by ellipsometry, allowing to extract the complex permittivity $\varepsilon(\omega) = \varepsilon_1(\omega) + i\varepsilon_2(\omega)$ and the optical losses $LF(\omega) = -\mathrm{Im}[\varepsilon^{-1}(\omega)] = [\varepsilon_2(\omega)/(\varepsilon_1^2(\omega) + \varepsilon_2^2(\omega)]$. In Figure 7.8a below, we show the $(\varepsilon_1(\omega), \varepsilon_2(\omega))$ data of a SNO//LSAT film (70 nm) grown at optimal argon pressure. Data for SNO//GSO films of the same thickness are virtually identical (Appendix F.2). It can be appreciated that $\varepsilon_1(\omega) = 0$ at about 1.9 eV, thus signaling a plasma energy $\hbar\omega_p(\mathrm{SNO}) = 1.9$ eV, which is consistent with the $T(\lambda)$ data in Figure 7.7a.

In Figure 7.8b, where we plot $(\varepsilon_1(\omega), \varepsilon_2(\omega))$ for SVO//LSAT, it can be readily appreciated that the plasma frequency of SVO occurs at significantly smaller energy $\hbar\omega_p(\mathrm{SVO}) = 1.3$ eV, and thus SVO is fully transparent in the visible range. In the simplest Drude model, the plasma frequency is given by $\hbar\omega_p = \hbar e\sqrt{n/(m^*\varepsilon_0\varepsilon_r)}$, where e is the elementary charge, $(\varepsilon_0, \varepsilon_r)$ are the vacuum and relative permittivity of the material, respectively, and m^* its electronic effective mass. Therefore, as the carrier density in both systems are very similar ($1.7 \times 10^{22}\,\mathrm{cm}^{-3}$ for SNO, as shown

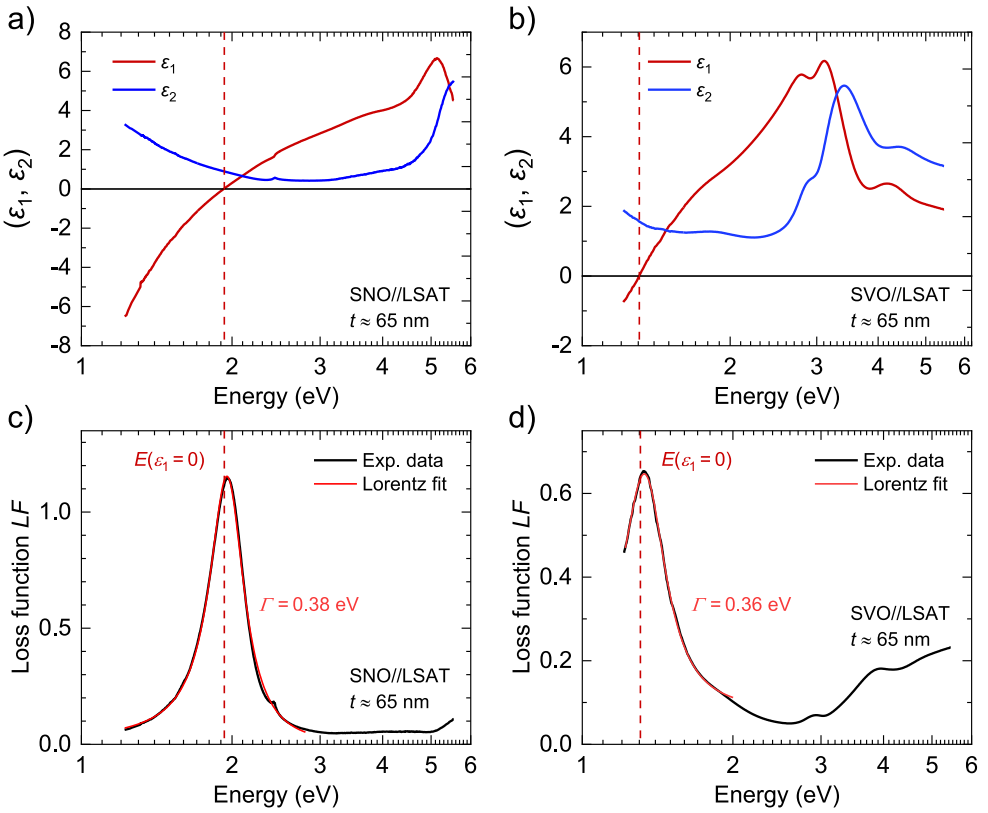

FIGURE 7.8: Ellipsometric data of (a,c) SNO and (b,d) SVO films (about 65 nm thick). Figures (a-b) represent the optical constants $(\varepsilon_1, \varepsilon_2)$ extracted from the ellipsometic angles (Δ, Ψ), while (c-d) contain their loss function $LF = \varepsilon_2/(\varepsilon_1^2 + \varepsilon_2^2)$.

in Figure 7.5c, and $2.1 \times 10^{22}\,\mathrm{cm}^{-3}$ for SVO, see Chapter 4), it follows that the effective mass for free carriers is smaller in SNO than in SVO ($m^*(\mathrm{SNO}) < m^*(\mathrm{SVO})$). This observation is consistent with the larger size of the $4d$ orbitals compared to the $3d$ ones, that weakens electron-electron correlations and electron-phonon coupling (as explored in Chapter 6) and thus reduces m^* of SNO with respect to SVO. Oka et al. [31] inferred a similar conclusion from their analysis of the temperature dependence of the conductivity.

Having established that SNO and SVO both display a well-defined $\varepsilon_1(\omega_\mathrm{p}) = 0$ crossing, which signals the plasma frequency, we turn now to the corresponding optical losses. In Figure 7.8c-d, we depict the corresponding $LF(\omega) = -\mathrm{Im}[\varepsilon^{-1}(\omega)]$ calculated from $(\varepsilon_1(\omega), \varepsilon_2(\omega))$ data. It can be observed that $LF(\omega)$, for both SNO and SVO, displays a pronounced peak (LF_max) occurring at energies ($E(LF_\mathrm{max})$) close to the corresponding plasma frequency, suggesting that losses are attributable to plasmon excitations. A more detailed inspection of data in Figure 7.8 reveals that the plasma energy determined from $\varepsilon_1 = 0$ crossing (1.93 eV) is slightly shifted from the maximum of the loss function (1.96 eV). Similarly, for SVO, the corresponding values are 1.30 and 1.32 eV, respectively. This red shift (≈ 0.02-0.03 eV) is a signature of the damping (scattering time τ) of free carriers in the metal, and thus it can be used to estimate τ. It turns out that: $\hbar/\tau = \sqrt{(E(LF_\mathrm{max}))^2 - (\hbar\omega_\mathrm{p}(\varepsilon_1 = 0))^2}$ [23, 252]. Therefore, we estimate $\tau \approx 1.93 \times 10^{-15}$ s for SNO. The damping of plasmons, so-called dephasing time T_2, is manifested in the full width at half maximum (Γ) of the resonant LF_max peak. More specifically, $T_2 = 2\hbar/\tau$ with $T_2 \approx 2\tau'$ [256], leading to $\tau' = \hbar/\Gamma$. A fit of a Lorentzian function to the $LF(\hbar\omega_\mathrm{p})$ data of Figure 7.8c gives $\Gamma \approx 0.38$ eV, corresponding to $\tau \approx 1.73 \times 10^{-15}$ s for SNO. This dephasing time value is in good agreement with the previous evaluation ($\tau \approx \tau'$), suggesting electron scattering as the primary cause of plasmon damping. Available data does not allow to gain further insight into the microscopic nature of plasmon damping mechanisms. However, it turns out that the electron scattering time of SNO, deduced from the measured conductivity and the carrier density is within a similar τ_ee range ($\approx 1.4 \times 10^{-15} - 4.6 \times 10^{-15}$ s), depending on the actual effective mass used for calculations (either $m^* \approx 1.5 m_0$, as deduced from the corresponding plasma frequency, or $m^* \approx 0.46 m_0$ from Seebeck coefficient or DFT [257, 258]). A similar agreement has been reported in Au [259].
For SVO films, the redshift of LF (≈ 0.02 eV) and the width of $LF(\hbar\omega_\mathrm{p})$ ($\Gamma \approx 0.36$ eV), leading to 2.86×10^{-15} s and 1.83×10^{-15} s, respectively, which are obviously very close to each other and similar to SNO. The scattering rate deduced from transport measurements, and using the effective mass either from our ellipsometric measurements ($m^* \approx 4.28 m_0$) or other literature-reported values ($m^* \approx 3 m_0$ [123, 124, 163]) is equal to $\tau_\mathrm{ee} = 6.70 \times 10^{-15} - 9.56 \times 10^{-15}$ s, roughly coincident with

previously extracted values as well as the SNO values.
At this point, a comment on the validity of the Drude model connecting the plasma frequency to electron effective mass is required. The commonly used expressions are valid for simple parabolic electronic bands and allow comparison between data reported by different authors on related materials [18, 46, 123, 125, 163, 252, 257, 258, 260]. However, in nd^1-t_{2g} ($n=1,2$) metals such as SVO and SNO, the conduction bands (mainly xy, xz and yz) have different dispersion and thus reducing the effective mass to a single value should only be taken as a working approximation.

The observation of a strong peak in the bulk energy LF ($BELF$) function is related to the excitation of a bulk plasmon in the films, associated with the zero-crossing of the real part of the permittivity at the bulk plasma frequency. In general, longitudinal bulk plasmons cannot be excited by light because the latter are transversal waves. However, as earlier stressed by Abelès [261], at optical frequencies it is possible to excite plasmons by p-polarized light of proper frequency at oblique incidence. This observation is crucial to assign the peak observed in the loss function, which we discuss next.

	$\hbar\omega_p(\varepsilon_1=0)$ (eV)	LF_{max} (eV)	Γ (eV)	τ (fs)	τ' (fs)	m^* ($\times m_0$ kg)	τ_{ee} (fs)
$SrNbO_3$	1.93	1.96	0.38	1.93	1.73	0.46 – 1.56	1.35 – 4.63
$SrVO_3$	1.31	1.33	0.36	2.86	1.83	3 – 4.28	6.70 – 9.56

TABLE 7.1: Summary of calculations of the scattering rate in SNO and SVO films. The effective mass m^* was either taken from SNO [257, 258] and SVO [123, 124, 163] references, or from the our ellipsometry data (together with dc transport data). The relative permittivity value ($\varepsilon_r = 4$) used to calculate the m^* from ellipsometric data was taken from Makino et al. [123] and is estimated to be nearly identical for SVO and SNO.[1]

[1] Following Markino et al. [123] , the permittivity of the conduction electrons, ε_r is evaluated from the real part of the dielectric function $\varepsilon_1(\omega)$ at the energy were interband transitions first appear. From out Tauc plots of SNO, we deduced a band gap of about 4.5 eV and the corresponding $\varepsilon_1(\omega) \approx 4$ that we take as a proxy for ε_r.

7.5 Transmittance of (*s*, *p*) polarized light

To disentangle the origin of the observed plasmonic-like response we recall that when p-polarized light ($\boldsymbol{E}_\mathbf{p}$) is impinging the film surface at a certain angle θ measured with respect to the normal direction (that we take as the z-axis), its electric field has components both parallel ($\boldsymbol{E}_\mathbf{y}$) and perpendicular ($\boldsymbol{E}_\mathbf{z}$) to the film surface (Figure 7.9). The $\boldsymbol{E}_\mathbf{z}$ component can promote collective excitations of the electron gas in the film, which will oscillate along the z-axis with a characteristic plasmonic frequency ω_p. The coupling between light and bulk plasmons is mediated by discontinuities between two media, which give rise to surface charge densities [262]. These can be described by a gradient of the electron density n, which leads to a force ($\approx \mathrm{d}n/\mathrm{d}z$) that pushes the metal electrons along the z-direction, producing longitudinal density oscillations. The excitation of such volume plasmon should cause a minimum at the transmittance of p-polarized light (T_p), which should remain unobserved in the transmittance of s-polarized light (T_s). Therefore, the observation of a dip in the T_p spectrum and the absence of any such feature in the T_s spectrum would be the fingerprint of the excitation of the volume plasmon indicated by the *BELF* function [262]. In fact, this simple model had been used to describe plasmonic resonances in metallic thin films [263–266], as reviewed in Steinmann [267] and Oates et al. [20]. A distinctive fingerprint is that plasmonic oscillations can be excited by p-polarized light but not by s-polarized light; consequently, a dip in transmittance T_p should occur at resonance ($\omega = \omega_\mathrm{p}$) but not in T_s, as for s-polarization the normal component $\boldsymbol{E}_\mathbf{z}$ is absent.

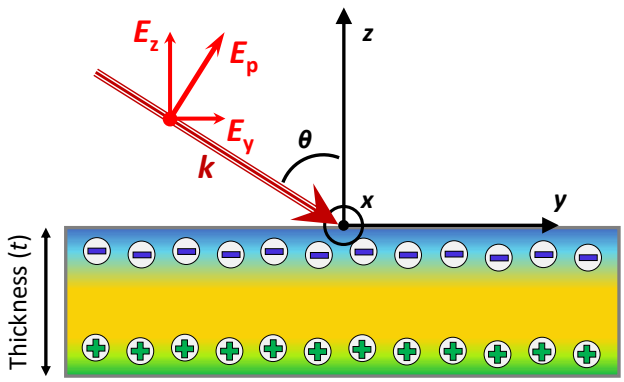

FIGURE 7.9: Sketch of the optical configuration for bulk plasmon excitation in thin films. A p-polarized light ($\boldsymbol{E}_\mathbf{p}$) impinging the film at an incidence angle θ, and its components perpendicular to the film ($\boldsymbol{E}_\mathbf{z}$) and parallel to the film surface ($\boldsymbol{E}_\mathbf{y}$) are indicated.

In the search for such difference, two different approaches were undertaken. First, ellipsometric data of SNO//GSO, SNO//LSAT and SVO//LSAT were used to evaluate (n, κ), from which the transmission coefficients (T_p and T_s) were calculated, and second polarization-dependent transmission experiments were performed at oblique angle of incidence. In the first strand, data extraction involves measuring the ellipsometric angles of the film/substrate sample and those of the substrate (Appendices F.2-F.5). With these inputs, WinElli software has been used to model the film/substrate bilayer system, and determine (T_p, T_s) of the films. In Figure 7.10a we show the (T_p, T_s) data of a SNO film (65 nm thick; SNO//LSAT). It is obvious that T_p displays a well pronounced dip at about 2 eV, which closely matches with the plasma energy of Figure 7.8. Importantly, whereas T_p displays a minimum at some energy, no feature can be observed in T_s. It is worth noticing that similar data analysis performed on ellipsometric data of SNO//LAO films, as reported by Wan et al. [46] display an identical response (Figure 7.10c). Therefore, we conclude that (T_p, T_s) data in SNO films provide a robust demonstration of its bulk plasmon origin. Evaluation of (T_p, T_s) from available ellipsometric data and possible observation of a similar T_p minimum in SVO films is challenging as its plasma frequency is ($\approx$ 1.3 eV) close to the lower-energy limit of the used ellipsometer. In Figure 7.10c, we show that the (T_p, T_s) data evaluated from the extracted (n, κ) of a SVO//LSAT film display a subtle minimum in T_p, which is also consistent with its plasmonic nature. In Figure 7.10d we include (T_p, T_s) of a SVO//LSAT film calculated from the scanned $(\varepsilon_1, \varepsilon_2)$ data reported by Zhang et al. [18] over a bigger energy range. It is rewarding to observe a similar emerging dip in T_p also in this SVO film. Disclosing a dip in T_p but not in T_s in both SVO and SNO films using data taken from different samples and ellipsometric measurements assesses the robustness of the present conclusions. Polarization dependent transmittance data were collected for *p*- and *s*-light (Appendix F.3). Its difference $T_p - T_s$ is shown in Figure 7.10e,f. In both bilayers, the presence of a dip in $T_p - T_s$ can be well appreciated. Moreover, the dips occur at energies that closely match the corresponding minima calculated from the ellipsometric data (Figure 7.10a-d). These experimental observations provide a strong experimental confirmation of the reduced transmissivity for *p*-light at the plasma frequency. In summary, oblique *p*-light incidence promotes bulk plasmonic excitations at epsilon-near-zero (ENZ) condition, in both SNO and SVO metallic films. Fingerprints of plasmonic excitations should also occur in reflectivity measurements, leading to distinct reflectivity for *p*- and *s*-light (R_p, R_s). However, it is known [268, 269] that their observation is challenged by the proximity of the Brewster angle, that largely dominates R_p (Appendix F.4).

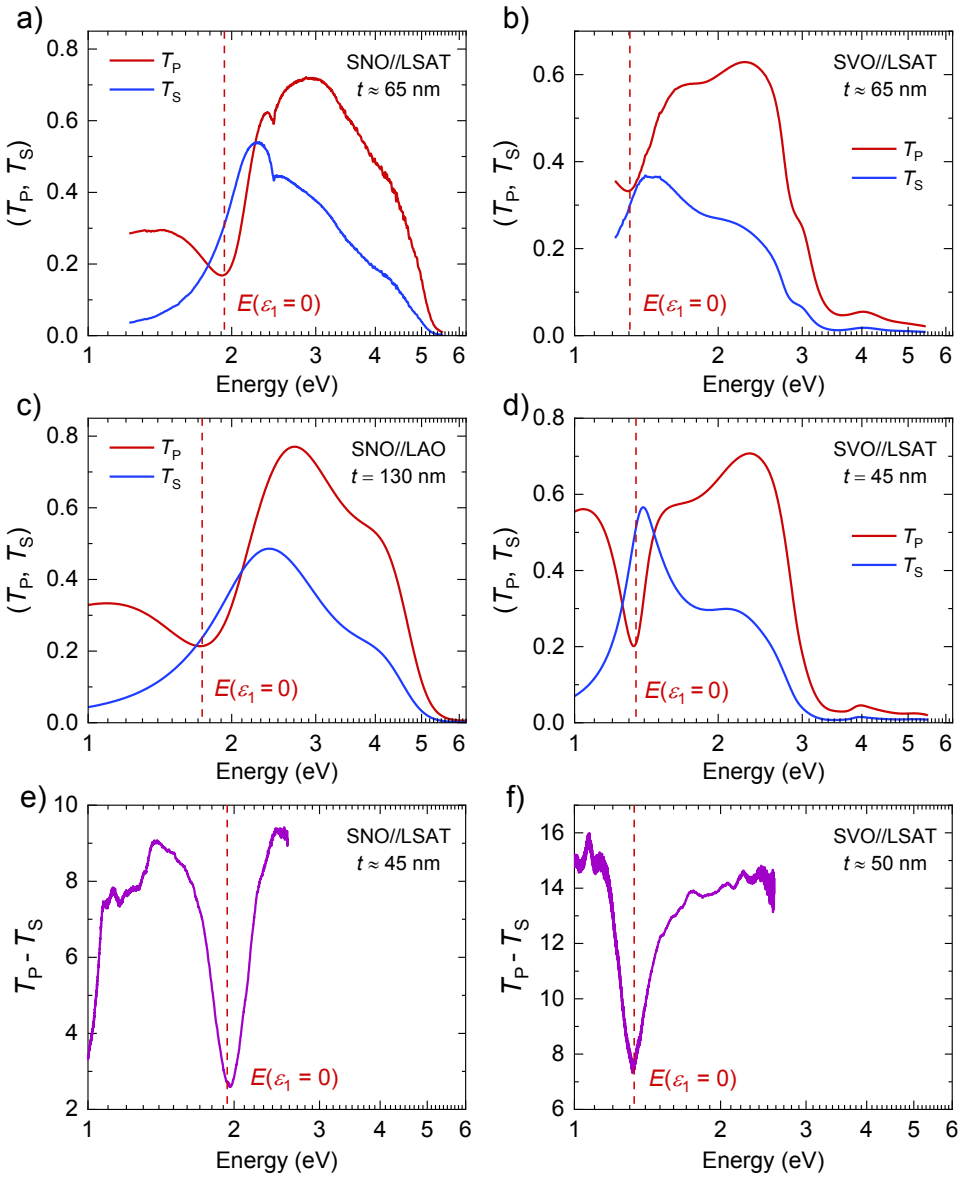

FIGURE 7.10: Simulated (T_p, T_s) data (at angle of incidence of 65°) from the measured optical constants of different SNO and SVO films: a) SNO//LSAT film (65 nm thick) from this work. b) SVO//LSAT film (65 nm thick) from this work. c) SNO//LAO film (130 nm thick) from Wan et al. [46]. d) SVO//LSAT (45 nm thick) from Zhang et al. [18]. Measured ($T_p - T_s$) spectra (at angle of incidence of 30°) of: e) SNO//LSAT film (45 nm thick), and f) SVO//LSAT film (50 nm thick).

7.6 Conclusions

Aiming at elucidating the nature of the optical response at visible wavelengths and particularly the nature of the epsilon-near-zero (ENZ) resonance in transparent metallic oxide thin films, we have reported here on the optimization of PLD-grown epitaxial $SrNbO_3$ thin films. It turns out that structural lattice mismatch with substrates plays a major role. Films deposited on optimally lattice-matching substrates (in this case, $GdScO_3$) always display higher conductivity and residual resistivity ratio than films grown simultaneously on other substrates (in this case, LSAT). In any event, there is a narrow (argon) pressure window required for optimal room-temperature conductivity. The earlier report on the observation of a related growth window in $SrVO_3$ suggests that the atmosphere during growth may be pivotal to reducing defects and improving stoichiometry.

SNO films are found to be transparent at the UV-visible with a noticeable absorption edge at $\lambda \approx 550\,\text{nm}$ that reduces the film IR-transparency when the thickness increases and probably account for the red color observed in bulk SNO materials. Spectroscopic ellipsometric measurements have shown that optical losses $LF(\omega)$ display a pronounced maximum LF_{max} at frequencies close to where the ENZ ($\varepsilon_1 = 0$) condition is fulfilled ($\omega = \omega_p$), thus suggesting that volume plasmons are excited by optical light at ω_p (about 2 eV). More precisely, it is observed that LF_{max} is red shifted with respect to $\omega_p(\varepsilon_1 = 0)$ as expected from the presence of damping in carrier motion. It is found that the estimates of damping time obtained from the mentioned red shift of optical losses, the width of the plasmonic resonance and the transport measurements, are relatively close. A similar set of consistent data has been obtained for SVO, where a smaller ω_p ($\approx 1.3\,\text{eV}$) is observed. Being SNO and SVO isoelectronic and having a similar carrier density, the difference in ω_p is attributed to the narrower character of the $3d$ bands in SVO compared to the $4d$ bands in SNO. However, the most decisive new information is provided by the observation of a dip in the transmission coefficient of the SNO and SVO films, at $\omega \approx \omega_p$. The fact that these dips are only observed for p-light but not for s-light is the strongest evidence of the plasmonic nature of the absorption losses at ω_p. At variance with earlier suggestions, bulk plasmons in SNO and SVO are found to be excited by optical light at oblique incidence, in continuous (unpatterned) thin films and without using any phase-matching optical tool. Transparent and metallic transition metal oxides films based on $4d$ cations, such as $SrMoO_3$, which have recently be grown with excellent conductivity (about $20\,\mu\Omega\,\text{cm}$) and optical transparency [39, 270], and received attention for plasmonic applications [47, 260], may display similar bulk plasmon excitations. From a broader perspective, the results presented here suggest that charge discontinuities at boundaries, and subsequent

charge gradients, are the underlying mechanism that allows to couple light to volume plasmons. This observation offers the interesting perspective of using intentionally interface engineering to display novel plasmon functionalities in complex heterostructures. This may include for instance, deliberately designed charge gradients - e.g., by grading the doping profile on an atomic scale at the interface, as done by Yamada et al. [271] - to engineer the coupling of light to volume plasmons. Otherwise fine tuning of plasmon resonance should rely on the dynamics of the electron system. The systematic shift of plasma resonance when expanding the bandwidth from SVO to SNO appears to open a promising route.

Chapter 8

Photoresponse in all-oxide heterostructures

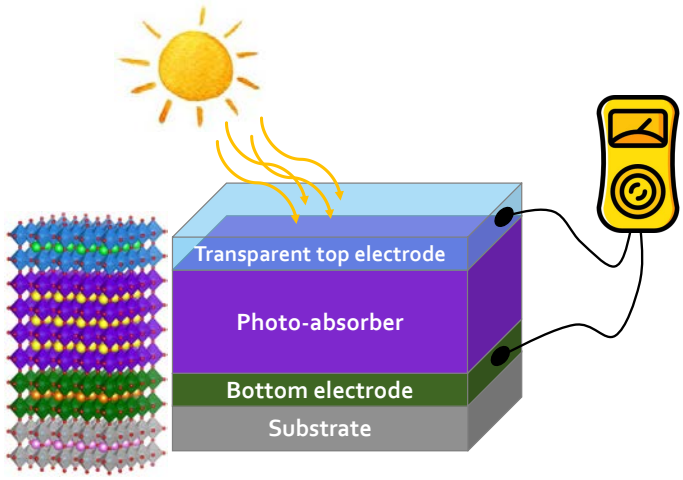

FIGURE 8.1: Illustration of an all-oxide heterostructure such as those designed in this work. The incorporation of each layer in such heterostructure is eased by their common perovskite crystalline structure.

In this chapter, we aim at studying the photoresponse of all-oxide all-perovskite heterostructures (as schematized in Figure 8.1). Perovskite materials possess many advantages for photovoltaics: low band gap, high power conversion efficiency (PCE), low cost of production, etc. In about one decade only, perovskite solar cells (PSCs) have exhibited the fastest growth in term of efficiency. To date, lead halide PSC have reached a record of efficiency of up to 25.5 %, which is comparable to the state-of-the-art for single-junction architectures, including crystalline Si-based solar cells (the ones dominating the market).[1] Oxide-based perovskite thin films

[1] https://www.nrel.gov/pv/cell-efficiency.html (Last accessed on April 15th 2021)
https://en.wikipedia.org/wiki/Solar_cell_efficiency (Last accessed on April 15th 2021)

with ABO_3 structure, with A a rare-earth element and B a transition metal, have reached more modest efficiencies, but yet competing with the state-of-the-art materials [272]. For instance, a PCE of 3.3 % was reported in single layers of multiferroic Bi_2FeCrO_6 and bandgap graded oxide multilayers (using a trilayer of Bi_2FeCrO_6 with different bandgaps) have shown the most promising results with efficiency of 8.1 % [273].

While band insulator perovskite crystals (e.g. $SrTiO_3$, $BaTiO_3$, etc.) usually show low photovoltaic potential due to their wide optical band gap (Fig. 8.2a), some other transition metal oxides show more interesting properties thanks to the peculiar nature of their band gap. For instance, Mott insulators or charge-transfer (CT) insulators usually have lower band gap. This is due to the nature of their valence and conduction bands. Mott and CT insulators are two types of materials predicted to be conductors by the conventional band theory, which only considers a partially filled degenerate d band, originating from the transition metal at the B-site. However, in perovskite oxide, the anisotropic crystal field splitting induced by octahedral cage oxygen cage, together with some eventual additional symmetry lowering effects (such as octahedral rotations, Jahn-Teller distortions, etc.) break the symmetry of the d orbitals and may lead to an insulating state of the material. By taking these effects into account, as well as the electronic correlations, the Hubbard model offers a more complete picture than the conventional band theory. In Figure 8.2a, we show the band structure of both Mott insulators and C-T insulators. According to the Hubbard model, one can define the electron-electron interaction U, which is responsible for the opening of a Mott-Hubbard band gap inside the d band, and the electron transfer energy Δ between the O $2p$ and the metal d bands. In a Mott insulator $U < \Delta$, while in a CT insulator $U > \Delta$ [187].

In this work, we have selected two insulating nonpolar (centrosymmetric) oxides as photoabsorbing layer:

- $LaVO_3$ (LVO) is a Mott insulator with a $3d^2$ electronic configuration, and a band gap $E_G \approx 1.1$ eV [274].
  LVO is a promising material for photovoltaics due to its optimal band gap for visible light absorption. In fact, it has shown to have similar absorption than c-Si, CdTe, etc. [275, 276], and multilayer devices synthesized by hybrid-MBE or PLD have shown some promising photoresponse [275, 277].

- $LaFeO_3$ (LFO) is a CT insulator with high-spin $3d^5$ ($t_{2g}^{3\uparrow}$, $e_g^{2\uparrow}$) electronic configuration, and a band gap $E_G \approx 2.2$ eV [274, 278, 279].
  LFO has a higher band gap than LVO but that still allows absorption of visible light. It has actually shown some interesting photoresponse in multilayers [77, 280, 281].

In Figure 8.2b, the band gap values of the materials studied in this work, together with some other promising oxides for photovolatics, are given (figure adapted from [282]).

In Section 8.1, we have first determined the PLD growth window of $LaVO_3$ and $LaFeO_3$ thin films as single layers. For this purpose, we have used XRD tools to characterize their cristallinity and AFM to ensure that the films were flat enough for their integration in a multilayer device. In the case of LVO, the electrical resistivity was also used to judge on the film quality. Once the optimal growth conditions were found, the optical properties (namely optical band gap, optical absorption...) were studied.
In Section 8.2, we have designed and characterized multilayer devices based on the previously optimized photoabsorbing materials (LVO and LFO). We have chosen the simple metal-insulator-metal (MIM) device architecture, where the photoabsorbing layer is "sandwiched" between two electrodes. The top electrode (TE) was either one of the TCO materials studied in this thesis or (semi-transparent) Pt, for sake of comparison. The bottom electrode (BE) was either a metallic oxide or also a TCO. The choice of materials combination for a given heterostructure was mainly based on their compatibility of PLD growth conditions (substrate temperature, nature of the gas in the chamber). For instance, LVO and SVO show excellent compatibility in term of grow conditions, as they both need to be grown in a highly reducing atmosphere, incompatible with many other oxides. On the other hand, LFO is grown in a O_2 background atmosphere so it was decided to use $La_{2/3}Sr_{1/3}MnO_3$ (LSMO) as bottom electrode and $Ba_{0.95}La_{0.05}SnO_3$ (BLSO), another promising TCO, as top electrode. The properties of BLSO single layers are reported in Appendix C. There, it is shown that BLSO, by its nature of doped wide band gap semiconductor, offers high optical transparency at the visible and high electrical conductivity (one order of magnitude smaller than in intrinsic TCO such as SVO or SNO though). Interestingly, metallic and transparent SVO was also successfully incorporated as top electrode on LFO (despite its the different growth conditions).
In summary, the heterostructures (bottom electrode/photoabsorber/top electrode) studied in this chapter were designed as follow:

- For LVO-based heterostructures:
  - SVO/LVO/SVO
  - SVO/LVO/Pt
- For LFO-based heterostructures:
  - LSMO/LFO/BLSO
  - LSMO/LFO/SVO
  - LSMO/LFO/Pt

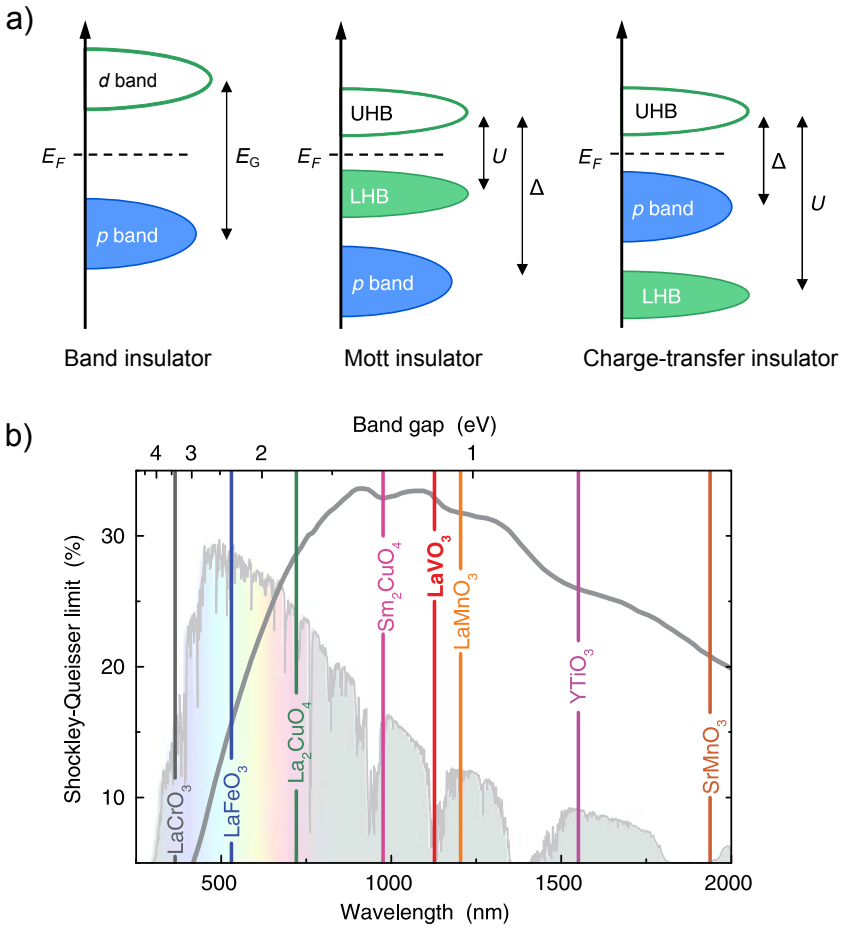

FIGURE 8.2: a) Schematic band structures of band, Mott and charge-transfer insulators. b) Shockley-Queisser limit as a function of band gap, along with the solar spectrum. The band gaps of various prototypical TMOs, including the ones studied in this work, are indicated. Figure adapted from [275].

8.1 Growth optimization and electro-optical properties of photo-absorbing materials

8.1.1 Lanthanum vanadate ($LaVO_3$) single layers

Growth window

Lanthanum vanadate $LaVO_3$ (LVO) has an orthorombic perovskite structure with $a = 5.549$ Å, $b = 5.555$ Å and $c = 7.843$ Å.[2] This can be approximated to a pseudocubic unit cell with cell parameter $a_{LVO} \approx 3.924$ Å. LVO films were therefore grown on (001) STO ($a_S = 3.905$ Å) and (001) LSAT ($a_S = 3.868$ Å) substrates. Both substrates have smaller lattice parameter than the bulk LVO, resulting in a compressive stress. The lattice mismatches, $f = [a_S - a_{LVO}]/a_S$, between substrate and film are: $f_{STO} = -0.49$ % and $f_{LSAT} = -1.45$ %.

Similarly to the growth of $SrVO_3$ (V^{4+}) films, it has been reported that to stabilise the $LaVO_3$ phase (where the vanadium cation has valency V^{3+}), films have to be grown in reducing atmosphere to avoid the formation of more stable phases with closed-shell V^{5+} cation (e.g. $LaVO_4$). Consequently, LVO films are usually grown in very low oxygen partial pressure [283–286]. Here, films were grown in UHV (no gas added in the chamber, which corresponds to a residual oxygen partial pressure $PO_2 \approx 4\times10^{-7}$ mbar). Three substrate temperatures (T) were explored: 500°C, 600°C and 700°C. The other main parameters were kept fixed: laser fluence of ≈ 2 J cm^{-2} and frequency of 2 Hz (following ref. [284, 285]). Films were deposited through 2000 laser pulses, and the resulting films thickness was ≈ 40 nm (as determined below by XRR or Laue fringes fittings); so that the growth rate is ≈ 0.2 Å/pulse. The main properties of the films are summarised in Table 8.1.

Sample code	T (°C)	XRR thick. (nm)	Laue thick. (nm)	rms (Å)	c (Å)	a (Å)	V_{uc} (Å^3)	$\rho(300\,K)$ (Ω cm)
STO-1	500	40.0	39.7	1.6	4.015	*3.905*	*61.22*	0.13
STO-2	600	-	38.3	1.7	3.992	3.905	60.87	0.22
STO-3	700	-	38.9	2.1	3.974	3.905	60.60	0.10
LSAT-1	500	40.2	38.4	1.6	4.046	*3.868*	*60.53*	1.88
LSAT-2	600	-	39.0	2.2	4.018	3.860	59.87	1.60
LSAT-3	700	39.3	39.4	2.8	3.981	*3.868*	*59.56*	1.62

TABLE 8.1: Summary of main characteristics of LVO films deposited on (001) STO and (001) LSAT substrates.

[2] ICDD Powder Diffraction File 04-016-5421 (www.icdd.com)

The XRD $\theta-2\theta$ scans of two illustrative samples grown on STO and LSAT (at $T = 600$°C) are shown in Figure 8.3a. One can observe that only the $(00l)$ (with $l = 1, 2, 3, 4$) reflection peaks of both substrate and LVO film are visible. Therefore, the LVO seems to have the expected (001) orientation both on LSAT and STO. In Figure 8.3b, an example of $2\theta-\chi$ scan shows the (001) and (002) reflections of LVO as well-defined round spots at vicinity of the substrate ones, which confirms that films are highly textured. Moreover, no spurious features (additional peaks, rings...) are visible, so the films seem to be single-phase (within this resolution).

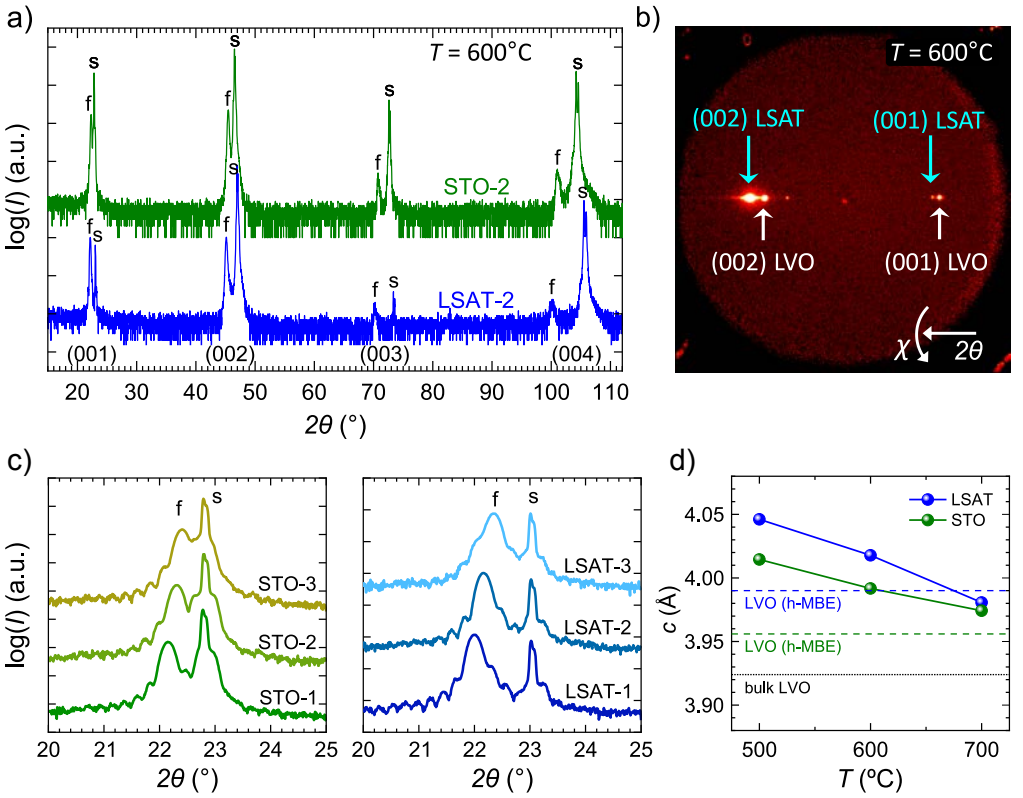

FIGURE 8.3: XRD measurements performed on LVO films deposited on LSAT and STO. a) Illustrative $\theta-2\theta$ scans of films deposited at $T = 600$°C. b) Illustrative $2\theta-\chi$ scan of LVO//LSAT deposited at $T = 600$°C. c) Zoom of the $\theta-2\theta$ scans around the (001) LSAT and STO reflections. d) Summary of c-axis values for all films. The dashed lines refer to c-axis taken from [277, 287, 288].

When taking a closer look at the (001) LVO reflection in the $\theta-2\theta$ scans (Figure 8.3c), one can see the Laue fringes of the LVO peak for each growth temperature and substrate used, which attests of the highly coherent crystalline order of

the films. The extracted c-axis are plotted in Figure 8.3d. We can observe that, for a given temperature, the c-axis is longer on LSAT than on STO. This is a hint than films are coherently strained to the substrate lattice. Indeed, as LSAT applies a more compressive strain on the LVO film, the resulting c-axis is expected to be longer, according to the principle of volume conservation. This was confirmed by measurements of the a-axis (the RSM around the (103) reflections for two illustrative samples are shown in Figure 8.4), where one can see that the LVO film grows fully strained both on LSAT and STO. It can be also observed that the (103) film reflection is a very narrow spot, which hints at the high film crystalline quality. In Figure 8.3d, the c-axis tends to decrease (for both LVO//LSAT and LVO//STO) while increasing the growth temperature, and approaches the optimal c-axis values reported for stoichiometric films grown by h-MBE [277, 287, 288]. Therefore, a possible explanation is the reduction of defects and/or a better cation stoichiometry in the films grown at the highest temperature.

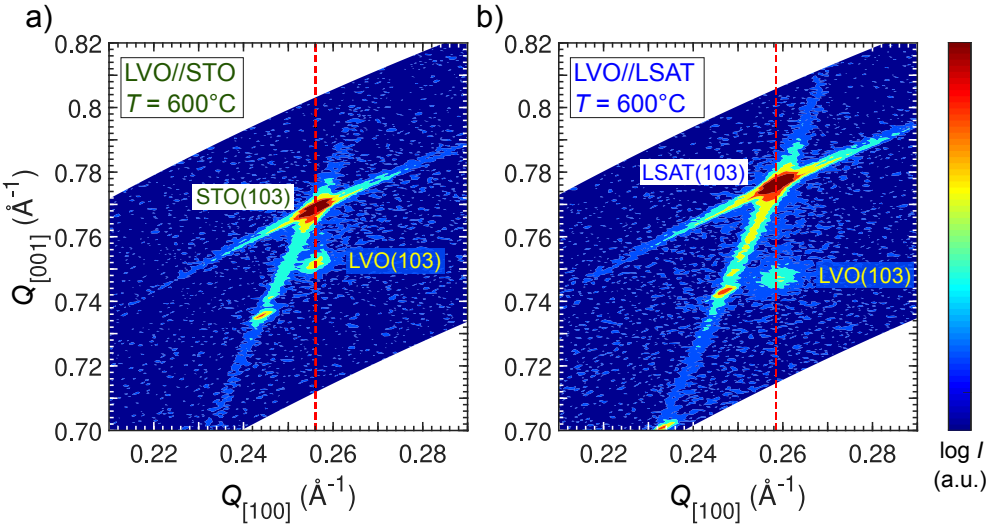

FIGURE 8.4: RSM around the (103) LVO reflection of sample deposited at $T = 600$°C, on a) STO , and b) LSAT substrates.

As seen in Figure 8.5, the film thickness was determined by fitting of XRR spectra and/or fitting of the Laue fringes. There is an excellent agreement between both values, as summarised in Table 8.1, which confirms the high crystalline order (out of plane) of the films.

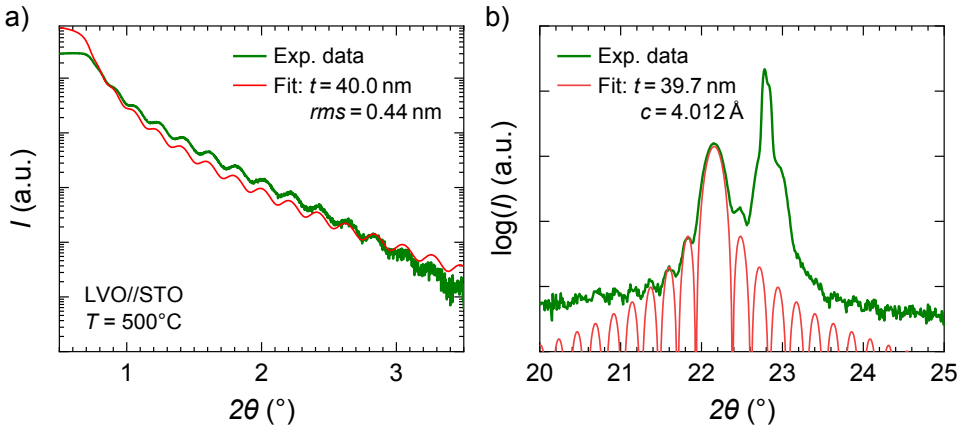

FIGURE 8.5: a) XRR scan of sample STO-1. b) Fitting of the Laue fringes of the (001) reflection of the same sample).

The film surface morphology was explored by AFM (see Figure 8.6). All films show great flatness with a rms roughness below 3 Å. Moreover, terraces and steps were observed in LVO//LSAT samples (especially those deposited at $T \leq 600$°C), indicating a layer-by-layer growth mode. On LVO//STO, terraces and steps are slighty visible for the sample deposited at $T = 600$°C only. The observation of clear terraces and steps were reported in LVO films grown by h-MBE on TiO_2-terminated STO substrate, while the same films deposited on non-terminated STO did not show any [287]. The authors concluded that the surface morphology of stoichiometric LVO films was considerably dictated by the substrate preparation and termination. Therefore, the absence of pronounced terraces and steps in our LVO//STO films could be due to the presence of multiple (SrO, TiO_2) terminations in our STO substrates.

Electrical properties

LVO has a $3d^2$ electronic configuration and is expected to be semiconducting due to its small Mott gap. However, it can occur that a slight doping increases its conductivity. This doping can be due to defects in the films (for instance due to cation non-stoichiometry), creating states in the band gap. It was indeed reported by Zhang et al. that, in films grown by hybrid-MBE, the stoichiometric films have the highest resistivity. On the other hand, upon doping due to non-stoichiometric defects the resistivity decreases by orders of magnitude [277].

The room-temperature resistivity $\rho(300\,K)$ of our films was thus measured (by Van der Pauw technique) as a probe for film quality, and values are given in Table 8.1. In the case of LVO//LSAT films, $\rho(300\,\mathrm{K}) = 1.60 - 1.88\,\Omega\,\mathrm{cm}$, which is very close to

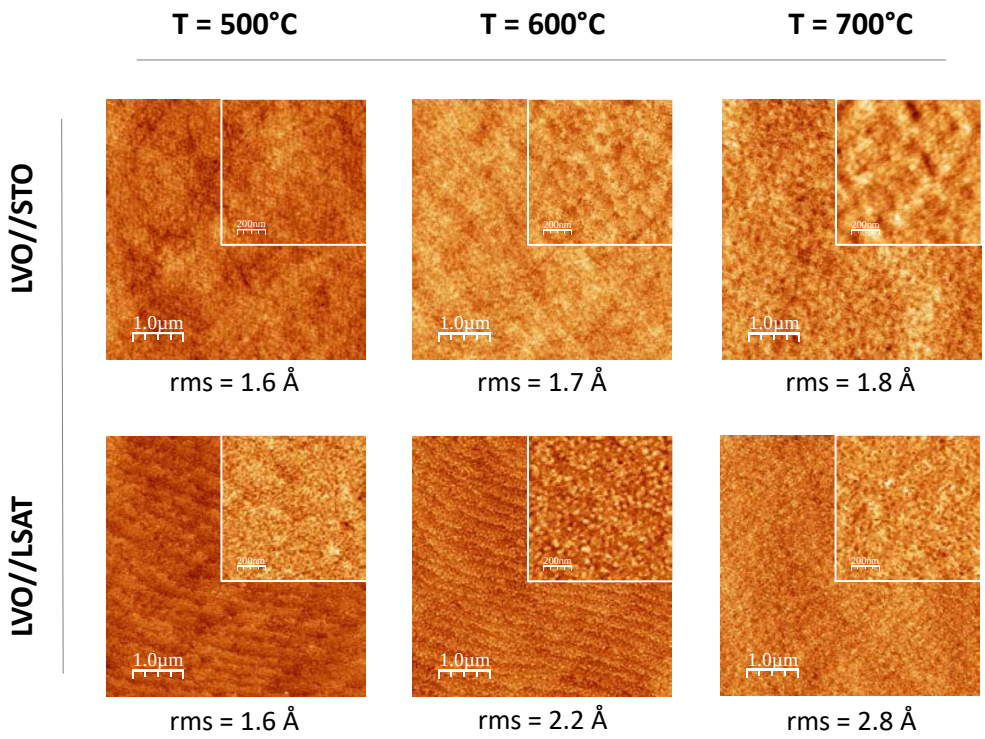

FIGURE 8.6: AFM topographic images, 5 µm×5 µm in size (1 µm×1 µm for the insets), of LVO films grown on STO (top images) and LSAT (bottom images) substrates at various temperatures. The root-mean square (rms) roughness is indicated below each image.

the value of $\rho(300\,\mathrm{K}) = 5\,\Omega\,\mathrm{cm}$ reported for stoichiometric films grown by hybrid-MBE [277], or to the one of $\rho(300\,\mathrm{K}) = 0.8\,\Omega\,\mathrm{cm}$ reported for PLD-grown LVO//LSAT by Sano et al. [289]. Zhang et al. [277] observed a reduced resistivity (by orders of magnitude) in V-rich films. In our case, we have used a PLD target of $LaVO_4$ with cationic ratio [La/V] = 1.01 ± 0.09, therefore slightly V-rich (see Appendix A.5 for details on the target fabrication and characterization). Assuming an exact stoichiometry transfer, this could explain the smaller resistivity that we have measured (only by a factor ≈ 3 though) compared to optimal h-MBE-grown films.
In the case of LVO//STO films, the resistivity was about one order of magnitude smaller. Hotta et al. [290] report similar resistivity in LVO grown on TiO_2-terminated STO substrate. The authors attributed this low resistivity to the formation of a 2 dimensional gas at the interface (2DEG) forming at the LVO//TiO_2-STO interface due to a polar discontinuity between $La^{3+}V^{3+}(O^{2-})_3$ and $Sr^{2+}Ti^{4+}(O^{2-})_3$. However, in our

case, the STO substrates have not been treated and have supposedly no particular dominant termination. The low film resistivity could be either due to some interdiffusion and intermixing between Ti and V cations at the interface, or, as mentionned by He et al. [291] and Rotella et al. [285], to the migration of oxygen vacancies from the STO substrate to the film. They indeed also report similar values of resistivity than in our films.

Optical properties

The optical properties of LVO films were investigated by spectroscopic ellipsometry. In Figure 8.7a, we show illustrative extracted (n, k) of an illustrative LVO//LSAT sample (LSAT-2). From the extinction coefficient k, we have plotted in Figure 8.7b the absorption coefficient α (defined as $\alpha = 4\pi k/\lambda$) of two LVO films (LSAT-2 and LSAT-3). One can observe several absorption peaks in the visible range, with the first one centered at ≈ 1.5 eV. Similar peaks were observed in h-MBE films [277] and single-crystals [292] and were attributed to optical interband transitions from O $2p$ and the V t_{2g} (constituting the lower Hubbard band, LHB) to the V t_{2g} (upper Hubbard band, UHB) and V e_g bands, as sketched in Figure 8.7c. Moreover, we can observe in Fig. 8.7b a strong resemblance between our absorption coefficient (α) spectra and the one of a V-rich LVO film deposited by h-MBE [277]. Finally, we shall mention that similar absorption coefficient than in our films was reported in PLD-grown LVO films [275, 285].

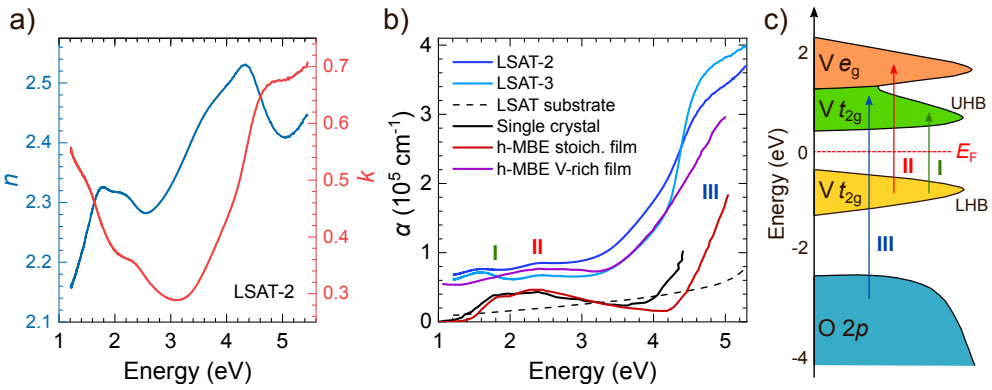

FIGURE 8.7: Optical properties of LVO films. a) (n, k) optical constants of an illustrative LVO//LSAT sample. b) Plot of the absorption coefficient α of two LVO//LSAT samples. For comparison, we show reported spectra for h-MBE films [277] and single crystal (adapted from [292]). Some absorption peaks are identified by the numbers I, II and III, and the corresponding transitions are illustrated in sketch (c), adapted from [277].

Tauc plots (not shown here) based on the ellipsometric data did not allow to determine the bandgap value of LVO since the measured range (1.2-5.4 eV) is above the expected value of ≈ 1.1 eV [277]. However, due to the strong resemblence of our optical data with the ones reported in literature, one can safely assume that our LVO films have a similar bandgap and hereafter we shall use this value.

In conclusion of this section, highly-crystalline epitaxial LVO thin films were successfully deposited. By judging on their electrical and optical properties, films show similar quality to that of optimally-grown thin films by h-MBE [277]. Moreover, the bandgap is expected to be ≈ 1.1 eV which is optimal for use as photoabsorbing layer in solar cells.

8.1.2 Lanthanum ferrite ($LaFeO_3$) single layers

Growth window

Lanthanum ferrite $LaFeO_3$ (LFO) has an orthorombic perovskite structure with $a = 5.551$ Å, $b = 5.559$ Å and $c = 7.850$ Å.[3] This can be approximated to a pseudocubic unit cell with $a_{LFO} \approx 3.927$ Å. Therefore, due to close proximity of cell parameters, it was decided to grow LFO films on 0.5 wt% Nb-doped STO (001) substrates (Nb:STO). The Nb:STO substrate, with $a_S = 3.905$ Å, applies a compressive stress on the LFO film. The resulting lattice mismatch is: $f = [a_S - a_{LFO}] / a_S = -0.64$ %. As there are many reports [77, 280, 281, 293–296] of PLD-deposited LFO films with outstanding crystalline quality (flat surface, observation of Laue fringes, etc.), we have explored here only three sets of (PO_2, T) growth parameters, as summarized in Figure 8.8. The other main parameters were kept fixed: laser fluence of ≈ 2 J cm^{-2} and frequency of 5 Hz. All films were deposited through 2500 laser pulses and their thickness was ≈ 35 nm (determined by fitting of the XRR scan or of the Laue fringes; data not shown here); so that the growth rate is ≈ 0.14 Å/pulse. A summary of growth conditions and main structural properties of our samples, together with some literature results, are given in Table 8.2.

[3] ICDD Powder Diffraction File 04-011-7994 (www.icdd.com)

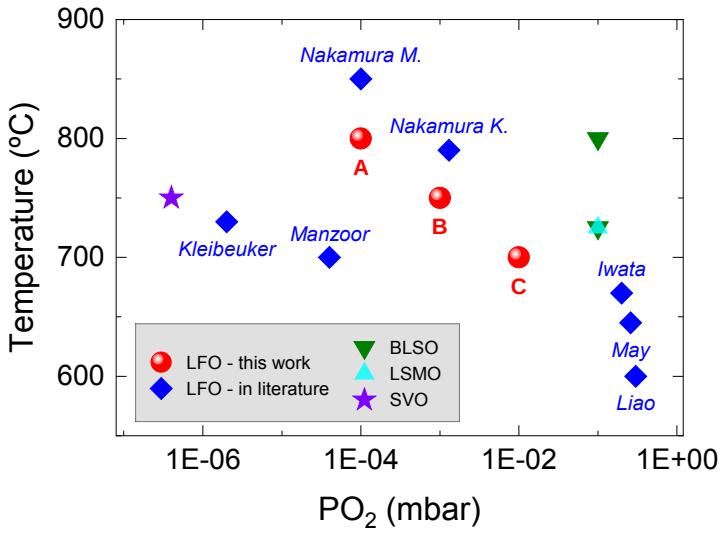

FIGURE 8.8: Explored growth window of LFO films grown on (001) Nb:STO substrates, as a function of PO_2 and T during growth. Blue diamonds are growth conditions found in literature (labels indicating first author's last name) [77, 280, 281, 293–296]. The optimal growth conditions of metallic oxides used in this thesis (BLSO, LSMO, SVO) are also given.

Sample code	T (°C)	PO_2 (mbar)	XRR thickn. (nm)	Laue thickn. (nm)	rms (Å)	c (Å)	a (Å)	V_{uc} (Å^3)
A	800	10^{-4}	37.2	37.6	3.6	4.004	3.902	60.97
B	750	10^{-3}	37.2	36.9	4.2	4.013	3.896	60.91
C	700	10^{-2}	34.3	33.3	2.9	4.016	3.898	60.97
Manzoor	700	4×10^{-5}	65		5	4.042	3.904	61.60
May	645	2.6×10^{-1}	25		8.6	–	–	–
Nakamura K.	790	1.3×10^{-3}	18–55		–	4.01	3.91	61.31
Nakamura M.	850	1.3×10^{-4}	30		–	3.96	–	–

TABLE 8.2: Summary of main characteristics of LFO films deposited on Nb:STO(001), together with some literature-reported values [77, 280, 281, 296].

The XRD $\theta-2\theta$ scan of sample C is shown in Figure 8.9a. All (00l) reflections (l = 1,2,3,4) of film and substrate are well visible. In Fig. 8.9b, we show a zoom around the (002) reflections for all films. Interestingly, all films display Laue fringes, which indicate high film crystallinity and film flatness. The extracted c-axis values are summarized in Table 8.2, and are comparable to literature values [280]. From the $2\theta-\chi$ scans (Fig. 8.9c), no spurious phase was detected and some well-defined LFO round spots were observed next to the substrate reflections. The RSMs showed fully strained films (Fig. 8.9d), coherent with the observed c-axis elongation, that we attribute to volume conservation.

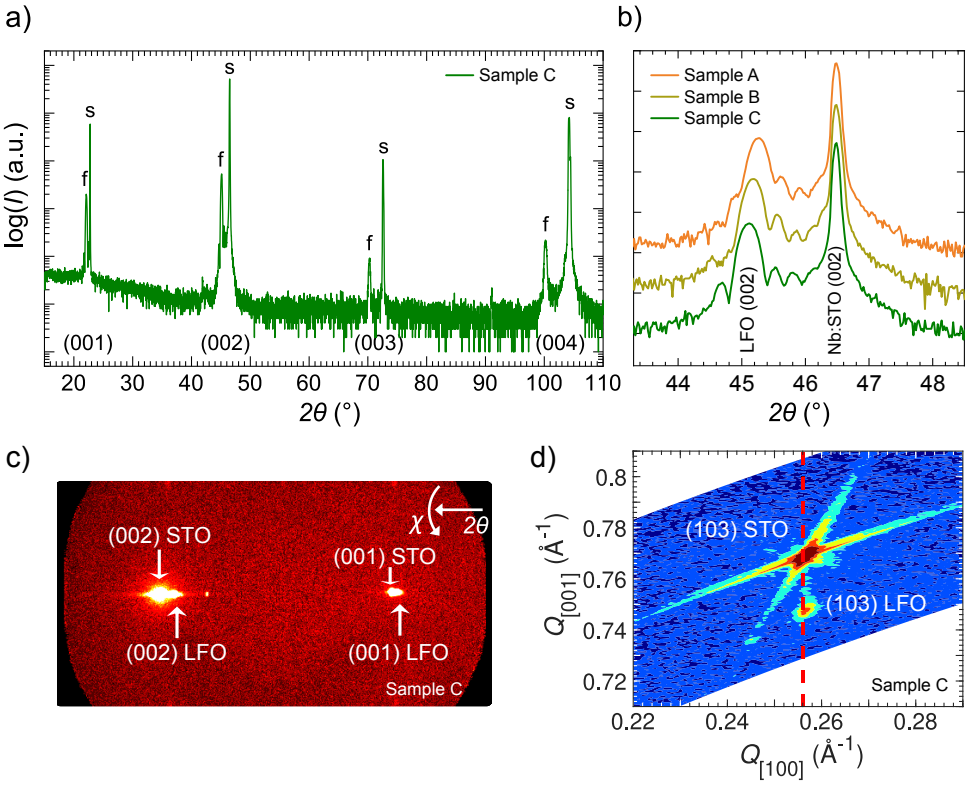

FIGURE 8.9: Illustrative XRD measurements performed on LFO//Nb:STO films. a) $\theta-2\theta$ scan of sample C. b) Zoom of the $\theta-2\theta$ scans around the (002) reflections. c) $2\theta-\chi$ scan of sample C. d) RSM around the (103) reflection of sample C.

The surface morphology was measured by AFM (see Figure 8.10). For every samples, one can observe a very flat surface with low rms roughness of ≈ 3-4 Å (≈ 1 uc). Note that sample A (grown at the lowest pressure and highest temperature) shows a high granularity.

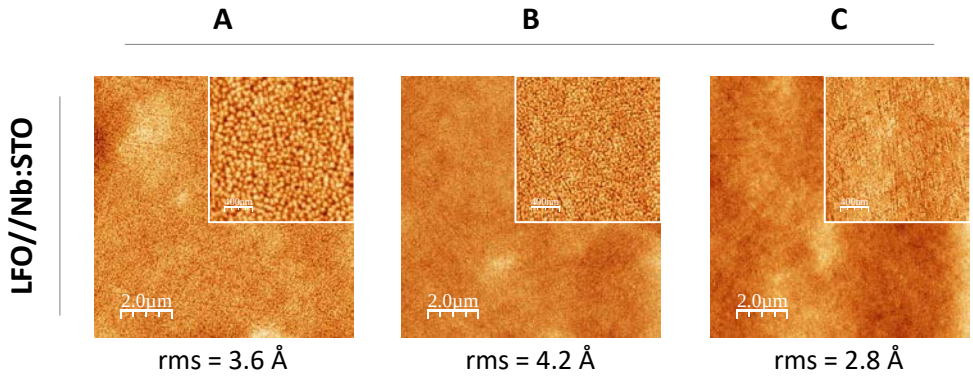

FIGURE 8.10: Surface morphology of LFO films.

From the structural results above, we conclude that all samples show excellent crystallinity and any of the growth conditions investigated is suitable for the growth of flat epitaxial LFO thin films.

Optical properties

The optical properties of LFO films were investigated by spectroscopic ellipsometry. In Figure 8.11a, we show illustrative extracted (n, k) of one LFO film (sample "C"). From its extinction coefficient k, we have plotted in Figure 8.11b the absorption coefficient α (defined as $\alpha = 4\pi k/\lambda$). One can observe an onset of absorption at ≈ 2.5 eV. From the Tauc plots (Fig. 8.11c), we have determined an indirect bandgap of ≈ 2.4 eV and a direct bandgap of ≈ 2.6 eV (Table 8.3). Similar bandgap values were reported in thin films [75, 281, 297] and polycrystals [274, 279], as summarized in Table 8.3.

The absorption peak (Fig. 8.11b) at ≈ 3 eV was attributed to interband transitions from a valence band consisting of hybridized Fe $3d$-e_g majority spin and O $2p$ states to a conduction band comprised of primarily Fe $3d$-t_{2g} minority spin states. The peak at ≈ 4.5 eV was attributed to the excitation of carriers from the valence band to unoccupied minority spin e_g states [297–299].

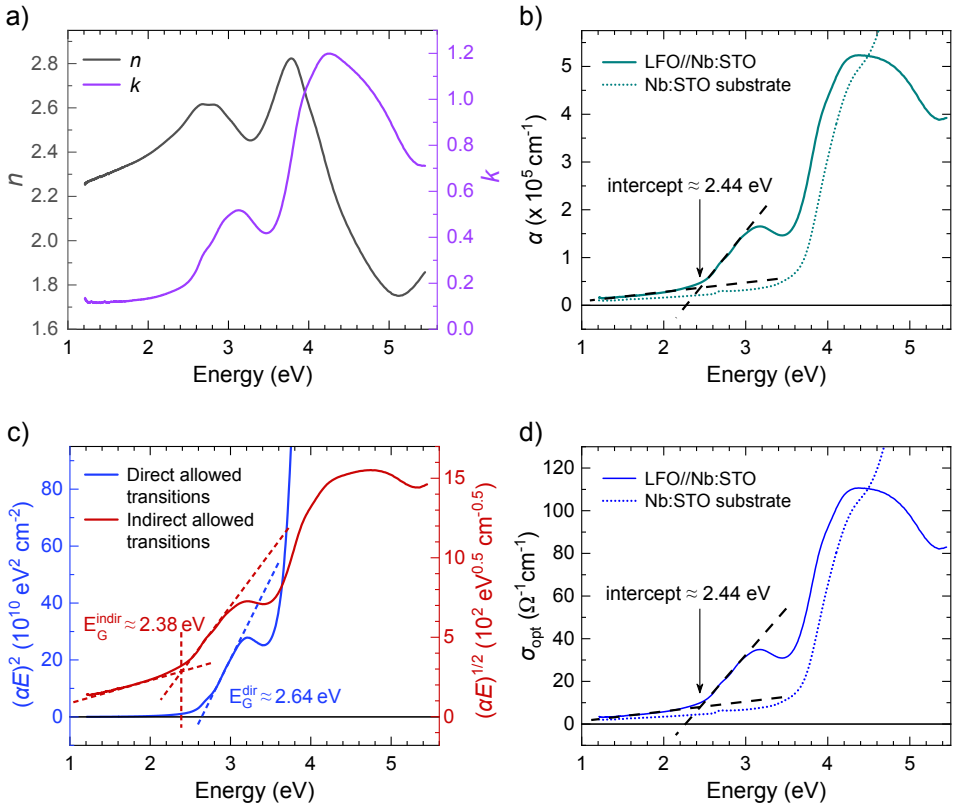

FIGURE 8.11: Optical properties of LFO films. a) (n, k) optical constants of an illustrative LFO film. b) Absorption coefficient α. c) Tauc plots for direct and indirect transitions. d) Optical conductivity σ_{opt}.

It is worth noticing that many publications use ≈ 2.1 eV as band gap of LFO [77, 280, 281], supporting this choice either by the value determined for polycrystals by Arima et al. [274, 279] or by their own ellipsometry measurements. First, it is worth mentioning that Arima et al. determined the bandgap via the onset of the increase of the optical conductivity (itself derived from optical reflectivity measurements). The optical conductivity σ_{opt} is directly related to the absorption coefficient α by the relation:

$$\sigma_{\text{opt}} = \frac{c\,\varepsilon_0}{4\,\pi}\,\alpha \tag{8.1}$$

where c is the velocity of light in vacuum and ε_0 the vacuum permittivity [277]. It is thus obvious from Equation 8.1, that determining the bandgap by the linear intercept of α (as done in Fig. 8.11b) or σ_{opt} (Fig. 8.11d) is equivalent. By doing so, we have determined a value of 2.45 eV, somehow higher than the 2.1 eV from Arima et al. and interestingly equal to the value reported by Scafetta et al. [297].

This latter has also determined similar values of direct and indirect bandgaps than ours (from the Tauc plots shown in Fig. 8.11c).

In conclusion, in our LFO thin films, a bandgap value $E_G \approx 2.4-2.5$ eV seems to be a more realistic value than the usual 2.1 eV found in literature.

Sample type	Band gap (eV)				
	Indirect allowed	Direct allowed	Direct forbidden	Absorption coeff. α	Optical conduct. σ_{opt}
Dense polycrystals [274, 279]	–	–	–	–	2.1
MBE thin films [297]	2.25	2.64	–	–	2.45
MBE thin films [75]	–	–	2.3	–	–
PLD thin films [281]	–	–	–	2.25	–
PLD thin films [77]	2.1	3.6	–	–	–
PLD thin films (this work)	2.38 (2.1)	2.64	2.73	2.44 (2.25)	2.44

TABLE 8.3: Summary of LFO bandgap values reported in literature and determined in this work, for dense polycrystalline samples (measured by optical reflectivity) and thin films (measured by spectroscopic ellipsometry). When two values are specified, the first one is determined by the dashed lines shown in the corresponding figure, while the one in parenthesis is taken from the intercept at "$y = 0$". The first method seems more reliable as it ensures that no remaining spurious substrate component (in spite of the film (n, k) extraction) interfere in the bandgap determination.

In conclusion of this section, we have successfully deposited epitaxial LFO thin films with high crystalline quality and flatness, which is ideal for integration in heterostructures. The measured bandgap (≈ 2.5 eV) is similar to reported values for MBE- and PLD-grown thin films and somehow bigger than reported values in polycrystals.

8.2 Photoresponse in all-oxide and oxide/metal multilayers

In this section, we describe the fabrication and characterization of multilayers with metal-insulator-metal (MIM) structure, where the insulating layer is either LFO or LVO.

8.2.1 $LaFeO_3$-based multilayers

To study the photoresponse and photovoltaic potential of LFO, the latter was sandwiched between two electrode materials: LSMO was used as bottom electrode and BLSO, SVO or Pt as top electrodes (TE), as sketched in Figure 8.12. The electrodes thickness was kept constant (27 nm for LSMO, 40 nm for BLSO and SVO, and 7 nm for Pt), while three LFO thicknesses were used: 50, 100 and 200 nm. The whole structure was deposited onto (001) LSAT single-crystal substrates. The growth conditions of LFO are the ones of sample C described in Section 8.1.2. LSMO was deposited at $PO_2 = 0.01$ mbar and $T = 725$ °C (see [83] for growth optimization). SVO was deposited at $P(Ar) = 0.03$ mbar and $T = 700$ °C. The growth conditions of BLSO and Pt are given in Appendix C and Section 2.1.2 of the methodology chapter, respectively. For a given LFO thickness, two LSAT substrates were placed on the heater. The LSMO and LFO layers were first deposited and then removed from the PLD chamber. There, a shadow mask for Pt sputtering was placed ex-situ on top of one of the LSAT/LSMO/LFO substrate, and a shadow mask for oxide electrodes was placed onto the other substrate (see Chapter 2 for more details on device fabrication). The Pt electrodes were 60x60 µm², while the oxide electrodes were either 100x100 µm², 200x200 µm² squares or round shapes with 100/200 µm diameter.

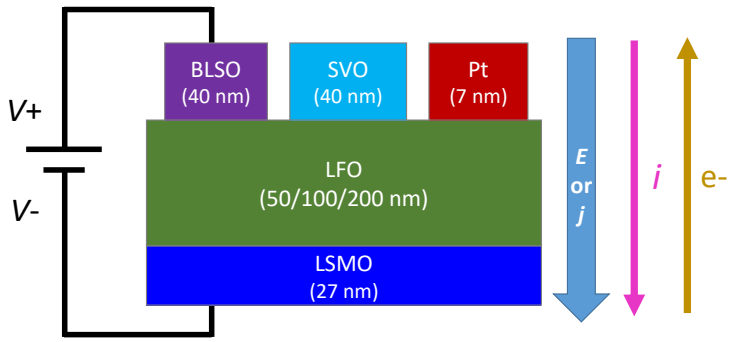

FIGURE 8.12: Sketch illustrating the LFO-based MIM devices fabricated for electrical characterization. The bottom electrode was always connected to the ground. The current convention is shown for a positive bias voltage ($V_{bias} > 0$), for which a positive voltage is applied on the top electrode, thus corresponding to an electron (resp. hole) flow from the bottom to the top (resp. from the top to the bottom) of the device.

Structural characterization

In Figure 8.13a, we show an illustrative $\theta-2\theta$ scan of LSAT/LSMO/LFO/Pt heterostructure (with t_{LFO} = 50 nm). It shows good crystallinity with c-axis of LSMO ($\approx$ 3.87 Å) and LFO (4.017 Å) similar than those of single layers of similar thicknesses (see [83] for LSMO and Section 8.1.2 for LFO). Laue fringes of the (001) LFO reflection are slightly visible which confirms the high crystallinity with flat interface/surface. Note that Pt electrodes are deposited at RT and therefore are typically polycrystalline. Their poor crystallinity plus the fact that they represent few diffracting volume make that no diffraction spot is observed (within the resolution of the diffractometer, and for this measurement geometry). An illustrative RSM (Figure 8.13b) shows that the LSMO and LFO (50 nm) layers are fully strained to the LSAT substrate.

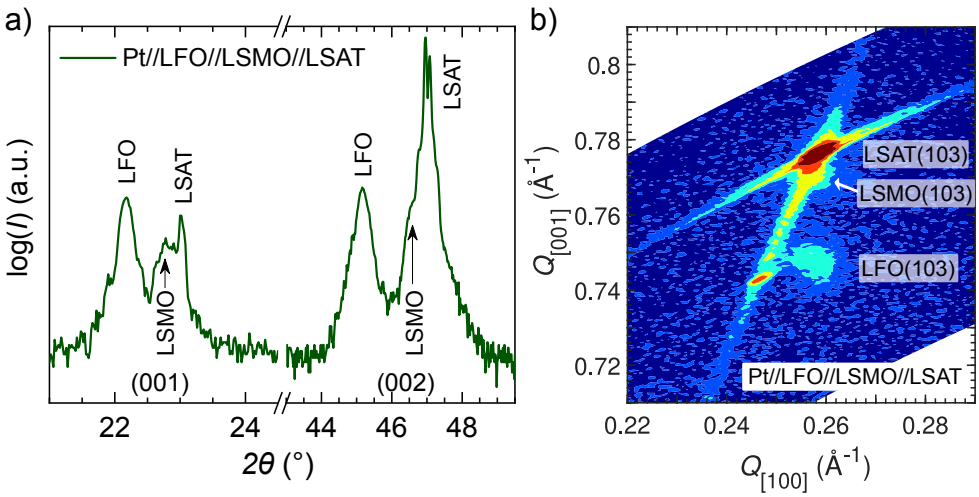

FIGURE 8.13: a) XRD $\theta-2\theta$ scan of an illustrative sample of 50 nm LFO with Pt TE. b) Corresponding RSM around the (103) substrate reflection.

J-V characteristics in dark

Exploring the electrical properties of the heterostructures without external stimuli (such as light) can be very instructive to understand the mechanisms responsible of their eventual photoresponse. Therefore, $I-V$ characteristics were measured in complete darkness, where the sample was covered for several hours (usually overnight) prior measurement to avoid contribution of eventual photo-excited carriers. A bias voltage V_{bias} ranging from -1 V to +1 V was applied on the top electrode. The LSMO bottom electrode was connected to the ground (see sketch

Figure 8.12). For better comparison between samples, the resulting current I through the heterostructures was divided by the electrode area to convert it in density of current J.
In Figure 8.14a,c,f,h, we show the $J-V$ curves of the LSMO/LFO/BLSO devices. It is clear (e.g. for t_{LFO} = 50 nm) that there is an asymmetry between negative and positive bias voltage. It is strongly rectifying (conducting) at negative forward bias, with a current density J about one of magnitude bigger than at positive bias voltage. The rectifying behavior is nearly identical for any thickness. Moreover, it can be appreciated that the overall conductivity decreases when the thickness of LFO increases.
On the contrary, we observe nearly symmetric $J-V$ curves when using SVO (Fig. 8.14d,i) or Pt (Fig. 8.14b,e,g,j) top electrodes. The current flowing through the device is also higher (at a given thickness), indicating smaller Schottky barrier for hole (majority carrier) injection at the LFO/Pt and LFO/SVO contacts, compared to the LFO/BLSO contact.

In order to understand the conduction mechanisms in LFO capacitors, it can be instructive to study the variation of the leakage current with bias voltage. Child's law states that, if the leakage current is dictated by the carrier mobility through the dielectric layer, this resulting space-charge-limited current (SCLC) varies with V^2 as:

$$J = \frac{9\varepsilon\mu V^2}{8t^3} \tag{8.2}$$

where ε is the permittivity of the insulating material, μ its carrier mobility, and t is the film thickness.
In Figure 8.15a-b, we have plotted $\log(J)$ vs $\log(V)$ of some illustrative samples. At high voltage the curve is linear with a slope of $\approx 2.1-2.5$, as expected from Equation 8.2. The small deviation from the ideal value of 2 may indicate the presence of trap states either at the LFO/electrode interface or in the bulk of LFO [78]. Therefore, the $\log(J)$ vs $\log(V)$ plots have the typical shape of space-charge-limited current characteristics. In Figure 8.15c-d, we have also plotted J vs V^2 of the same samples and extracted the slope of the linear part at high voltage.

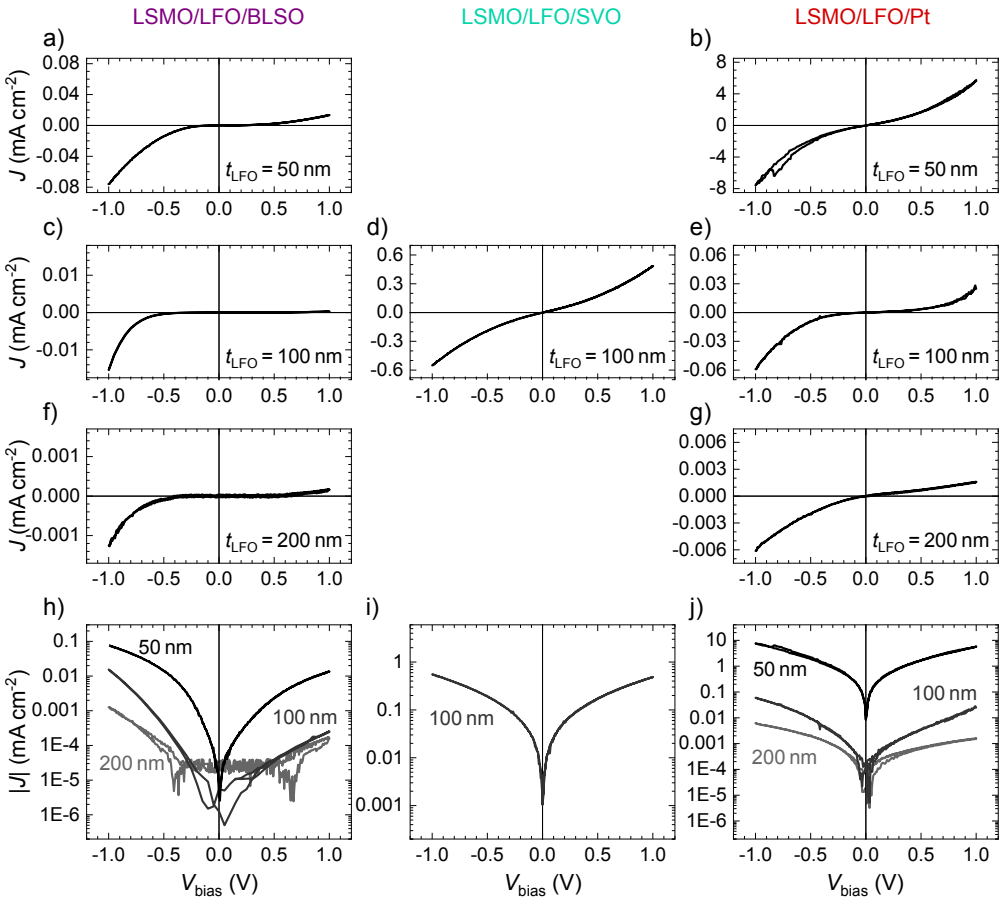

FIGURE 8.14: $J-V$ characteristics measured in dark of: (a,c,f) LSMO/LFO/BLSO, (d) LSMO/LFO/SVO, and (b,e,g) LSMO/LFO/Pt heterostructures. In (h,i,f) the corresponding $abs(J)-V$ plots are gathered to emphasize the symmetric/asymmetric curve shape. All graphs have same units, i.e. J in mA cm^{-2} and V_{bias} in volts.

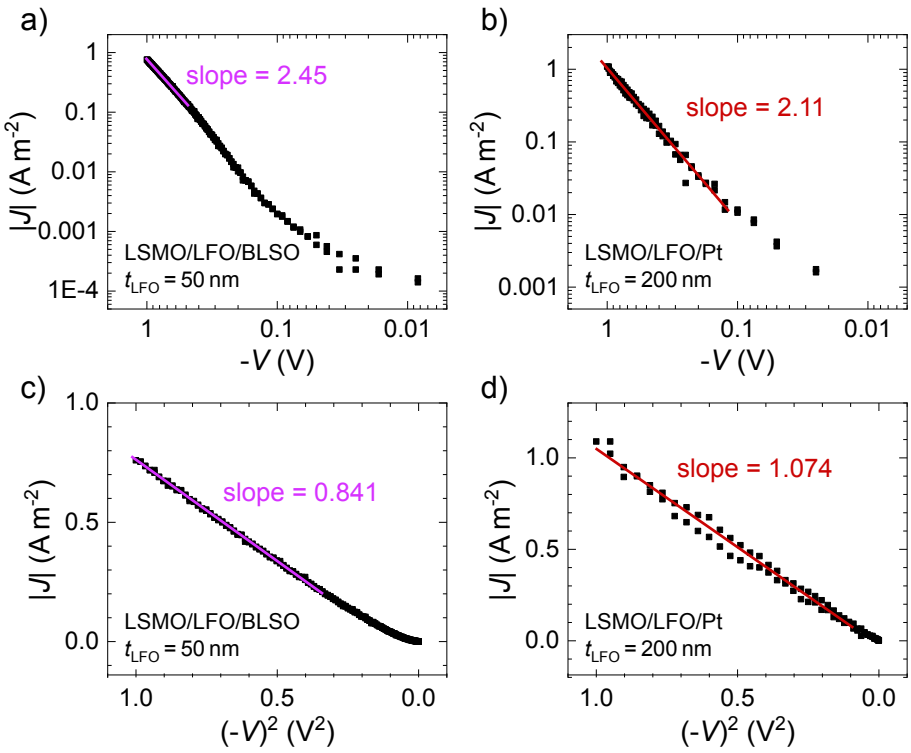

FIGURE 8.15: Illustrative plots of: a,b) $|J|$ vs $-V$ in log scale to emphasize that the V^2 term dominates in a substantial region (at negative bias voltage). c,d) $|J|$ vs $(-V)^2$.

The slope of the J *vs* V^2 plots in the linear region was extracted for samples with different TE and thickness. By using Equation 8.2 and the reported dielectric permittivity $\varepsilon = 35$ for LFO [281], one can extract the carrier mobility of the LFO layer, as summarized in Figure 8.16. The mobility values are in the range $3\times10^{-9} - 3\times10^{-7}$ cm^2 V^{-1} s^{-1}. No report of mobility was found in literature for comparison. However, considering that holes are probably the majority carriers in LFO [298, 300–302], one could thus expect such low carrier mobility[4]. Furthermore, Li et al. reported a mobility of $\approx 10^{-5}$ cm^2 V^{-1} s^{-1} in (Ba,Sr)TiO_3 (BST) thin films by using a similar data analysis protocol [78].

[4]In the following we consider fully depleted (insulating) LFO layers. However, these references suggest that LFO single-crystals and thin films tend to be p-type upon doping by growth-induced defects. In such p-type TMOs, holes are indeed located in the localized O $2p$ orbitals, hence responsible of their low mobility.

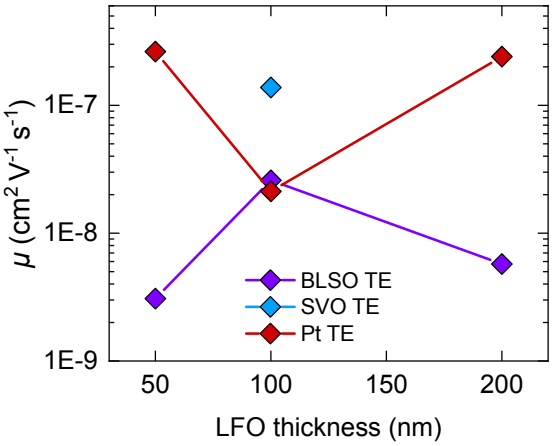

FIGURE 8.16: Compilation of mobility values extracted from the $J-V$ characteristics, using Equation 8.2.

Predicted band alignment in $LaFeO_3$-based multilayers

Based on the previous observations, it is obvious that the nature of the top electrode has a crucial role on the shape of the $J-V$ curve. When using BLSO as top electrode, the capacitor is strongly rectifying (conducting) at negative bias. On the other hand, both SVO or Pt TE give nearly symmetric $J-V$ characteristics (Figure 8.14). These results presume of the presence of a nonzero built-in potential V_{BI} through the LSMO/LFO/BLSO structure, which should be much smaller in LSMO/LFO/SVO and LSMO/LFO/Pt devices.

As well summarized by Lopez-Varo et al. [272], when an insulating (or semiconducting) material is sandwiched between two metallic electrodes having work functions ϕ_1 and ϕ_2, a built-in potential V_{BI} emerges, such that:

$$V_{BI} = \frac{\phi_1 - \phi_2}{q} \tag{8.3}$$

with q the positive elementary charge. In the following, we have used the reported work function (WF) of each material and, using Equation 8.3, we have calculated a rough estimation of the built-in potential V_{BI} through each heterostructure.
In literature, there seems to be a good agreement for the reported work functions of LSMO ($\phi_{LSMO} = 4.8\,eV$ [303–305]), Pt ($\phi_{Pt} = 5.6\,eV$ [306–311]) and, with fewer references encountered, SVO ($\phi_{SVO} = 4.5\,eV$ [218]). However, there is few report on the work function of BLSO. Baniecki et al. performed in-situ XPS/UPS of BLSO thin films [312]. They report an ionization potential $I_P \approx 7.5\,eV$ (distance from the

top of the valence band to the vacuum level[5]), and from their band diagram one can deduce $\phi_{BLSO} \approx 4.2\,eV$. Other references report an electron affinity $\chi \approx 4.2\,eV$ (distance from the bottom of the conduction band to the vacuum level[5]) in the undoped $BaSnO_3$ parent [314, 315], which could be considered as an approximation of the (doped) BLSO WF; in particular if we assume that the doping shifts the Fermi level near the conduction band minimum. In the following, we have thus used 4.2 eV as an estimation of the BLSO WF.

Based on the different electrodes WF, the resulting V_{BI} predicted by Equation 8.3 are:

- In LSMO/LFO/BLSO structure: $(V_{BI})_{BLSO} = 0.6\,eV$ (Fig. 8.17a),
- In LSMO/LFO/SVO structure: $(V_{BI})_{SVO} = 0.3\,eV$ (Fig. 8.17b),
- In LSMO/LFO/Pt structure: $(V_{BI})_{Pt} = -0.8\,eV$ (Fig. 8.17c).

On the other hand, the LFO bandgap was determined in Section 8.1.2 ($\approx 2.5\,eV$) and the LFO electron affinity $\chi_{LFO} = 3.3\,eV$ was found in literature [316]. In Figure 8.17, we summarize the band alignment of the different heterostructures after contact (equalization of the Fermi levels). For the sake of clarity, we have assumed a fully depleted LFO layer (flat bands), which does not hamper the following discussions and interpretations of the results.

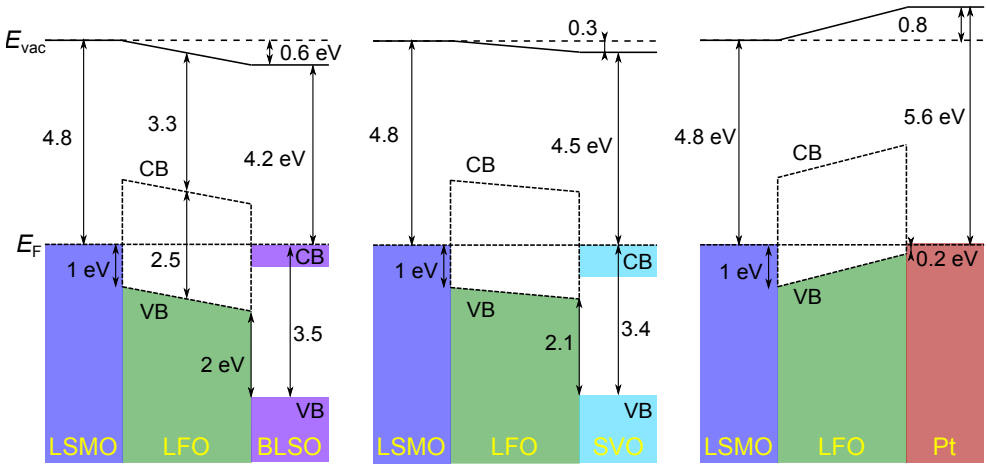

FIGURE 8.17: Theoretical energy band alignment in MIM multilayers of this work. All units are eV. The LFO layer is assumed to be fully depleted (flat bands) for sake of clarity.

[5]For the definition of ionization potential I_P, electron affinity χ, and work function ϕ in a transparent conducting oxide, one may want to consult the didactic reference [313].

In Figure 8.17a, we have predicted the presence of a built-in electric field through the LSMO/LFO/BLSO structure (with $(V_{BI})_{BLSO} = 0.6\,eV$), similar to the one observed in a classical pn junction. In such capacitor, we have a rectifying behavior at negative bias voltage (applied to the TE; see convention used here in Fig. 8.12). This is fully consistent with the shape of the measured dark $J-V$ curves shown in Fig. 8.14a,c,f,h. In Figure 8.18, we show how the band diagram of LSMO/LFO/BLSO operating at different bias voltages is modified. In the case of LSMO/LFO/SVO structure, the rectifying behavior is present but very small and the $J-V$ is nearly symmetric (Fig. 8.14d,i), which is also coherent with the small built-in voltage calculated $(V_{BI})_{SVO} = 0.3\,eV$ and thus the predicted band alignment in Fig. 8.17b (considering the eventual small error of the literature-reported LSMO and SVO work functions). Surprisingly, in the case of LSMO/LFO/Pt structure, the high difference of work function between LSMO and Pt (Fig. 8.17c) suggests a built-in potential of opposite sign ($(V_{BI})_{Pt} = -0.8\,eV$) compared to BLSO- and SVO-based structures. Therefore one should expect a rectifying behavior at positive bias voltage, which has not been observed experimentally (Fig. 8.14b,e,g,j). Instead, we observe a small rectifying behavior at negative voltage, similarly to the SVO case. In the following section, we shall study the actual band alignment by XPS measurements.

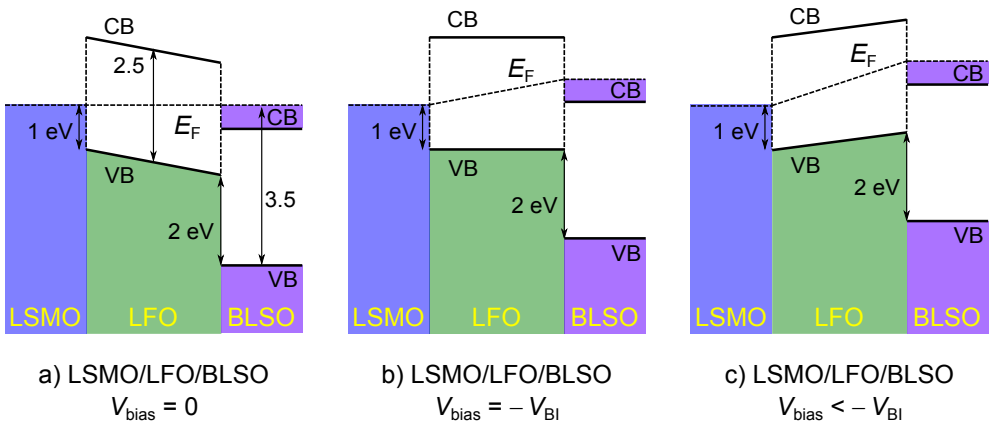

FIGURE 8.18: Energy band diagrams of LSMO/LFO/BLSO capacitors under different bias voltage: a) $V_{bias} = 0\,V$, b) $V_{bias} = -V_{BI}$, and c) $V_{bias} < -V_{BI}$. We recall here that a negative bias voltage results in a flow of electrons (resp. holes) from the top to the bottom electrode (resp. from the bottom to the top electrode).

Measured band alignment in LSMO/$LaFeO_3$/Pt multilayers

In order to validate the predicted band diagrams constructed in the previous section (Fig. 8.17), the valence band offsets (VBOs) at the interfaces between the different consecutive bilayers, namely LSMO/LFO and LFO/Pt, were investigated by XPS. To this aim, we followed the methodology first introduced Kraut, Waldrop et al. [69, 71] and then widely used to determine the VBO at oxide-oxide interfaces [41, 72–77], or the Schottky barrier height for hole injection (ϕ_p) at oxide-metal[6] interfaces [27, 78, 79]. In short (more details are given in methodology Section 2.5.3), at the interface of a bilayer, the valence bands (VB) of both materials, semiconductors or metals, usually overlap. Hence, the measurement of the VB of a bilayer is not enough to determine the VBO between both materials. The method used here consists in measuring the displacement of the core levels (rather than the VB) of the topmost layer of the bilayer, and comparing it to the position of the core levels (CLs) of a reference (a bulk sample of the same material).

The LSMO/LFO interface was first investigated. To this aim, several LSMO/LFO bilayers were measured varying the LFO thickness (1, 3 and 5 nm) deposited on top of a thick LSMO layer. In the thick LSMO layer, 2 CLs were used as reference (Mn 2p, Sr 3d) and their distance to the VBM (at ≈ 0 eV) were measured (as illustrated in Figure 8.19a). Similarly 2 CLs were chosen in the film LFO (Fe 2p and Fe 3p). Choosing several CL for a given material allow to collect several values of VBO and confirm that there is a parallel shift of the topmost layer CLs in comparison to the ones of the bottom layer. Here, by collecting the values for 2 LFO CLs and 2 LSMO CLs, we are able to calculate 4 different VBO values (4 combinations). Indeed, in bilayers of thin LFO film onto LSMO, the distance between one LSMO CL and one LFO CL was calculated and therefore 4 values were also collected, such as illustrated in Figure 8.19b. The corresponding XPS measurements in LSMO and LFO thick layers and LSMO/LFO interfaces are shown in Figure 8.20. The calculation of the VBO (ΔE_{VBM}) is based on the following equation:[7]

$$\begin{aligned}\Delta E_{VBM} = (E_{LFO-CL} - E_{VBM})^{thick-LFO} - (E_{LSMO-CL} - E_{VBM})^{thick-LSMO} \\ - (E_{LFO-CL} - E_{LSMO-CL})^{interface}\end{aligned} \tag{8.4}$$

[6] In the case of a metal, the valence band maximum is equal to the Fermi energy

[7] also shown at the bottom of Figure 8.20 with the color code associated to the measured sample.

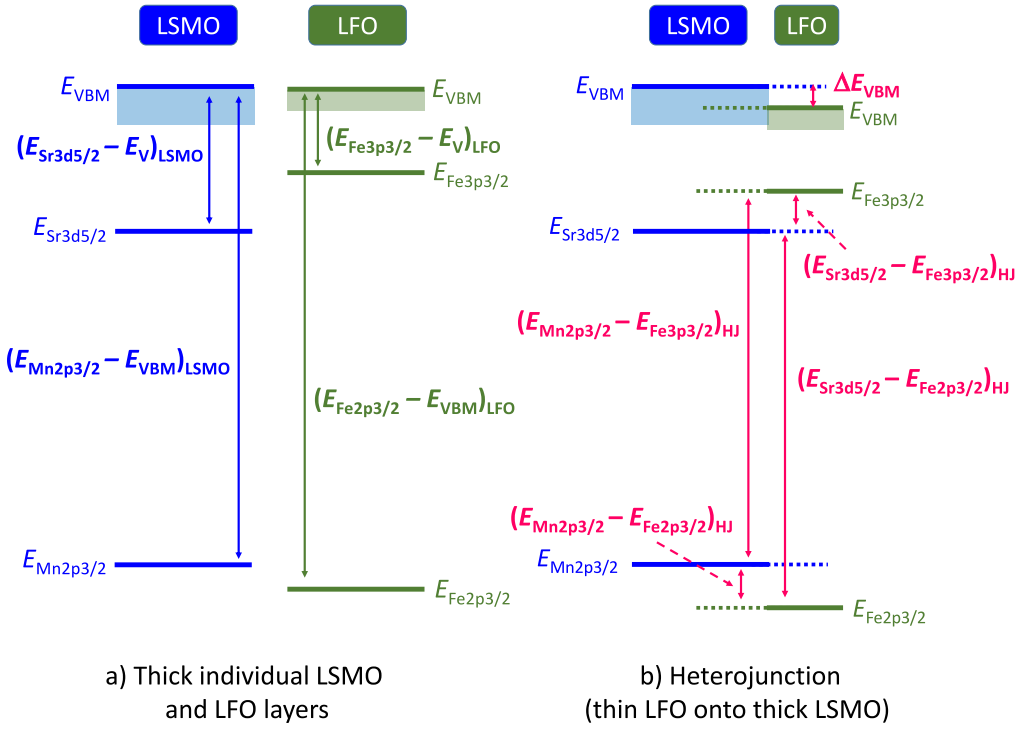

FIGURE 8.19: Sketch illustrating the core levels and valence band measured by XPS, in: a) LSMO and LFO thick single layers, and b) LSMO/LFO interface.

In Table 8.4, we have gathered the 4 VBO values obtained using Equation 8.4, for each sample, and their average value. In the case of 1 nm LFO//LSMO, for example, one can observe that these values are nearly identical and equal to −1 eV (considering the precision of ≈ 0.1 eV of this method) and the average value of −1.06 eV given in the last column will be considered as the VBO for this sample (1 nm LFO//LSMO). In the samples of 3 nm and 5 nm of LFO onto LSMO, similar VBOs were measured. Note that the Mn 2*p* CL has disappeared in the thickest sample, which could be expected considering the inelastic mean free path of electrons originating from this CL.

Interestingly, the average measured VBO between LSMO and LFO valence band maxima is equal, for all LFO thicknesses, to $\Delta E_{VBM} \approx -1$ eV. The negative sign indicates that the $(VBM)_{LFO}$ is below $(VBM)_{LSMO}$. This result is in perfect agreement with our prediction made in Figure 8.17 of the previous section. Moreover, the fact that this value is independent of the LFO thickness presumes of a negligible band bending at the interface.

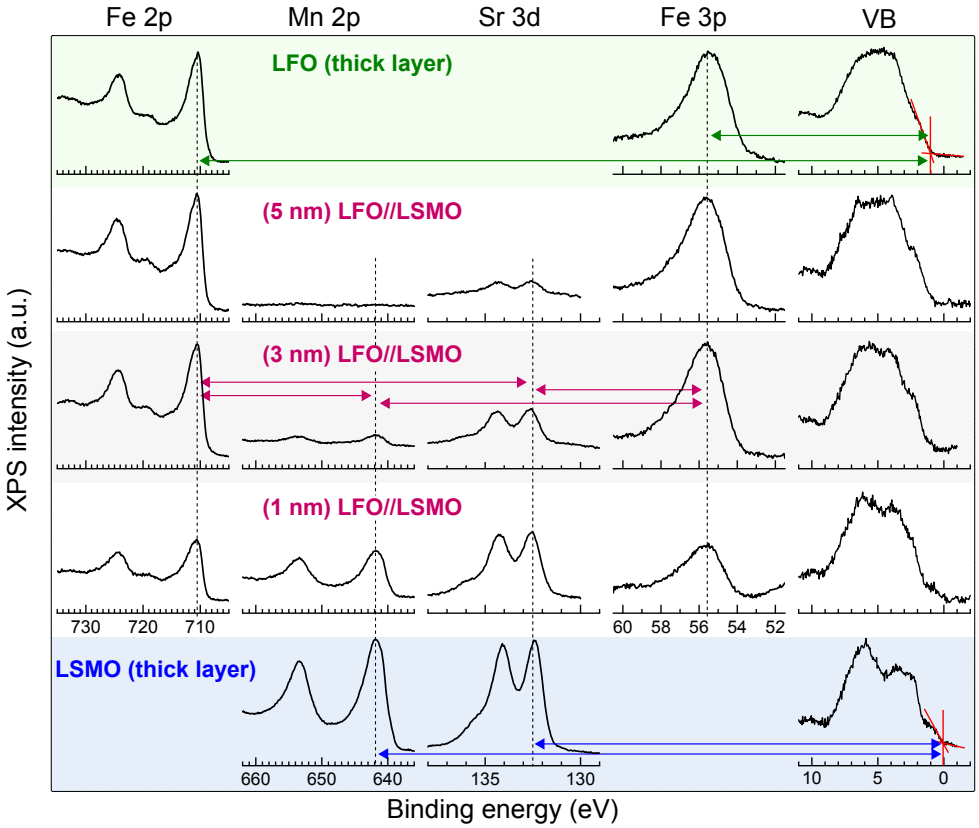

FIGURE 8.20: XPS study of the VBO at the LSMO/LFO interface, as a function of LFO coverage (1, 3 or 5 nm).

LFO thick.	VBO ΔE_{VBM} (eV)				
	Fe $2p \rightleftharpoons$ Mn $2p$	Fe $2p \rightleftharpoons$ Sr $3d$	Fe $3p \rightleftharpoons$ Mn $2p$	Fe $3p \rightleftharpoons$ Sr $3d$	Average
1 nm	−1.06	−1.12	−1.01	−1.07	−1.06 ± 0.06
3 nm	−1.04	−1.00	−1.02	−0.98	−1.01 ± 0.03
5 nm	x	−1.07	x	−1.02	−1.04 ± 0.03

TABLE 8.4: Summary of VBOs measured at the LSMO/LFO interface as a function of LFO coverage. The first four columns indicate the VBOs for each pair of CL, while the last one gives the average value.

We turn now to the topmost interface of the LSMO/LFO/Pt capacitor, for which the same methodology was applied. Three different LFO/Pt interfaces were deposited with a Pt coverage of 1, 2 and 3 nm (note that for 5 nm, the LFO CLs had completely disappeared). The PLD-deposited LFO film was transferred in-situ to the sputtering chamber to avoid surface contamination. As summarized in Figure 8.21, three LFO CLs (La $3d$, Fe $2p$ and La $4d$) and one Pt CL (Pt $4f$) were measured, leading to 3 VBOs values for each sample. The Table 8.5 gathered all the different VBO values calculated for different pairs of CLs and using the following equation:[8]

$$\begin{aligned}\Delta E_{\mathrm{VBM}} = (E_{\mathrm{Pt-CL}} - E_{\mathrm{VBM}})^{\mathrm{thick-Pt}} - (E_{\mathrm{LFO-CL}} - E_{\mathrm{VBM}})^{\mathrm{thick-LFO}} \\ - (E_{\mathrm{Pt-CL}} - E_{\mathrm{LFO-CL}})^{\mathrm{interface}}\end{aligned} \tag{8.5}$$

Once again, one can observe a good agreement between the different pairs of CLs for a given sample. For example, in the case of 1 nm Pt//LFO, all VBO values vary around 0.75 ± 0.03 eV, which confirms the systematical shifts between Pt and LFO CLs. Surprisingly, the VBO measured for thicker Pt coverage (2 and 3 nm) is slightly bigger with $\Delta E_{\mathrm{VBM}} \approx 1.2$ eV. Schafranek et al. [79] report on similar experiments of VBO measurements at the Nb:$SrTiO_3$/Pt and (Ba,Sr)TiO_3/Pt interfaces. They observed a similar shift in barrier height (for electrons) when the Pt coverage was ≤ 1 nm and attributed it to an eventual incomplete Pt layer (small islands not yet coalesced) at the beginning of the deposition. They also observed a nearly constant barrier height for Pt thicknesses > 1 nm and considered this value as the actual one. Therefore, here we consider the VBO (barrier height for holes) between LFO and Pt to be $\Delta E_{\mathrm{VBM}} \approx 1.2$ eV, where the positive sign indicates that the Fermi energy of Pt is above the VBM of LFO.

[8] also at the bottom of Fig. 8.21 with color code indicating which measurement gives which value.

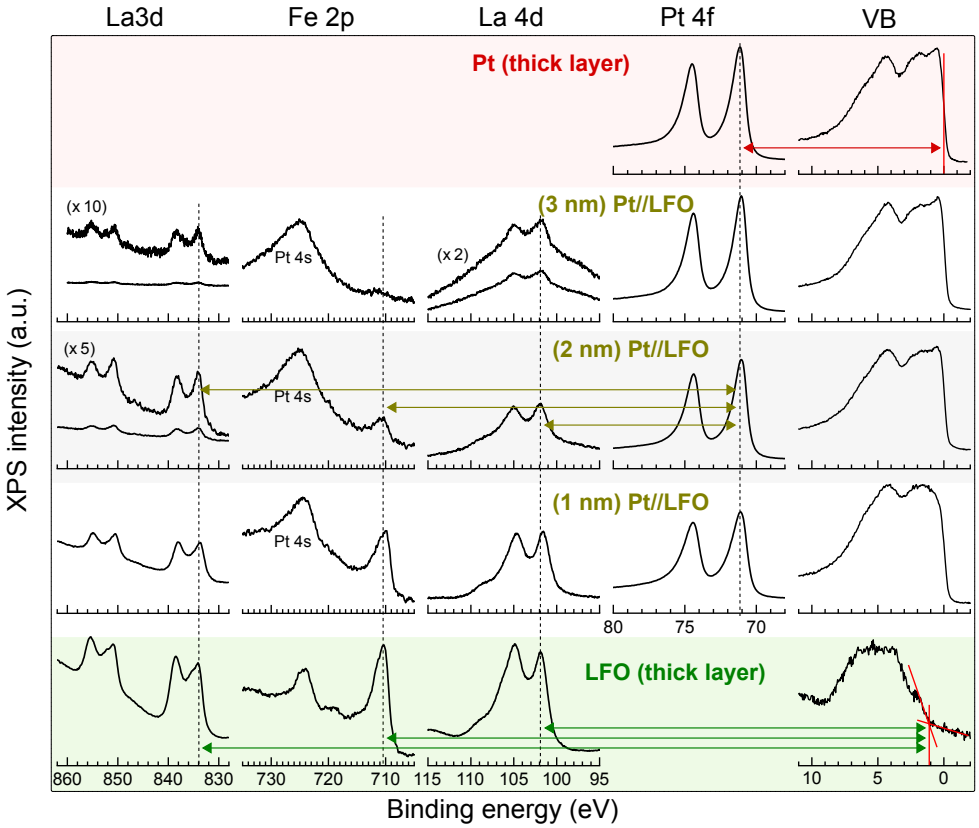

FIGURE 8.21: XPS study of the VBO at the LFO/Pt interface, as a function of Pt coverage (1, 2 or 3 nm).

Pt thickness	VBO ΔE_{VBM} (eV)			
	Pt $4f \rightleftharpoons$ La $3d$	Pt $4f \rightleftharpoons$ Fe $2p$	Pt $4f \rightleftharpoons$ La $4d$	Average
1 nm	0.77	0.72	0.76	0.75 ± 0.02
2 nm	1.17	1.26	1.17	1.20 ± 0.06
3 nm	1.15	x	1.14	1.14 ± 0.01

TABLE 8.5: Summary of VBOs measured at the LFO/Pt interface as a function of Pt coverage.

In Figure 8.22, we summarize the energy band diagrams of the LSMO/LFO/Pt structure. In Fig. 8.22a, we repeat the predicted band alignment done in the previous section (Fig. 8.17c) to compare it to the one determined by XPS (Fig. 8.22b). While the predicted band alignment gave a built-in potential $(V_{BI})_{Pt} = -0.8\,eV$ through the structure, the measured one indicates rather a value of $(V_{BI})_{Pt} = 0.2\,eV$, which is not only a difference of 1 eV, but also induces a change of sign of the latter. Such discrepancy of band alignment between calculations based on the materials' WF and the experimental determination has actually been widely observed when using Pt (or other metals) as top electrode onto some oxide layers. In those cases, this so-called *Fermi level pinning* was attributed to the reduction of the oxide layer at the interface, due to the harsh sputter deposition conditions of the metallic layer [27, 78, 79]. In the present study, further investigation on the nature of the observed Fermi level pinning in LSMO/LFO/Pt would be necessary to deduce any conclusion.

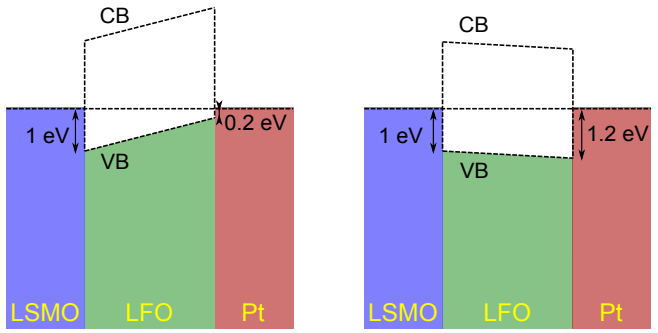

FIGURE 8.22: Energy band diagrams in the LSMO/LFO/Pt heterostructures. a) Predicted alignment. b) Actual alignment measured by XPS.

To the greatest interest, the band alignment measured in LSMO/LFO/Pt (Fig. 8.22b), indicating a small positive built-in potential $\approx 0.2\,eV$, is now in perfect agreement with the dark $J-V$ curves measured in the previous section (Fig. 8.14), which were indicating a small rectifying behavior at negative bias voltage, similarly to the case of LSMO/LFO/SVO capacitors and, with smaller V_{BI}, of LSMO/LFO/BLSO ones.

Measured band alignment in LSMO/$LaFeO_3$/BLSO multilayers

The band alignment in LSMO/LFO/BLSO capacitors was measured by the same method. As the bottom interface is the same than for LSMO/LFO/Pt, the band alignment is expected to be the same, and only additional measurements of the LFO/BLSO topmost interface were needed. Three different LFO/BLSO interfaces were deposited with a BLSO coverage of 2, 3 and 5 nm. Several CLs were measured in BLSO (Ba 3d, Sn 3d and Ba 4d) and LFO (Fe 2p and Fe 3p, but as both gave same sets of VBOs we are showing here only the results using Fe 3p). In Figure 8.23, one can observe a large displacement of the BLSO and LFO CLs in the BLSO//LFO bilayer samples, compared to the thick BLSO and LFO layers. This is attributed to some strong charging of the samples. This charging was neither observed in thick BLSO (because the layer is conducting) nor in thick LFO layer, probably because the latter was deposited on conducting Nb:STO substrate. Here, a 50 nm LFO film was deposited directly onto an (undoped) STO substrate and then the thin BLSO layer was deposited. This charging was neither observed in the LFO/Pt interface probably because Pt is metallic at very thin thickness, while ultrathin BLSO films are probably less conducting than thick films (see appendix Section C.2). Moreover, the peak shifts are not parallel and the resulting sets of VBO calculated for various CLs of a single sample are not equal (see Table 8.6). Similarly, in thin $Ba_{0.6}Sr_{0.4}TiO_3$ (BST) films deposited onto Pt, Schafranek et al. attributed the nonparallel peak shifts to the yet incomplete development of the electronic structure of the topmost material [79].
The following equation[9] was used to calculate the different VBO values:

$$\begin{aligned}\Delta E_{\mathrm{VBM}} = (E_{\mathrm{BLSO-CL}} - E_{\mathrm{VBM}})^{\mathrm{thick-BLSO}} - (E_{\mathrm{LFO-CL}} - E_{\mathrm{VBM}})^{\mathrm{thick-LFO}} \\ - (E_{\mathrm{BLSO-CL}} - E_{\mathrm{LFO-CL}})^{\mathrm{interface}}\end{aligned} \tag{8.6}$$

The average VBO extracted from these measurements, $\Delta E_{\mathrm{VBM}} \approx -2.7 \pm 0.5$ eV (the negative sign indicating that the VBM of BLSO is below that of LFO), is therefore very inaccurate. Nonetheless, it is worth noticing that this value is close to the predicted value calculated above (i.e. -2 eV, as shown, in Fig. 8.17a). These results seem to confirm the presence of a high positive built-in potential in the LSMO/LFO/BLSO heterostructure, responsible of the rectifying current at negative bias voltage.

[9] also at the bottom of Fig. 8.23 with color code indicating which measurement gives which value.

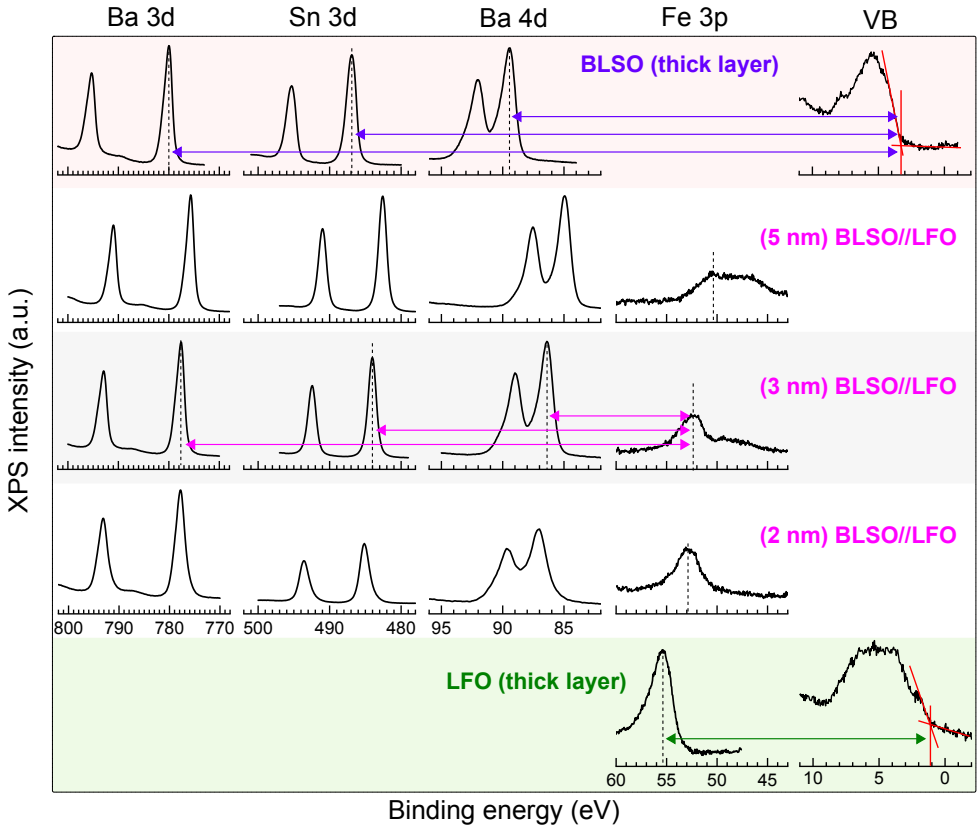

$$\Delta E_{VBM} = (E_{BLSO\text{-}CL} - E_{VBM})^{\text{thick BLSO}} - (E_{LFO\text{-}CL} - E_{VBM})^{\text{thick LFO}} - (E_{BLSO\text{-}CL} - E_{LFO\text{-}CL})^{\text{interface}}$$

FIGURE 8.23: XPS study of the VBO at the LFO/BLSO interface, as a function of BLSO coverage (2, 3 or 5 nm).

BLSO thickness	VBO ΔE_{VBM} (eV)			
	Fe $3p \rightleftharpoons$ Ba $3d$	Fe $3p \rightleftharpoons$ Sn $3d$	Fe $3p \rightleftharpoons$ Ba $4d$	Average
2 nm	−2.61	−2.99	−2.37	−2.66 ± 0.33
3 nm	−2.99	−2.53	−2.34	−2.62 ± 0.37
5 nm	−2.94	−2.91	−2.79	−2.88 ± 0.09

TABLE 8.6: Summary of VBOs measured at the LFO/BLSO interface as a function of BLSO coverage.

Photoresponse in LFO multilayers

As mentioned earlier, bulk LFO is centrosymmetric. Therefore, here the only electric field that could extract photo-excited e-h pairs after separation is resulting from the built-in potential V_{BI} induced by the different electrodes work functions. We have previously shown that by changing the top electrode (TE), one can tune V_{BI}, and that: $(V_{BI})_{BLSO} > (V_{BI})_{SVO} \geq (V_{BI})_{Pt}$. Therefore, one can expect a different photoresponse in LFO-multilayers as a function of TE.
The $J-V$ characteristics under illumination of the LFO-multilayers are presented in Figure 8.24. One can observe the emergence of a photovoltaic effect in all devices, with a nonzero negative open-circuit voltage V_{OC}, consistent with the built-in electric field, and a nonzero short-circuit photocurrent density J_{SC}.

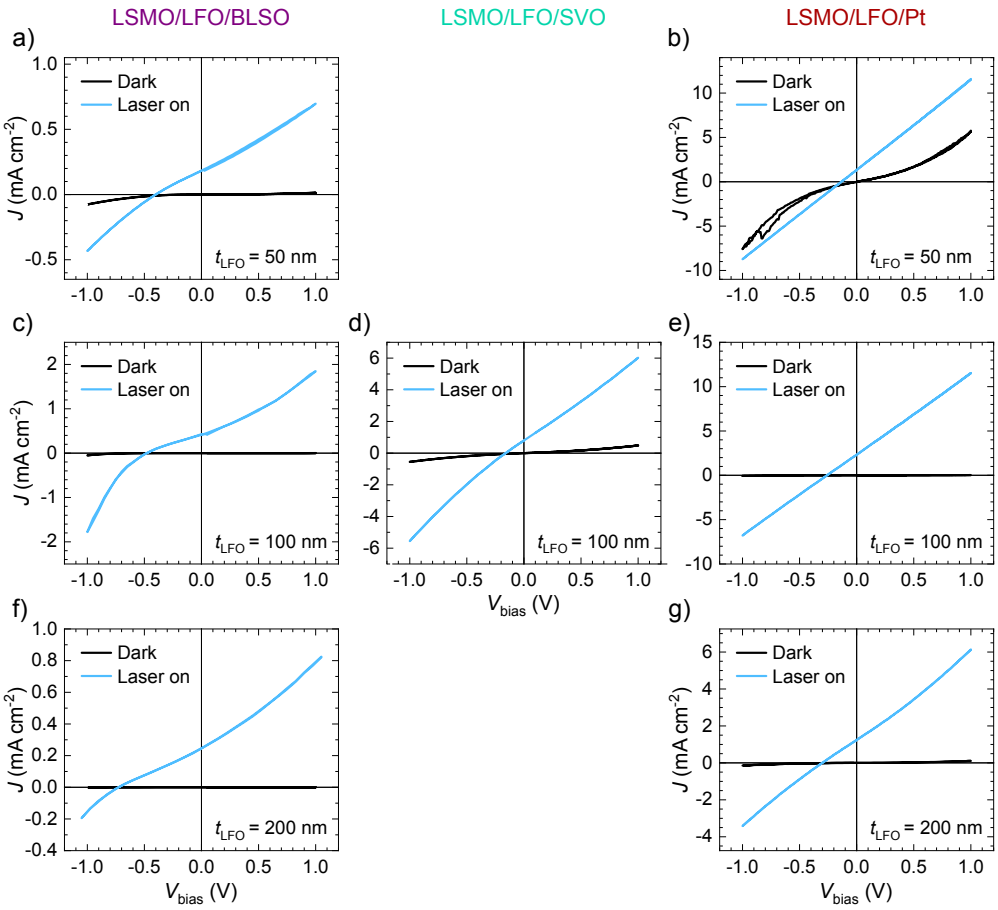

FIGURE 8.24: $J-V$ characteristics measured in dark and under laser illumination of: (a,c,f) LSMO/LFO/BLSO, (d) LSMO/LFO/SVO, and (b,e,g) LSMO/LFO/Pt, for different LFO thicknesses.

To get a further insight on the PV performances of the different heterostructures, the V_{OC} and J_{SC} values have been plotted as a function of LFO thickness. In Figure 8.25b, one can observe an increase of J_{SC} with LFO thickness (in particular for BLSO top electrodes). This increase of J_{SC} is attributed to the absorbance of the LFO layer. Beer-Lambert law predicts a decrease of the transmittance T of a thin film when increasing its thickness t:

$$T(\lambda, t) = \frac{I_T(\lambda, t)}{I_0(\lambda)} = \exp[-\alpha(\lambda)\, t] \tag{8.7}$$

where I_0 and I_T are the intensities of the incident and transmitted light, respectively; and α is the absorption coefficient. From Equation 8.7, one can estimate the absorbance A of the films as:

$$A(\lambda, t) = 1 - T(\lambda, t) \tag{8.8}$$

where we neglect the reflectance for the sake of simplicity. At the laser operation wavelength (405 nm), the absorption coefficient of LFO was found to be $\alpha \approx 1.5 \times 10^{-5}\,\mathrm{cm}^{-1}$ (see Section 8.1.2), so that the absorbance of LFO films can be estimated to: 53 %, 77.7 % and 95 %, for LFO thicknesses of 50, 100 and 200 nm, respectively. Similar value of absorbance was reported by Nakamura K. et al. [280]. In LSMO/LFO/Pt heterostructures, J_{SC} seems to stagnate at $t_{LFO} = 100\,\mathrm{nm}$ and then to decrease again when increasing LFO thickness from 100 to 200 nm. This could be due to an enhanced electron-hole trapping, thus precluding extraction.

It is worth noticing that, in similar capacitor heterostructures, Nakamura M. et al. [281] reported a $|V_{OC}| \approx 0.2\,\mathrm{eV}$ and $J_{SC} \leq 0.05\,\mathrm{mA\,cm}^{-2}$ for a similar laser power density (see Section 2.3.3 of the methodology chapter). Considering that the thickness of their LFO layer was 30 nm, these values roughly compare well with ours.

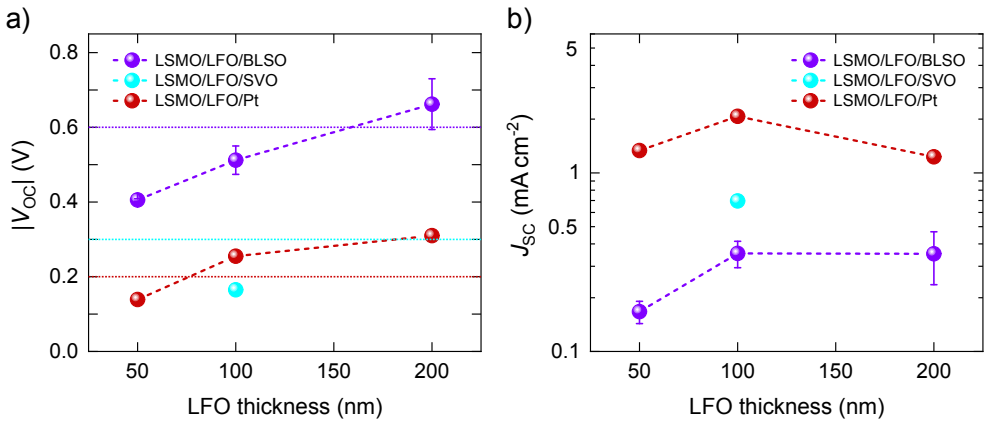

FIGURE 8.25: Photoresponse in LFO multilayers. a) Summary of open-circuit voltage V_{OC} (absolute value), and b) Summary of short-circuit photocurrent density J_{SC}, as a function of LFO thickness. In Fig. a), the dotted lines indicate the built-in potential V_{BI} of the different heterostructures.

On the other hand, the open-circuit voltage V_{OC} of the different heterostructures were plotted in Figure 8.25a.

Interestingly, one can observe that the highest V_{OC} values are obtained in LSMO/LFO/BLSO structures, and are smaller in LSMO/LFO/SVO and LSMO/LFO/Pt ones, which perfectly scales with the built-in potentials V_{BI} determined in the previous sections (and indicated by the dotted lines in the Fig. 8.25a). The small remaining discrepancy between V_{OC} and V_{BI} could be attributed to a small error made in the estimations or measurements of V_{BI}.

Looking at the LFO thickness dependence of $|V_{OC}|$ for the LSMO/LFO/BLSO structures, for instance, we observe a clear increase with thickness. This could be related to the typical expression encountered in diode-like solar cell, which relates V_{OC} and J_{SC} such as:

$$V_{OC} = \frac{m k_B T}{q} \ln\left(\frac{J_{SC}}{J_0}\right) \tag{8.9}$$

where T is the temperature of operation of the solar cell, q is the elementary positive charge, J_0 is a thermal carrier generation term called the dark saturation current density, and m is the diode ideality factor [272, 317, 318]. From Equation 8.9, the increase of J_{SC} with LFO thickness could be responsible of the increase of V_{OC} too. In the case of LSMO/LFO/BLSO for instance, as J_{SC} reaches at maximum for $t_{LFO} = 200\,\text{nm}$ (nearly 100 % absorption of the laser's photons), V_{OC} also reaches its maximum and $V_{OC} \approx V_{BI}$.

8.2.2 $LaVO_3$-based multilayers

In this section, we have studied the electrical and photoresponse properties of LVO-based MIM heterostructures, as sketched in Figure 8.26. In both types of heterostructure a 40 nm thick SVO film was used as bottom electrode (BE). The top electrode (TE) was either a 40 nm SVO layer (as well as the BE), or a 7 nm thick Pt layer. Both TE materials were deposited with shadow masks, as described in Section 2.3.3 of the methodology chapter. SVO layers (resp. LVO) were deposited at $P(Ar) = 0.03$ mbar and $T = 750$ °C (resp. $T = 700$ °C). The growth conditions of Pt are given in Section 2.1.2 of the methodology chapter. The whole structure was deposited on (001) LSAT single-crystal substrates. For a given LVO thickness, two LSAT substrates were placed on the heater. The SVO and LVO layers were first deposited and then removed from the PLD chamber. There, a shadow mask for Pt sputtering was placed ex-situ on top of one of the LSAT/SVO/LVO substrate, and a shadow mask for oxide electrodes was placed onto the other substrate (as described in Section 2.3.3). The Pt electrodes were 60x60 µm², while the SVO electrodes were either 100x100 µm², 200x200 µm² squares or round shapes with 100/200 µm diameter.

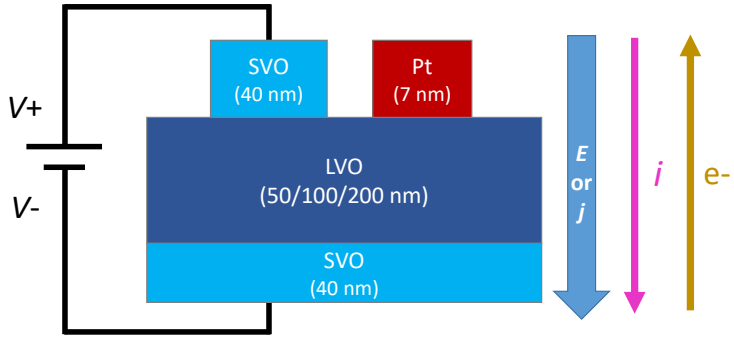

FIGURE 8.26: Sketch illustrating the LVO-based MIM devices fabricated for electrical characterization. The bottom electrode was always connected to the ground. The current convention is shown for a positive bias voltage, for which a positive voltage is applied on the top electrode, thus corresponding to an electron flow from the bottom to the top of the device.

Structural characterization

In Figure 8.27a, we show an illustrative $\theta-2\theta$ scan of a LSAT/SVO/LVO/Pt heterostructure (with t_{LVO} = 50 nm). The (001) LVO reflection is well visible and accompanied by Laue fringes, while the (001) SVO is nearly superposed the the substrate one. The c-axis of LVO (4.036 Å) is slightly higher than for a LVO//LSAT single layer grown in similar conditions (see Section 8.1.1). Laue fringes of the LVO layer are slightly visible which indicates high crystallinity with flat interface/surface. Note that Pt electrodes were not detected due to their lower diffracting volume (within the resolution of the diffractometer in the present measurement geometry). In Figure 8.27b, the RSM of the same sample indicates that both the SVO and LVO (50 nm) layers are fully strained to the substrate. Moreover, the well-defined round spot of LVO presumes of the high crystalline quality of the whole multilayer.

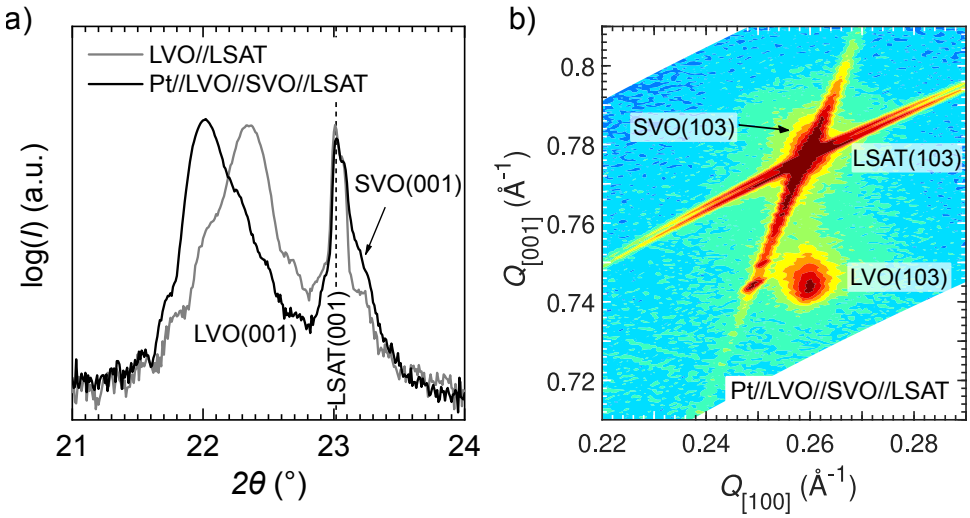

FIGURE 8.27: a) XRD $\theta-2\theta$ scan of an illustrative sample of 50 nm LVO with Pt TE. b) Corresponding RSM around the (103) substrate reflection.

J-V characteristics in dark and under illumination

In Figure 8.28, we show the $J-V$ characteristics of the LVO multilayers with either SVO or Pt electrodes. By first looking at the Fig. 8.28a of SVO/LVO(50 nm)/SVO, one can observe a symmetric dark $J-V$ curve, thus no rectifying behavior. Under illumination the current increases slightly, probably due to photoexcited electron-hole pairs (photoconductive effect). However, no open-circuit voltage V_{OC} nor short-circuit photocurrent I_{SC} are measured. These observations suggest than this device structure has no built-in potential V_{BI}, which is reasonable considering that it has

SVO as bottom and top electrode (as discussed in the following section). Similar $J-V$ curves are measured in SVO/LVO/SVO multilayers with $t_{LVO} = 100/200$ nm (Fig. 8.28c,e). One can also notice that the conductance decreases when increasing LVO thickness, as similarly found in LFO-based multilayers (Figure 8.14).
In the case of SVO/LVO/Pt multilayers (Fig. 8.28b,d,f), similar behavior (no photovoltaic effect) is observed, and the increase of photoconductance under illumination is even negligible. One can also notice that the current flowing through the heterostructure (for a given thickness) is much higher (about two orders of magntitude) than in SVO/LVO/SVO multilayers and that the $J-V$ are nearly linear, indicating a more ohmic contact at the top LVO/Pt interface compared to the LVO/SVO one. At odds with SVO/LVO/SVO multilayers, no significant change of conductance is observed for different LVO thickness.

Band alignment in $LaVO_3$-based multilayers

In Figure 8.29, we have sketched the theoretical band alignment in SVO/LVO/SVO (Fig. 8.29a) and SVO/LVO/Pt (Fig. 8.29b) structures based on the different materials work functions found in literature, and the bandgap of LVO (≈ 1.1 eV [277], see Section 8.1.1). The work functions of SVO and Pt were chosen as 4.5 eV [218] and 5.6 eV [308–310], respectively. Note that some publications of PLD-grown LVO thin films (in similar growth conditions) report a p-type carrier doping [319] while some others report n-type doping [275, 285, 320]. In our sketch, we have assumed an undoped LVO film with Fermi level in the middle of the gap.

It is obvious that in the case of SVO/LVO/SVO structures, by using Equation 8.3, we should expect a zero built-in potential $(V_{BI})_{SVO} = 0$ eV, with no rectifying behavior. At this point, it is worth mentioning that Li et al. [78] have shown a rectifying behavior (asymmetric IV curves) in ITO/BST/ITO capacitors and concluded that the deposition sequence affects the barrier height for electron injection, which is thus different at ITO/BST and BST/ITO interfaces. They also report a similar effect in Pt/BST/Pt capacitors. Nevertheless, here no rectifying $J-V$ curve was measured in dark and no photovoltaic effect (zero open-circuit voltage and zero short-circuit photocurrent) was neither observed, that could attributed to a negligible built-in potential.

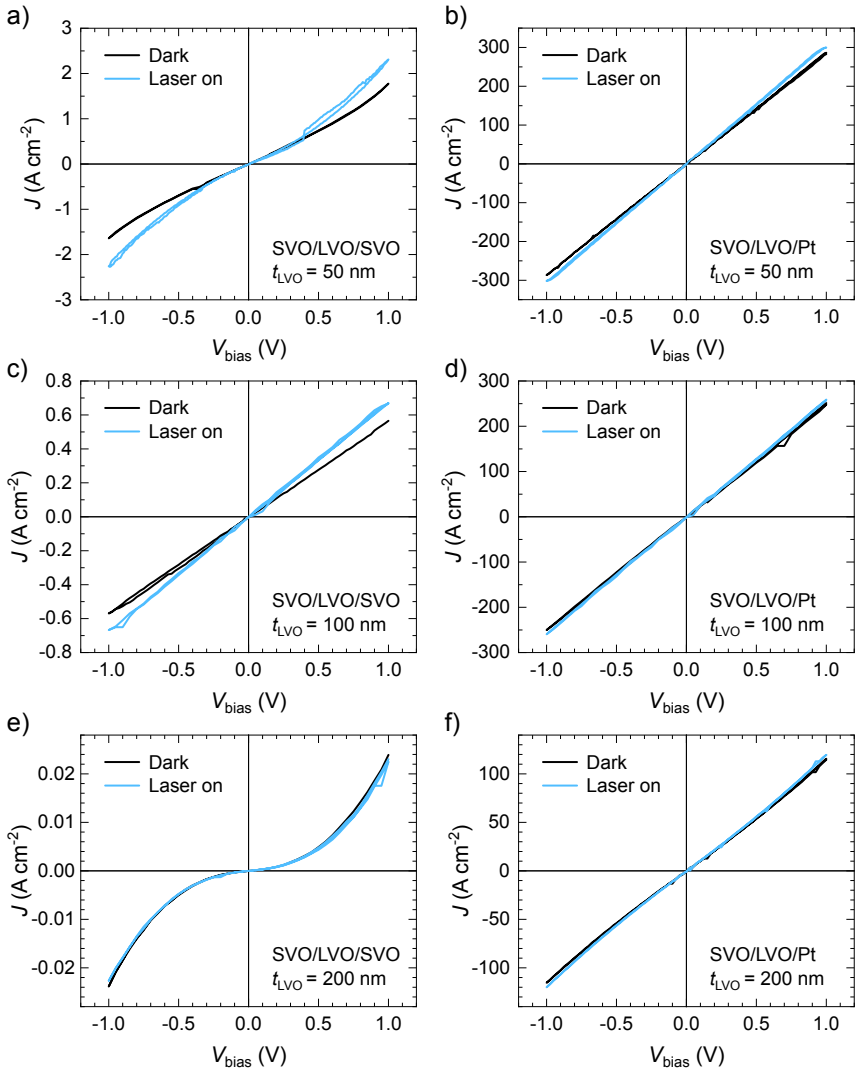

FIGURE 8.28: $J-V$ characteristics measured in dark and under laser illumination of: (a,c,e) SVO/LVO/SVO, and (b,d,f) SVO/LVO/Pt multilayers; for various LVO thicknesses: 50 nm (a-b), 100 nm (c-d), and 200 nm (e-f).

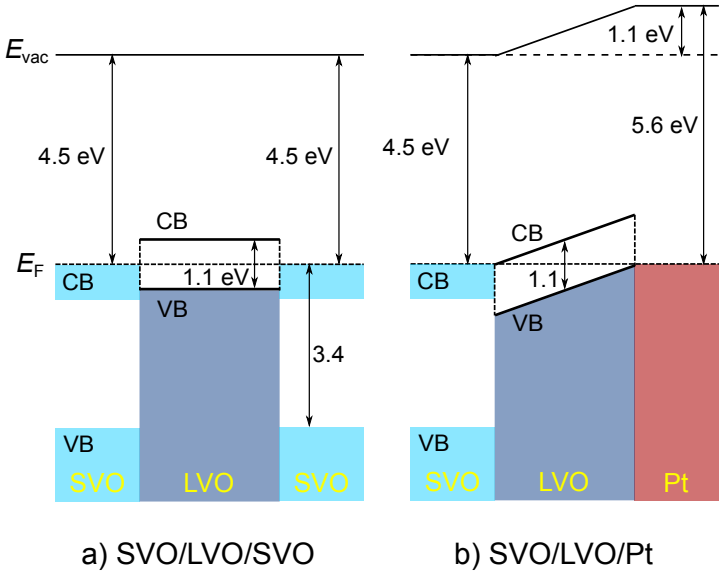

FIGURE 8.29: Theoretical energy band diagrams of LVO-based MIM multilayers using either a) SVO TE, or b) Pt TE. The LVO layer is assumed to be fully depleted (flat bands) for sake of clarity. All units are eV.

On the other hand, in the case of SVO/LVO/Pt structures, one should expect a built-in potential $(V_{BI})_{Pt} = -1.1$ eV (as shown in Fig. 8.29b) and therefore a photovoltaic effect could have been observed. However, as already mentioned in the previous section the conductance of SVO/LVO/Pt heterostructures is too high as an ohmic response is observed. Therefore, the barrier at LVO/Pt interface is not as predicted (and sketched in Fig. 8.29b). In similar device architecture Nb:STO/LVO/Au, Wang et al. reported rectifying $J-V$ curves. However, no photovoltaic effect was observed in this device and the authors attributed it to the poor diffusion of the carriers before recombination, therefore not reaching the electrode materials [282]. In our case the nonobservation of a photovoltaic effect could be attributed to the high recombination rate, as reported by Wang et al. and/or an eventual Fermi level pinning at the LVO/Pt interface (see Fig. 8.30), similarly to what has been observed in LSMO/LFO/Pt devices in the previous Section 8.2.1, and as reported when using metal electrodes on BST [78, 79], or PZT [27]. The observed nonrectifying dark $J-V$ curves go in the same direction of a negligible built-in potential due to Fermi level pinning or else.

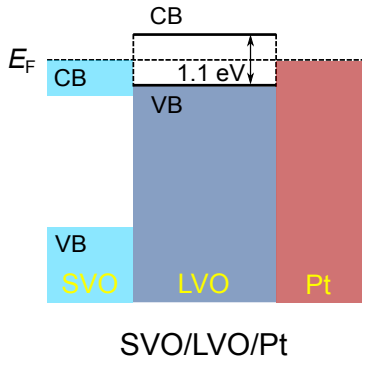

FIGURE 8.30: Possible energy band diagrams in SVO/LVO/Pt multilayers including zero built-in potential induced by Fermi level pinning (in the middle of the LVO bandgap) at the LVO/Pt interface.

In conclusion, although a small increase of current is observed under illumination (photoconductive effect), no photovoltaic effect is observed in LVO-based devices, such as we designed them here. This could be attributed to the nature of the electrodes chosen, which would not create any built-it electric field (in the case of Pt, it may be due to a strong Fermi level pinning at the LVO/Pt interface). Moreover, an eventual bad quality of the interfaces (not allowing carriers extraction) combined with a high recombination rate could also hamper the device performances.

8.3 Conclusions and outlook

To summarize, in this chapter, we have successfully:

- optimised the PLD growth of two photoabsorbing materials, namely LVO and LFO,
- integrated these photoabsorbing materials in capacitor-like devices for photoresponse measurement. By doing so, we have also successfully integrated some of the TCOs studied in this thesis,
- measured a photovoltaic effect in LFO-based multilayers, while none was observed in LVO ones,
- studied the effect of the electrodes work function on the band alignment of both LFO- and LVO-based multilayers, and related it to the shape of the dark $J-V$ characteristics and the presence/absence of photovoltaic effect,
- shown that oxide electrodes have the strong asset of showing no Fermi level pinning, thus following the behavior predicted by the band diagrams. On the other hand, Pt electrodes seem to show strong Fermi level pinning where the measured band alignment is inconsistent with predictions using the metal

work function. As the Fermi level is pinned nearly in the middle of the gap, it explains the nearly symmetric $J-V$ characteristics and poor PV performances.

In such centrosymmetric oxides, several approaches could be adopted to further improve their PV efficiency:

- We have established that the energy band diagrams of all-oxide heterostructures can be roughly predicted by the knowledge of their work function only, and that in such devices the photovoltaic effect is governed by the built-in potential V_{BI}. Therefore, one could try to design more efficient devices by using different electrode materials to max out the built-in potential, such that $V_{BI} \approx E_G$. For instance, in Figure 8.31, we show the predicted band diagram of a LFO-based MIM structure (such as the ones studied in Section 8.2.1) where the LSMO bottom electrode (BE) is replaced by $SrRuO_3$ (SRO). Bulk SRO has a pseudocubic cell parameter of 3.93 Å [28], thus perfectly matching the one of LFO (and even LVO), and a reported work function of 5.2 eV [303, 321] which could improve the hole extraction at the BE/LFO interface compared to LSMO. Furthermore, one could use a different TE with smaller work function than BLSO to reduce the barrier height for electron extraction at the LFO/TE interface.

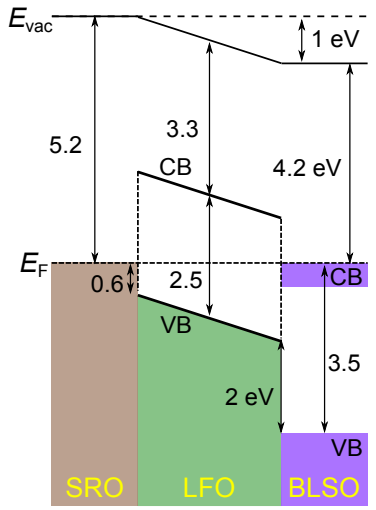

SRO/LFO/BLSO

FIGURE 8.31: Theoretical energy band diagrams (after contact) of LFO-based MIM multilayers using SRO bottom electrode to improve hole extraction at the SRO/LFO interface.

Importantly, in this chapter we have not explored the suitability of SNO as top electrode. However, the WF of SNO was estimated to be 3.5 eV (see Figure F.6 in Appendix F). This value is smaller than any electrode WF mentioned in this chapter, and could result in a higher built-in potential. For instance, if we substitute BLSO by SNO as top electrode in the structure proposed in Fig. 8.31, the resulting built-in potential could be ≈ 1.7 eV (3 times higher than in the LSMO/LFO/BLSO structure studied in the chapter).

- A step further would be to combine LVO and LFO to form a band gap graded solar cell with increased photoabsorption (as earlier report suggests [276]). Such device (illustrated in Figure 8.32a) could be similar to the LSMO/LFO/BLSO one presented in Section 8.2.1, but with a LVO layer below the LFO one to absorb the lower-energy photons not absorbed by this latter. However, the growth conditions of the different layers might be incompatible and an alternative would be to use a SVO bottom electrode, as shown in Figure 8.32b, although this would probably reduce the built-in potential.[10]

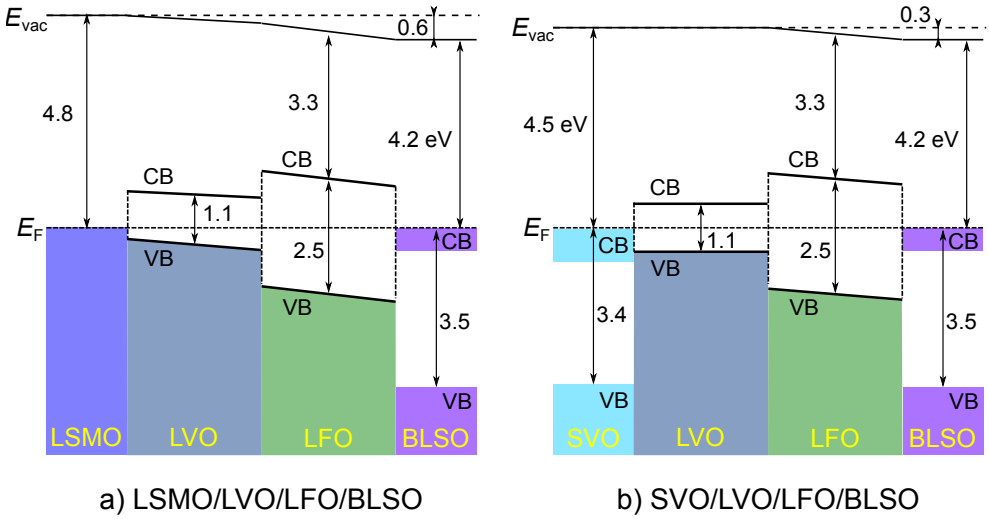

FIGURE 8.32: Theoretical energy band diagrams of LVO-based MIM multilayers using either a) SVO TE, or b) Pt TE. The LVO and LFO layers are assumed to be fully depleted (flat bands) for the sake of clarity. All units are eV.

In a different approach, the bandgap of a photoabsorbing layer might be tunable by change of stoichiometry induced by the growth conditions [273].

[10] Here again, if compatibility of growth conditions allows it, one could maybe use SRO as bottom electrode and SNO as top one to max out the built-in potential.

- Finally, an approach that we have not discussed so far consists in generating a bulk photovoltaic (BPV) effect by interface engineering. As reported by Nakamura et al. [281], a polar discontinuity in LFO/STO heterojunctions was observed in TiO_2- or SrO-terminated STO substrates, where the direction of the built-in electric field could even be switched. It was also suggested by Assmann et al. [276] that a bandgap graded LVO/LFO structure with polar discontinuity at the interface could generate a BPV effect.

From these examples, it is clear that such material combinations and surface engineering offer unlimited possibilities of devices, and therefore demonstrate the strong asset of nonpolar (centrosymmetric) oxides with low bandgap for photovoltaics.

Chapter 9

Summary and outlook

With the general purpose of finding alternative materials that could substitute indium-tin oxide (ITO) as transparent conducting oxide, we have studied the properties of transition metal oxides with partially filled conduction band of d parentage, namely $SrVO_3$ ($3d^1$) and $SrNbO_3$ ($4d^1$), which are known for exhibiting high electrical conductivity, close to that of conventional metals (Pt, Au, etc.). Whereas the latter class of materials has many drawbacks: structural incompatibility with oxides, instability, non-transparency, and high cost, researchers attention is pointing towards oxides, with excellent functional properties, stability, and low cost.

9.1 Summary of the results

This work includes the growth optimization by pulsed laser deposition (PLD) of $SrVO_3$ (SVO) and $SrNbO_3$ (SNO) single layers, measurement of their electrical and optical properties, investigation of their electronic structure, and their incorporation in oxide multilayers. In particular, we have addressed the following key issues:

1. **Growth optimization of $SrVO_3$ and $SrNbO_3$ thin films:** In vanadate and niobate compounds, a rich phase diagram can be anticipated. The multivalent character of vanadium and niobium may indeed lead to the formation of many phases. This makes it challenging to stabilize SVO and SNO, where the B-site cation (V and Nb, respectively) has valency 4+. As a matter of fact, it was already reported that thin films of these two materials need to be grown at ultra-low oxygen partial pressure (usually the vacuum residual pressure of the growth chamber) to avoid the formation of spurious phases. As growth conditions can slightly vary from one PLD setup to the other, we have determined the optimal (PO_2, T) for single-phase and highly conducting films in our setup. It turns out that both materials need to be grown at high substrate temperature, T = 700-800 °C, and, as anticipated, in ultra-high vacuum

(i.e. the residual chamber atmosphere). Films present flat surface roughness (typically < 0.5 nm) which facilitates their incorporation in all-oxide heterostructures. Nonetheless, it is shown that, in the case of SVO, films can still be grown at small PO_2 and maintain relatively low resistivity and high transparency, which broadens its compatibility with other oxides thin films if used as top electrode.[1]

2. **Transparency of $SrVO_3$ and $SrNbO_3$ thin films:** SVO and SNO films were found to have both high transparency to visible light. For instance, both films (≈ 50 nm thick, free-standing) exhibit a transmittance of about 80 % at $\lambda = 550$ nm. However, whereas SVO has a screened plasma energy $E^*_{\omega_p} \approx 1.3$ eV, the one of SNO is $E^*_{\omega_p} \approx 1.9$ eV, and thus SNO is less transparent in the NIR region. These values of plasma energy together with the measured DC conductivity allowed to estimate a carrier effective mass $m^* \approx 4\, m_e$ and $m^* \approx 1.5\, m_e$ in SVO and SNO, respectively, which is agreement with the nature of the conduction band ($3d$ and $4d$, resp.) and their bandwidth. On the other hand, SNO is more transparent in the near-UV, as its bandgap value (≈ 4.1 eV; as determined by Tauc plots) is greater than that of SVO (≈ 2.7 eV). All in all, our SNO and SVO films have lower resistivity than the best ITO films, for a comparable transmittance.[2]

3. **Reduction of growth-induced defects:** One drawback of physical vapor deposition techniques (such as PLD or sputtering) is the high energy of impinging atoms onto the substrate during deposition. This effect is even accentuated in the case of PLD-deposited SVO and SNO films, as no oxygen can be introduced in the chamber to *thermalize* the plasma plume. This obstacle was largely observed in PLD-grown SVO films where RT-resistivity of $\rho(300\,\mathrm{K}) \approx 100\,\mu\Omega\,\mathrm{cm}$ and $RRR \approx 2$ were typically reported. On the other hand, hybrid-MBE-grown SVO films hold the record with best crystalline quality and transport properties,[3] with $\rho(300\,\mathrm{K}) \approx 29\,\mu\Omega\,\mathrm{cm}$ and $RRR = 222$ [18, 42]. We have shown that one way to get around this issue is to use an inert gas (e.g. argon) to thermalize the plasma plume while avoiding the over-oxidation of the film. Consequently, the growth of SVO films in argon leads to improved properties, i.e. $\rho(300\,\mathrm{K}) \approx 31\,\mu\Omega\,\mathrm{cm}$ and $RRR = 12$, which are record values for PLD-deposited film. The increased carrier mobility ($\mu = 8.3\,\mathrm{cm^2\,V^{-1}\,s^{-1}}$)

[1] Under this growth conditions, the progressive appearance of spurious phase(s) (namely $Sr_3V_2O_8$, $Sr_2V_2O_7$...), while not hampering the use of SVO as top electrode, is detrimental to its use as bottom electrode.

[2] As recently emphasized by Park et al. [38] for SNO films and Zhang et al. [18] for SVO films in their Figure-of-Merit for transparent conductors. Both our data on SNO and SVO films fall onto the ones shown by these authors.

[3] Hybrid-MBE has the advantages of precisely controlling the growth rate, to impose a layer-by-layer growth mode, and the film stoichiometry by adjusting the amounts of gaseous precursors.

and film transparency (about 10 % higher to that of films of same thickness deposited in vacuum) were also found to be similar to that reported in h-MBE films. We have concluded that the growth using a nonreactive gas has a concomitant role in the reduction of nonstoichiometry-induced defects (by tuning the Sr/V cationic ratio) as well as in the reduction of point defects induced by the highly-energetic species impinging the film. As shown in a parallel study (in appendix), we have also tried other approaches to reduce SVO film defects, tuning other deposition parameters, but they have not been as efficient. Finally, the similar methodology was used on SNO films where best films (deposited on GSO) displayed a resistivity $\rho(300\,\mathrm{K}) \approx 50\,\mu\Omega\,\mathrm{cm}$ and mobility $\mu \approx 5\,\mathrm{cm^2\,V^{-1}\,s^{-1}}$, thus showing electrical properties close to the state-of-the-art.

4. **Impact of strain on the microstructure, and thus electrical and transport properties:** We have observed the crucial impact of strain on the electrical and optical properties of SVO and SNO. In *thick* SVO films ($t \approx 70\,\mathrm{nm}$), we have observed that the choice of substrate has a major affect on the strain state of the film. When using highly-mismatched substrates, either strain relaxation can occur (SVO//LAO) or the film can accommodate and remain fully strained (SVO//STO). Nonetheless, both cases result in the formation of planar defects that reduce the carrier mobility and thus increase the resistivity (up to a factor 2). Best properties are obtained when using a lattice-matching substrate (NGO, LSAT). Interestingly, the effective mass ($m^* = 4-5\,m_e$) is barely affected by strain and the plasma energy remains in the NIR region, preserving the film transparency. In the case of SNO, a similar observation has been made: most conducting films were deposited on GSO (fully strained) rather than LSAT (relaxed) substrates. In SNO though, the change of resistivity from one substrate to the other is smaller, which could be either related to the greater spatial expansion of the $4d$ orbitals compared to the one of $3d$ orbitals in SVO, or to a lower amount of planar defects.

5. **Role of strain on orbital ordering and hybridization in $SrVO_3$ films:** In the previous paragraph, we have not mentioned that strain also has a strong impact on the electronic structure of the material. It is known that in cubic perovskite, the degeneracy of the d orbitals is broken by ligand field into t_{2g}, forming the conduction band, and e_g at higher energy. Traditionally, SVO is described as a $3d^1$ metallic oxide where each unit cell provides one free electron occupying the t_{2g} manifold (xy, xz, yz). Here, we claim that this rigid band picture image cannot hold. First, we have observed (by XAS/XLD measurements of the V $L_{2,3}$-edge) that, although not fully degenerate, the hierarchy of the xy, xz, yz orbitals is modified by lattice distortion of the VO_6

octahedra.[4] Second, the hybridization between O $2p$ and V $3d$ is relevant as confirmed by the presence of an O K-edge, and seems to vary with the tetragonal distortion c/a. In other words, the occupancy at the metal site is modulated by tetragonal distortion from $c/a<1$ (for films under tensile strain) to $c/a>1$ (for films under compressive strain). This observation was validated by first-principles calculations of the DOS. In some oxides, this distortion of the lattice and the subsequent charge redistribution may lead to a metal-insulator transition by opening of a Mott gap, which was not observed here, even in our thinnest films (10 nm). Nonetheless, this could explain the change of electrical conductivity observed as a function of strain, that would result in the variation of the carrier effective mass m^* mentioned in the previous paragraph.

6. **Transport properties of $SrVO_3$ films explained by polarons:** The transport properties of $SrVO_3$ are often interpreted via the Fermi liquid theory where some properties, such as carrier mass (m^*) enhancement (e.g. responsible of the material's transparency), are attributed to strong electronic correlations. However, in the case of SVO, some key observations called the applicability of the Fermi liquid model into question. These include: the departure of the temperature-dependent resistivity to a purely T^2 function, or even the discrepancy of the amplitude of the A_{ee} prefactor compared to theoretical predictions. Based on these observations, here we have proposed two different features that may be responsible for the transport properties of SVO films. First, we have proposed that, in materials where the Fermi surface has a 2D-like character (in SVO for example, it is made by imbrication of cylindrical sheets), the $e-ph$ scattering may account for the $\approx T^2$ dependence of the resistivity (at least in some temperature range that we have estimated to be roughly $T \approx 240-480$ K). The observed finite magnetoresistance seems to validate this scenario. Second, we have proposed that electron transport is influenced by the ionic lattice, that is polaronic transport. In this model the phonons dress the electrons and the subsequent strong electron-phonon coupling is responsible for the effective mass enhancement. The expression of the temperature-dependent resistivity given by the polaronic model, and assuming only one phonon mode ($\hbar\omega_0$), turned out to fit perfectly our data. Moreover, the electron-phonon coupling $A_{\text{e-ph}}$ extracted from fits of our data leads to an effective mass $6 < m^*_{\text{e-ph}}/m^*_{\text{band}} < 11$, which is consistent with

[4] Here, we have the c/a ratio, measured by X-ray diffraction, to quantify the tetragonal distortion of the VO_6 octahedra. The c/a ratio was mainly tuned by epitaxial strain, i.e. by growing on different substrates and, to a lesser extent, by varying the film thickness. Films grown under tensile strain (SVO//STO) have $c/a<1$, while the ones under compressive strain (SVO//LAO) have $c/a>1$. Films on best-matching substrates (NGO) have the closest c/a to 1.

the values extracted from the Seebeck coefficient or ellipsometry measurements. Remarkably, the same trend, the decrease m^* when increasing c/a, was observed either by resistivity fits using the polaron model or by extraction from the measured plasma energy (and carrier density).[5] This observation reinforces the validity of the *e-ph* has main ingredient to the effective mass renormalization in SVO.

7. **The nature of the optical excitations occurring at the plasma energy:** In metals, the plasma energy, occurring at epsilon-near-condition (ENZ) condition such that $E_{\omega_p} = E(\varepsilon_1 = 0)$, is usually interpreted as a collective excitations of the free electrons. In SNO films however, the nature of these plasmons (surface or volume) has remained puzzling. By ellipsometry measurements, we have confirmed that the resonance at ENZ condition is due the optical plasmon resonance, since the loss function displays a pronounced peak at nearly the same energy. To further solve the question on the nature of the plasmons, we have calculated (from the ellipsometric optical constants) and also measured the film transmittance T_p and T_s at oblique incidence (for *p*- and *s*-polarized light respectively). It turns out that the calculated T_p displays a clear dip in transmittance that is known to occur when volume plasmons are optically excited by *p*-polarized light. Instrumental to these calculations, the measured T_p displayed a dip at same energy. The same results have been observed in SNO and SVO. We have thus concluded that at ENZ condition, volume plasmons are excited by (*p*-polarized) oblique-incident light, without the need of any phase-matching arrangements, but only by the presence of charge density gradients at the film surface. These observations open the way to applications in the field of plasmonics.

8. **Photoresponse in all-oxide multilayers:** We have successfully integrated SVO as top electrode in capacitor-like MIM heterostructures. As photoabsorbing insulator layer, we chose two centrosymmetric oxides with low band gaps: $LaFeO_3$ (LFO; CT-insulator) and $LaVO_3$ (LVO; Mott insulator). For the sake of comparison, we have also used other top electrodes with different work functions (La:$BaSnO_3$ and Pt in LFO-based multilayers, and Pt in LVO-based multilayers). It turned out that clear photoresponse and photovoltaic effect were observed; and the latter was found to depend on the nature of the top electrode. We have attributed this dependence to the electrode work function, that modulates the built-in potential through the multilayer (as also indicated by the shape of the dark $J-V$ curves). In LVO-based multilayers, no photovoltaic effect has been observed, which we attributed to the

[5] This trend was attributed to the change of orbital occupancy and $p-d$ hybridization with tetragonal distortion of the VO_6 (tuned by epitaxial strain).

concomitant choice of electrode material, resulting in a negligible built-in potential, and the possible high amount of defects in the LVO layer, hampering the separation of e-h pairs. This preliminary work confirms the suitability of SVO as transparent electrode for all-oxide solar cells, and opens the way to a multitude of material combination (for instance using centrosymmetric photoabsorbers in band gap graded solar cells).

9. **Film stability over air exposure:** A key feature that has not been discussed so far is the stability of these *reduced* oxides (deposited in reducing atmosphere) after being exposed to air. Here, it is worth emphasizing that several SVO and SNO films were remeasured several times over a time span of about two years, and their electrical properties remained constant.[6]

Overall, this work highlights the suitability of PLD-grown $SrVO_3$ and $SrNbO_3$ thin films, with high crystalline quality and remarkable functional properties, as transparent conductors. As in transition metal oxides there is a strong interplay between orbital, charge and spin degrees of freedom, they usually display a rich variety of properties, which in turn makes their physical origin difficult to grasp. Here, we have broken down and addressed some key issues concerning the optical and transport observed in $SrVO_3$ and $SrNbO_3$ films. We believe that addressing these issues will help to understand the physical properties of similar systems.

9.2 Outlook

From the results above, we have observed the following trends when going from a $3d^1$ (SVO) to $4d^1$ (SNO) electronic configuration:

- a decrease of effective mass: from $m^*_{\mathrm{SVO}} \approx 4.5\,m_{\mathrm{e}}$ to $m^*_{\mathrm{SNO}} \approx 1.5\,m_{\mathrm{e}}$.
- an increase of plasma energy: from $E^*_{\omega_{\mathrm{p}};\mathrm{SVO}} \approx 1.3\,\mathrm{eV}$ to $E^*_{\omega_{\mathrm{p}};\mathrm{SNO}} \approx 1.9\,\mathrm{eV}$.
- a decrease of work function: from $\phi_{\mathrm{SVO}} \approx 4.5\,\mathrm{eV}$ ([218]) to $\phi_{\mathrm{SNO}} \approx 3.5\,\mathrm{eV}$.
- an increase of (bulk) lattice constant: from $a_{\mathrm{SVO}} \approx 3.84\,\text{Å}$ to $a_{\mathrm{SNO}} \approx 4.02\,\text{Å}$.

The data above strongly suggest the possibility of tuning these properties in a controlled manner, e.g. by growing a hybrid $Sr(V,Nb)O_3$ system, or even SVO/SNO multilayers, which might result in a tuning of the bandwidth.[7] For instance, it was reported that in the isoelectronic $Ca_xSr_{1-x}VO_3$ system, there is a progressive (although minor) change of bandwidth and thus effective mass with x. Nonetheless,

[6] While one can naturally think that growing films in high vacuum and then exposing to air would have a detrimental impact on their properties, here it seems that only the surface gets over-oxidized, then forming a protective layer. However, this is just a qualitative observation and further investigation is needed.

[7] This could be further extended to similar systems: $Ca(V,Nb)O_3$ or even in molybdates.

in regard of the results listed above, changing the B cation may offer a better way to tune the electronic properties of these systems.
On another hand, a tunable plasmon resonance could find applications in plasmonics, or for water splitting (where TCOs would act as *plasmonic photocatalyst* [322]).

It may also be interesting to study the validity of the polaronic transport in the $Sr(V,Nb)O_3$ system. Indeed, a similar $\approx T^2$ dependence of the resistivity was observed in SNO films, as encountered in SVO, but the data have not been explored in detail. However, our suggestion that the Fermi liquid model cannot account for the $\approx T^2$ dependence of the resistivity of SVO films might also apply to SNO. In fact, as the *d* bandwidth of SNO is broader than the one of SVO, the electronic correlations are expected to be weaker in SNO, and other mechanism such as the *e-ph* coupling may account for its transport properties. Moreover, the model could perhaps be applied to the whole $Sr(V,Nb)O_3$ system.
Here, it should be added that a direct evidence of these phonon modes has not been provided in this thesis. This could be investigated, for instance, by means of some far-IR spectroscopy technique.

Finally, armed by all these TCOs, one could design heterostructures using the appropriate electrodes to max out the device efficiency. For instance, a precise control of the electrode work function could allow to tune the built-in potential in a solar cell, or the band alignment in general. In addition, as suggested in this work, the possibility to build band-gap-graded all-oxide heterostructures offers an appealing way to increase the device photoresponse.

Appendix A

Fabrication of PLD targets

In this appendix, we describe the synthesis of ceramic targets that have been fabricated for the purpose of this thesis. It is well-known that, during the PLD deposition, the stoichiometry transfer from target to substrate is quite steady [323]. It can be slightly tuned by the gas added in the chamber or by the laser parameters, but usually one tries to have the same cationic ratio both in the target and in the film to be deposited. For instance, in the case of the deposition of perovskite thin films with composition ABO_3, one will seak to use preferentially a target with cationic ratio [A/B] = 1. Therefore, the target may have one of the following compositions: $A_2B_2O_7$, ABO_3, ABO_4.

A.1 Solid-state reaction route

The PLD targets were prepared by solid-state reaction route (SSRR) where two reactants (two oxide powders in our case), one containing the A element and one containing the B element, are mixed in stoichiometric amount and submitted to a thermal treatment (without reaching their melting point though) to make them react. This reaction will eventually lead to the formation of a new phase containing both A and B elements. A singe-phase pellet, having the right A/B cationic ratio, is often sign of good homogeneity and should ensure a good reproducibility during the deposition of thin films by PLD. A sketch of the SSRR process is shown in Figure A.1. Due to the principle of conservation of mass, the two reactants have to be introduced in stoichiometric amount, following a chemical reaction equation. For instance:

$$2 \times ACO_3 + B_2O_5 \rightarrow A_2B_2O_7 + 2 \times CO_2 \tag{A.1}$$

where, in this example, ACO_3 is an alkaline earth carbonate and B_2O_5 a transition metal oxide.

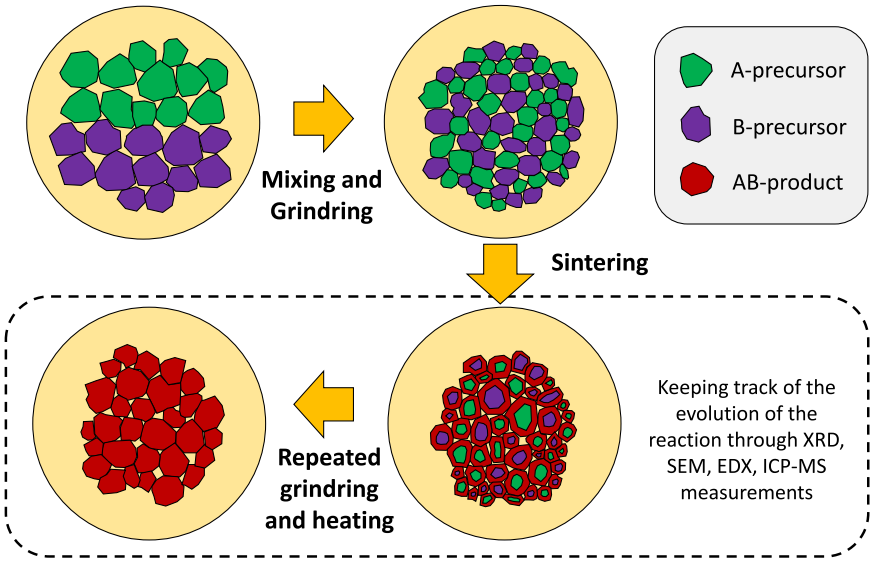

FIGURE A.1: Sketch of the SSRR procedure.

A.2 Experimental procedure for targets preparation

The procedure is the same for every targets with composition $A_2B_2O_7$, ABO_4 or ABO_3:

1. Drying of the A/B precursors. Some oxide precursors are hygroscopic and need to be carefully dried prior to use in order to remove eventual water moisture content present in the powder. In this thesis, every precursors used have been dried prior to use, usually overnight. List of precursors and main characteristics (including drying temperature) are summarized in Table A.1. The whole drying procedure is detailed below in Subsection A.2.1

2. Weighting separately the dried precursors. The precursors are introduced in stoichiometric amount according to the corresponding chemical reaction equation (for example equation A.1). The stoichiometric calculations are explained in Subsection A.2.2 below

3. Mixing and grinding together the precursors, for about one hour. This step aims at increasing the reactivity by increasing the surface of contact between grains. Illustration of precursors before mixing is given in Figure A.9a

4. Pelleting the resulting mixture. This step was done disposing the powder in a one inch diameter dry pressing die (from MTI Corporation), followed by cold

isostatic pressing. An example of resulting pellet is shown in Figure A.9b. The purpose of compacting the powder before each sintering is to ensure a good proximity between grains and thus a good reactivity

5. Sintering the pellet. For this, we used a tubular furnace. All thermal treatments were done in ambient air, i.e. no gas was added and the tube was not hermetically closed at its extremities

6. Checking the composition by powder-XRD, SEM-EDX and/or ICP-MS; and checking the grains morphology by SEM imaging

7. Re-grinding and repeating steps 4 to 6: either to reach single-phase (if previous sintering(s) was(were) not enough to get a single-phase powder, one might want to increase the sintering temperature/time), or simply to improve homogeneity and/or density of the (already) single-phase pellet.

Precursors	Purity (%)	Melting point (°C)	Hygroscopicity	Drying temp. (°C)
$SrCO_3$	99.994	1494	No	450
V_2O_5	99.99	690	No	200
Nb_2O_5	99.9985	1512	No	200
La_2O_3	99.999	2315	Yes	1100
Fe_2O_3	99.998	1565	No	200

TABLE A.1: Description of the oxide powders used as precursors for the synthesis of PLD targets by SSRR. All products were bought from Alfa Aesar (www.alfa.com).

A.2.1 Drying of the precursors

As mentioned in Chapters 3-6, the stoichiometry of TCO films (e.g. $SrVO_3$ [42] or $SrNbO_3$ [31]) is determinant to reach high crystallinity and good functional properties, namely high optical transparency at the visible and high electrical conductivity. Therefore, it is crucial to mix the right amount of precursors during the target fabrication process. A source of error can be done during the precursors weighting, especially if powders contain humidity. That is the reason why a proper drying of these precursors is necessary. In Figure A.2 is shown the mass evolution of some precursors. In Figure A.2a-b, one can observe that the mass of V_2O_5 and Nb_2O_5 is completely constant upon heating (not exceeding the melting point temperature). In the case of $SrCO_3$ (Figure A.2c), it seems that the powder mass decreases slightly ($\approx 0.6\,\%$) between 20°C and 400°C, maybe due to some water evaporation. Between 800°C and 1000°C a more pronounced mass decrease ($\approx 30\,\%$) occurs. This drop is

attributed to the decomposition of $SrCO_3$ in SrO and CO_2 (which is vaporised). It was thus decided to dry this latter at 450°C and the former ones at 200°C. Lanthanum oxide La_2O_3 is known to be highly hygroscopic, forming lanthanum hydroxide $La(OH)_3$ when in contact with H_2O from ambient air. Therefore, it was dried at 1100°C. All powders were dried in an alumina crucible and weighted when their temperature was still ≈ 200°C to minimize H_2O/CO_2 absorption when cooling down to RT.

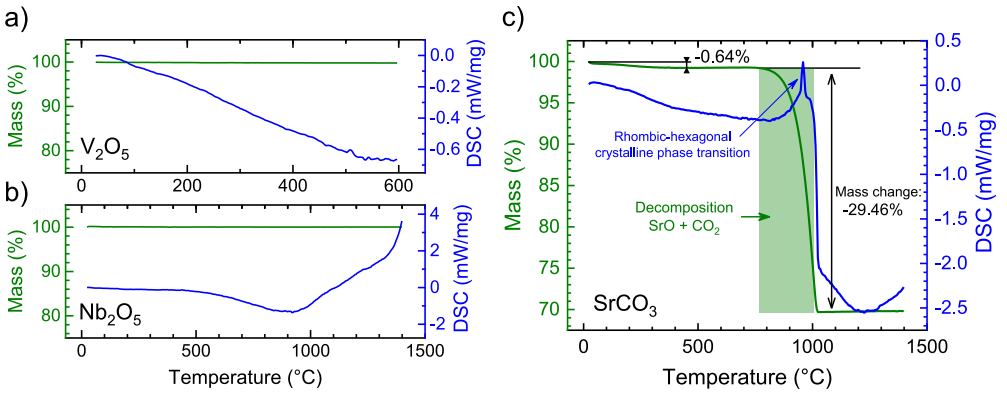

FIGURE A.2: TGA-DSC measurements of: a) V_2O_5, b) Nb_2O_5, and c) $SrCO_3$ powders.

A.2.2 Weighting of precursors in stoichiometric amount

The equation A.1 describes the chemical reaction taking place during the SSRR synthesis of a $A_2B_2O_7$ polycristalline ceramics. It is therefore valid for the fabrication of a $Sr_2V_2O_7$ target, which will take as example for the following stoichiometric calculation. This strontium vanadate phase (with closed shell V^{5+} orbitals) is more stable than $SrVO_3$ (V^{4+}) in ambient atmosphere and therefore is more likely to form during the SSRR synthesis in ambient atmosphere. Thus, to obtain a single-phase $Sr_2V_2O_7$ powder, one needs to mix two moles of $SrCO_3$ and one mole of V_2O_5, as illustrated by equation A.7. The stoichiometry calculations are done as followed:

1. the target volume V is calculated based on the die diameter d (in our case we used a dry pressing pelleting die of diameter d = 1 in = 2.54 cm) and the desired height h. Let's suppose h = 0.5 cm.

$$V = \pi \times \left(\frac{d}{2}\right)^2 \times h = \pi \times \left(\frac{2.54}{2}\right)^2 \times 0.5 \approx 2.534\, cm^3 \tag{A.2}$$

2. the target mass m is calculated based on the desired volume V calculated above, and the density ρ of the material it is made of. For example, the density of a $Sr_2V_2O_7$ single crystal (assuming no porosity) is: $\rho = 4.043\ g\,cm^{-3}$,[1] therefore:

$$m = \rho \times V = 4.043 \times 2.534 \approx 10.243\,g \tag{A.3}$$

This amount of $Sr_2V_2O_7$ is then calculated in moles (n) based on its molar mass $M = 389.12\ g\,mol^{-1}$ and using the following equation:

$$n = \frac{m}{M} = \frac{10.243}{389.12} \approx 0.0263\,mol \tag{A.4}$$

3. the mass of precursors to introduce is calculated accordingly, and using equation A.1, which indicates that to produce 1 mol of $Sr_2V_2O_7$, it is necessary to mix 2 mol of $SrCO_3$ with 1 mol of V_2O_5. It follows that for 0.0263 mol of $Sr_2V_2O_7$ (necessary for a target of volume V) one needs to mix the following amounts:

$$m_{SrCO_3} = 2 \times n_{Sr_2V_2O_7} \times M_{SrCO_3} = 2 \times 0.0263 \times 147.63 \approx 7.773\,g \tag{A.5}$$

$$m_{V_2O_5} = 1 \times n_{Sr_2V_2O_7} \times M_{V_2O_5} = 1 \times 0.0263 \times 181.88 \approx 4.788\,g \tag{A.6}$$

It will be seen in Section A.3 that in practice the pellet does not reach 100 % of the single-crystal density. It is porous and its volume is actually bigger than V.

A.3 Strontium vanadate $Sr_2V_2O_7$ target for $SrVO_3$ films

The $Sr_2V_2O_7$ (SVO) target was prepared by mixing of the $SrCO_3$ and V_2O_5 precursors in stoichiometric amounts according to the following chemical reaction equation:

$$2 \times SrCO_3 + V_2O_5 \rightarrow Sr_2V_2O_7 + 2 \times CO_2 \tag{A.7}$$

In Figure A.3a, one can see the $SrCO_3$ and V_2O_5 precursors right after drying and weighting, and ready to be mixed and grinded. The Figure A.3b is a picture of the final target showing good homogeneity.

[1] According to the International Centre for Diffraction Data (ICDD) Powder Diffraction File (PDF) n°04-012-5309 (www.icdd.com).

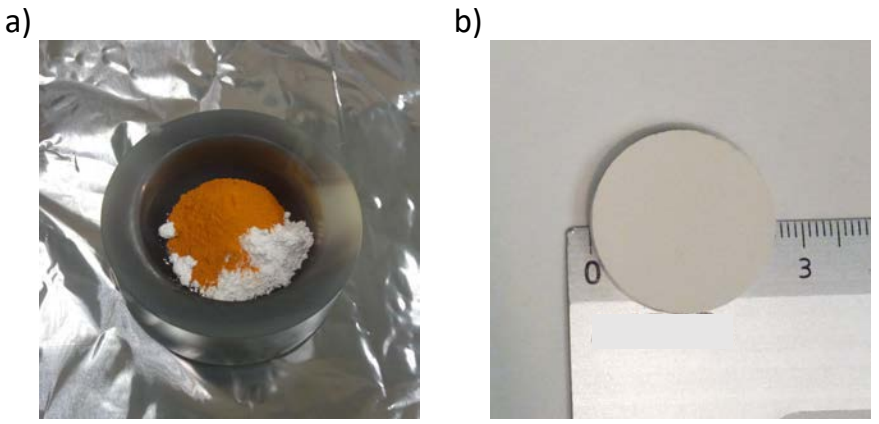

FIGURE A.3: a) Picture of the precursors before grinding. $SrCO_3$ is the white powder and V_2O_5 is the yellow one. b) Picture of the final SVO target. The ruler's numbers indicate the scale, in cm.

First, note that V_2O_5 has a melting point of 690°C, which is relatively low for the SSRR procedure, where powders are usually sintered at temperatures of ≈ 1000°C to ensure dense and single-phase PLD targets. Therefore, special care is taken to not use too high sintering temperatures, which would alter the target composition. As summarized in Table A.2, a first sintering at 400°C was performed but the XRD measurement (Figure A.4a) revealed the presence of several phases: the two precursors $SrCO_3$ and V_2O_5, but also the SrV_2O_6 resulting from the partial reaction of the precursors. A second sintering at higher temperature (650°C) was enough to achieve a single-phase powder of the expected $Sr_2V_2O_7$ phase, as confirmed by XRD (Figure A.4b). Two additional grinding and sintering steps were performed to improve target homogeneity and density. Although the density remained constant (≈ 55 %) all along the process, the stiffness was suitable for depositions.

Sintering step n°	Temp. (°C)	Time (h)	Present phases	Density ($g\,cm^{-3}$)	Relative density (%)
1	400	6	$SrCO_3 + V_2O_5$ + SrV_2O_6	2.21	54.66
2	650	10	$Sr_2V_2O_7$	2.14	52.93
3	750	6	$Sr_2V_2O_7$	2.14	52.93
4	800	24	$Sr_2V_2O_7$	2.24	55.40

TABLE A.2: Sintering steps followed for the synthesis of the SVO target. The pelleting pressure was ≈ 70 MPa for each step. Present phases were determined by analysis of the powder diffraction spectra. The relative density is equal to the measured pellet density divided by the single-cristal density, i.e. 4.043 $g\,cm^{-3}$ (according to ICDD PDF 04-012-5309).

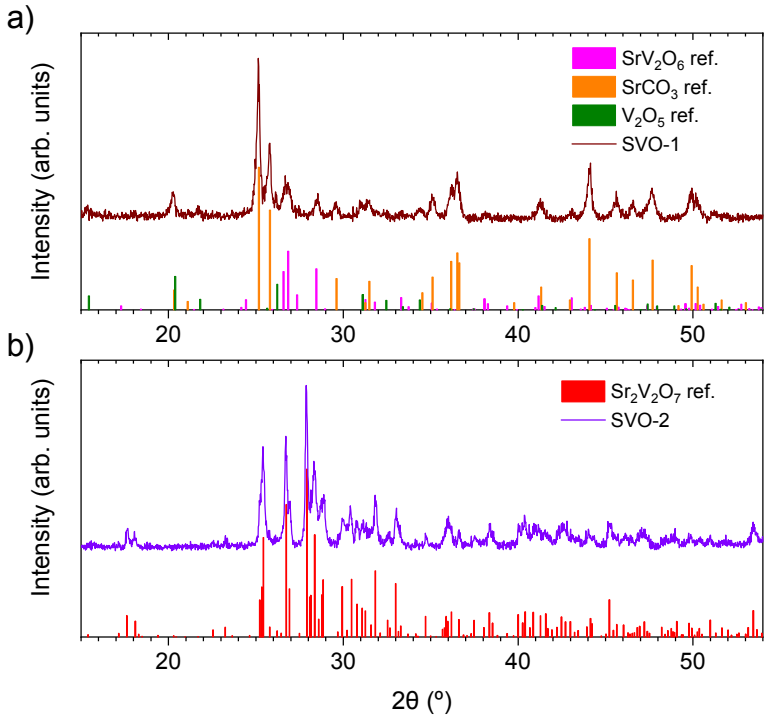

FIGURE A.4: XRD patterns of SVO powders: a) after 1st sintering (wine curve). The pink, green and green column graphs are taken as reference patterns (from ICDD 04-020-6693, 00-005-0418 and 04-007-0398, resp.). b) after 2nd sintering (violet curve). The red column graph is taken as reference pattern (ICDD 04-012-5309). The data after 3rd and 4th sinterings are not shown here for sake of clarity.

The composition of the target was determined both by SEM-EDX and ICP-MS. First, we notice from SEM micrography (Figure A.5a) a homogeneous surface where all grains seem to have the same composition, confirming good reaction between precursors and thus good target homogeneity. The analysis of the EDX spectrum (Figure A.5b) revealed a cationic ratio [Sr/V] $\approx 0.97 \pm 0.05$. The composition of a sample taken from the final target was also measured by ICP-MS and gave [Sr/V] $\approx 0.96 \pm 0.05$. This composition was also found later in $SrVO_3$ film grown on $NdGaO_3$(110) substrate (at 750°C and the base pressure of the chamber). See Section 4.3.1 for a more detailed analysis of the composition of $SrVO_3$ thin films.

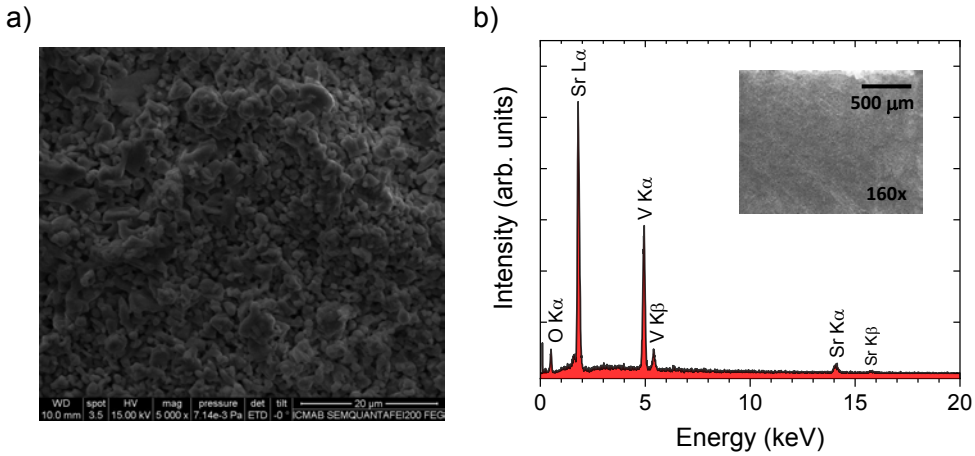

FIGURE A.5: a) SEM micrography of the SVO target surface. Magnification is 5000x. b) EDX spectrum of an area of the SVO target. The accelerating voltage used is 30 kV.

A.4 Strontium niobate $Sr_2Nb_2O_7$ target for $SrNbO_3$ films

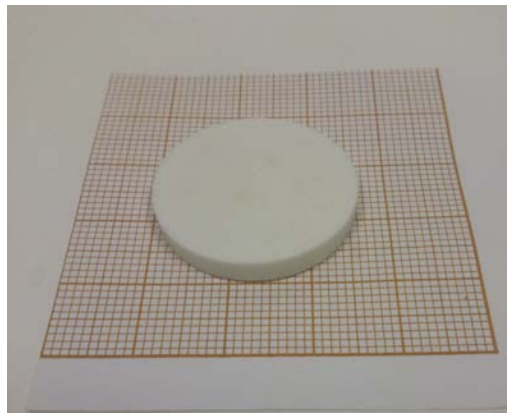

FIGURE A.6: Picture of the $Sr_2Nb_2O_7$ target. The distance between two consecutive ticks of the graph paper is equal to 1 mm.

The $Sr_2Nb_2O_7$ (SNO) target was prepared by mixing of the $SrCO_3$ and Nb_2O_5 precursors in stoichiometric amounts according to the following chemical reaction equation:

$$2 \times SrCO_3 + Nb_2O_5 \rightarrow Sr_2Nb_2O_7 + 2 \times CO_2 \tag{A.8}$$

As summarized in Table A.3, a first sintering at 900°C was performed but the XRD measurement (Figure A.7a) revealed the presence of several phases: the two precursors $SrCO_3$ and Nb_2O_5, but also the $Sr_5Nb_4O_{15}$ resulting from the partial reaction of the two first ones. Moreover, the pellet relative density was of only $\approx 35.4\,\%$. After a second sintering at higher temperature (1100°C), the XRD (Figure A.7b) revealed the presence of the expected $Sr_2Nb_2O_7$ phase, with a priori no other spurious phase. However, the density of the pellet was still too low. After two additional grinding and sintering steps, the target density increased to $\approx 94.8\,\%$. A similar target densification behaviour with sintering temperature was actually observed in literature [Liou Y.-C., Ceramics International 41 (2015)]. After the last (4^{th}) sintering, the target was still single-phase (Figure A.7b).

Sintering step n°	Temp. (°C)	Time (h)	Present phases	Density ($g\,cm^{-3}$)	Relative density (%)	[Sr/Nb] ratio (ICP-MS)
1	900	12	$SrCO_3 + Nb_2O_5$ + $Sr_5Nb_4O_{15}$	1.867	35.49	0.987±0.01
2	1100	12	$Sr_2Nb_2O_7$	2.185	41.54	0.983±0.01
3	1200	12	$Sr_2Nb_2O_7$	2.284	43.42	-
4	1400	12	$Sr_2Nb_2O_7$	4.988	94.83	0.961±0.02

TABLE A.3: Sintering steps followed for the synthesis of the SNO target. The pelleting pressure was ≈ 70 MPa for each step. Present phases were determined by analysis of the powder diffraction spectra. The relative density is equal to the measured pellet density divided by the single-cristal density, i.e. 5.26 $g\,cm^{-3}$ (according to ICDD 04-008-8703).

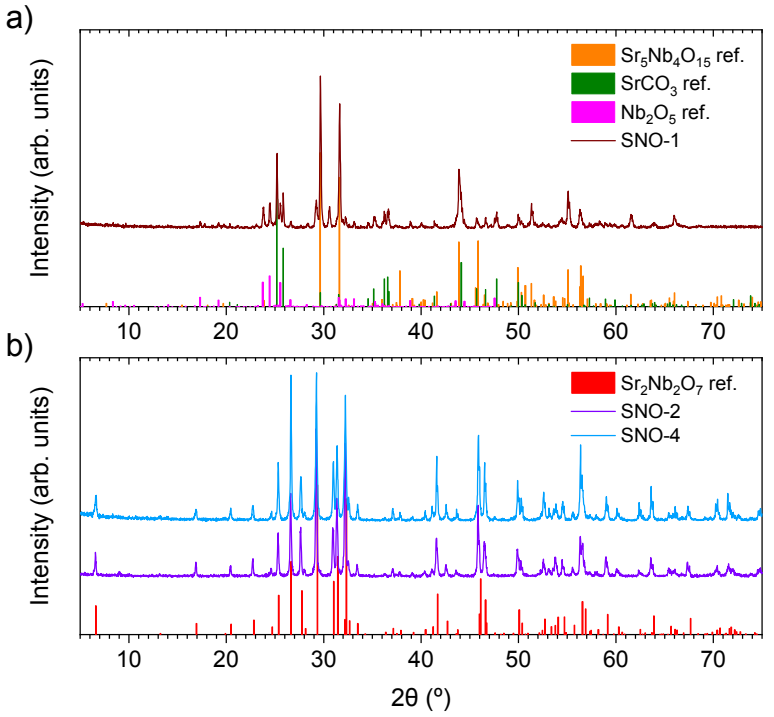

FIGURE A.7: XRD patterns of SNO powders: a) after 1st sintering (wine curve). The orange, green and cyan column graphs are taken as reference patterns (from ICDD 00-048-0421, 01-084-1778 and 04-007-0451, resp.). b) after 2nd (violet curve) and 4th sintering (blue curve). The red column graph is taken as reference pattern (ICDD 04-008-8703). The data after 3rd sintering is not shown here for sake of clarity.

The target composition was investigated by SEM-EDX. In Figure A.8a, the SEM micrography reveals a homogeneous dense surface. The EDX measurements (Figure A.8b) were performed in several areas of the target and the extracted cationic ratio was of [Sr/Nb] = 1.05 ± 0.01, which is slightly above, yet quite close, to the expected value of 1. In addition, after each sintering a sample of the pellet was taken and analysed by ICP-MS. Results are indicated in the last column of Table A.3. Although the Sr/Nb ratio seems to have decreased from [Sr/Nb] ≈ 0.99 (composition after 1st sintering) to ≈ 0.96 (final target composition), more interesting is the difference of value compared to the one obtained by EDX. Indeed, even if we consider an average composition of Sr/Nb = 0.98, this value is closer to 1. Therefore, this latter value should rather be retained, since ICP-MS is a much more accurate technique than EDX for composition quantization.

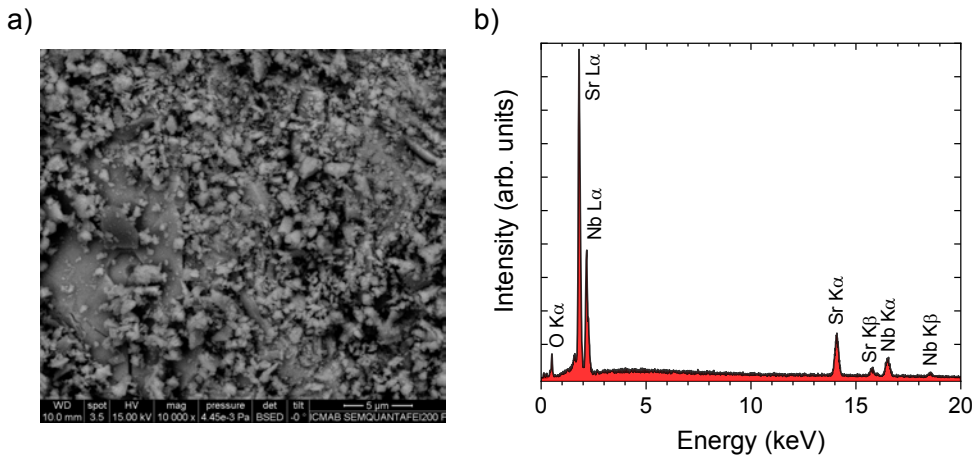

FIGURE A.8: a) SEM micrography (backscattered electrons) of a SNO target sample. Magnification is 10000x. b) EDX spectrum of the SNO target. The accelerating voltage used is 30 kV.

A.5 Lanthanum vanadate $LaVO_4$ target for $LaVO_3$ films

The $LaVO_4$ (LVO) target was prepared by mixing of the La_2O_3 and V_2O_5 precursors in stoichiometric amounts according to the following chemical reaction equation:

$$La_2O_3 + V_2O_5 \rightarrow 2 \times LaVO_4 \tag{A.9}$$

In Figure A.9a, one can see the La_2O_3 and V_2O_5 precursors right after drying and weighting, and ready to be mixed and grinded. The Figure A.9b is a picture of the final target showing good homogeneity.

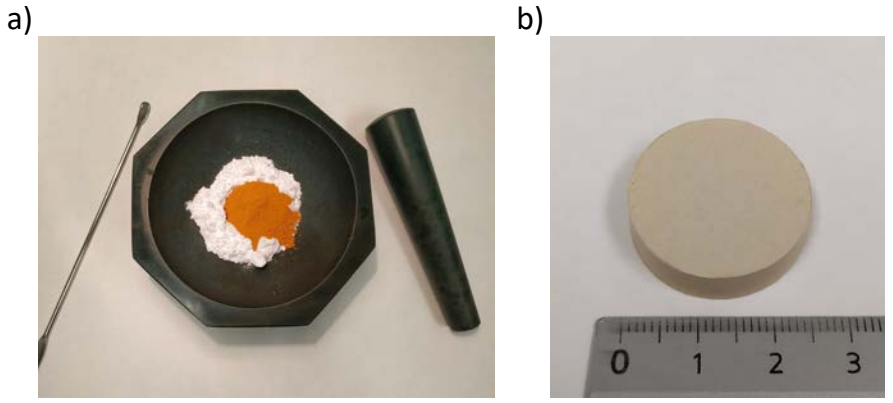

FIGURE A.9: a) Picture of the precursors before grinding. La_2O_3 is the white powder and V_2O_5 is the yellow one. b) Picture of the final LVO target. The ruler's numbers indicate the scale, in cm.

As summarized in Table A.4, the powder mixture was submitted to 4 thermal treatments at relatively low temperature since V_2O_5 has a low melting point, as previously mentioned (Table A.1). Fortunately, the desired $LaVO_4$ phase formed already during the first sintering, as seeing in the powder diffraction spectra in Figure A.10, which shows a very good matching between the reference spectrum and our experimental data. Therefore, the next treatments were done to improve homogeneity of the powder and densify the pellet. This latter reached a relative density of ≈ 67 % after the 4^{th} and last sintering, and show good stiffness, suitable for depositions.

Sintering step n°	Temp. (°C)	Time (h)	Present phases	Pelleting pressure (MPa)	Density ($g\,cm^{-3}$)	Relative density (%)
1	600	16	$LaVO_4$	58	2.338	46.27
2	600	16	$LaVO_4$	77	3.213	63.59
3	600	24	$LaVO_4$	135	3.376	66.82
4	700	24	$LaVO_4$	155	3.390	67.10

TABLE A.4: Sintering steps followed for the synthesis of the $LaVO_4$ target. Present phases were determined by analysis of the powder diffraction spectra. Pelleting pressure refers to the pressure applied to press the powder into a pellet before its sintering. The density is the pellet density after sintering. The relative density is calculated as the measured pellet density divided by the single-cristal density, i.e. 5.053 $g\,cm^{-3}$ (according to ICDD 01-083-4266).

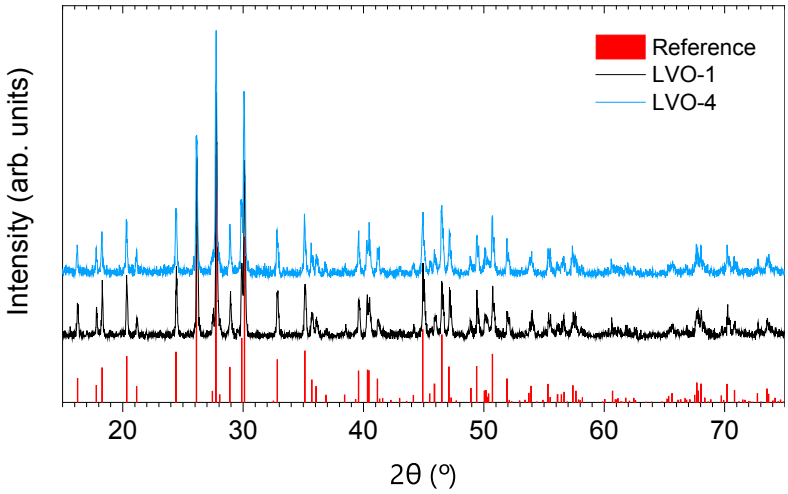

FIGURE A.10: X-ray powder diffraction patterns of LVO powders after 1st sintering (black curve) and 4th sintering (blue curve). The red column graph is taken from the reference pattern (ICDD 01-083-4266). The data after 2nd and 3rd sinterings are not shown here for the sake of clarity.

The SEM micrography in Figure A.11a shows a target surface with uniform composition. EDX analysis was attempted, bus as we can see in Figure A.11b, some emission lines of La and V overlap which makes difficult the quantization of the cationic La/V ratio by this technique. A rough estimate from integration of the La L and V K emission lines (in 4 different regions of the target) was found to be [La/V] = 1.01 ± 0.09, which yet is close to the expected value of 1.

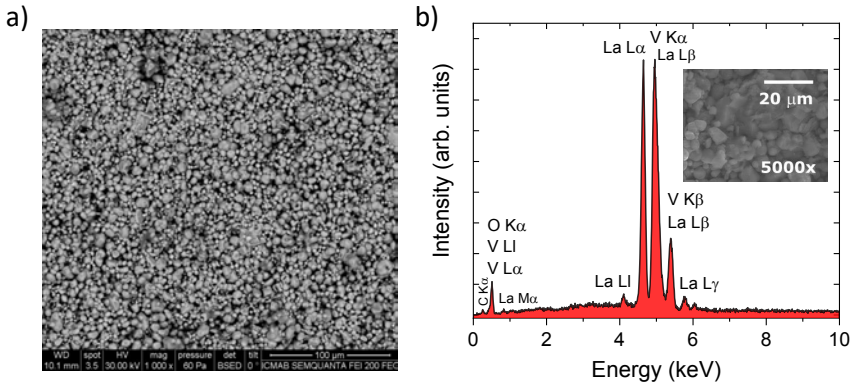

FIGURE A.11: a) SEM micrography (backscattered electrons) of LVO target. Magnification is 1000x. b) EDX spectrum of the LVO target. The accelerating voltage used is 30 kV.The inset shows the probed area.

A.6 Lanthanum ferrite $LaFeO_3$ target for $LaFeO_3$ films

The $LaFeO_3$ (LFO) target was prepared by mixing of the La_2O_3 and Fe_2O_3 precursors in stoichiometric amounts according to the following chemical reaction equation:

$$La_2O_3 + Fe_2O_3 \rightarrow 2 \times LaFeO_3 \tag{A.10}$$

As summarized in Table A.5, the LFO target was obtained after three consecutive sinterings. After the two first sinterings at 1000°C and 1100°C, the $LaFeO_3$ phase was formed but the precursors phases were still present in minor amounts. In the XRD data (Figure A.12), one can indeed observe some additionnal peaks (for example at $2\theta \approx 29°$ and $2\theta \approx 30°$ for the La_2O_3 phase, or $2\theta \approx 33°$ and $2\theta \approx 35.7°$ for the Fe_2O_3 phase) in the spectra of powders measured after the 1st (LFO-1) and 2nd (LFO-2) sinterings. However, although the measurement is noisy because a small volume of powder was measured, these peaks seem to disappear after a 3rd (LFO-3) sintering at 1200°C. At this point the target had a density of 54.5 % of the bulk crystal and showed a good stiffness for depositions.

Sintering step n°	Temp. (°C)	Time (h)	Present phases	Pelleting pressure (MPa)	Density ($g\,cm^{-3}$)	Relative density (%)
1	1000	16	La_2O_3 + Fe_2O_3 + $LaFeO_3$	68	x	x
2	1100	16	La_2O_3 + Fe_2O_3 + $LaFeO_3$	68	x	x
3	1200	16	$LaFeO_3$	68	3.628	54.51

TABLE A.5: Sintering steps followed for the synthesis of the $LaFeO_3$ target. Present phases were determined by analysis of the powder diffraction spectra. Pelleting pressure refers to the pressure applied to press the powder into a pellet before its sintering. The density is the pellet density after sintering. The relative density is calculated as the measured pellet density divided by the single-cristal density, i.e. 6.656 $g\,cm^{-3}$ (according to ICDD 04-011-7994).

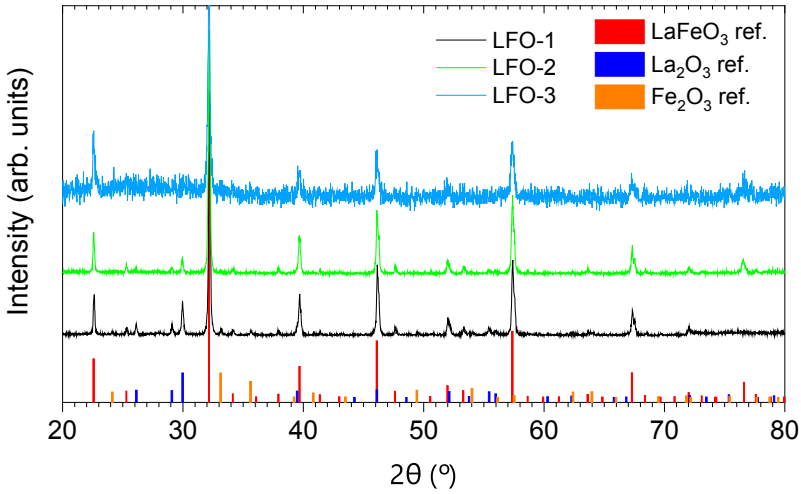

FIGURE A.12: XRD spectra of LFO powders after 1st (black curve), 2nd (green curve) and 3rd sintering (light blue curve). The red, dark blue and orange column graphs are taken from the reference patterns (resp. ICDD 01-082-3106, 01-071-5408 and 01-089-0596).

The analysis of the composition by SEM shows homogeneous grains (Figure A.13a). The EDX analysis (Figure A.13b) was performed in 4 different regions of the target and the cationic La/Fe ratio from integration of the La L and Fe K emission lines was found to be [La/Fe] = 1.02 ± 0.02, as expected.

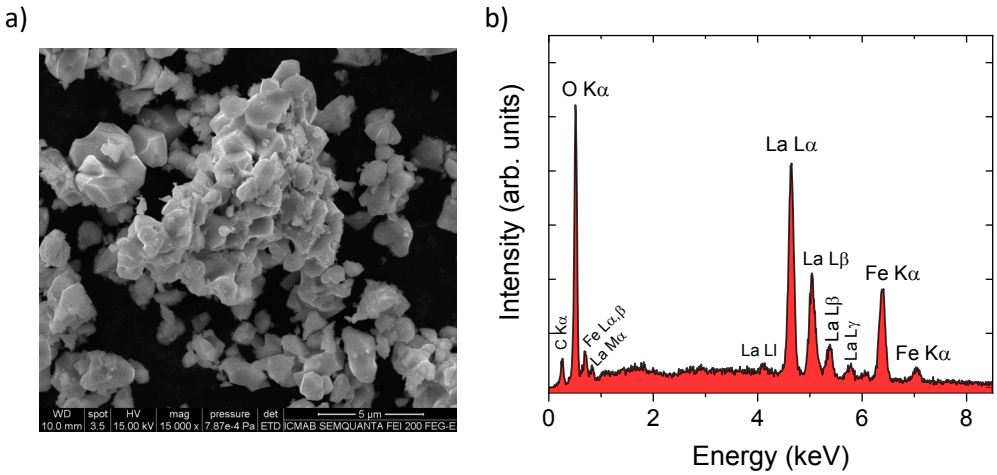

FIGURE A.13: a) SEM micrography of a LFO target sample. Magnification is 15000x. b) EDX spectrum of the LFO target. The accelerating voltage used is 15 kV.

Appendix B

Other attempts to reduce growth kinetics induced defects in $SrVO_3$ thin films

In Chapter 4, we have shown the efficiency of using argon as background gas during deposition to reduce the amount of defects in $SrVO_3$ films, produced by the growth in UHV. It has been observed that a high $P(Ar)$ (≈ 0.1 mbar) is necessary to considerably decrease defects in the films, therefore increasing the film crystallinity, conductivity, carrier mobility, RRR and optical transparency. This has been the most promising way to improve the quality of PLD-grown $SrVO_3$ films.

Here, we are reporting different approaches to attempt to reduce defects by changing other growth parameters. These are laser parameters (energy, frequency...) or physical parameters (distance between target and substrate). It is worth recalling that the growth in argon as two main effects: reducing the energy of the species before reaching the substrate and improving the stoichiometry by preferential scattering. Therefore, a high $P(Ar)$ can result in the formation of non-stoichiometric spurious phases. This is the case with $SrVO_3$ films where, at high $P(Ar)$, $Sr_3V_2O_8$ nanostructures tend to form (supposedly at the film surface, cf. discussion in Chapter 4 for more details). Nevertheless, it is generally desirable to have a single-phase and flat film to facilitate its incorporation in a heterostructure. On that account, the following experiments might help getting around this issue.

B.1 Change of laser supersaturation

In Figure 2.1 of Section 2.1, we have described the PLD setup and in particular we have sketched how the laser beam is focused on the target by using some adequate optical accessories such as mirrors and lenses. In the sketch one can see that a mask (made of iron steel) is placed on the laser beam path. This mask contains a

rectangular aperture that allow to reduce the beam divergence and have a more defined beam spot at the target surface. Changing the aperture of this mask changes accordingly the laser spot size at the target surface. It permits to have the same nominal fluence but different energy per pulse (at we cut out a part of the laser beam), thus different growth rate per pulse (supersaturation) can be achieved.

This method of controlling the growth kinetics has been used to grow homoepitaxial $SrTiO_3$ [324] or even $BaTiO_3/SrTiO_3$ superlattices [325], where it has been suggested that the lower growth rate induced by the smaller mask aperture reduces the amount of point defects in the films.

Here, we have deposited SVO films on (001) LSAT and (001) STO substrates using four different laser masks having different rectangular apertures, as summarized in Table B.1 below. The corresponding laser pulse energy is indicated. As the SVO growth rate is varied in these experiments (Figure B.1), a thickness calibration was first performed and all films presented here have same thickness (≈ 70 nm). Films were grown at the base pressure of the chamber ($P \approx 2\times10^{-6}$ mbar). Other parameters such as laser frequency, fluence, etc. were kept constant.

Mask ref.	Height (mm)	Width (mm)	Aperture area (mm^2)	Energy/pulse (mJ)
M1	18	5.7	102.6	97
M2	16	4	64	60.2
M3	15.1	2.13	32.163	32.2
M4	15.1	1.15	17.365	17.2

TABLE B.1: Description of the laser masks used to control the laser supersaturation. Note that M1 is the standard mask used in all other experiments of this thesis.

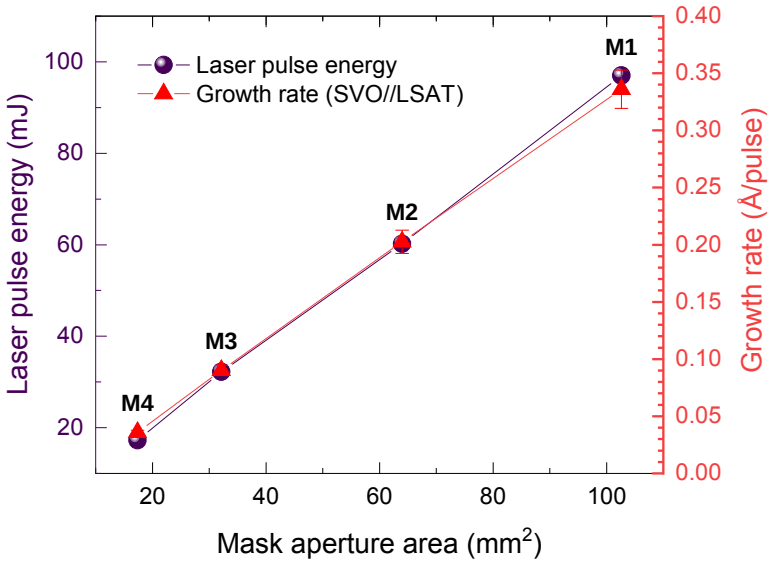

FIGURE B.1: Energy per laser pulse and SVO growth rate as a function of laser mask aperture.

X-ray diffraction 2θ–χ scans (not shown) did not reveal the presence of any spurious phase, suggesting that all films were single-phase and (001)-oriented. The surface morphology of all films was investigated by AFM, as depicted in Figure B.2. In SVO films deposited on LSAT (lower mismatch), we observe low rms roughness of 0.3-0.4 nm, slightly reducing for the mask with smaller aperture (M4). For all films, a multi-islands terraces is observed. This "wedding-cake" structures are typical in oxides and metals [326–328]. It is commonly attributed to the Ehrlich–Schwoebel (ES) energy barrier for adatoms diffusion [329, 330], that promotes multi-terrace island formation. In SVO//STO this growth mode leads to higher roughness, especially for the mask M3/M4 (lowest growth rate). Note that a similar trend was observed in the growth mode of $La_{0.7}Sr_{0.3}Mn_{03}$ (a_{LSMO} = 3.87 Å [331]) grown on STO (applying high tensile lattice mismatch $f = -0.8\,\%$). In ref. [332], the authors reported a transition from 2D to 3D while decreasing the supersaturation (via control of the laser fluence though).

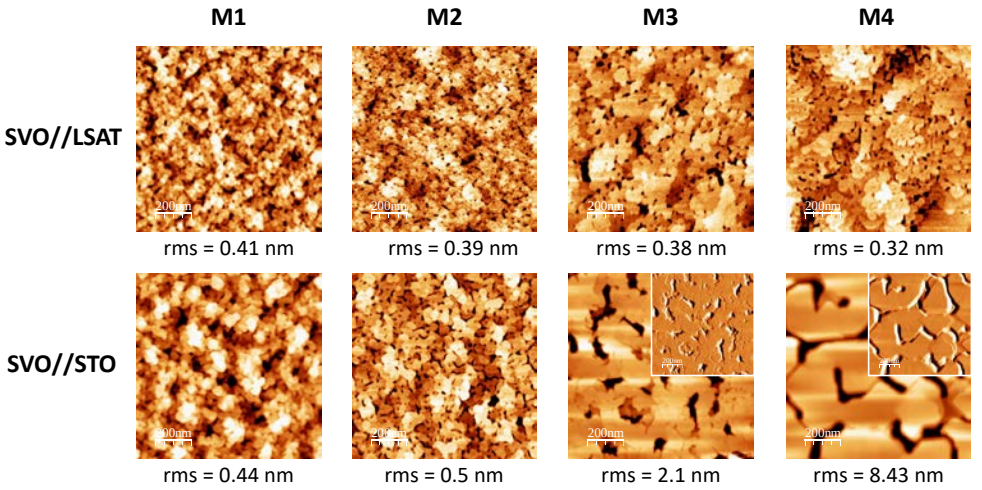

FIGURE B.2: Surface morphology of $SrVO_3$ films grown at different supersaturations. Images are $1\mu m \times 1\mu m$ in size. Insets are the corresponding amplitude images.

The electrical properties are summarized in Figure B.3. Interestingly, one can observe a decrease by a factor ≈ 2 of the RT-resistivity ($\rho(300\,K)$) (Figure B.3a) at the lowest supersaturation (smallest mask aperture), which leads to an increase of carrier mobility (μ) also by a factor ≈ 2 (Figure B.3d). This change is attributed to an improvement of the film crystallinity, which is also reflected in the RRR that increased by a factor 1.5-3 as we use the smallest growth rate.

In conclusion, reducing the instantaneous growth rate -the supersaturation- helps at reducing the amount of point defects induced by the growth kinetics. While the improvement of the electrical properties (lower RT-resistivity $\rho(300\,K)$, higher carrier mobility μ and RRR) of the films indicate of higher film quality, the results do not reach the ones achieved by growing in an inert argon atmosphere.

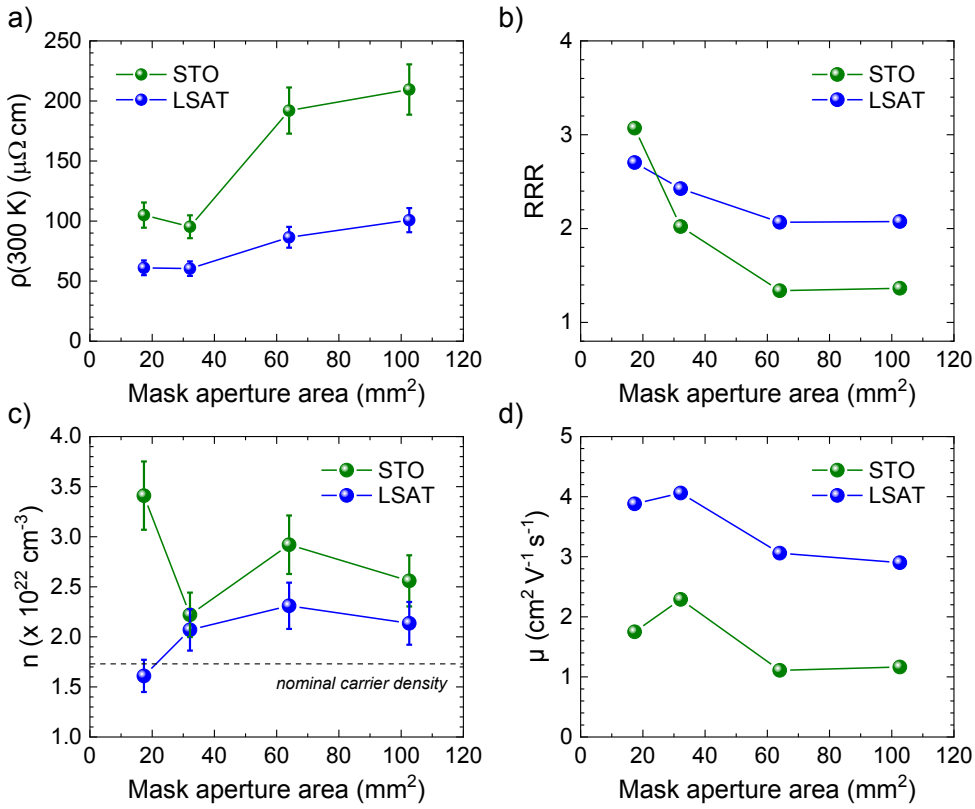

FIGURE B.3: Transport properties of $SrVO_3$ films grown using different supersaturations: a) RT-resistivity ($\rho(300\,K)$), b) Residual resistivity ratio (RRR), c) Carrier density (n), d) Carrier mobility (μ).

B.2 Modification of the target-to-substrate distance

There are several reasons to why tuning the target-to-substrate (T-S) distance may lead to better film crystallinity:

- The velocity of species in the plume may decrease upon distance. This effect is expected to be prominent for depositions using a background gas atmosphere (such as argon, as in our case), where scattering events would increase with T-S distance,
- In a similar way, we have mentioned in Chapter 4 that, when increasing the $P(Ar)$, there might be a preferential scattering of the lighter elements (namely vanadium atoms) inside the plasma plume. Therefore, placing the substrate closer or farther to the target (and thus to the plume) could lead to further changes in the film composition,
- On another hand, increasing the T-S distance might help at reducing eventual damages done to the substrate by the plasma plume (especially for deposition in UHV).

From these simple assumptions it seems difficult to predict the effects of changing the T-S distance.

Recently, Wang et al. [112] reported on the change of surface morphology in SVO films deposited in a mixture or Ar and O_2 background atmosphere, on STO substrates. The authors observed a transition from a 3D (with granular and rough films) to a 2D growth mode (with terraces and steps) upon decreasing the T-S distance (with 3D growth in 44-50 mm range of T-S distance, and 2D growth in the 28-42 mm one). At optimal T-S distance of 42 mm, the films had the lowest resistivity and optimal c-axis, while at lowest T-S distance (28 mm) the longer c-axis and worse electrical properties were attributed to cation nonstoichiometry or point defects. All in all, the authors concluded that there is a concomitant role of the oxidation and stoichiometry of the species in the plume (tunable by varying the $P(Ar)$ and T-S distance), both affecting the morphology and electrical properties of SVO films.

Here, three different target-substrate distance were used: 41, 47 (the "standard" one) and 59 mm. Films were grown simultaneously on the best-matching LSAT (+0.65 %) and NGO (+0.52 %) substrates. Two argon pressures were explored: $P(Ar) = 0$ mbar (base pressure of the chamber) and $P(Ar) = 0.08$ mbar (relatively high $P(Ar)$, leading to formation of spurious $Sr_3V_2O_8$ phase).

The transport data are summarized in Figure B.4 below. Two behaviours are observed:

- The properties of films grown in vacuum ($P(Ar) = 0$ mbar) slightly improve when increasing the T-S distance from 41/47 mm to 59 mm. A 20 % reduction of the RT-resistivity (Figure B.4a) and a 15-30 % increase of the carrier mobility are observed (Figure B.4c). These improvements could be attributed to a decrease of the amount of defects in the films associated to a lower kinetic energy of the impinging species. However, the *RRR* remains constant (Figure B.4b), signalling that the improvement of the film quality is minor.

- For films grown at $P(Ar) = 0.08$ mbar, it turns out that increasing the T-S distance has the opposite effect. Indeed, upon increasing the T-S distance, the films present a 60-100 % higher RT-resistivity. The carrier mobility decrease by about 30 %, and again the *RRR* remain constant. Therefore, the films may contain more defects that could be related to a change in the film stoichiometry.

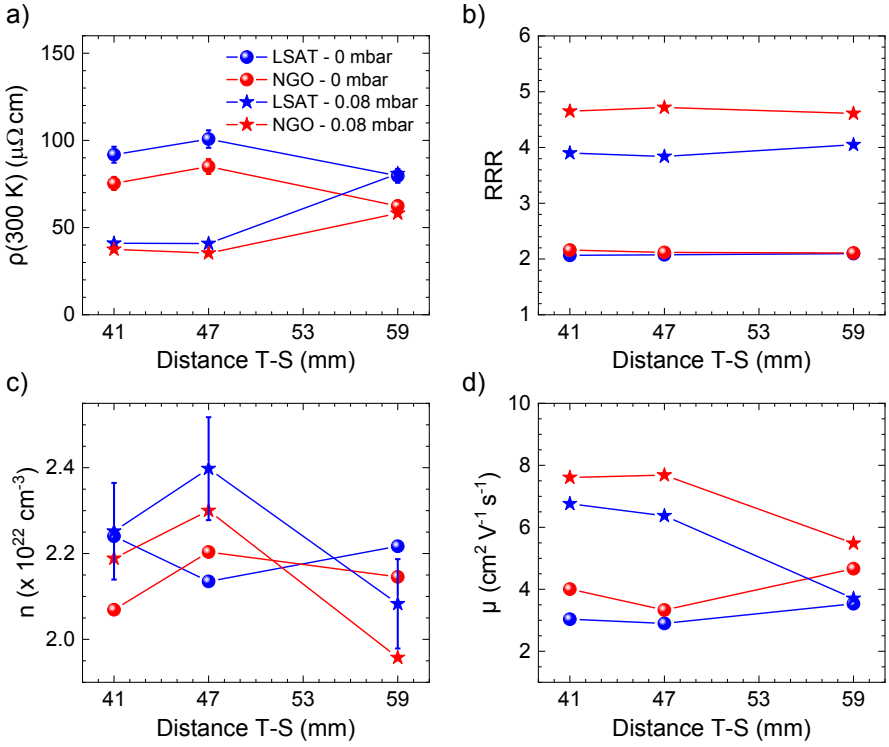

FIGURE B.4: Transport properties of $SrVO_3$ films as a function of target-to-substrate (T-S) distance: a) Room-temperature resistivity ($\rho(300\,K)$), b) Residual resistivity ratio (*RRR*), c) Carrier density (n), d) Carrier mobility (μ). Circles indicate films grown at $P(Ar) = 0$ mbar and stars account for films grown at $P(Ar) = 0.08$ mbar.

However, for any $P(Ar)$ (0 or 0.08 mbar) or substrate, no noticeable change was observed neither in the structural data from XRD, nor in the surface morphology (data not shown), compared to films grown at standard growth conditions in Chapter 4.

In conclusion, we have shown that a T-S distance within the 41-47 mm range is optimal for the growth conditions used here. At high $P(Ar)$, it gives best RT-resistivity and carrier mobility. The range of T-S distances explored here did not lead to further improvement of the surface morphology.

B.3 Impact of the laser frequency

After each laser pulse, species arrive at the substrate surface where they can move until they reach an equilibrium position. Their degree of freedom of moving at the substrate surface depends on the energy that is providing to them through substrate heating, on the chemical interactions with substrate atoms, etc. Another experimental parameter is the laser frequency. For instance, one could expect a change of growth mode from 2D to 3D if the laser frequency is too high. This could explain the granular texture of our SVO films grown in UHV (cf. Chapter 3).

Here, we have tried to decrease the frequency to see if the quality of $SrVO_3$ films improves. We chose to growth films at three different frequencies: 1, 3 and 5 Hz (the "standard" one). Films were grown on the four substrates used in Chapter 3, namely: LAO (-1.37 %), LSAT (+0.65 %), NGO (+0.52 %) and STO (+1.59 %). A series of films was grown in vacuum (same growth conditions than in Chapter 3, labelled here $P(Ar) = 0$ mbar series). Another series was grown in optimal growth conditions as determined in Chapter 4, i.e. an argon pressure $P(Ar) = 0.1$ mbar, and NGO and LSAT substrates.

The transport data are summarized in Figure B.5 below. One general trend is observed: the film properties seem to improve slightly at the lowest frequency. Indeed, in Figure B.5a we observe a small decrease of the RT-resistivity for films grown at $P(Ar) = 0$ mbar, while the one of films grown $P(Ar) = 0.1$ mbar remains quite constant. A similar increase (resp. constant) of the carrier mobility is observed (Figure B.5c) in the films deposited at $P(Ar) = 0$ mbar (resp. $P(Ar) = 0.1$ mbar). Finally, the RRR seems to increase slightly at the smallest frequency (Figure B.5b) for all films.

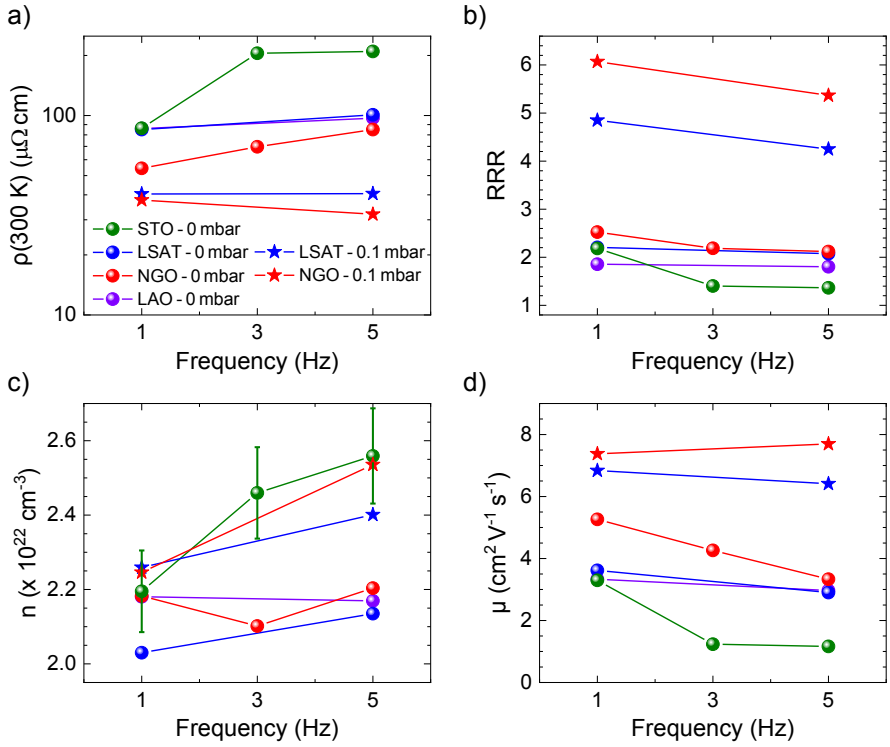

FIGURE B.5: Transport properties of $SrVO_3$ films as a function of laser frequency: a) Room-temperature resistivity ($\rho(300\,K)$), b) Residual resistivity ratio (RRR), c) Carrier density (n), d) Carrier mobility (μ). Circles indicate films grown at $P(Ar) = 0$ mbar and stars account for films grown at $P(Ar) = 0.1$ mbar.

All in all, the laser frequency seems to have few impact on the electrical properties of the SVO films, although a small improvement has been observed in films deposited in UHV ($P(Ar) = 0$ mbar) when decreasing the frequency.

B.4 Interrupted growth

In Chapter 4, we have shown that growing SVO films with a small $P(Ar)$ (of 0.03 mbar) leads to a considerable decrease of the film roughness and, eventually, the observation of terraces and steps (for a 70 nm thick SVO film deposited on LSAT). However, it seems that the films still contain point defects related to the growth kinetics, as attests the low carrier mobility μ and the low RRR. As decreasing the supersaturation (instantaneous growth rate) or the laser frequency (average growth rate), or even modifying the target-to-substrate distance did not improve considerably the film properties, we have tried here a different approach called *interrupted growth*. It consists in depositing enough material onto the substrate to constitute only one unit cell, and giving enough time to the species to migrate (to "relax") onto the surface until forming a continuous layer. The step is repeated until reaching the aimed thickness. By doing so, one can expect to impose a layer-by-layer 2D growth where the standard growth mode of continuously shot laser pulses would lead to an island-like 3D growth.

This procedure has been successful for imposing layer-by-layer growth of homoepitaxial $SrTiO_3$ [333–336], cuprates superlattices [335], ultrathin $NdNiO_3$ [337], (1 u.c.)$LaNiO_3$/(1 u.c.)$LaAlO_3$ heterostructures [338], and also sputtered Ag on Ag(111) [339, 340].

Therefore, here we have grown a series of films on the same substrates used until now (i.e. LAO, LSAT, NGO, and STO, to apply different strain state on the ongrowing SVO film) using the *interrupted growth* (*IG*) mode. The argon pressure was kept to $P(Ar) = 0.03$ mbar, which previously led to flat films (Chapter 4). In the standard growth mode used in Chapter 4, films deposited at this $P(Ar)$ had a growth rate of 0.325 Å/pulse (a film deposited via 2000 pulses having a thickness of 65 nm). In these experiments, the number of pulses is kept to 2000. However, this time they are shot at the target by sets of 12 pulses (needed to deposit approximately a unit cell of 3.9 Å) at a frequency of 10 Hz, and sets are separated by a "relaxation" time of 20 s. By doing so, 166 sets of 12 pulses are necessary to reach 2000 pulses.

B.4.1 Structural characterization

Of the highest interest, on best-matching substrates (namely NGO and LSAT), the surface morphology images shown in Figure B.6 indicate that the *IG* mode seems to favour the formation of 3D wedding-cake-like structures displaying clear terraces separated by 1 u.c. steps. On the other hand, on the less-matching (LAO and STO) substrates, the roughness is very high, signalling the presence of a dense distribution of 3D islands. We indeed observe terraces and steps on NGO and LSAT with rms roughness of $\approx$ 1.2 nm and $\approx$ 0.6 nm, respectively. The relatively high

rms roughness is due to the presence of islands, suggesting that the 2D growth is not step-flow-like. Nonetheless, the profile lines extracted in some regions of the surface show clear steps of 1 u.c. height (≈ 4 Å). On the other hand, SVO films deposited on LAO and STO clearly show grainy texture with dips between grains about 10 nm deep in the case case of SVO//STO, and as deep as the thickness of the film (≈ 50 nm) in the case of SVO//LAO.

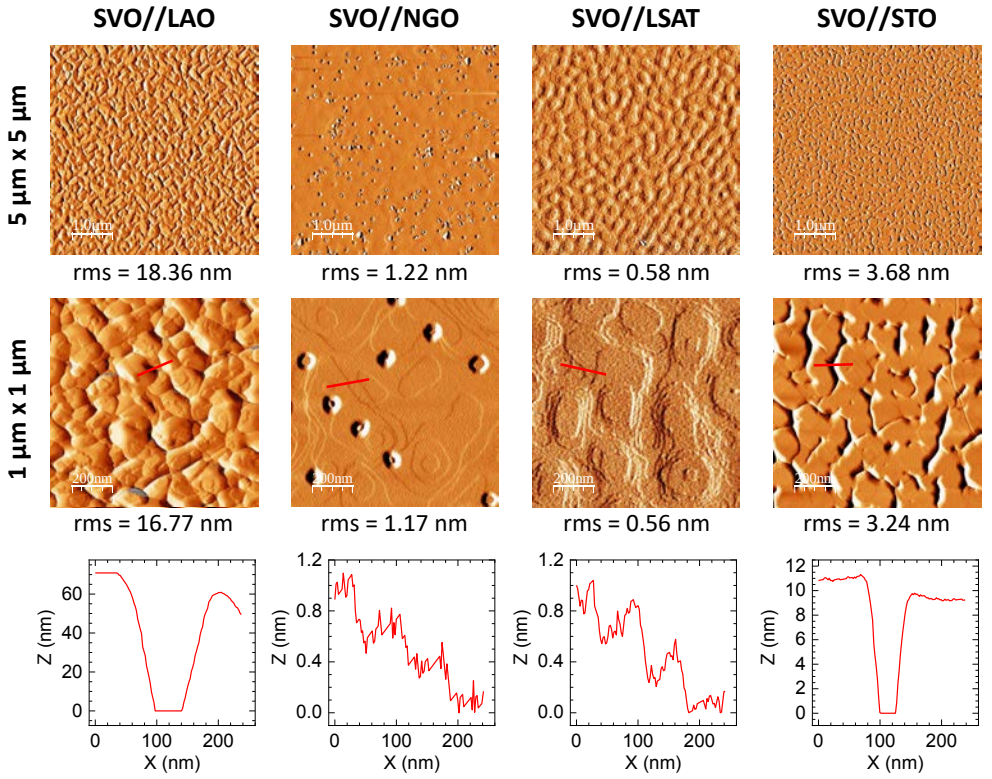

FIGURE B.6: Surface morphology of $SrVO_3$ films grown using the *interrupted growth* mode. Top (resp. bottom) images are 5 µm × 5 µm (resp. 1 µm × 1 µm) in size. Only amplitude images are shown here as they emphasize best the surface morphology of these samples. On each topographic image, a profile line of the surface was extracted and plotted below its corresponding amplitude image.

In Figure B.7a, we are showing the $\theta-2\theta$ scans of the films grown by the *IG* mode. Interestingly, one can observe that the 002 SVO reflection is accompanied by Laue oscillations for films grown on NGO and LSAT. It seems to be also the case for LAO and STO, although the Laue fringes are very shallow and blurred out by the high film roughess (as seen in Figure B.6). The film thickess was extracted by fitting of

the Laue fringes and by XRR and coincide on ≈ 50 nm for all films. Notice that in the standard growth mode films had a thickness of 65 nm, for the same number of pulses. This observation seems to indicate that, in films grown using the *IG* mode, i.e. by allowing each layer (of 1 u.c.) to "relax", the porosity is largely reduced and therefore the growth rate too. On the contrary, films grown by the standard way are thicker, probably due to porosity between grains. The *c*-axis were also extracted from the $\theta-2\theta$ scans and are depicted in Figure B.7b, together with *c*-axes of films grown by the standard mode at $P(Ar) = 0-0.03$ mbar (both pressures showing similar values of *c*-axis for a given substrate), for sake of comparison. For films grown on substrates imposing tensile strain (NGO, LSAT, and STO), we observe a considerable decrease of *c*-axis compared to standard films. For SVO//LSAT, c = 3.823 Å, which is the value predicted by Poisson's equation, as largely explained in Chapters 3/4. This indicates two things: that the film is expected to be fully strained to the substrate (as expected with this low mismatch), and the amount of point defects greatly reduced in comparison to the standard growth mode. In fact, the reciprocal space map shown in Figure B.7d shows that the film grown under the highest tensile strain, i.e. on STO, is fully strained; thus the same results are expected for films grown on NGO and LSAT. In the case SVO//LAO, c = 3.842 Å which is the cell parameter of bulk SVO, indicating that the film is fully relaxed (confirmed by the reciprocal space map in Figure B.7c) and also presents no *c*-axis elongation due to point defects.

It is also important to mention that no spurious phase was detected in the 2θ–χ scans (not shown) and that therefore all films seem to be single-phase.

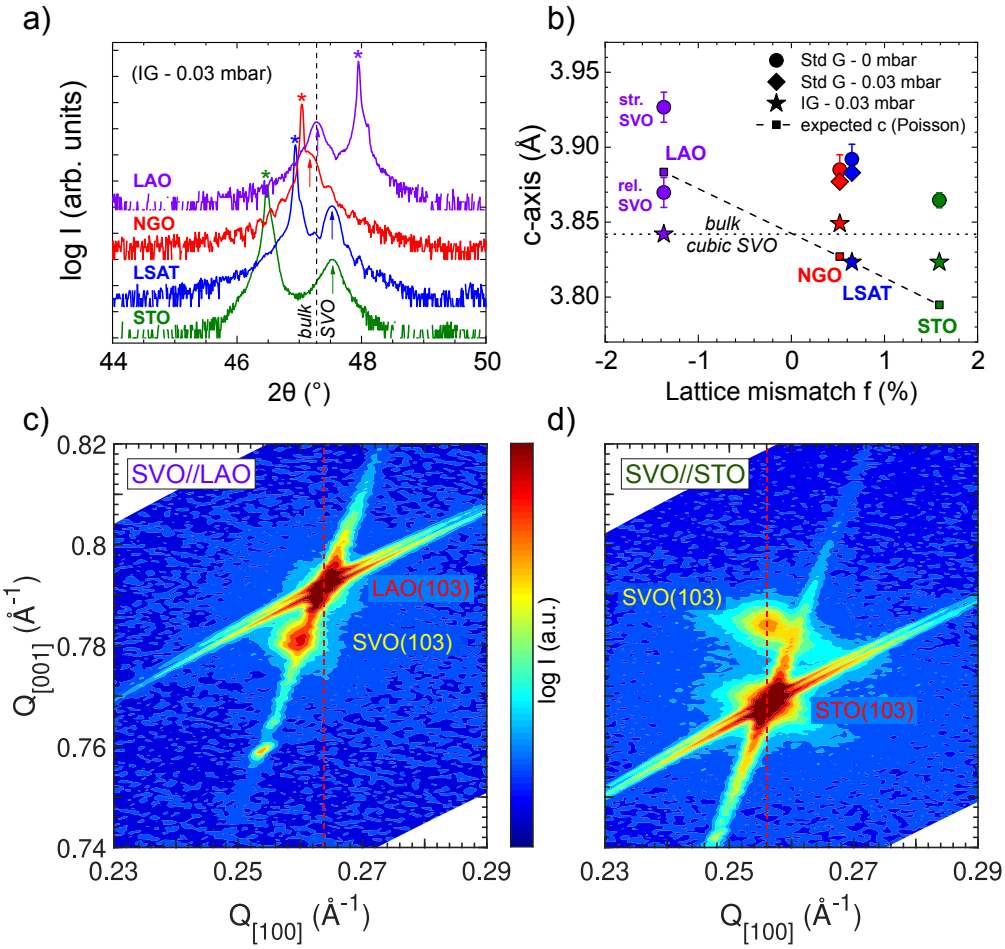

FIGURE B.7: a) XRD $\theta-2\theta$ scans of films grown using the *interrupted growth* mode on different substrates. The (002) reflection of the substrate is indicated by a star and the one of SVO by an arrow. The spectra are vertically shifted for clarity. The expected peak position for bulk SVO is indicated by a vertical dashed line. b) Out-of-plane cell parameters (c-axis) of the films as a function of the lattice mismatch with the substrate. Circles (resp. diamond) indicate films grown at $P(Ar) = 0$ mbar (resp. 0.03 mbar) using the standard growth mode; while stars account for films grown at $P(Ar) = 0.03$ mbar using the *interrupted growth* mode. Small squares represent the expected c-axis values for fully strained films, evaluated using Poisson's equation and assuming unit cell volume conservation. c,d) XRD reciprocal space maps around (103) reflections of SVO films deposited on LAO and STO, respectively, using the *interrupted growth* mode.

B.4.2 Transport properties

The transport properties of SVO films grown using the *IG* mode are summarized and compared to the standard growth mode in Figure B.8. For films grown on LAO, NGO and LSAT there is a clear improvement of the film properties. A reduction of the RT-resistivity by a factor 2-3, an increase of *RRR* by about a factor 2 and an increase of the carrier by a factor 2-3 are observed. In the case of SVO//STO, an increase of one order of magnitude of the RT-resistivity is observed which may be due to a higher concentration of planar defects (as already observed in thick SVO films deposited on STO, see Chapter 3).

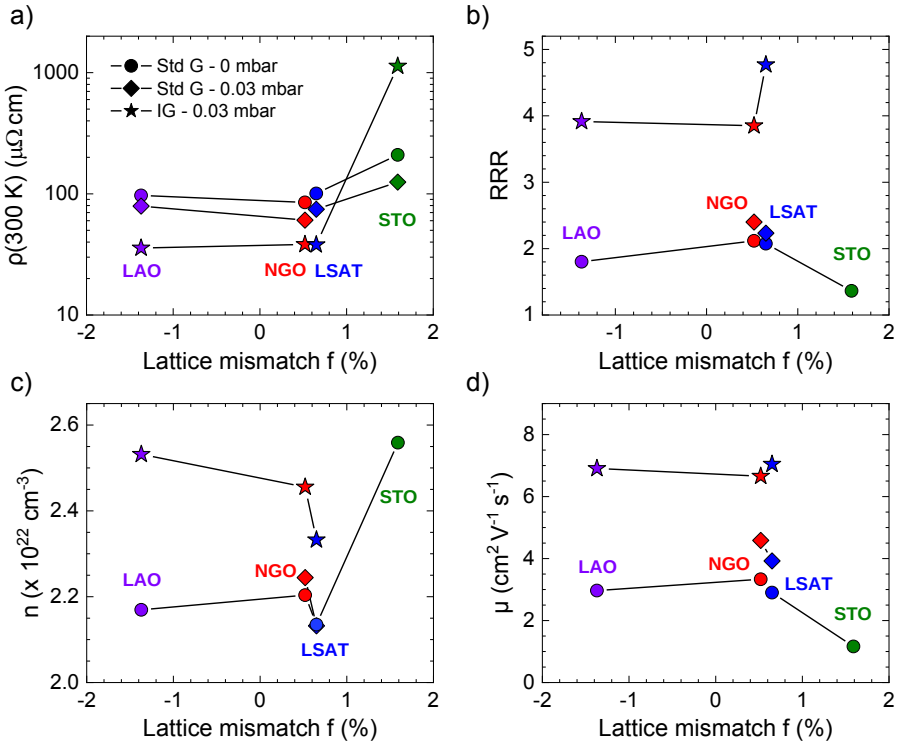

FIGURE B.8: Transport properties of $SrVO_3$ films grown using different growth modes: a) Room-temperature resistivity ($\rho(300\,K)$), b) Residual resistivity ratio (*RRR*), c) Carrier density (n), d) Carrier mobility (μ). Circles (resp. diamond) indicate films grown at $P(Ar) = 0$ mbar (resp. 0.03 mbar) using the standard growth mode; while stars account for films grown at $P(Ar) = 0.03$ mbar using the interrupted growth mode.

In conclusion, the approach attempted here with the *IG* mode seems to be promising. Although the surface morphology of the films is not optimal (due to a mixed 2D/3D growth), the approach shows a good improvement of transport

properties of the SVO films, close to the properties reached when using argon as background gas (Chapter 4). Furthermore, the optimal (a, c) lattice parameters observed in some cases signal an optimal unit cell volume, and thus presume of high film crystallinity with fewer point defects than by the standard growth mode. All in all, these results suggest that a refinement of the number of pulses per set or relaxation time between sets could further improve the film quality and transport properties.

B.5 Conclusions

We have shown here different approaches as attempts to reduce point defects in SVO thin films. Although most of them have led to small improvements, the *interrupted growth* approach is promising and should be further explored.

Appendix C

Electro-optical properties of $Ba_{0.95}La_{0.05}SnO_3$ thin films

In this thesis, a considerable effort has been spent on growing and studying the properties of transparent conducting oxides (TCO) that are intrinsically metallic. It turned out that to stabilize single-phase, highly conducting $SrVO_3$ and $SrNbO_3$ thin films, the PLD deposition has to be done at extremely low pressure (UHV), thus avoiding the formation of spurious phases resulting from the multivalency of V and Nb. Only an inert background gas can be used to reduced the amount of defects related to the high kinetics of the impinging atoms. However, these extreme growth conditions are not necessarily compatible with the growth conditions of other functional oxides. That could be the case for $LaFeO_3$ (LFO) thin films for example, which need to be grown in O_2 atmosphere. This is one of the reasons why we decided to use a different TCO materials as top electrodes in LFO multilayers (Chapter 8); whereas $SrVO_3$ and $SrNbO_3$ can be easily combined with $LaVO_3$ for example. In Chapter 8, we also motivate more in details the use of different electrodes with different work functions in MIM structures.

Barium stannate (chemical formula $BaSnO_3$) is a wide bandgap ($E_G \approx 3$ eV [74]) semiconductor. Substituting the A-site cation Ba^{2+} by La^{3+} introduces free electrons in the Sn-5s conduction band and makes it metallic [341]. By doing so, La:$BaSnO_3$ thin films combine high optical transparency (due to its large bandgap) and metallic conductivity. Moreover, the mobility of carriers moving within a band of dominant *s* character is much higher than for $3d$ or $4d$ metallic oxides. Yet, in this degenerate semiconductor the electrical conductivity is limited by the low carrier density imposed by the doping, and thus lower than in intrinsic metallic oxides.

In this work, we have deposited 5%-doped $Ba_{0.95}La_{0.05}SnO_3$ (abbreviated BLSO) thin films by PLD. The growth optimization was part of the Master's thesis of David Bugallo Ferrón (first semester 2016). As summarised in Figure C.1, BLSO films were grown on STO substrates varying PO_2 (0.1, 0.2 or 0.3 mbar) and substrate temperature T (725 °C or 800 °C). The other main parameters were kept fixed: laser fluence

of ≈ 2 J cm^{-2} and frequency of 5 Hz. The film thickness was of ≈ 200 nm reached with 3000 laser pulses. The resulting growth rate is 0.67 Å/pulse. After growth films were cooled down in PO_2 = 200 mbar to fill eventual oxygen vacancies. The optimal growth conditions are summarized in Table C.1.

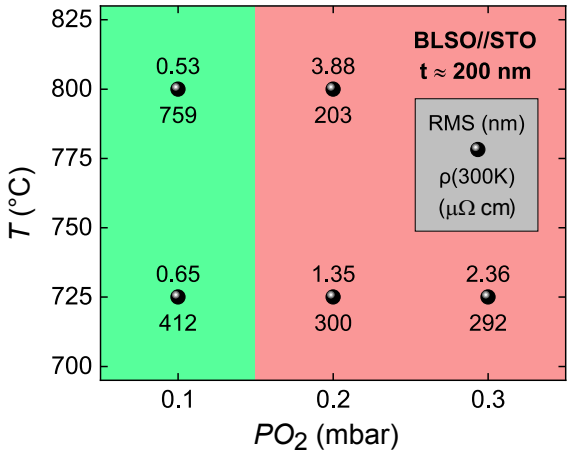

FIGURE C.1: Growth window of BLSO films grown on (001) STO substrates, as a function of PO_2 and T during growth. The numbers indicated below (resp. above) each point are the room-temperature resistivity data $\rho(300\,K)$ in μΩ cm (resp. the RMS roughness, in nm). The green color indicates the region of low roughness.

Set of conditions	T (°C)	$P(O_2)$ (mbar)	$\rho(300\,K)$ (μΩ cm)	RMS roughness (nm)	c-axis (Å)
A	725	0.1	412	3.88	4.123
B	800	0.2	203	0.65	4.123

TABLE C.1: Optimal growth conditions of BLSO//STO thin films and main properties. Films were about 200 nm thick.

To further investigate the transport and optical properties of BLSO thin films, films of different thicknesses (ranging from 30 to 90 nm) have been grown on STO (c = 3.905 Å) and LAO (c = 3.791 Å) substrates simultaneously. Both STO and LAO substrates have a smaller lattice cell parameter than bulk BLSO (with lattice constant a_{bulk} = 4.112 Å) resulting in a mismatch f(STO) = -5.3% and f(LAO) = -8.47%, respectively. Therefore, both induce a compressive strain on the BLSO film. Growth

conditions "A" (see Table C.1) were chosen as they show the best compromise of low RT-resistivity and low RMS roughness.

C.1 Structural characterization and surface morphology

The XRD $\theta-2\theta$ scans of two illustrative BLSO films (90 nm thick) deposited on STO and LAO are shown in Figure C.2a. For both samples, the (00l) Bragg reflections of the film are visible next to the substrate ones and no additional peak is observed, supposing epitaxial growth. However, the ω-scans (or "rocking curves") of the (002) reflections of one illustrative BLSO//STO sample (see Figure C.2c reveal a much broader film peak compared to the substrate one, indicating a worse film crystallinity. The 2θ–χ scans (not shown) have not revealed the presence of any spurious phase. Therefore, all films seem to be single-phase.

In Figure C.2b, we summarize the c-axis extracted for all films. Interestingly, no trend is observed neither depending on substrate type nor film thickness and all values are close to the bulk BLSO lattice constant c = 4.112 Å. Consequently, it seems that all films are fully relaxed. Indeed, if films were fully strained, the volume conservation unit cell would provoke a c-axis expansion. Calculations via Poisson equation (considering a Poisson ratio ν = 0.3) predict $c \approx 4.29$ Å (respectively ≈ 4.39 Å) for strained BLSO grown on STO (resp. on LAO). Film relaxation is was expected considering the high lattice mismatch between film and substrate, and earlier reports of similar films [108].

In Figure C.3, we show reciprocal spaces maps around the (103) reflections of the films. In agreement with the previous assumptions, films are fully relaxed with $a_{\text{film}} \approx a_{\text{bulk}}$.

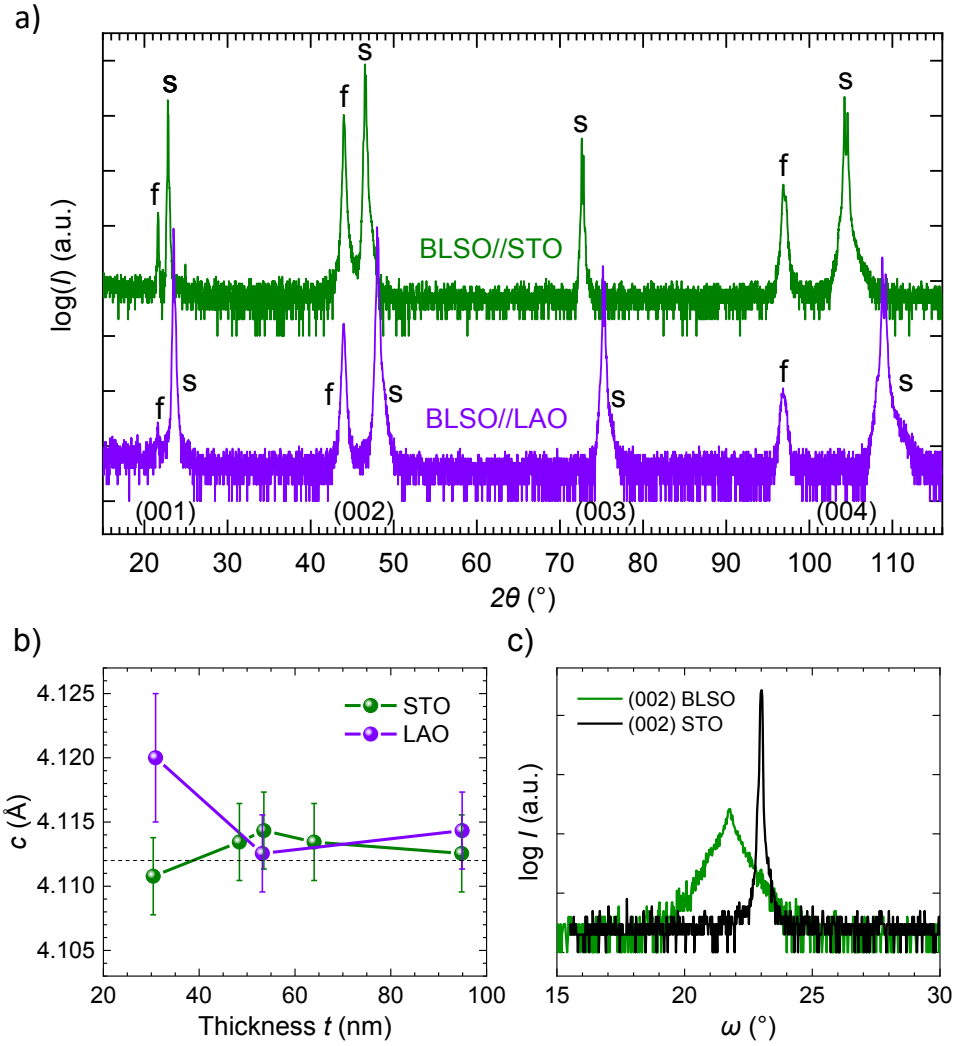

FIGURE C.2: a) Illustrative XRD $\theta-2\theta$ scans of BSLO films, 90 nm thick, grown on STO and LAO. The (00l) substrate and film reflections are indicated by the letters "s" and "f", respectively. The spectra are vertically shifted for clarity. b) Out-of-plane cell parameters (c-axis) of the films as a function of thickness. The dashed line indicates the bulk lattice parameter of cubic BLSO. c) Illustrative ω-scans the (002) film and substrate relections of a BLSO film (50 nm thick) deposited on STO, and illustrating the lower crystalline quality of the BLSO layer.

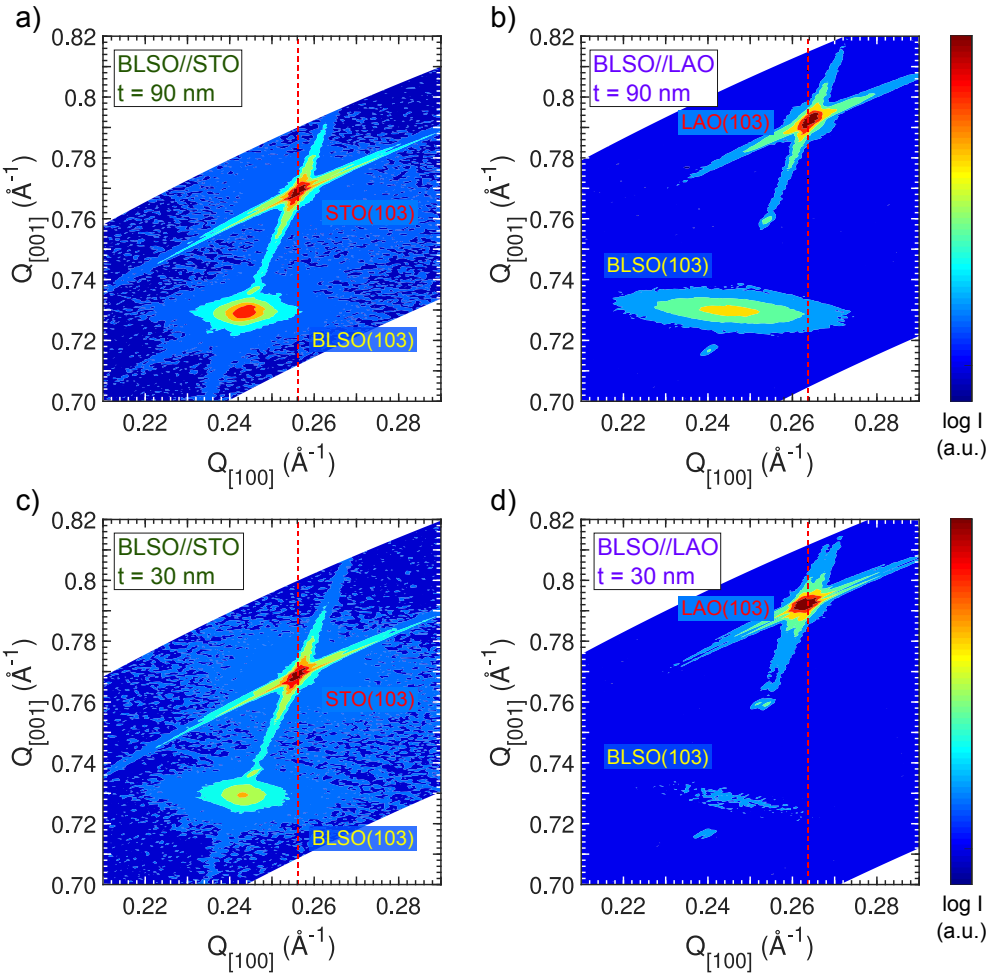

FIGURE C.3: RSM around the (103) reflection of BLSO samples, 90 nm (top panels) and 30 nm (bottom panels) thick, deposited on STO (left) and LAO (right).

The surface morphology of BLSO films (90 nm thick) deposited on STO and LAO is shown is Figure C.4. The films show low rms roughness (≈ 0.5 nm) as expected for these growth conditions (as mentioned in Figure C.1). However, a closer of the surface (insets of Figure C.4) reveals a high granularity.

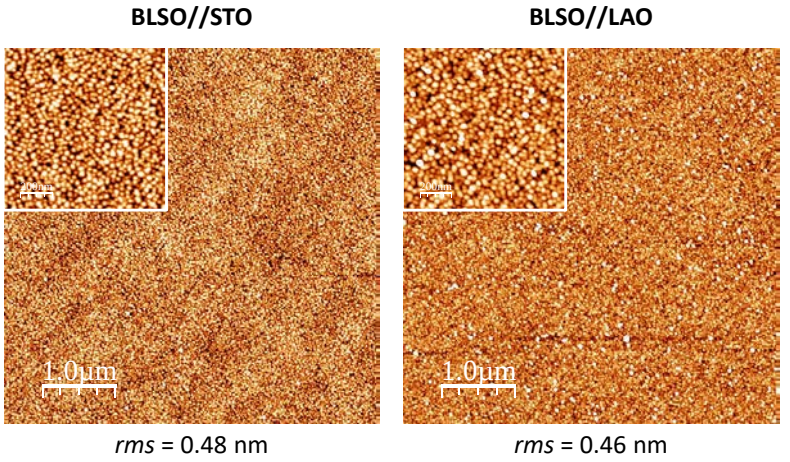

FIGURE C.4: AFM topographic images, 5 µm×5 µm in size (1 µm×1 µm for the insets), of BLSO films grown on STO (left) and LAO (right). The rms roughness is indicated below each image.

C.2 Transport properties

In Figure C.5a, we show $\rho(300\,K)$ for various film thickness and substrate. A clear trend shows that $\rho(300\,K)$ is smaller for films deposited on STO compared to those grown on LAO, for a given thickness (e.g. 60 or 90 nm). Second, for a given substrate, $\rho(300\,K)$ decreases with increased thickness which could suggest that the density defects such as misfit dislocations is higher in thinnest films. Note that the BLSO//LAO film of $t = 30$ nm turned out to be highly insulating, probably due to a critical amount of such defects. In Figure C.5b, we can observe $\rho(T)/\rho(300\,\mathrm{K})$ for some illustrative samples. We can observe that all samples are metallic over the whole temperature range, and that the resistivity varies more or less with T^2. Similar trend as been observed in PLD- and MBE-grown films [108, 342, 343]. The corresponding RRR was extracted and summarized in Figure C.5c where, for instance for BLSO//STO, we can observe a small increase of RRR with thickness, which goes in the direction of a decrease of the density of defects in thicker films.

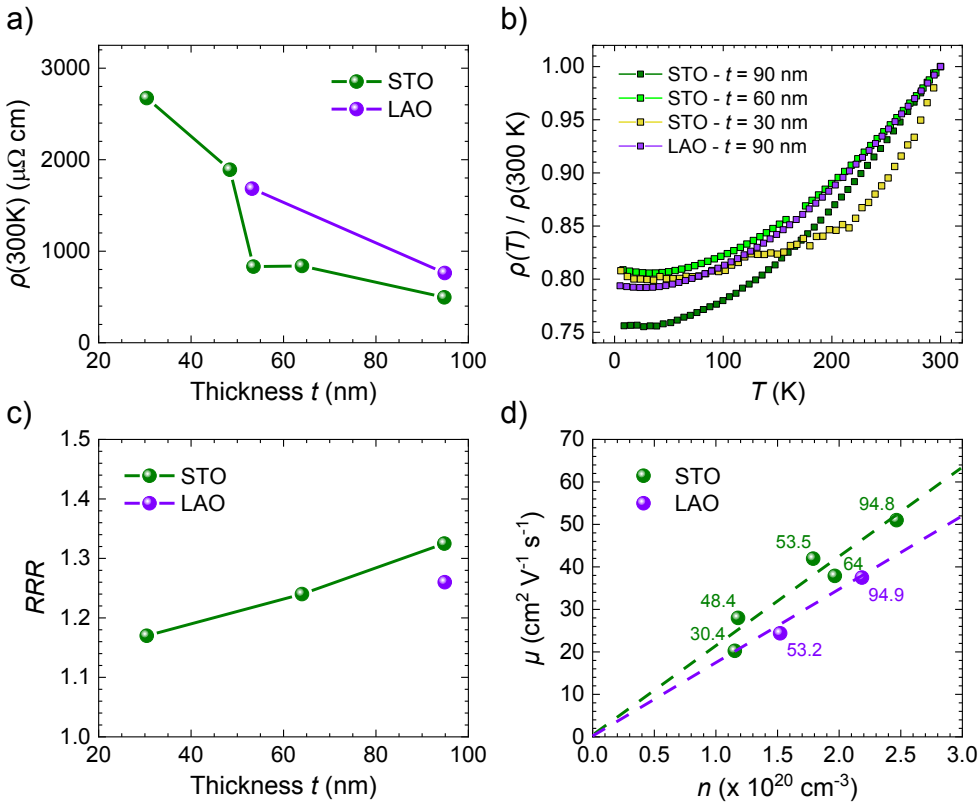

FIGURE C.5: Transport properties of BLSO films of various thicknesses, grown on STO and LAO. a) RT-resistivity $\rho(300\,K)$ as a function of film thickness t. b) Temperature dependence of the normalized resistivity $\rho(T)/\rho(300\,K)$, for some illustrative samples. c) Residual resistivity ratio ($RRR = \rho(300\,K)/\rho(5\,K)$.) of the corresponding samples. d) Carrier density (μ) vs carrier mobility (n).

In Figure C.5d, we have plotted the carrier mobility (μ) as a function of carrier density (n) determined by Hall effect at RT. Note that, from the negative slope of the Hall resistance (not shown here), carriers are electrons, as expected. The highest mobility observed $\mu \approx 51$ cm^2 V^{-1} s^{-1} (for $n = 2.6 \times 10^{20}$ cm^{-3}) was reached for a 90 nm thick BLSO//STO, which of the same order of magnitude than literature reported values [106, 108]. Moreover, we can observe an increase of μ with n and the thickness t. This known trend, where $\mu \propto n^b$, $b > 0$, is typical of doped semiconductor. This might be due to a lower density of misfit dislocations in thicker films and/or a reduction of scattering from the interface [106, 108]. The observation of a higher carrier mobility μ, at a given carrier density n, for BLSO//STO than for BLSO//LAO (higher mismatch) indicates a higher concentration of dislocations in the latter, due to its higher lattice mismatch f. We should also notice that the

maximum carrier density measured in these samples does not exceed $n = 3 \times 10^{20}$ cm^{-3}. We recall that the nominal carrier density, considering a 5 % doping level, is $n_{\text{nom}} = 7.25 \times 10^{20}$ cm^{-3}. This observation suggests that a high amount of electrons is trapped by defects such as threading dislocations. However, the precise dopant concentration has not been measured.

C.3 Optical properties

Optical transmittance in the 200-1600 nm range of a 50 nm BLSO//STO is shown in Figure C.6. Of the highest importance is the observation that the film shows a transmission coefficient of ≈100 % over the whole visible-IR range. Between 400 nm the transmittance sharply drops to 0%. This is attributed to the onset of absorption of the STO substrate ($E_G \approx 3.2$ eV = 387.5 nm). However, as above-mentioned, the bandgap of BLSO is expected to be ≈ 3.1 eV, so here it is difficult to extract a precise value. One can also notice that the in the visible range the transmittance of the film alone (measured using a pristine substrate as reference) is slightly higher than 100 %. This is also visible in the fact the transmittance of the BLSO//STO bilayer is slightly higher the one of the pristine STO substrate alone. One can deduced either that the STO substrate becomes a bit more transparent after the deposition process (due to a reduction of substrate defects by the high temperature exposure), or that the reflectivity of the bilayer is reduced, compared to the pristine substrate alone. This observation is also visible in the sample picture (Figure C.6, right), where the BLSO//STO sample (top) is slightly more transparent than pristine STO substrate (bottom).

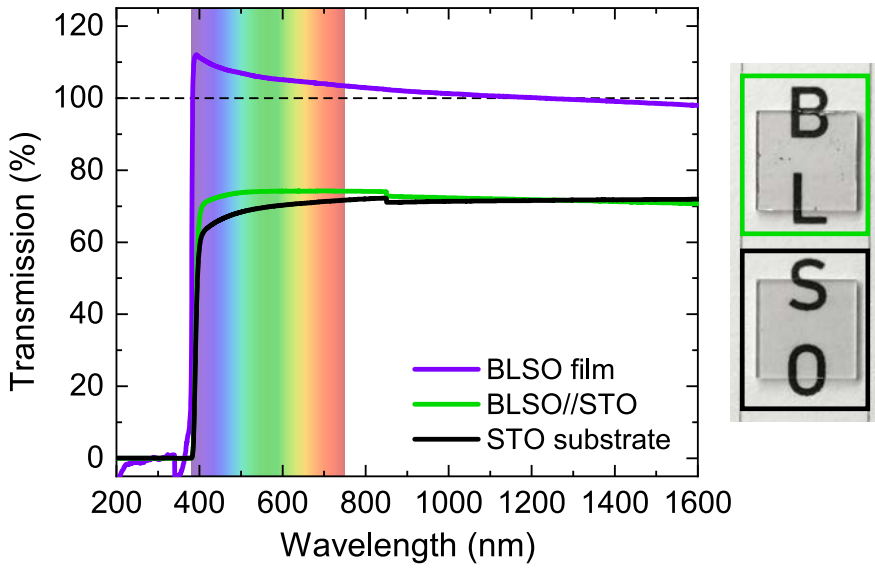

FIGURE C.6: Optical transmittance of BLSO film (48 nm thick) deposited on double side polished STO substrate. To emphasize the complete film transparency to visible light, a picture of the BLSO//STO sample (top sample) next to a pristine STO substrate (bottom sample) is shown on the right.

Appendix D

Appendix to Chapter 5

D.1 Surface morphology

In Figure D.1, top panels (resp. D.2) below, we show AFM topographic images of the thickest SVO films (70 nm) grown at $P(Ar) = 0.03$ mbar (resp. 0 mbar) on different substrates. A morphology of multi-islands terraces one-unit cell (u.c.) high in 3D steps (≈ 0.4 nm) can be observed, reminiscent of so-called "wedding-cake" structures, as commonly observed in thin films of oxides [326, 327] or metals [328] and commonly attributed to the Ehrlich–Schwoebel barrier (ES) energy barrier for adatoms diffusion [329, 330], that promotes multi-terrace island formation. As indicated in Figure D.1 and D.2 the roughness of these thick films is of about one-unit cell ($rms \approx 0.2$-0.4 nm for an image size up to 5×5 μm^2) depending on the substrate. Naturally, topographic images of thinner films display a reduced roughness (Figure D.1, bottom panels).

D.2 X-ray diffraction measurements

In Figure D.3 we show the $\theta-2\theta$ scans of the SVO films of $t = 10/20/70$ nm, grown at $P(Ar) = 0$ mbar (BP). The continuous line through the data are the results of the optimal simulation used to extract the c-axis and the film thickness. The corresponding reciprocal maps measured around the (-103) reflection are shown in Figure D.4. For SVO//STO, the film reflection is clearly visible above the substrate one, which confirms fully tensile strained films. For SVO//NGO, film and substrate reflections are perfectly superposed due to close structural mismatch. For SVO//LAO, the film peak is located below the substrate one. In the thickest film one small portion of the peak is vertically aligned with the substrate and the rest shows strain relaxation. However, in thinner SVO//LAO samples, the film seems almost fully strained with fewer signs of relaxation.

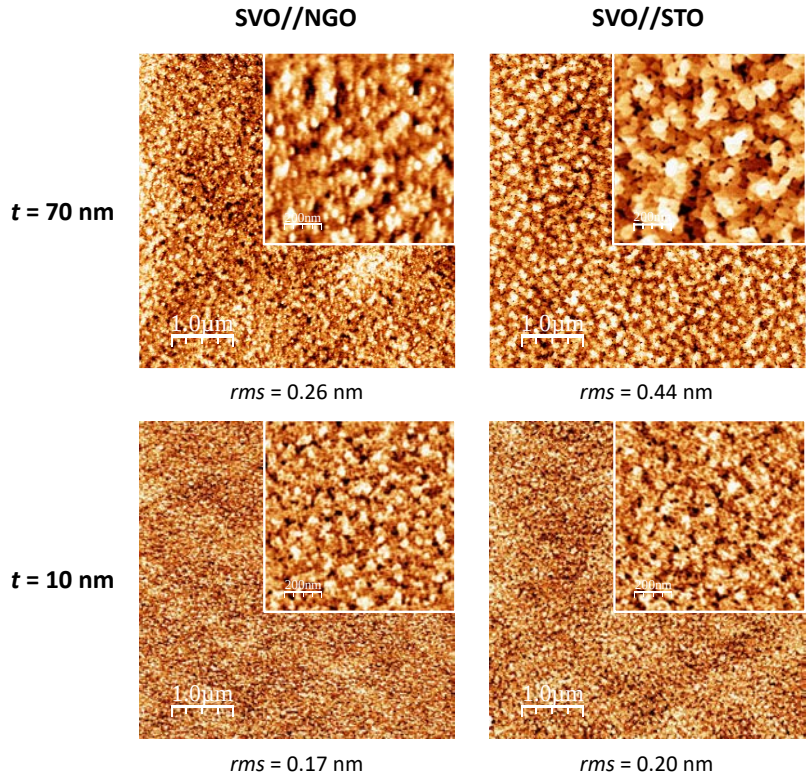

FIGURE D.1: AFM topographic images of SVO films, about 70 nm (top) and 10 nm (bottom) thick, deposited on LAO, NGO and STO, at $P(Ar) = 0.03$ mbar.

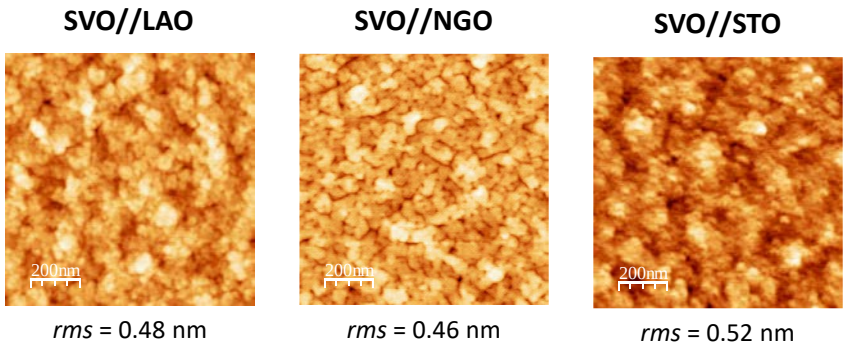

FIGURE D.2: AFM topographic images of SVO films, about 70 nm thick, deposited on LAO, NGO and STO, at $P(Ar) = 0$ mbar.

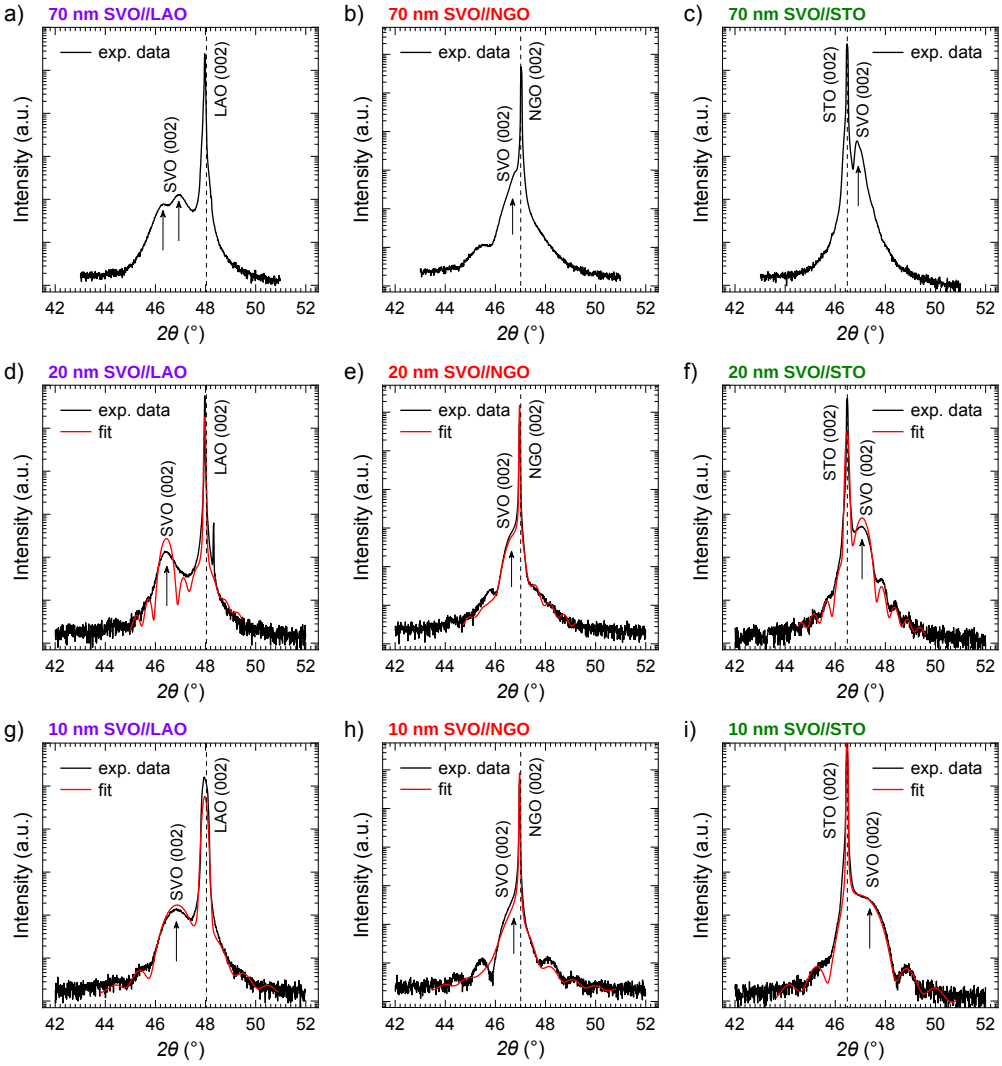

FIGURE D.3: $\theta-2\theta$ scans of the SVO films of $t = 10/20/70$ nm, grown at BP, on STO, NGO and LAO. The continuous red line through the data are the results of the optimal simulation used to extract the c-axis and the film thickness.

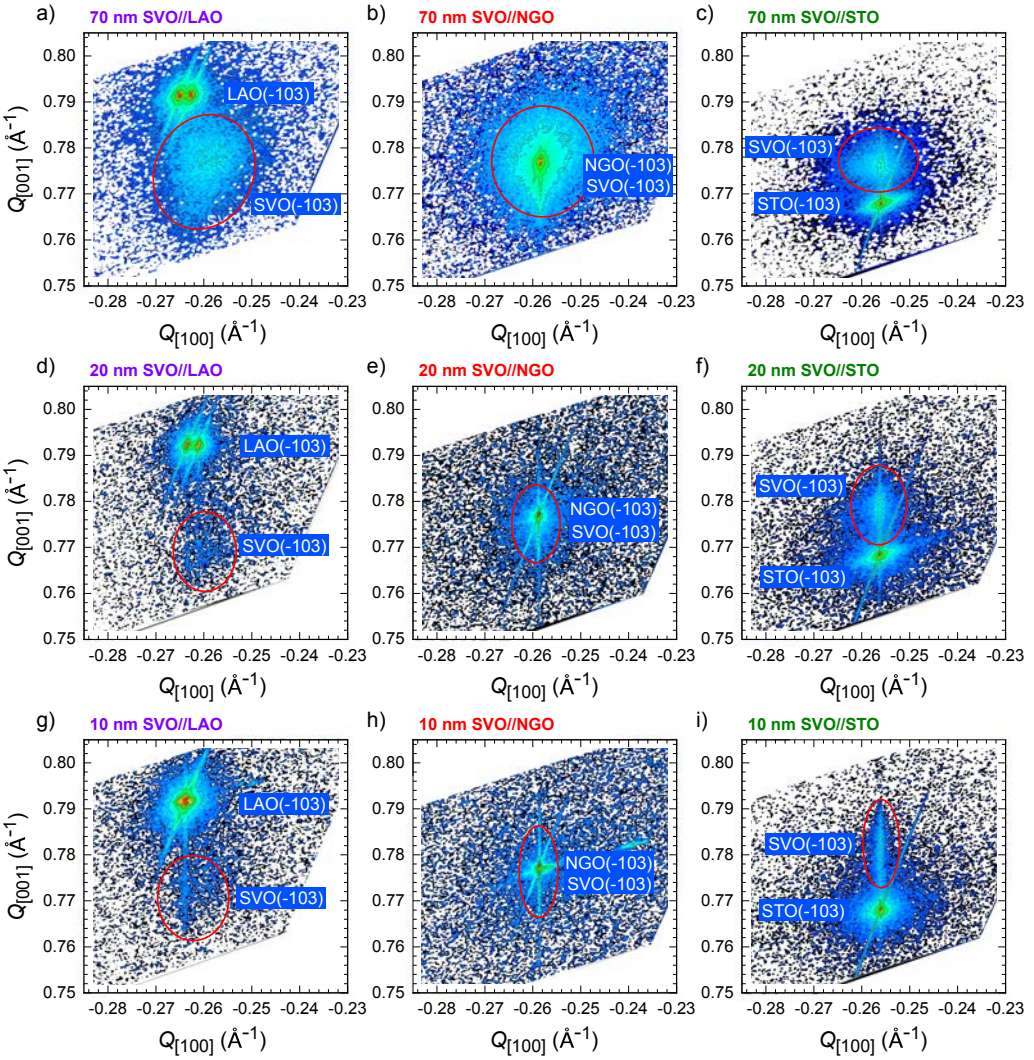

FIGURE D.4: Corresponding reciprocal space maps measured around the (-103) reflection.

D.3 Temperature-dependent resistivity and *RRR*

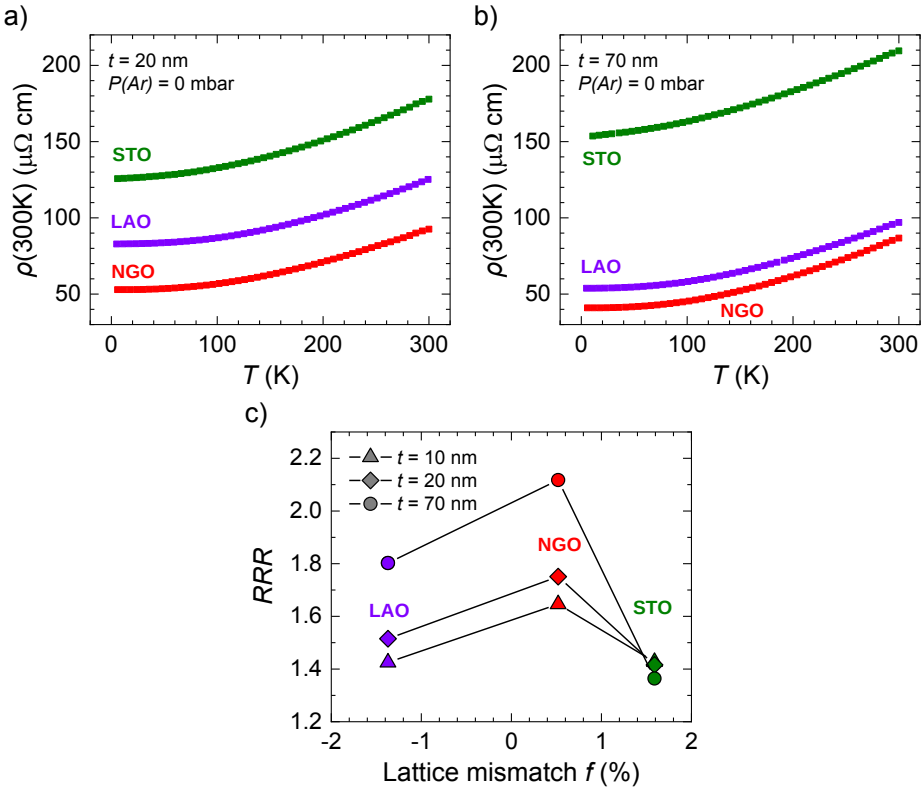

FIGURE D.5: a-b) Temperature-dependent resistivity data of SVO films (20 and 70 nm) deposited at $P(Ar) = 0$ mbar (BP) on various substrates. All films are metallic and the resistivity is smaller on best-matching substrate (NGO). c) Corresponding residual resistivity ratio ($RRR = \rho(300\,\mathrm{K})/\rho(5\,\mathrm{K})$) for all thicknesses (10, 20, and 70 nm). Films deposited on the best-matching NGO substrate have highest RRR, due to a lower presence of planar defects (as shown in Chapter 3).

D.4 XAS measurements at grazing *vs* normal incidence

In Figure D.6, we show the XAS spectra of both V $L_{2,3}$ and O K pre-peak absorption edges for 10 nm SVO//STO sample measured at: a) grazing incidence angle ($\theta = 30°$), and b) a nearly normal incidence angle ($\theta = 85°$) from the sample surface. The spectra were collected for horizontally (H) and vertically (V) polarized lights and the XLD = $H - V$ is shown in the bottom part of the (a,b) panels. The electric field $\boldsymbol{E}$ of H-polarized light varies from b-axis (in-plane) to c-axis (out-of-plane) from grazing to normal incidence as shown in the sketches given below the (a,b) panels, respectively. While, the $\boldsymbol{E}$ of V-polarized light is parallel to the a-axis, ($\boldsymbol{E}_{\mathrm{a}}$ or commonly $\boldsymbol{E}_{\mathrm{ab}}$) for any light incidence angle. It appears from the data that the XLD is absent in the normal incidence as expected due to the $3d$-orbital symmetry in the film plane, but a clear difference in the grazing incidence as the orbital occupancy differs the light absorption intensities. Furthermore, the spectra do not seem to have any discernible shift in the peak positions either at V $L_{2,3}$ or O K pre-peak edges – within the experimental resolution (< 10 meV) – suggesting that, within the sensitive penetration depth, the SVO films are electronically homogeneous; this hints that the vanadium valency remains same throughout the film within the x-rays probing limit.

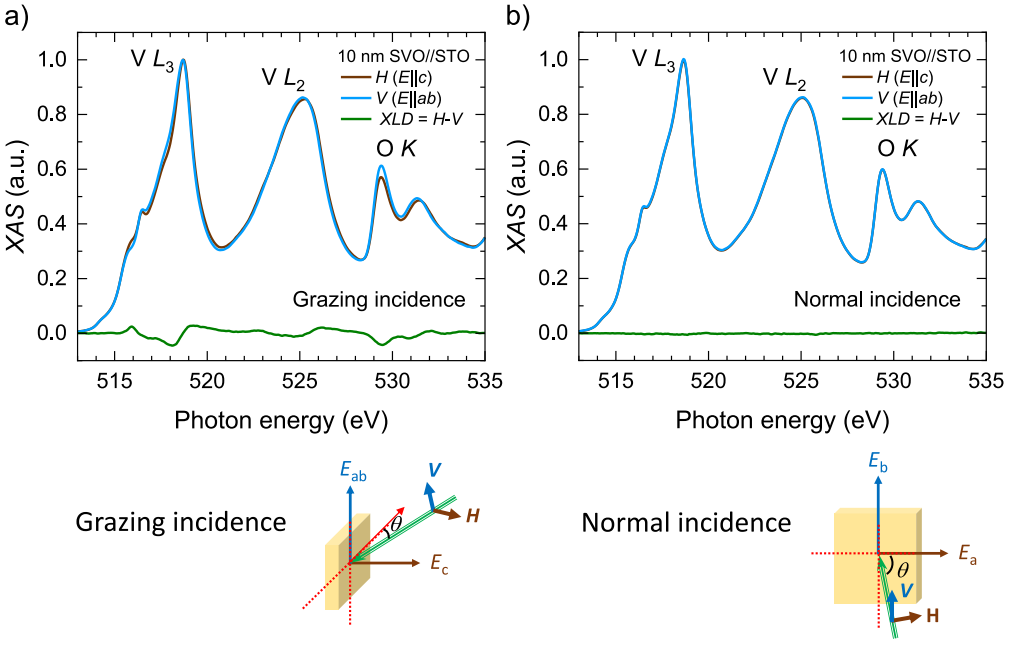

FIGURE D.6: XAS and XLD spectra of V $L_{2,3}$ and O K pre-peak for 10 nm SVO//STO recorded at: a) grazing ($\theta = 30°$), and b) normal incidence ($\theta = 85°$) angles.

D.5 Temperature-dependence of the XAS/XLD spectra

In Figure D.7a, we show *H*- and *V*-polarized XAS of SVO//STO, as well as XLD at the V $L_{2,3}$-edges of 10 nm thick SVO films grown on various substrates (STO, NGO, and LAO) recorded at 2 K temperature. These data were collected at grazing incidence ($\theta = 30°$) as similar to the 300 K data in the Figure 5.4b of the manuscript. The *XLD-1* and *XLD-2* signals for positive and negative dichroism, respectively, follow the same trend as the 300 K data, i.e. largest amplitude for the SVO films on STO and reduces for the films on NGO and LAO. The magnitudes of *XLD-1* and *XLD-2* are given in the Figure D.7b for both 2 K and 300 K for a quantitative analysis. The data appear very similar to each other.

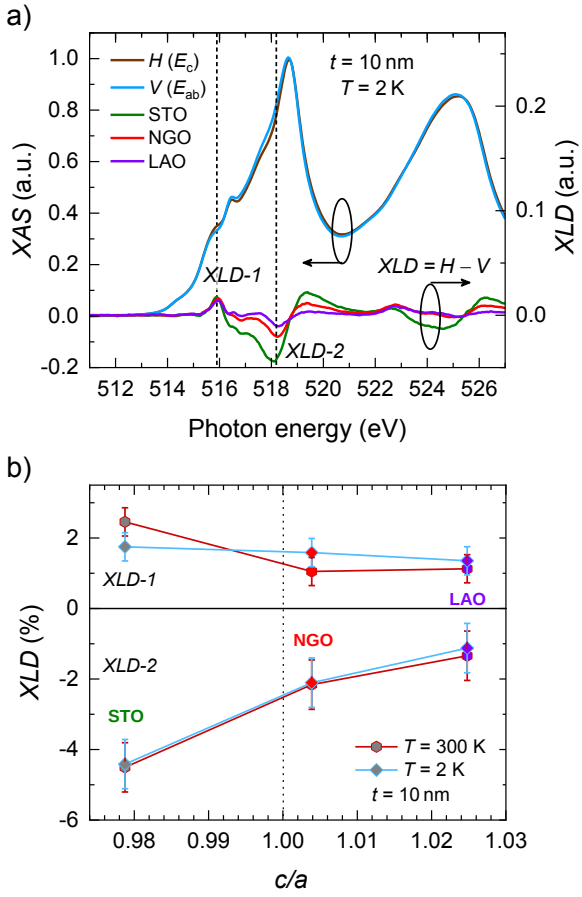

FIGURE D.7: a) *H*- and *V*-polarized XAS spectra of SVO//STO at the V $L_{2,3}$-edge, and XLD spectra of 10 nm SVO thin films on STO, NGO, and LAO substrates. Spectra were collected at 2 K. b) Temperature variation of the XLD maxima values (*XLD-1* and *XLD-2*) of 10 nm SVO films grown on various substrates.

D.6 Thickness-dependence of the XAS/XLD spectra

In Figure D.8a, we show the average XAS of SVO films on STO for thicknesses of 10, 20, and 70 nm recorded at grazing incidence, in the energy range of 510-555 eV where the V $L_{2,3}$ absorption edge is present and followed by the O K-edge. As already mentioned, the O K pre-peak doublet maxima appearing at M_1 ($\approx$ 529.5 eV) and M_2 ($\approx$ 531.5 eV) (arrows), which are known to be very sensitive to oxygen contents and the hybridization between O $2p$ and metal $3d$-t_{2g} and between O $2p$ and $3d$-e_g states, respectively. The relative intensity $I(M_1(t_{2g}))/I(M_2(e_g))$ is sensitive to the electronic occupancy at V $3d$ levels, which seems varying with the increasing thickness due to different surface oxidation in the films. This is very much consistent with the films grown on LAO and NGO for the increasing thicknesses from 10 to 70 nm.
In Figure D.8b-d, we show the XLD data for SVO films on STO, NGO, and LAO substrates for different thicknesses (10, 20, and 70 nm) recorded at grazing incidence. The XLD displays similar features and the amplitudes at *XLD-1* and *XLD-2* are reduced with the increasing thickness. These XLD amplitudes are already summarized in Figure 5.4d of the manuscript.

D.7 Angular-dependence of the XLD spectra

In Figure D.9, we show the XLD data of V $L_{2,3}$ and O K-edges recorded at different angles of incidence from the sample surface (8°, 30°, 60° and 85°) for the 10 nm SVO films on: a) STO, b) NGO, and c) LAO substrates. These data confirm the systematic variation of the XLD signal with the substrate as well as the angle. In Figure D.9d we summarize the amplitudes of the XLD maxima (*XLD-1* and *XLD-2*) for various substrates. The XLD maxima are plotted as a function of $\cos^2(\theta)$ to provide evidence of the concordance of the expected angular dependence with experimental data.

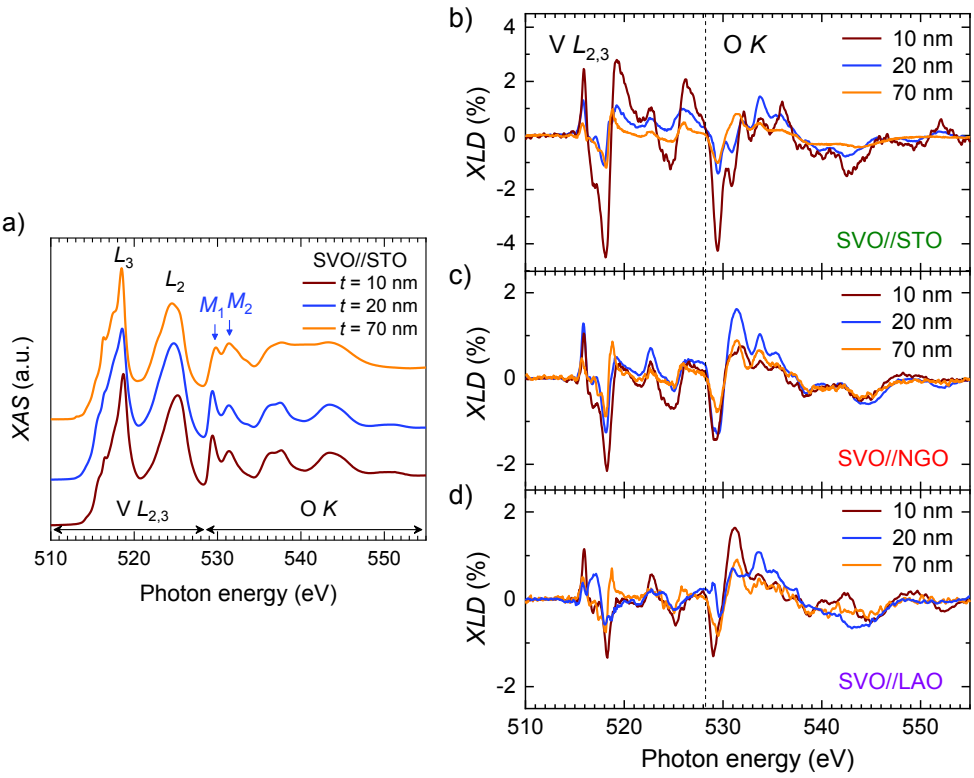

FIGURE D.8: a) The XAS of V $L_{2,3}$ and O K-edges of SVO//STO for different thicknesses (10, 20, and 70 nm) recorded at the grazing incidence ($\theta = 30°$). Thickness variation of XLD spectra of V $L_{2,3}$ and O K-edges for the SVO films on: b) STO, c) NGO, and d) LAO substrates recorded at the grazing incidence.

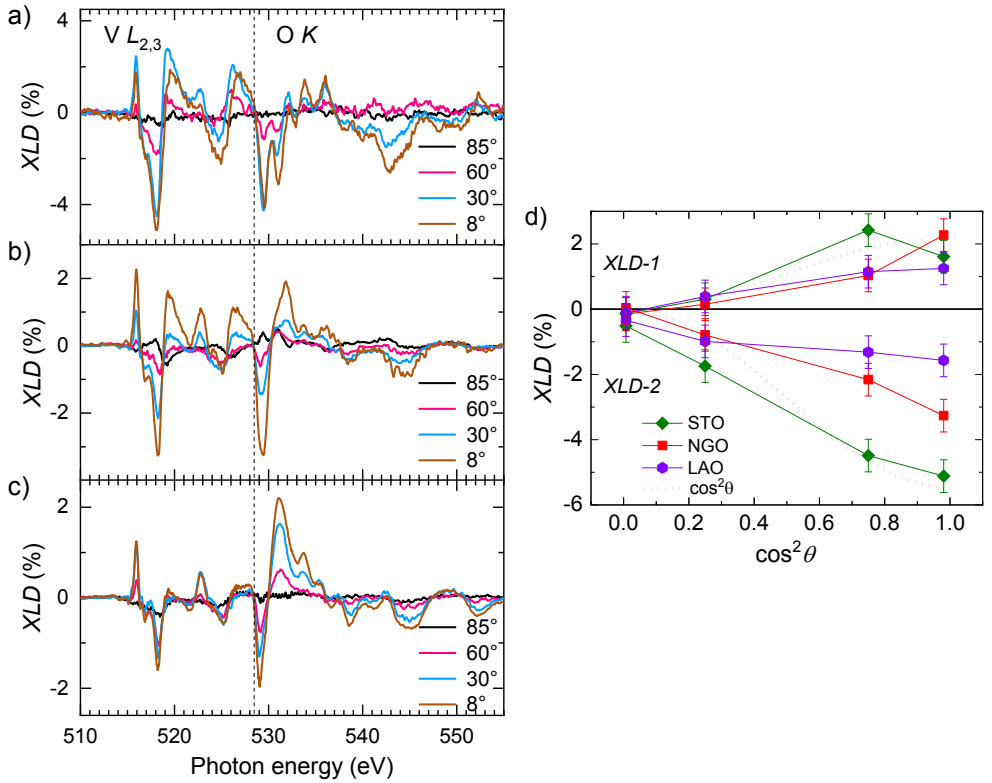

FIGURE D.9: a-c) Angular dependence of the XLD signals V L_3-edge for 10 nm SVO films on different substrates (STO, NGO, and LAO). d) Summary of the *XLD-1* and *XLD-2* maxima amplitudes for the different angles.

D.8 Strain-dependent *IDOS* of *d* orbitals

It can be appreciated in Figure D.10 that: (i) the occupancy of t_{2g} is larger than e_g as expected from the crystal field splitting of octahedral VO_6 coordination; (ii) the in-plane xy states are more occupied than xz, yz (which are degenerate) when $c/a<1$, illustrating that they are pushed down under tensile strain; the opposite trend holds for out-of-plane (xz, yz) when $c/a>1$; (iii) surprisingly the in-plane x^2-y^2 states display the opposite behavior, that is: they appear to be less occupied under tensile strain ($c/a<1$), and consistently, the z^2 states become less occupied under compressive strain ($c/a>1$). To explain this behavior it is helpful to calculate the center of mass E_{CM}, i. e. the average energy at which the d orbitals are located. Without any bonding-antibonding hybridization the DOS would be located around E_{CM}. When bonding-antibonding hybridization happens, the sign of $E_F - E_{CM}$ determines whether the bonding or the antibonding states have the dominant contribution below E_F. For the t_{2g} states $E_{CM}<E_F$, therefore the antibonding states, being partially occupied, control the behavior of the *IDOS*, as already explained in (i). For the e_g states, the antibonding states are unoccupied and lie at high energies and, as expected, $E_{CM}>E_F$, which results in the bonding states to be the only contribution to the *IDOS* below E_F. With respect to E_F the bonding states act exactly opposite to the antibonding states, and therefore, the *IDOS* for the e_g orbitals follows the opposite trend to the *IDOS* for t_{2g} states, as depicted in Figure D.10.

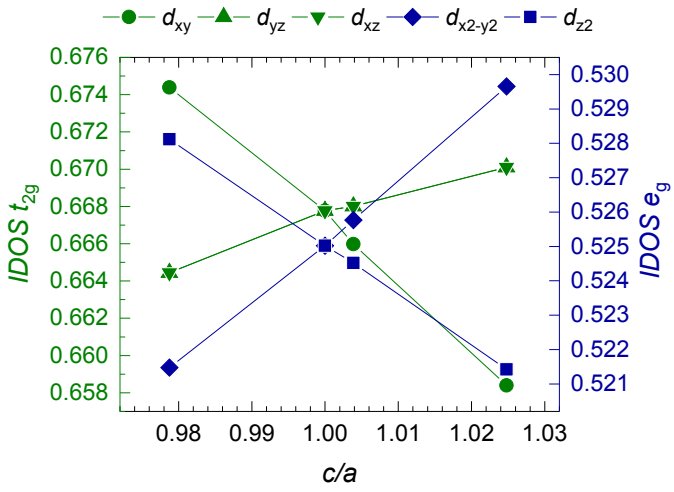

FIGURE D.10: *IDOS* of t_{2g} (left) and e_g (right) vs tetragonal distortion (c/a), for in-plane and out-of-plane orbitals, as indicated.

Appendix E

Appendix to Chapter 6

E.1 Transport data and Hall effect measurements

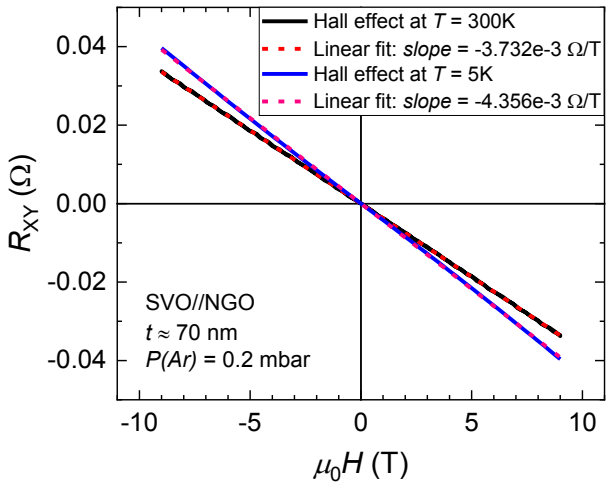

FIGURE E.1: Illustrative Hall effect measurements at 300 K and 5 K of a 70 nm thick SVO film deposited on NGO substrate, at $P(Ar) = 0.2$ mbar.

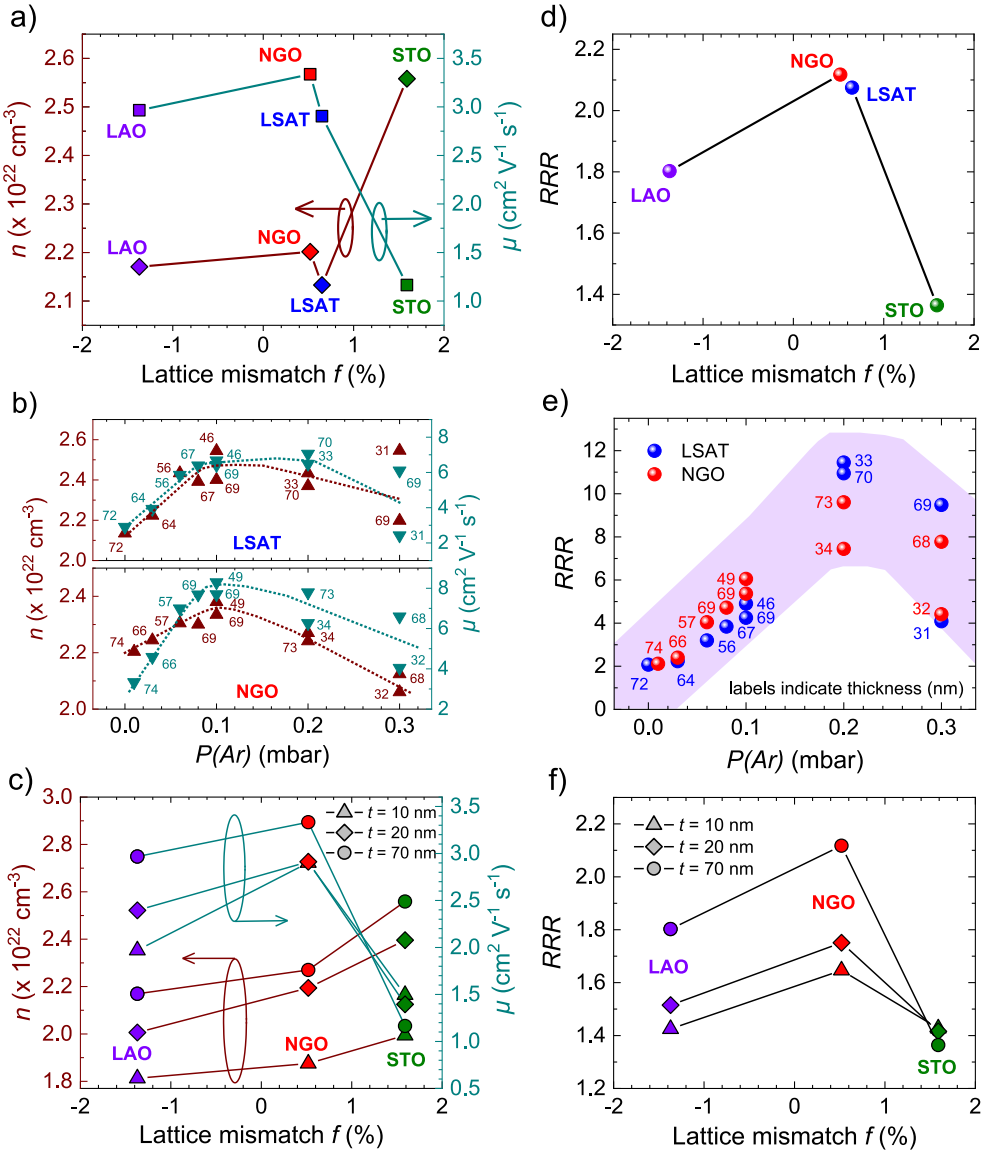

FIGURE E.2: Transport data for most SVO films of this study. From top to bottom row: strain series (different substrates), $P(Ar)$ series on LSAT and NGO, and thickness series (10, 20 and 70 nm) on various substrates. Left panels show the room-temperature carrier density n and mobility μ. Right panels show residual resistivity ratio (RRR) of the corresponding samples.

E.2 Fits of resistivity data to a quadratic temperature dependence and polaronic models

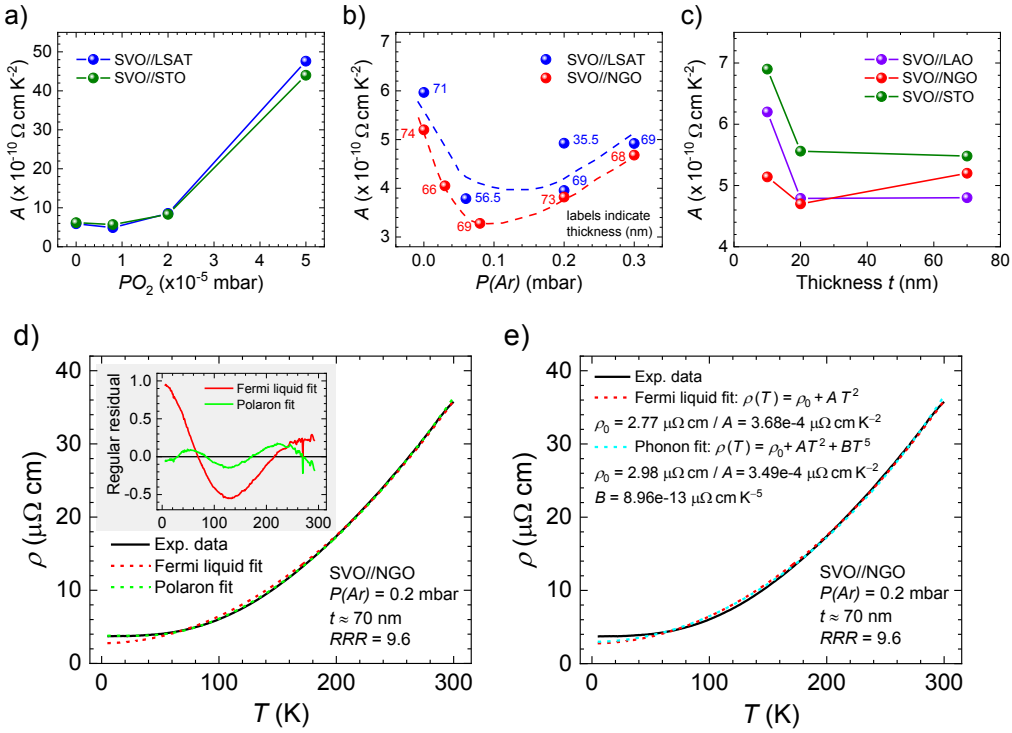

FIGURE E.3: Compilation of A values extracted from the fitting function $\rho(T) = \rho_0 + AT^2$. a) PO_2 series on STO and LSAT substrates. b) $P(Ar)$ series on LSAT and NGO substrates. c) Thickness series on LAO, NGO and STO substrates. d) Illustrative results of the fit of $\rho(T)$ using the T^2-dependence and the polaronic model. Inset show the residual difference $[\rho_{\text{exp}} - \rho_{\text{fit}}]$. Notice that the residual difference at $T < 180$-200 K becomes about a factor 10 larger in the quadratic model. e) Comparison of the T^2 and $AT^2 + BT^5$ fits together with the polaronic model, for an illustrative film.

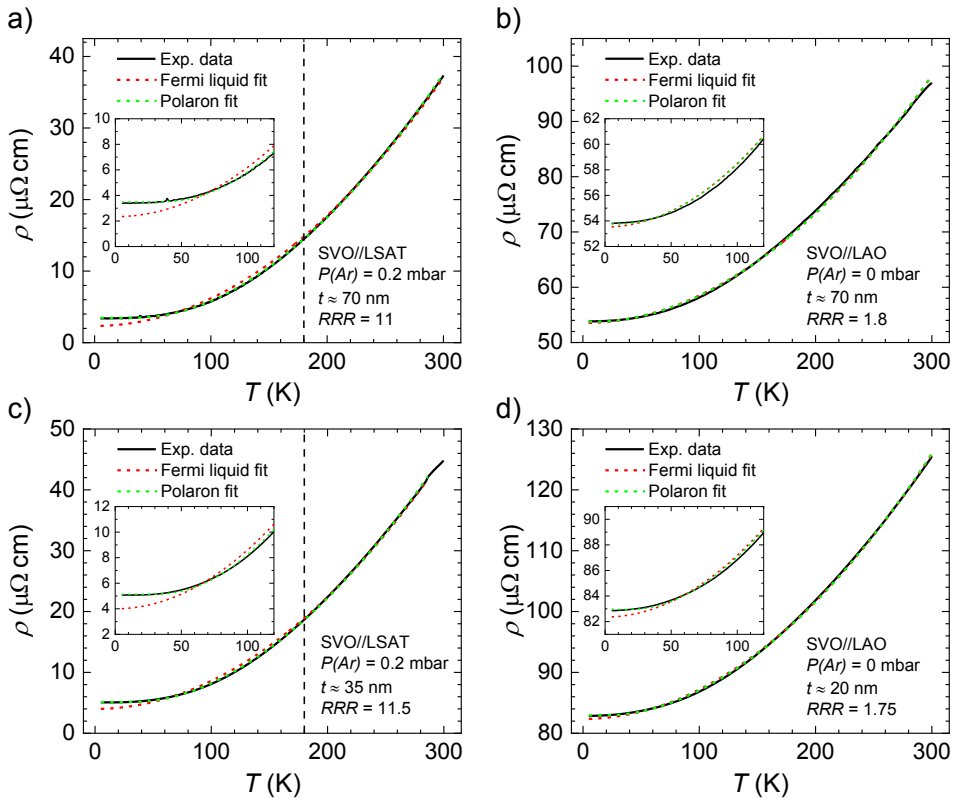

FIGURE E.4: Additional $\rho(T)$ data of SVO films together with Fermi liquid fit (red dashed curve) and polaron model fit (green dashed curve). Left panels show SVO of thickness: a) 70 nm and c) 35 nm thick film; deposited on LSAT at $P(Ar) = 0.2$ mbar. Right panels show SVO film of thickness: b) 70 nm and d) 20 nm; deposited on LAO at $P(Ar) = 0$ mbar. Insets are zooms of the low temperature region where the Fermi liquid fits show highest discrepancy.

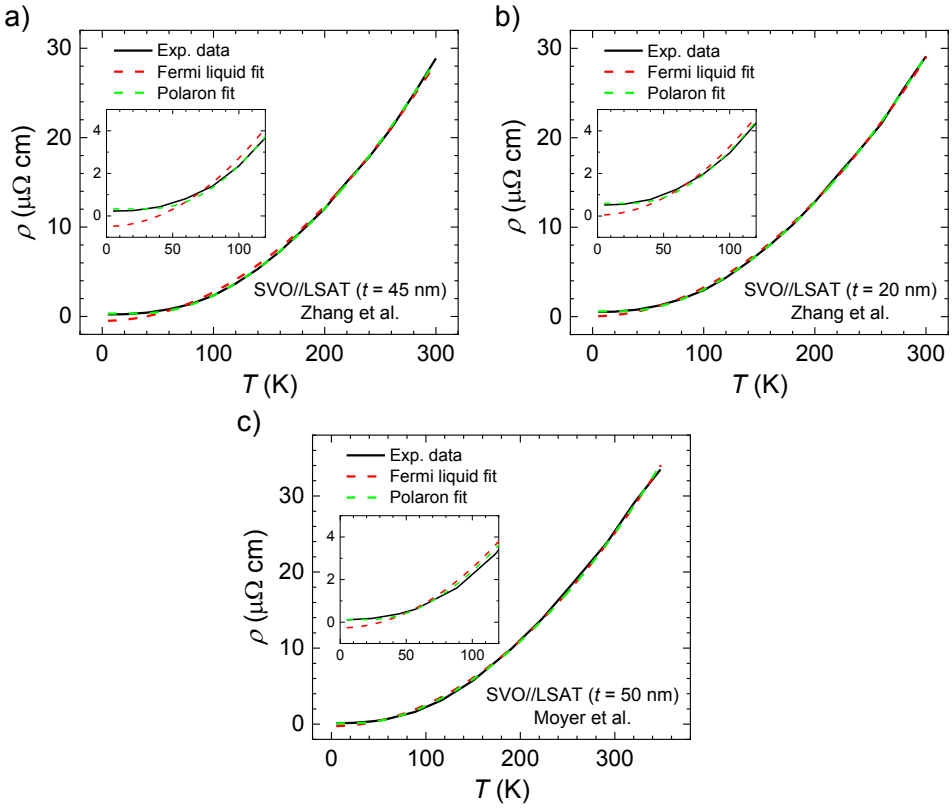

FIGURE E.5: Literature $\rho(T)$ data of SVO films grown on LSAT by hybrid-MBE, together with Fermi liquid fit (red dashed curve) and polaron model fit (green dashed curve). Data in (a,b) represent digitized data of 45 and 20 nm thick films, respectively, from Zhang et al. [18] Data in (c) are taken from Moyer et al. [42] (50 nm thick). Insets are zooms of the low temperature region where the Fermi liquid fits show highest discrepancy.

Sample	Fit	R^2	A_{ee} [Ω cm K^{-2}]	A^*_{e-ph} [Ω m s]	$\hbar\omega_0$ [meV]
SVO//STO (Fig. 5c)	Fermi liquid (fixed ρ_0)	0.99**314**	6.35e-10 ± 2.14e-12	x	x
	Fermi liquid	0.99**860**	6.72e-10 ± 1.46e-12	x	x
	Polaronic	0.99**995**	x	1.20e-20 ± 1.29e-23	20.6 ± 0.11
SVO//NGO (Fig. 5d)	Fermi liquid (fixed ρ_0)	0.99**867**	4.955e-10 ± 7.12e-13	x	x
	Fermi liquid	0.99**962**	5.07e-10 ± 5.74e-13	x	x
	Polaronic	0.99**980**	x	9.78e-21 ± 2.77e-22	12.74 ± 0.35
SVO//LAO (Fig. 5e)	Fermi liquid (fixed ρ_0)	0.99**899**	9.04e-10 ± 1.12e-12	x	x
	Fermi liquid	0.99**954**	9.20e-10 ± 1.15e-12	x	x
	Polaronic	0.99**962**	x	8.30e-21 ± 4.58e-22	10.75 ± 0.58

TABLE E.1: Fitting parameters for Fermi liquid (constrained and unconstrained) and polaronic fits, for some illustrative SVO films: SVO films (10 nm) on STO, NGO and LAO (data are shown in Figure 6.5). Notice the errors of parameters are < 6 %.

Sample	Initial $\hbar\omega_0$ [meV]	Initial A^*_{e-ph} [Ω m s]	Reduced chi-squared	R^2	$\hbar\omega_0$ [meV]	Dependency	A^*_{e-ph} [Ω m s]	Dependency
SVO//NGO (Fig. 5d)	**10**	**1e-20**	**0.0374**	**0.9998**	**12.74**	**0.9996**	**9.78e-21**	**0.9996**
	100	1e-20	0.0374	0.9998	12.74	0.9996	9.78e-21	0.9996
	1	1e-20	0.0374	0.9998	12.74	0.9996	9.78e-21	0.9996
	10	1e-19	0.0374	0.9998	12.74	0.9996	9.78e-21	0.9996
	10	1e-21	0.0374	0.9998	12.74	0.9996	9.78e-21	0.9996
	100	1e-19	0.0374	0.9998	12.74	0.9996	9.78e-21	0.9996
	100	1e-21	0.0374	0.9998	12.74	0.9996	9.78e-21	0.9996
	1	1e-19	0.0374	0.9998	12.74	0.9996	9.78e-21	0.9996
	1	1e-21	0.0374	0.9998	12.74	0.9996	9.78e-21	0.9996

TABLE E.2: Comparison of fitted parameters depending on input parameters for the polaronic fit. It can be appreciated that the input parameters can varied by about 3 orders of magnitude but the fitted values are virtually identical.

E.3 Softening of selected optical phonon modes with increasing tetragonality

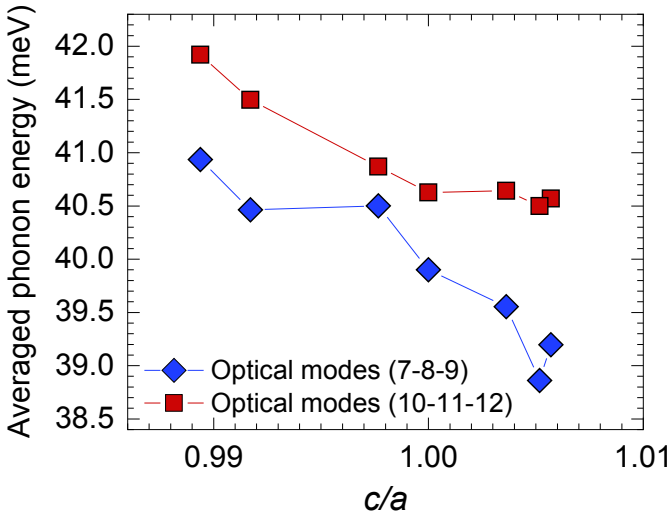

FIGURE E.6: Phonons in SVO. Phonon energies at Gamma-point of SVO have been calculated as a function of c/a using density functional perturbation theory available in Quantum Espresso. Preliminary data for phonons displaying the strongest e-phonon coupling are shown. The (7-12) indexes refer to optical modes of increasing energy. As the modes 7, 8 and 9, as well as the modes 10, 11 and 12, are split due to the tetragonal distortion, here we plot the averaged values for each group of modes.

E.4 Ellipsometric data

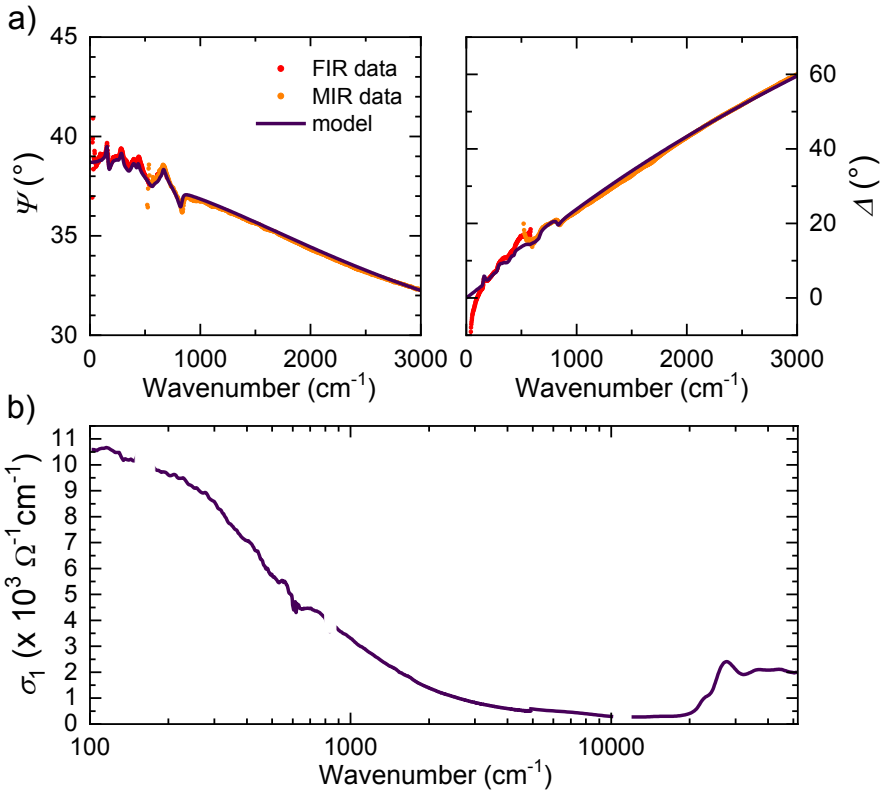

FIGURE E.7: a) Ellipsometric data (FIR + MIR) of a SVO film (72 nm thick) deposited on LSAT substrate. The measured (Ψ, Δ) spectra are fitted with a substrate/film/ambient model, where only the film response is varied. Substrate response was determined from ellipsometric measurements on a bare substrate [344]. The far-infrared response of the film is dominated by a Drude component. The extracted unscreened plasma frequency is $\omega_p = 19500\,\mathrm{cm}^{-1}$ ($\approx 2.42\,\mathrm{eV}$) and broadening $\gamma = 680\,\mathrm{cm}^{-1}$, which corresponds to a screened plasma energy $E^*_{\omega p} = 1.21\,\mathrm{eV}$ (considering $\varepsilon_\infty = 4$, as reported by Makino et al. [123]). The corresponding effective mass $m^* \approx 4.1 m_e$. Notice that we reported similar values in our previous studies (Chapters 3-4), and that similar values were encountered in literature [18]. Features in the Ψ/Δ spectra below $1000\,\mathrm{cm}^{-1}$ originate from the substrate phonons. b) Optical conductivity σ_1 of the SVO film up to UV (6.2 eV, $50000\,\mathrm{cm}^{-1}$) resulting from point-by-point fit to ellipsometry data.

E.5 Extended universal scaling between the prefactor of the T^2-dependent resistivity and the Fermi energy

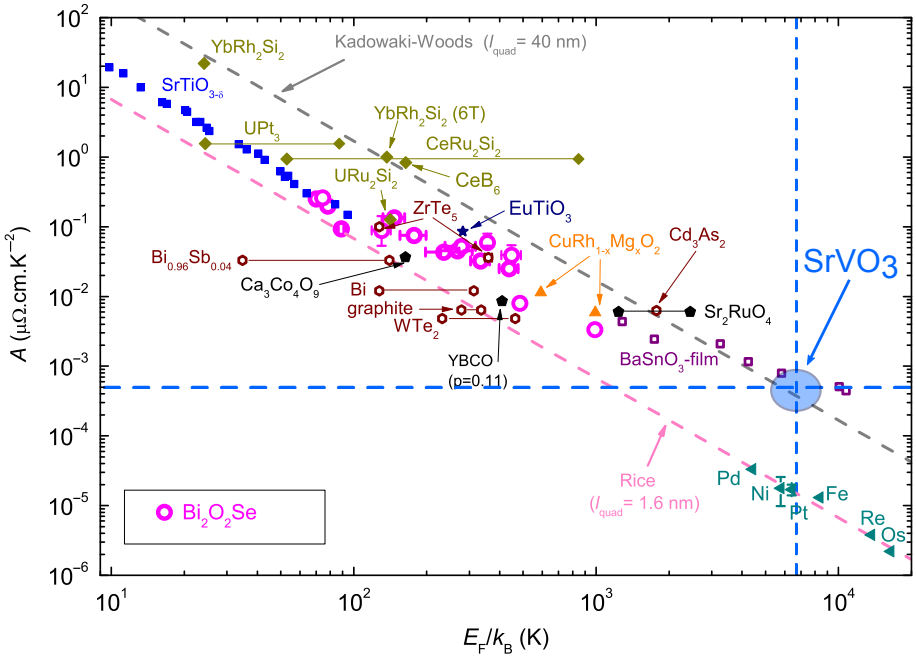

FIGURE E.8: Scaling between the prefactor of the T^2-dependent resistivity and the Fermi energy. Our data for SVO are plotted on top of data taken from Wang et al. [194].

Appendix F

Appendix to Chapter 7

F.1 Comparison of our experimental data with reported DFT simulations of optical properties.

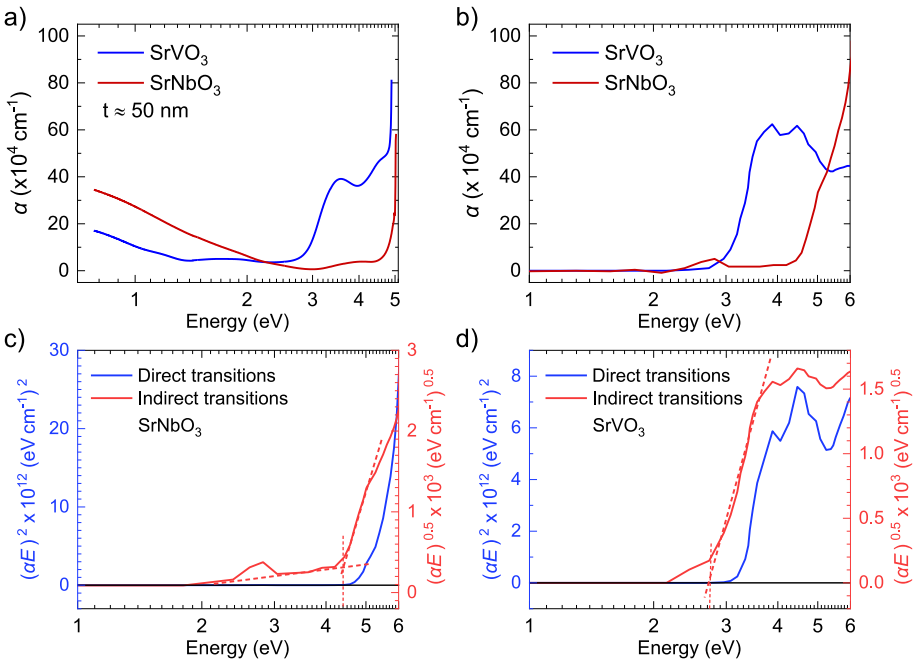

FIGURE F.1: a) Absorption coefficients ($\alpha = (-1/t)\ln T$) obtained from the transmittance data of SVO//LSAT (50 nm) and SNO//LSAT (45 nm) samples shown in Figure 7.7 of the Chap. 7. Note the strong onset of absorption at ≈ 2.7 eV and ≈ 4.5 eV for SVO and SNO respectively, in agreement with the Tauc plots shown in Figure 7.7c-d. b) DFT simulated absorption coefficients as reported by Paul et al. [255]. c-d) Corresponding Tauc plots, i.e. using the simulated absorption coefficients from [255].

F.2 Ellipsometric raw data.

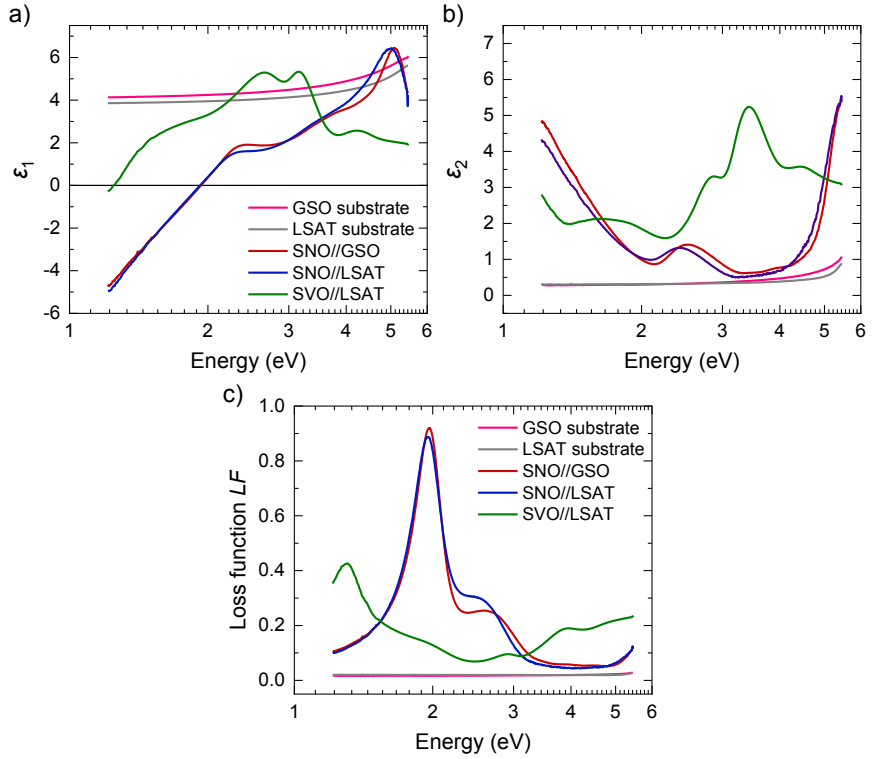

FIGURE F.2: Raw ellipsometric data for pristine GSO substrate, pristine LSAT substrate, SNO//GSO (65 nm), SNO//LSAT (65 nm), and SVO//LSAT (65 nm). a) ε_1, b) ε_2, and c) *LF*.

F.3 Polarization dependent transmittance measurements.

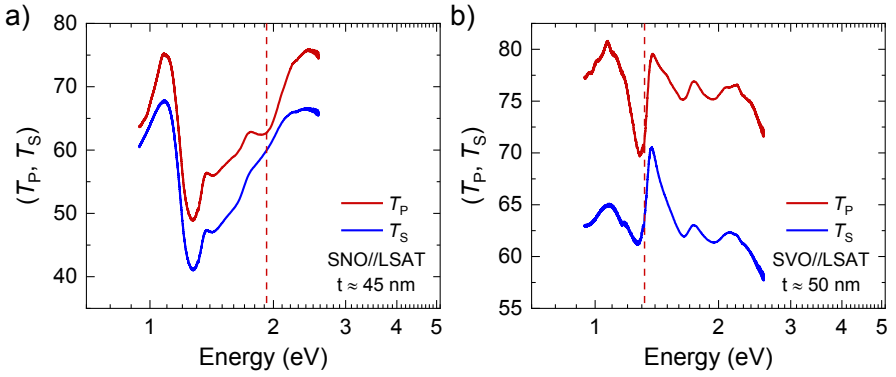

FIGURE F.3: Transmittance T_p and T_s collected at an angle of incidence of 30°, for: a) SNO//LSAT (50 nm) and b) SVO//LSAT (50 nm) bilayers. The dashed lines indicate the expected position of the dip in T_p.

F.4 Reflectance, transmittance and Brewster angle.

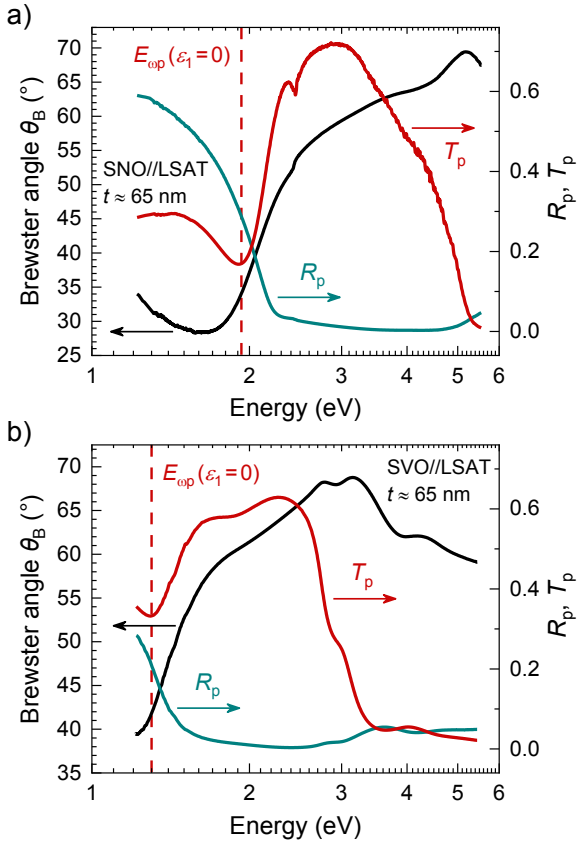

FIGURE F.4: (Left axis) Brewster angle $\theta_B = \arctan(n_{film}/n_{air})$ as a function of energy. (Right axis) Simulated p-polarized light reflectance R_p and transmittance T_p (at angle of incidence of 65°); for two illustrative samples: a) SNO//LSAT (65 nm), and b) SVO//LSAT (65 nm).

F.5 Losses in $SrNbO_3$ films of different thicknesses.

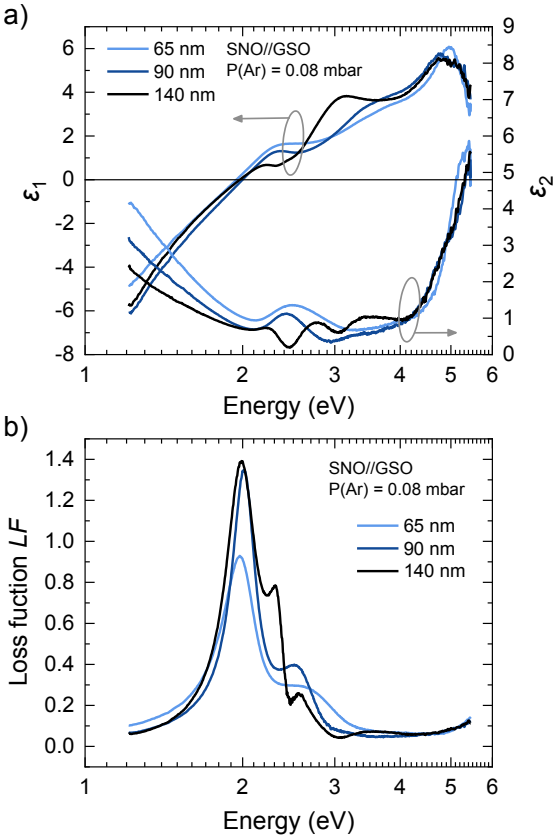

FIGURE F.5: Additional ellipsometry raw data of SNO//GSO films for different film thicknesses. a) $(\varepsilon_1, \varepsilon_2)$, and b) LF.

F.6 Work function of $SrNbO_3$ film measured by in-situ UPS.

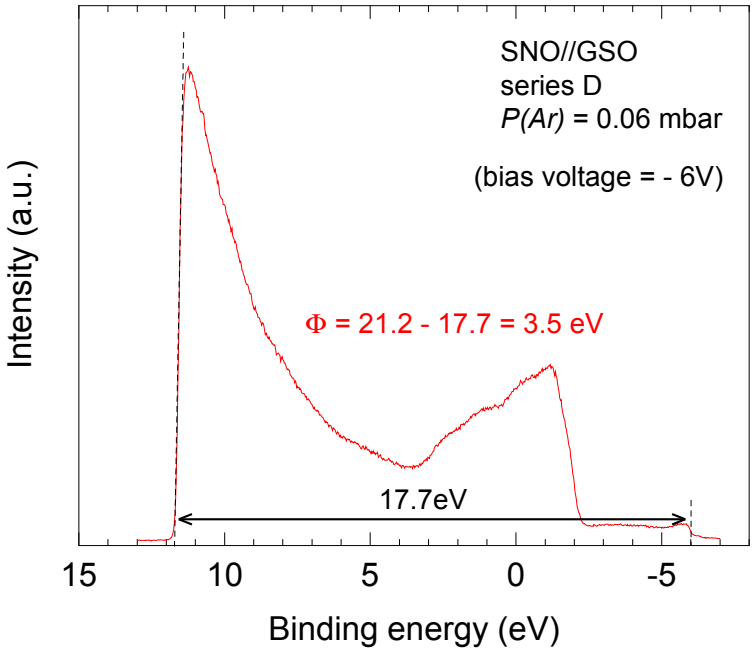

FIGURE F.6: UPS spectrum of a SNO//GSO film measured in-situ (by transferring the sample to the XPS chamber without breaking the vacuum, at T.U. Darmstadt). A bias voltage of -6 eV was applied. The extracted work function is 3.5 eV.

List of publications

Mathieu Mirjolet, Florencio Sánchez, and Josep Fontcuberta. “High Carrier Mobility, Electrical Conductivity, and Optical Transmittance in Epitaxial $SrVO_3$ Thin Films.” In: *Advanced Functional Materials* 29.14 (2019), p. 1808432. DOI: 10.1002/adfm.201808432.

Mathieu Mirjolet, Hari Babu Vasili, Lluís López-Conesa, Sònia Estradé, Francesca Peiró, José Santiso, Florencio Sánchez, Pamela Machado, Pierluigi Gargiani, Manuel Valvidares, and Josep Fontcuberta. "Independent Tuning of Optical Transparency Window and Electrical Properties of Epitaxial $SrVO_3$ Thin Films by Substrate Mismatch." In: *Advanced Functional Materials* 29.37 (2019), p. 1904238. DOI: 10.1002/adfm.201904238.

Mathieu Mirjolet, Francisco Rivadulla, Premysl Marsik, Vladislav Borisov, Roser Valentí, and Josep Fontcuberta. "Electron-Phonon Coupling and Electron-Phonon Scattering in $SrVO_3$" In: *Advanced Science* 21 (2021), p. 2004207. DOI: 10.1002/advs.202004207.

Mathieu Mirjolet, Mikko Kataja, Tommi K. Hakala, Philipp Komissinskiy, Lambert Alff, Gervasi Herranz, and Josep Fontcuberta. "Optical Plasmon Excitation in Transparent Conducting $SrNbO_3$ and $SrVO_3$ Thin Films." In: *Submitted.*

Mathieu Mirjolet, Hari Babu Vasili, Adrian Valadkhani, José Santiso, Vladislav Borisov, Pierluigi Gargiani, Manuel Valvidares, Roser Valentí, and Josep Fontcuberta. "Orbital Occupancy and Hybridization in Strained $SrVO_3$ Epitaxial Films." In: *Submitted.*

List of contributors

Mathieu Mirjolet: PLD deposition; sputter deposition; target fabrication; electrical measurements in single layers (with PPMS/Lakeshore setups) including contact preparation, measurements and data analysis; electrical measurements in capacitor-like devices; XRD data analysis; AFM image analysis; ellipsometric measurements and data analysis; UV-vis-NIR measurements and data analysis; XPS/UPS data analysis; SEM/EDX measurements and data analysis.

Dr. Florencio Sánchez & Raúl Solanas & Dr. Mengdi Qian: PLD and sputter depositions.

Dr. Hari Babu Vasili: XAS measurements and data analysis.

Prof. Roser Valentí & Dr. Vladislav Borisov & Adrian Valadkhani: first-principles calculations and data analysis.

Dr. Gervasi Herranz & Dr. Mikko Kataja & Prof. Tommi K. Hakala: polarization-dependent reflectance/transmittance measurements and data analysis.

Dr. Anna Crespi & Xavier Campos & Joan Esquius: XRD measurements and data analysis.

Dr. Bernat Bozzo & Dr. Ferran Vallès: PPMS measurements.

Anna Esther & Judith Oró: SEM measurements.

Maite Simón & Andrés Gómez: AFM measurements.

Dr. José Santiso & Dr. Jessica Padilla: XRD measurements and data analysis.

Dr. Francesca Peiró & Dr. Lluís López-Conesa & Dr. Sònia Estradé: TEM measurements.

Dr. Francisco Rivadulla: Seebeck measurements and data analysis.

Dr. Jordi Fraxedas & Dr. Guillaume Sauthier: XPS measurements and data analysis.

Prof. Christian Bernhard & Dr. Premysl Marsik: FIR ellipsometric measurements and data analysis.

Dr. Manuel Valvidares & Dr. Pierluigi gargiani: XAS measurements.

Dr. Mariona Coll and Pamela Machado: ellipsometric data analysis.

Dr. Ibraheem Yousef: synchrotron measurements.

Dr. Ignasi Villarroya: ICP-MS measurements.

Dr. Javier Saiz: FTIR measurements.

Roberta Ceravola: TGA measurements.

Bibliography

[1] Hideomi Koinuma. “Chemistry and electronics of oxides from carbon dioxide to perovskite”. In: *Thin Solid Films* 486.1-2 (2005), pp. 2–10. DOI: 10.1016/j.tsf.2004.11.243.

[2] Ramamoorthy Ramesh and Darrell G Schlom. “Whither Oxide Electronics ?” In: *MRS Bulletin* 33.11 (2008), pp. 1006–1014. DOI: 10.1557/mrs2008.220.

[3] Sieu D. Ha and Shriram Ramanathan. “Adaptive oxide electronics: A review”. In: *Journal of Applied Physics* 110.7 (2011), p. 071101. DOI: 10.1063/1.3640806.

[4] M. Lorenz et al. “The 2016 oxide electronic materials and oxide interfaces roadmap”. In: *Journal of Physics D: Applied Physics* 49.43 (2016), p. 433001. DOI: 10.1088/0022-3727/49/43/433001.

[5] M. Coll et al. “Towards Oxide Electronics: a Roadmap”. In: *Applied Surface Science* 482 (2019), pp. 1–93. DOI: 10.1016/j.apsusc.2019.03.312.

[6] J. G. Bednorz and K. A. Müller. “Possible High-Tc Superconductivity in the Ba-La-Cu-O system”. In: *Zeitschrift für Physik B Condensed Matter* 64 (1986), 189–193. DOI: 10.1007/BF01303701.

[7] Arthur P. Ramirez. “Oxide Electronics Emerge”. In: *Science* 315.5817 (2007), pp. 1377–1378. DOI: 10.1126/science.1138578.

[8] David S Ginley and David C Paine. *Handbook of Transparent Conductors*. 2011. ISBN: 9781441916372. DOI: 10.1007/978-1-4419-1638-9.

[9] Roy G Gordon. “Criteria for Choosing Transparent Conductors”. In: *MRS Bulletin* 25.8 (2000), pp. 52–57. DOI: 10.1557/mrs2000.151.

[10] Brian G Lewis and David C Paine. “Applications and Processing of Transparent Conducting Oxides”. In: *MRS Bulletin* 25.8 (2000), pp. 22–27. DOI: 10.1557/mrs2000.147.

[11] Claes G. Granqvist. “Transparent conductors as solar energy materials : A panoramic review”. In: *Solar Energy Materials and Solar Cells* 91 (2007), pp. 1529–1598. DOI: 10.1016/j.solmat.2007.04.031.

[12] Monica Morales-masis et al. “Transparent Electrodes for Efficient Optoelectronics”. In: *Advanced Electronic Materials* 3.5 (2017), p. 1600529. DOI: 10.1002/aelm.201600529.

[13] Saravanan Rajendran et al. *Metal and Metal Oxides for Energy and Electronics*. ISBN: 9783540228608. DOI: 10.1007/978-3-030-53065-5.

[14] Muhammad Arif Riza et al. “Prospects and challenges of perovskite type transparent conductive oxides in photovoltaic applications . Part I – Material developments”. In: *Solar Energy* 137 (2016), pp. 371–378. DOI: 10.1016/j.solener.2016.08.042.

[15] Andreas Klein. “Transparent Conducting Oxides: Electronic Structure–Property Relationship from Photoelectron Spectroscopy with in situ Sample Preparation”. In: *Journal of the American Ceramic Society* 96.2 (2013), pp. 331–345. ISSN: 00027820. DOI: 10.1111/jace.12143.

[16] Tadatsugu Minami. “Transparent conducting oxide semiconductors for transparent electrodes”. In: 35 (). DOI: 10.1088/0268-1242/20/4/004.

[17] K Ellmer. “Past achievements and future challenges in the development of optically transparent electrodes”. In: *Nature Photonics* 6.December (2012), pp. 809–817. DOI: 10.1038/nphoton.2012.282.

[18] Lei Zhang et al. “Correlated metals as transparent conductors”. In: *Nature Materials* 15.2 (2016), pp. 204–210. DOI: 10.1038/nmat4493.

[19] Yi Song et al. “Challenges and opportunities for graphene as transparent conductors in optoelectronics”. In: *Nano Today* 10.6 (2015), pp. 681–700. DOI: 10.1016/j.nantod.2015.11.005.

[20] T. W.H. Oates, H. Wormeester, and H. Arwin. “Characterization of plasmonic effects in thin films and metamaterials using spectroscopic ellipsometry”. In: *Progress in Surface Science* 86.11-12 (2011), pp. 328–376. ISSN: 00796816. DOI: 10.1016/j.progsurf.2011.08.004.

[21] P. B. Johnson and R. W. Christy. “Optical Constant of the Nobel Metals”. In: *Physical Review B* 6.12 (1972), pp. 4370–4379. DOI: 10.1103/PhysRevB.6.4370.

[22] Paul R. West et al. “Searching for better plasmonic materials”. In: *Laser and Photonics Reviews* 4.6 (2010), pp. 795–808. DOI: 10.1002/lpor.200900055.

[23] Mark Fox. *Optical Properties of Solids*. 2nd. Oxford, UK: Oxford University Press, 2010. ISBN: 978–0–19–957336–3.

[24] Muhammad Arif Riza et al. “Prospects and challenges of perovskite type transparent conductive oxides in photovoltaic applications . Part II – Synthesis and deposition”. In: *Solar Energy* 139 (2016), pp. 309–317. DOI: 10.1016/j.solener.2016.08.045.

[25] Abhinav Prakash et al. “Wide bandgap BaSnO3 films with room temperature conductivity exceeding 10^4 S cm-1”. In: *Nature Communications* 8.May (2017), p. 15167. ISSN: 20411723. DOI: 10.1038/ncomms15167.

[26] A J Freeman et al. “Chemical and Thin-Film Strategies for New Transparent Conducting Oxides”. In: *MRS Bulletin* AUGUST (2000), pp. 45–51.

[27] Feng Chen et al. “Reduction-induced Fermi level pinning at the interfaces between Pb(Zr,Ti)O3 and Pt, Cu and Ag metal electrodes”. In: *Journal of Physics D: Applied Physics* 44.25 (2011). ISSN: 00223727. DOI: 10.1088/0022-3727/44/25/255301.

[28] Gertjan Koster et al. “Structure, physical properties, and applications of SrRuO3 thin films”. In: *Reviews of Modern Physics* 84.1 (2012), pp. 253–298. DOI: 10.1103/RevModPhys.84.253.

[29] Ichiro Nagai et al. “Highest conductivity oxide SrMoO3 grown by a floating-zone method under ultralow oxygen partial pressure”. In: *Applied Physics Letters* 87.2 (2005), p. 024105. DOI: 10.1063/1.1992671.

[30] Lambert Alff et al. “The role of cationic and anionic point defects in pulsed laser deposition of perovskites”. In: *Journal of Physics D: Applied Physics* 47.3 (2014), p. 034012. ISSN: 00223727. DOI: 10.1088/0022-3727/47/3/034012.

[31] Daichi Oka et al. “Intrinsic high electrical conductivity of stoichiometric SrNbO3 epitaxial thin films”. In: *Physical Review B* 92.20 (2015), p. 205102. ISSN: 1098-0121. DOI: 10.1103/PhysRevB.92.205102.

[32] Masao Nakamura et al. “Perovskite LaRhO3 as a p-type active layer in oxide photovoltaics”. In: *Applied Physics Letters* 106.7 (2015), p. 072103. ISSN: 00036951. DOI: 10.1063/1.4909512.

[33] M. Huijben et al. “Critical thickness and orbital ordering in ultrathin La0.7Sr0.3MnO3 films”. In: *Physical Review B* 78.9 (2008), p. 094413. DOI: 10.1103/PhysRevB.78.094413.

[34] Mingwei Zhu et al. “Effect of composition and strain on the electrical properties of LaNiO3 thin films”. In: *Applied Physics Letters* 103.14 (2013), p. 141902. DOI: 10.1063/1.4823697.

[35] Sucharita Madhukar et al. “Effect of oxygen stoichiometry on the electrical properties of La0.5Sr0.5CoO3 electrodes”. In: *Applied Physics Letters* 81.8 (2001), p. 3543. ISSN: 00036951. DOI: 10.1063/1.364991.

[36] Aldin Radetinac. “Hochleitfähiges SrMoO3: Vom Schichtwachstum zur Anwendungseignung”. PhD thesis. 2017. URL: http://tuprints.ulb.tu-darmstadt.de/id/eprint/6005%0D.

[37] G. Haacke. “New figure of merit for transparent conductors”. In: *Journal of Applied Physics* 47.9 (1976), pp. 4086–4089. ISSN: 00218979. DOI: 10.1063/1.323240.

[38] Yoonsang Park et al. “SrNbO3 as a transparent conductor in the visible and ultraviolet spectra”. In: *Communications Physics* 3.102 (2020), pp. 1–7. DOI: 10.1038/s42005-020-0372-9.

[39] Aldin Radetinac et al. “Highly conducting SrMoO3 thin films for microwave applications”. In: *Applied Physics Letters* 105.11 (2014), p. 114108. DOI: 10.1063/1.4896339.

[40] P. Salg et al. “Atomically interface engineered micrometer-thick SrMoO3 oxide electrodes for thin-film BaxSr1- xTiO3 ferroelectric varactors tunable at low voltages”. In: *APL Materials* 7.5 (2019), p. 051107. ISSN: 2166532X. DOI: 10.1063/1.5094855.

[41] F. Chen et al. “Energy band alignment between Pb(Zr,Ti)O3 and high and low work function conducting oxides - From hole to electron injection”. In: *Journal of Physics D: Applied Physics* 43.29 (2010), p. 295301. ISSN: 00223727. DOI: 10.1088/0022-3727/43/29/295301.

[42] Jarrett A. Moyer, Craig Eaton, and Roman Engel-Herbert. “Highly Conductive SrVO3 as a Bottom Electrode for Functional Perovskite Oxides”. In: *Advanced Materials* 25.26 (2013), pp. 3578–3582. ISSN: 09359648. DOI: 10.1002/adma.201300900.

[43] Javier Macías, Aleksey A. Yaremchenko, and Jorge R. Frade. “Enhanced stability of perovskite-like SrVO3-based anode materials by donor-type substitutions”. In: *Journal of Materials Chemistry A* 4.26 (2016), pp. 10186–10194. DOI: 10.1039/c6ta02672a.

[44] Brandon H. Smith and Michael D. Gross. “A highly conductive oxide anode for solid oxide fuel cells”. In: *Electrochemical and Solid-State Letters* 14.1 (2011), B1–B5. DOI: 10.1149/1.3505101.

[45] Zhihong Du et al. “Optimization of strontium molybdate based composite anode for solid oxide fuel cells”. In: *Journal of Power Sources* 274 (2015), pp. 568–574. DOI: 10.1016/j.jpowsour.2014.10.062.

[46] D. Y. Wan et al. “Electron transport and visible light absorption in a plasmonic photocatalyst based on strontium niobate”. In: *Nature Communications* 8.April (2017), p. 15070. ISSN: 20411723. DOI: 10.1038/ncomms15070.

[47] Matthew P. Wells et al. “Tunable, Low Optical Loss Strontium Molybdate Thin Films for Plasmonic Applications”. In: *Advanced Optical Materials* 5.22 (2017), p. 1700622. DOI: 10.1002/adom.201700622.

[48] Milton Ohring. *Materials Science of Thin Films*. 2nd. Academic Press, 2002. ISBN: 9780125249751. DOI: 10.1016/B978-012524975-1/50010-0.

[49] Mario Birkholz. *Thin Film Analysis by X-Ray Scattering*. Wiley-VCH, 2006. ISBN: 9783527310524.

[50] M A Moram and M E Vickers. "X-ray diffraction of III-nitrides". In: *Reports on Progress in Physics* 72.3 (2009), p. 036502. DOI: 10.1088/0034-4885/72/3/036502.

[51] Bob B. He. *Two-Dimensional X-Ray Diffraction*. Wiley, 2009. ISBN: 9780470227220. DOI: 10.1002/9780470502648.

[52] Vitalij K. Pecharsky and Peter Y. Zavalij. *Fundamentals of Powder Diffraction and Structural Characterization of Materials*. Ed. by Springer. Vol. 84. 4. 1989, pp. 571–576. ISBN: 9780387095783. DOI: 10.1007/978-0-387-09579-0.

[53] J. B. Nelson and D. P. Riley. "An experimental investigation of extrapolation methods in the derivation of accurate unit-cell dimensions of crystals". In: *Proceedings of the Physical Society* 57.3 (1945), pp. 160–177. DOI: 10.1088/0959-5309/57/3/302.

[54] Juri Banchewski. "Transient Liquid Assisted Growth of YBCO Superconducting Films: Growth Kinetics, Physical Properties and Vortex Pinning". PhD thesis. Universitat Autònoma de Barcelona, 2020. URL: http://hdl.handle.net/10803/671035.

[55] D. Pesquera et al. "X-ray interference effects on the determination of structural data in ultrathin La2/3Sr1/3MnO3 epitaxial thin films". In: *Applied Physics Letters* 99.22 (2011), p. 221901. ISSN: 00036951. DOI: 10.1063/1.3663574.

[56] Matts Björck and Gabriella Andersson. "GenX: An extensible X-ray reflectivity refinement program utilizing differential evolution". In: *Journal of Applied Crystallography* 40.6 (2007), pp. 1174–1178. DOI: 10.1107/S0021889807045086.

[57] L.J. van der Pauw. *A method of measuring specific resisivity and hall effect of discs of arbitrary shape*. 1958. DOI: 10.1142/9789814503464{_}0017.

[58] L.J. van der Pauw. "A method of measuring the resistivity and hall coefficient on lamallae of arbitrary shape". In: *Philips Technical Review* 20.8 (1958), p. 220.

[59] A. B. Pippard. *Magnetoresistance in metals*. Cambridge University Press, 1989. ISBN: 0-521-32660-5.

[60] Harland G. Tompkins and Eugene A. Irene. *Handbook of Ellipsometry*. 2005, pp. 1–870. ISBN: 9780815517474. DOI: 10.1515/arh-2005-0022.

[61] R_M_A_Azzam and N_M_Bashara. *Ellipsometry and Polarized Light*. North-Holland Publishing Company, 1977. ISBN: 0-7204-0694-3.

[62] Hiroyuki Fujiwara. *Spectroscopic Ellipsometry: Principles and Applications*. 2007, pp. 1–369. ISBN: 0470016086. DOI: 10.1002/9780470060193.

[63] C. Bernhard, J. Humlícek, and B. Keimer. "Far-infrared ellipsometry using a synchrotron light source - The dielectric response of the cuprate high Tc superconductors". In: *Thin Solid Films* 455-456 (2004), pp. 143–149. ISSN: 00406090. DOI: 10.1016/j.tsf.2004.01.002.

[64] John F. Moulder et al. *Handbook of X-ray Photoelectron Spectroscopy*. Physical Electronics, Inc., 1992. ISBN: 0-9648124-1-X.

[65] John F. Watts and John Wolstenholme. *An Introduction to Surface Analysis by XPS and AES*. Wiley, 2003. ISBN: 0470847123.

[66] C. N. Berglund and W. E. Spicer. "Photoemission studies of copper and silver: Theory". In: *Physical Review* 136.4A (1964), pp. 1030–1044. ISSN: 0031899X. DOI: 10.1103/PhysRev.136.A1030.

[67] C. N. Berglund and W. E. Spicer. "Photoemission studies of copper and silver: Experiment". In: *Physical Review* 136.4A (1964), pp. 1044–1064. ISSN: 0031899X. DOI: 10.1103/PhysRev.136.A1044.

[68] Dhruv Shah et al. "Tutorial on interpreting x-ray photoelectron spectroscopy survey spectra: Questions and answers on spectra from the atomic layer deposition of Al2O3 on silicon". In: *Journal of Vacuum Science & Technology B* 36.6 (2018), p. 062902. ISSN: 2166-2746. DOI: 10.1116/1.5043297.

[69] E. A. Kraut et al. "Precise Determination of the Valence-Band Edge in X-Ray Photoemission Spectra: Application to Measurement of Semiconductor Interface Potentials". In: *Physical Review Letters* 44.24 (1980), pp. 1620–1623. DOI: 10.1103/PhysRevLett.44.1620.

[70] E. A. Kraut et al. "Semiconductor core-level to valence-band maximum binding-energy differences: Precise determination by x-ray photoelectron spectroscopy". In: *Physical Review B* 28.4 (1983), pp. 1965–1977. ISSN: 01631829. DOI: 10.1103/PhysRevB.28.1965.

[71] J. R. Waldrop et al. "Measurement of semiconductor heterojunction band discontinuities by x-ray photoemission spectroscopy". In: *Journal of Vacuum Science & Technology A* 3.3 (1985), pp. 835–841. ISSN: 0734-2101. DOI: 10.1116/1.573326.

[72] S. A. Chambers et al. "Instability, intermixing and electronic structure at the epitaxial LaAlO3/SrTiO3(001) heterojunction". In: *Surface Science Reports* 65.10-12 (2010), pp. 317–352. ISSN: 01675729. DOI: 10.1016/j.surfrep.2010.09.001.

[73] S. A. Chambers et al. “Band alignment, built-in potential, and the absence of conductivity at the LaCrO3/SrTiO3(001) heterojunction”. In: *Physical Review Letters* 107.20 (2011), p. 206802. ISSN: 00319007. DOI: 10.1103/PhysRevLett.107.206802.

[74] Scott A. Chambers et al. “Band alignment at epitaxial BaSnO3/SrTiO3(001) and BaSnO3/LaAlO3(001) heterojunctions”. In: *Applied Physics Letters* 108.15 (2016), p. 152104. ISSN: 00036951. DOI: 10.1063/1.4946762.

[75] Ryan Comes and Scott Chambers. “Interface Structure, Band Alignment, and Built-In Potentials at LaFeO3/n-SrTiO3 Heterojunctions”. In: *Physical Review Letters* 117.22 (2016), p. 226802. ISSN: 10797114. DOI: 10.1103/PhysRevLett.117.226802.

[76] Robert Schafranek et al. “PbTiO3/SrTiO3 interface: Energy band alignment and its relation to the limits of Fermi level variation”. In: *Physical Review B* 84.4 (2011), p. 045317. ISSN: 10980121. DOI: 10.1103/PhysRevB.84.045317.

[77] Kevin J. May et al. “Thickness-dependent photoelectrochemical water splitting on ultrathin LaFeO3 films grown on Nb:SrTiO3”. In: *Journal of Physical Chemistry Letters* 6.6 (2015), pp. 977–985. ISSN: 19487185. DOI: 10.1021/acs.jpclett.5b00169.

[78] Shunyi Li et al. “Electrical properties of (Ba,Sr)TiO3 thin films with Pt and ITO electrodes: Dielectric and rectifying behaviour”. In: *Journal of Physics Condensed Matter* 23.33 (2011), p. 334202. ISSN: 09538984. DOI: 10.1088/0953-8984/23/33/334202.

[79] R. Schafranek et al. “Barrier height at (Ba,Sr)TiO3/Pt interfaces studied by photoemission”. In: *Physical Review B* 77.19 (2008), p. 195310. ISSN: 10980121. DOI: 10.1103/PhysRevB.77.195310.

[80] D. Pesquera et al. “Surface symmetry-breaking and strain effects on orbital occupancy in transition metal perovskite epitaxial films”. In: *Nature Communications* 3 (2012), p. 1189. ISSN: 20411723. DOI: 10.1038/ncomms2189.

[81] Hari Babu Vasili et al. “In operando adjustable orbital polarization in LaNiO3 thin films”. In: *Physical Review Materials* 4.4 (2020), p. 044404. ISSN: 24759953. DOI: 10.1103/PhysRevMaterials.4.044404.

[82] Ankit S Disa et al. “Orbital Engineering in Symmetry-Breaking Polar Heterostructures”. In: *Physical Review Letters* 114.2 (2015), p. 026801. DOI: 10.1103/PhysRevLett.114.026801.

[83] David Pesquera. “Strain and interface-induced charge, orbital and spin orderings in transition-metal oxide perovskites”. PhD thesis. Universitat Autònoma de Barcelona, 2014.

[84] Heiko Wende. “Recent advances in x-ray absorption spectroscopy”. In: *Reports on Progress in Physics* 67.12 (2004), pp. 2105–2181. ISSN: 00344885. DOI: 10.1088/0034-4885/67/12/R01.

[85] M. W. Haverkort. “Spin and orbital degrees of freedom in transition metal oxides and oxide thin films studied by soft x-ray absorption spectroscopy”. PhD thesis. Universität zu Köln, 2005. URL: http://arxiv.org/abs/cond-mat/0505214.

[86] Joachim Stöhr. *NEXAFS Spectroscopy*. Ed. by G. Ertl, R. Gomer, and D. L. Mills. Berlin: Springer-Verlag, 1992. ISBN: 978-3-540-54422-7. DOI: 10.1007/978-3-662-02853-7.

[87] J. Stöhr and H. C. Siegmann. *Magnetism: from fundamentals to nanoscale dynamics*. Springer, 2006. ISBN: 9783540302827.

[88] Alessandro Barla et al. “Design and performance of BOREAS, the beamline for resonant X-ray absorption and scattering experiments at the ALBA synchrotron light source”. In: *Journal of Synchrotron Radiation* 23.6 (2016), pp. 1507–1517. DOI: 10.1107/s1600577516013461.

[89] Federica Frati, Myrtille O.J.Y. Hunault, and Frank M.F. De Groot. “Oxygen K-edge X-ray Absorption Spectra”. In: *Chemical Reviews* 120.9 (2020), pp. 4056–4110. ISSN: 15206890. DOI: 10.1021/acs.chemrev.9b00439.

[90] C. T. Chen et al. “Out-of-plane Orbital of instrinsic and doped Holes in La(2-x)Sr(x)CuO(4)”. In: *Physical Review Letters* 68.16 (1992), pp. 2543–2546. DOI: 10.1103/PhysRevLett.68.2543.

[91] Nader Jalili and Karthik Laxminarayana. “A review of atomic force microscopy imaging systems: Application to molecular metrology and biological sciences”. In: *Mechatronics* 14.8 (2004), pp. 907–945. ISSN: 09574158. DOI: 10.1016/j.mechatronics.2004.04.005.

[92] Shaoyang Liu and Yifen Wang. *A Review of the Application of Atomic Force Microscopy (AFM) in Food Science and Technology*. Vol. 62. 2011, pp. 201–240. ISBN: 9780123859891. DOI: 10.1016/B978-0-12-385989-1.00006-5.

[93] I. Horcas et al. “WSXM: A software for scanning probe microscopy and a tool for nanotechnology”. In: *Review of Scientific Instruments* 78.1 (2007), p. 013705. ISSN: 00346748. DOI: 10.1063/1.2432410.

[94] Kathryn L. Linge and Kym E. Jarvis. “Quadrupole ICP-MS: Introduction to instrumentation, measurement techniques and analytical capabilities”. In: *Geostandards and Geoanalytical Research* 33.4 (2009), pp. 445–467. ISSN: 16394488. DOI: 10.1111/j.1751-908X.2009.00039.x.

[95] Klaus Koepernik and Helmut Eschrig. "Full-potential nonorthogonal local-orbital minimum-basis band-structure scheme". In: *Physical Review B* 59.3 (1999), pp. 1743–1757. ISSN: 1550235X. DOI: 10.1103/PhysRevB.59.1743.

[96] I. Opahle, K. Koepernik, and H. Eschrig. "Full-potential band-structure calculation of iron pyrite". In: *Physical Review B* 60.20 (1999), pp. 14035–14041. ISSN: 1550235X. DOI: 10.1103/PhysRevB.60.14035.

[97] H. Eschrig, K. Koepernik, and I. Chaplygin. "Density functional application to strongly correlated electron systems". In: *Journal of Solid State Chemistry* 176.2 (2003), pp. 482–495. ISSN: 00224596. DOI: 10.1016/S0022-4596(03)00274-3.

[98] P. Hohenberg and W. Kohn. "Inhomogeneous Electron Gas". In: *Physical Review* 136.3B (1964), B864. DOI: 10.1103/PhysRev.136.B864.

[99] W. Kohn and L. J. Sham. "Self-Consistent Equations Including Exchange and Correlation Effects". In: *Physical Review* 140.4A (1965), pp. 1133–1138. URL: https://doi.org/10.1103/PhysRev.140.A1133.

[100] John P. Perdew, Kieron Burke, and Matthias Ernzerhof. "Generalized Gradient Approximation Made Simple". In: *Physical Review Letters* 77.18 (1996), pp. 3865–3868. ISSN: 10797114. DOI: 10.1103/PhysRevLett.77.3865.

[101] Paolo Giannozzi et al. "QUANTUM ESPRESSO: a modular and open-source software project for quantum simulations of materials". In: *Journal of Physics Condensed Matter* 21.39 (2009), 395502 (19 pp). ISSN: 09538984. DOI: 10.1088/0953-8984/21/39/395502.

[102] Joerg Heber. "Materials science: Enter the oxides". In: *Nature* 459.7243 (2009), pp. 28–30. ISSN: 00280836. DOI: 10.1038/459028a.

[103] Darrell G. Schlom and Loren N. Pfeiffer. "Oxide electronics: Upward mobility rocks!" In: *Nature Materials* 9.11 (2010), pp. 881–883. ISSN: 14764660. DOI: 10.1038/nmat2888.

[104] A. Ohtomo and H. Y. Hwang. "A high-mobility electron gas at the LaAlO3/SrTiO3 heterointerface". In: *Nature* 427.6973 (2004), pp. 423–426. ISSN: 0028-0836. DOI: 10.1038/nature04773.

[105] X. Luo et al. "High carrier mobility in transparent Ba1-xLaxSnO3 crystals with a wide band gap". In: *Applied Physics Letters* 100.17 (2012), p. 172112. ISSN: 00036951. DOI: 10.1063/1.4709415.

[106] Hyung Joon Kim et al. "High Mobility in a Stable Transparent Perovskite Oxide". In: *Applied Physics Express* 5.06 (2012), p. 061102. DOI: 10.1143/APEX.5.061102.

[107] Hyung Joon Kim et al. “Physical properties of transparent perovskite oxides (Ba,La)SnO3 with high electrical mobility at room temperature”. In: *Physical Review B* 86.16 (2012), p. 165205. ISSN: 10980121. DOI: 10.1103/PhysRevB.86.165205.

[108] Santosh Raghavan et al. “High-mobility BaSnO3 grown by oxide molecular beam epitaxy”. In: *APL Materials* 4.1 (2016), p. 016106. ISSN: 2166532X. DOI: 10.1063/1.4939657.

[109] S. M. Sze and K. Ng Kwok. *Physics of Semiconductor Devices*. Ed. by Wiley-Interscience. 3rd. Hoboken, New Jersey: John Wiley & Sons, 2007. ISBN: 0471143235.

[110] Craig Eaton et al. “Growth of SrVO3 thin films by hybrid molecular beam epitaxy”. In: *Journal of Vacuum Science & Technology A* 33.6 (2015), p. 061504. DOI: 10.1116/1.4927439.

[111] Matthew Brahlek et al. “Accessing a growth window for SrVO3 thin films”. In: *Applied Physics Letters* 107.14 (2015), p. 143108. ISSN: 00036951. DOI: 10.1063/1.4932198.

[112] Jun Wang, Guus Rijnders, and Gertjan Koster. “Complex plume stoichiometry during pulsed laser deposition of SrVO3 at low oxygen pressures”. In: *Applied Physics Letters* 113.22 (2018), p. 223103. ISSN: 0003-6951. DOI: 10.1063/1.5049792.

[113] W. C. Sheets, B. Mercey, and W. Prellier. “Effect of charge modulation in (LaVO3)m(SrVO3)n superlattices on the insulator-metal transition”. In: *Applied Physics Letters* 91.19 (2007), p. 192102. ISSN: 00036951. DOI: 10.1063/1.2805222.

[114] Bruno Bérini et al. “Control of High Quality SrVO3 Electrode in Oxidizing Atmosphere”. In: *Advanced Materials Interfaces* 3.18 (2016), p. 1600274. ISSN: 21967350. DOI: 10.1002/admi.201600274.

[115] A. Boileau et al. “Optical and electrical properties of the transparent conductor SrVO3 without long-range crystalline order”. In: *Applied Physics Letters* 112.2 (2018), p. 021905. ISSN: 00036951. DOI: 10.1063/1.5016245.

[116] Arnaud Fouchet et al. “Study of the electronic phase transition with low dimensionality in SrVO3 thin films”. In: *Materials Science and Engineering B* 212 (2016), pp. 7–13. ISSN: 09215107. DOI: 10.1016/j.mseb.2016.07.009.

[117] Arnaud Fouchet et al. “Interface chemical and electronic properties of LaAlO3/SrVO3 heterostructures”. In: *Journal of Applied Physics* 123.5 (2018), p. 055302. ISSN: 10897550. DOI: 10.1063/1.4998004.

[118] K. Yoshimatsu et al. “Dimensional-crossover-driven metal-insulator transition in SrVO3 ultrathin films”. In: *Physical Review Letters* 104.14 (2010), p. 147601. ISSN: 00319007. DOI: 10.1103/PhysRevLett.104.147601.

[119] D. H Kim et al. “Electrical properties of SrVO3/SrTiO3 superlattices grown by laser molecular beam epitaxy”. In: *Solid State Communications* 114.9 (2000), pp. 473–476. DOI: 10.1016/S0038-1098(00)00095-8.

[120] Dong-Wook Kim et al. “Interface chemistry and electrical properties of SrVO3/LaAlO3 heterostructures”. In: *Journal of Applied Physics* 88.12 (2000), p. 7056. DOI: 10.1063/1.1326896.

[121] Masaki Kobayashi et al. “Emergence of Quantum Critical Behavior in Metallic Quantum-Well States of Strongly Correlated Oxides”. In: *Scientific Reports* 7.1 (2017), p. 16621. ISSN: 20452322. DOI: 10.1038/s41598-017-16666-x.

[122] Gabriele Sclauzero and Claude Ederer. “Structural and electronic properties of epitaxially strained LaVO3 from density functional theory and dynamical mean-field theory”. In: *Physical Review B* 92.23 (2015), p. 235112. ISSN: 1550235X. DOI: 10.1103/PhysRevB.92.235112.

[123] H. Makino et al. “Bandwidth control in a perovskite-type-correlated metal II. Optical spectroscopy”. In: *Physical Review B* 58.8 (1998), pp. 4384–4393. ISSN: 1550235X. DOI: 10.1103/PhysRevB.58.4384.

[124] I. H Inoue et al. “Bandwidth control in a perovskite-type 3d1-correlated metal Ca1-xSrxVO3. I. Evolution of the electronic properties and effective mass”. In: *Physical Review B* 58.8 (1998), p. 4372. ISSN: 0295-5075. DOI: 10.1209/epl/i2001-00406-6.

[125] Alexis Boileau et al. “Tuning of the Optical Properties of the Transparent Conducting Oxide SrVO3 by Electronic Correlations”. In: *Advanced Optical Materials* 7.7 (2019), p. 1801516. DOI: 10.1002/adom.201801516.

[126] Koustav Ganguly et al. “Mobility-electron density relation probed via controlled oxygen vacancy doping in epitaxial BaSnO3”. In: *APL Materials* 5.5 (2017), p. 056102. ISSN: 2166532X. DOI: 10.1063/1.4983039.

[127] Masaki Kobayashi et al. “Origin of the Anomalous Mass Renormalization in Metallic Quantum Well States of Strongly Correlated Oxide SrVO3”. In: *Physical Review Letters* 115.7 (2015), p. 076801. ISSN: 10797114. DOI: 10.1103/PhysRevLett.115.076801.

[128] B. L. Chamberland and P. S. Danielson. “Alkaline-earth vanadium (IV) oxides having the AVO3 composition”. In: *Journal of Solid State Chemistry* 3.2 (1971), pp. 243–247. ISSN: 1095726X. DOI: 10.1016/0022-4596(71)90035-1.

[129] Jonathan R. Petrie et al. “Strain Control of Oxygen Vacancies in Epitaxial Strontium Cobaltite Films”. In: *Advanced Functional Materials* 26.10 (2016), pp. 1564–1570. ISSN: 16163028. DOI: 10.1002/adfm.201504868.

[130] Susanne Stemmer et al. “Oxygen vacancy ordering in epitaxial La0.5Sr0.5CoO3-δ thin films on (001) LaAlO3”. In: *Journal of Applied Physics* 90.7 (2001), pp. 3319–3324. ISSN: 00218979. DOI: 10.1063/1.1401793.

[131] Jaume Gazquez et al. “Atomic-resolution imaging of spin-state superlattices in nanopockets within cobaltite thin films”. In: *Nano Letters* 11.3 (2011), pp. 973–976. ISSN: 15306984. DOI: 10.1021/nl1034896.

[132] J. Gazquez et al. “Lattice mismatch accommodation via oxygen vacancy ordering in epitaxial La0.5Sr0.5CoO3-δ thin films”. In: *APL Materials* 1.1 (2013), p. 012105. ISSN: 2166532X. DOI: 10.1063/1.4809547.

[133] L. López-Conesa et al. “Evidence of a minority monoclinic LaNiO2.5 phase in lanthanum nickelate thin films”. In: *Physical Chemistry Chemical Physics* 19.13 (2017), pp. 9137–9142. ISSN: 14639076. DOI: 10.1039/c7cp00902j.

[134] X. W. Lin et al. “Valence states and hybridization in vanadium oxide systems investigated by transmission electron-energy-loss spectroscopy”. In: *Physical Review B* 47.7 (1993), pp. 3477–3481. ISSN: 01631829. DOI: 10.1103/PhysRevB.47.3477.

[135] M. Wu, J. C. Zheng, and H. Q. Wang. “Investigation of the vanadium L23-edge x-ray absorption spectrum of SrVO3 using configuration interaction calculations: Multiplet, valence, and crystal-field effects”. In: *Physical Review B* 97.245138 (2018), p. 245138. ISSN: 24699969. DOI: 10.1103/PhysRevB.97.245138.

[136] Gabriele Sclauzero, Krzysztof Dymkowski, and Claude Ederer. “Tuning the metal-insulator transition in d1 and d2 perovskites by epitaxial strain: A first-principles-based study”. In: *Physical Review B* 94.24 (2016), p. 245109. ISSN: 24699969. DOI: 10.1103/PhysRevB.94.245109.

[137] H. Koinuma et al. “Fabrication and anomalous conducting behavior of atomically regulated (SrVO3-x)/(SrTiO3-y) superlattices”. In: *Solid State Communications* 80.1 (1991), pp. 9–13. ISSN: 00381098. DOI: 10.1016/0038-1098(91)90588-M.

[138] Hirotoshi Nagata et al. “Laser molecular beam epitaxy of single-crystal SrVO3-x films”. In: *Thin Solid Films* 208.2 (1992), pp. 264–268. ISSN: 00406090. DOI: 10.1016/0040-6090(92)90654-T.

[139] Man Gu, Stuart A Wolf, and Jiwei Lu. “Metal-insulator transition in SrTi1-xVxO3 thin films”. In: *Applied Physics Letters* 103 (2013), p. 223110.

[140] Man Gu, Stuart A. Wolf, and Jiwei Lu. "Two-Dimensional Mott Insulators in SrVO3 Ultrathin Films". In: *Advanced Materials Interfaces* 1.7 (2014), p. 1300126. ISSN: 21967350. DOI: 10.1002/admi.201300126.

[141] David B. Geohegan. "Fast intensified-CCD photography of YBa2Cu3O7-x laser ablation in vacuum and ambient oxygen". In: *Applied Physics Letters* 60.22 (1992), pp. 2732–2734. ISSN: 00036951. DOI: 10.1063/1.106859.

[142] Alejandro Ojeda-G-P, Max Döbeli, and Thomas Lippert. "Influence of Plume Properties on Thin Film Composition in Pulsed Laser Deposition". In: *Advanced Materials Interfaces* 5.18 (2018), p. 1701062. ISSN: 21967350. DOI: 10.1002/admi.201701062.

[143] J. Gonzalo et al. "Imaging self-sputtering and backscattering from the substrate during pulsed laser deposition of gold". In: *Physical Review B* 76.3 (2007), p. 035435. ISSN: 10980121. DOI: 10.1103/PhysRevB.76.035435.

[144] K. Yoshimatsu et al. "Metallic Quantum Well States in Artificial Structures of Strongly Correlated Oxide". In: *Science.* 333 (2011), pp. 319–323.

[145] S. Backes et al. "Hubbard band versus oxygen vacancy states in the correlated electron metal SrVO3". In: *Physical Review B* 94.24 (2016), 241110(R). ISSN: 24699969. DOI: 10.1103/PhysRevB.94.241110.

[146] Patrick Dougier, John C C Fan, and John B Goodenough. "Etude des proprietes magnetiques, electriques et optiques des phases de structure perovskite SrVO2.90 et SrVO3". In: *Journal of Solid State Chemistry* 14.3 (1975), pp. 247–259. ISSN: 1095726X. DOI: 10.1016/0022-4596(75)90029-8.

[147] Robert W. Cheary, Alan A. Coelho, and James P. Cline. "Fundamental Parameters Line Profile Fitting in Laboratory Diffractometers". In: *Journal of Research of the National Institute of Standards and Technology* 109.1 (2004), pp. 1–25. ISSN: 1044677X. DOI: 10.6028/jres.109.002.

[148] Marcus H. Mendenhall et al. "High-precision measurement of the x-ray Cu Kα spectrum". In: *Journal of Physics B: Atomic, Molecular and Optical Physics* 50.11 (2017), p. 115004. ISSN: 13616455. DOI: 10.1088/1361-6455/aa6c4a.

[149] Chungwei Lin et al. "Final-state effect on x-ray photoelectron spectrum of nominally d1 and n-doped d0 transition-metal oxides". In: *Physical Review B* 92.3 (2015), p. 035110. ISSN: 1550235X. DOI: 10.1103/PhysRevB.92.035110.

[150] H. M. Ng et al. "The role of dislocation scattering in n-type GaN films". In: *Applied Physics Letters* 73.6 (1998), pp. 821–823. ISSN: 00036951. DOI: 10.1063/1.122012.

[151] Hyosik Mun et al. “Large effects of dislocations on high mobility of epitaxial perovskite Ba0.96La0.04SnO3 films”. In: *Applied Physics Letters* 102.25 (2013), p. 252105. ISSN: 00036951. DOI: 10.1063/1.4812642.

[152] John B. Goodenough. “The two components of the crystallographic transition in VO2”. In: *Journal of Solid State Chemistry* 3.4 (1971), pp. 490–500. ISSN: 1095726X. DOI: 10.1016/0022-4596(71)90091-0.

[153] D. B. McWhan et al. “Metal-Insulator Transitions in Pure and Doped V2O3”. In: *Physical Review B* 7.5 (1973), p. 1920. ISSN: 01631829. DOI: 10.1103/PhysRevB.7.1920.

[154] J. Park et al. “Spin and orbital occupation and phase transitions in V2O3”. In: *Physical Review B* 61.17 (2000), p. 11506. ISSN: 1550235X. DOI: 10.1103/PhysRevB.61.11506.

[155] M. W. Haverkort et al. “Orbital-Assisted Metal-Insulator Transition in VO2”. In: *Physical Review Letters* 95.19 (2005), p. 196404. ISSN: 00319007. DOI: 10.1103/PhysRevLett.95.196404.

[156] C. F. Hague et al. “Charge transfer at the metal-insulator transition in V2O3 thin films by resonant inelastic x-ray scattering”. In: *Physical Review B* 77.4 (2008), p. 045132. ISSN: 10980121. DOI: 10.1103/PhysRevB.77.045132.

[157] M. Abbate et al. “Soft-x-ray-absorption studies of the electronic-structure changes through the VO2 phase transition”. In: *Physical Review B* 43.9 (1991), p. 7263. ISSN: 0163-1829. DOI: 10.1103/PhysRevB.43.7263.

[158] Nagaphani B. Aetukuri et al. “Control of the metal-insulator transition in vanadium dioxide by modifying orbital occupancy”. In: *Nature Physics* 9.10 (2013), pp. 661–666. ISSN: 17452481. DOI: 10.1038/nphys2733.

[159] I. A. Nekrasov et al. “Comparative study of correlation effects in CaVO3 and SrVO3”. In: *Physical Review B* 72.15 (2005), p. 155106. ISSN: 1550235X. DOI: 10.1103/PhysRevB.72.155106.

[160] Zhicheng Zhong et al. “Electronics with Correlated Oxides: SrVO3/SrTiO3 as a Mott Transistor”. In: *Physical Review Letters* 114.24 (2015), p. 246401. ISSN: 10797114. DOI: 10.1103/PhysRevLett.114.246401.

[161] Man Gu et al. “Metal-insulator transition induced in CaVO3 thin films”. In: *Journal of Applied Physics* 113.13 (2013), p. 133704. ISSN: 00218979. DOI: 10.1063/1.4798963.

[162] Daniel E. McNally et al. “Electronic localization in CaVO3 films via bandwidth control”. In: *npj Quantum Materials* 4.6 (2019), p. 6. ISSN: 23974648. DOI: 10.1038/s41535-019-0146-3.

[163] I. H. Inoue et al. “Systematic Development of the Spectral Function in the 3d1 Mott-Hubbard System Ca1-xSrxVO3”. In: *Physical Review Letters* 74.13 (1995), p. 2539. DOI: 10.1039/C2DT30639E.

[164] F. M. F. de Groot et al. “Oxygen 1s x-ray-absorption edges of transition-metal oxides”. In: *Physical Review B* 40.8 (1989), pp. 5715–5723. DOI: 10.1103/PhysRevB.40.5715.

[165] R. Zimmermann et al. “Strong hybridization in vanadium oxides: evidence from photoemission and absorption spectroscopy”. In: *Journal of Physics: Condensed Matter* 10.25 (1998), pp. 5697–5716. ISSN: 09538984. DOI: 10.1088/0953-8984/10/25/018.

[166] R. J. O. Mossanek et al. “Minimal model needed for the Mott-Hubbard SrVO3 compound”. In: *Physical Review B* 79.3 (2009), p. 033104. ISSN: 10980121. DOI: 10.1103/PhysRevB.79.033104.

[167] F. Iga et al. “Determination of the Orbital Polarization in YTiO3 by Using Soft X-ray Linear Dichroism”. In: *Physical Review Letters* 93.25 (2004), p. 257207. ISSN: 00319007. DOI: 10.1103/PhysRevLett.93.257207.

[168] C. Aruta et al. “Orbital occupation, atomic moments, and magnetic ordering at interfaces of manganite thin films”. In: *Physical Review B* 80.1 (2009), p. 014431. ISSN: 10980121. DOI: 10.1103/PhysRevB.80.014431.

[169] Er Jia Guo et al. “Switchable orbital polarization and magnetization in strained LaCoO3 films”. In: *Physical Review Materials* 3.1 (2019), p. 014407. ISSN: 24759953. DOI: 10.1103/PhysRevMaterials.3.014407.

[170] J. Chakhalian et al. “Asymmetric Orbital-Lattice Interactions in Ultrathin Correlated Oxide Films”. In: *Physical Review Letters* 107.11 (2011), p. 116805. DOI: 10.1103/PhysRevLett.107.116805.

[171] S. Middey et al. “Epitaxial strain modulated electronic properties of interface controlled nickelate superlattices”. In: *Physical Review B* 98.4 (2018), p. 045115. ISSN: 24699969. DOI: 10.1103/PhysRevB.98.045115.

[172] J Chakhalian et al. “Orbital Reconstruction and Covalent Bonding at an Oxide Interface”. In: *Science.* 318 (2007), pp. 1114–1118. DOI: 10.1126/science.1149338.

[173] R. Werner et al. “YBa2Cu3O7/La0.7Ca0.3MnO3 bilayers: Interface coupling and electric transport properties”. In: *Physical Review B* 82.22 (2010), p. 224509. ISSN: 10980121. DOI: 10.1103/PhysRevB.82.224509.

[174] A. Galdi et al. “Electronic band redistribution probed by oxygen absorption spectra of (SrMnO3)n(LaMnO3)2n superlattices”. In: *Physical Review B* 85.12 (2012), p. 125129. ISSN: 10980121. DOI: 10.1103/PhysRevB.85.125129.

[175] T. C. Koethe et al. “Transfer of Spectral Weight and Symmetry across the Metal-Insulator Transition in VO2”. In: *Physical Review Letters* 97.11 (2006), p. 116402. ISSN: 00319007. DOI: 10.1103/PhysRevLett.97.116402.

[176] Ulrich Aschauer et al. “Strain-controlled oxygen vacancy formation and ordering in CaMnO3”. In: *Physical Review B* 88.5 (2013), p. 054111. ISSN: 10980121. DOI: 10.1103/PhysRevB.88.054111.

[177] M. Abbate et al. “Soft X-ray absorption spectroscopy of vanadium oxides”. In: *Journal of Electron Spectroscopy and Related Phenomena* 62.1-2 (1993), pp. 185–195. ISSN: 03682048. DOI: 10.1016/0368-2048(93)80014-D.

[178] Dimitrios Maganas et al. “L-edge X-ray absorption study of mononuclear vanadium complexes and spectral predictions using a restricted open shell configuration interaction ansatz”. In: *Physical Chemistry Chemical Physics* 16.1 (2014), pp. 264–276. ISSN: 14639076. DOI: 10.1039/c3cp52711e.

[179] Qiyang Lu et al. “Electrochemically Triggered Metal–Insulator Transition between VO2 and V2O5”. In: *Advanced Functional Materials* 28.34 (2018), p. 1803024. ISSN: 16163028. DOI: 10.1002/adfm.201803024.

[180] M. Liberati et al. “Epitaxial growth and characterization of CaVO3 thin films”. In: *Journal of Magnetism and Magnetic Materials* 321.18 (2009), pp. 2852–2854. ISSN: 03048853. DOI: 10.1016/j.jmmm.2009.04.037.

[181] C. Hébert et al. “Oxygen K-edge in vanadium oxides: simulations and experiments”. In: *European Physical Journal B* 28.4 (2002), pp. 407–414. ISSN: 14346028. DOI: 10.1140/epjb/e2002-00244-4.

[182] A. Gloskovskii et al. “Spectroscopic and microscopic study of vanadium oxide nanotubes”. In: *Journal of Applied Physics* 101.8 (2007), p. 084301. ISSN: 00218979. DOI: 10.1063/1.2716157.

[183] C. C. Ahn and O. L. Krivanek. *EELS Atlas: A Reference Guide of Electron Energy Loss Spectra Covering All Stable Elements*. Ed. by Gatan. Arizona State University, Warrendale Pa.: Ed. Gatan, 1983.

[184] D. S. Su et al. “High resolution EELS using monochromator and high performance spectrometer: Comparison of V2O5 ELNES with NEXAFS and band structure calculations”. In: *Micron* 34.3-5 (2003), pp. 235–238. ISSN: 09684328. DOI: 10.1016/S0968-4328(03)00033-7.

[185] M. G. Brik et al. “Fully relativistic calculations of the L2,3-edge XANES spectra for vanadium oxides”. In: *European Physical Journal B* 51.3 (2006), pp. 345–355. ISSN: 14346028. DOI: 10.1140/epjb/e2006-00243-5.

[186] J. G. Chen. "NEXAFS investigations of transition metal oxides, nitrides, carbides, sulfides and other interstitial compounds". In: *Surface Science Reports* 30.1-3 (1997), pp. 1–152. ISSN: 01675729. DOI: 10.1016/S0167-5729(97)00011-3.

[187] Masatoshi Imada, Atsushi Fujimori, and Yoshinori Tokura. "Metal-insulator transitions". In: *Reviews of Modern Physics* 70.4 (1998), pp. 1039–1263. DOI: 10.1103/RevModPhys.70.1039.

[188] J Hubbard and Proc R Soc Lond A. "Electron Correlations in Narrow Energy Bands". In: *Proceedings of the Royal Society of London. Series A. Mathematical and Physical Sciences* 276.1365 (1963), pp. 238–257. ISSN: 0080-4630. DOI: 10.1098/rspa.1963.0204.

[189] Junjiro Kanamori. "Electron Correlation and Ferromagnetism of Transition Metals". In: *Progress of Theoretical Physics* 30.3 (1963), pp. 275–289. ISSN: 0033-068X. DOI: 10.1143/ptp.30.275.

[190] Martin C. Gutzwiller. "Effect of Correlation on the Ferromagnetism of Transition Metals". In: *Physical Review Letters* 10.5 (1963), p. 159. DOI: 10.1103/PhysRev.134.A923.

[191] F. Rivadulla et al. "Suppression of ferromagnetic double exchange by vibronic phase segregation". In: *Physical Review Letters* 96.1 (2006), p. 016402. DOI: 10.1103/PhysRevLett.96.016402.

[192] Matthew Brahlek et al. "Opportunities in vanadium-based strongly correlated electron systems". In: *MRS Communications* 7.1 (2017), pp. 27–52. ISSN: 21596867. DOI: 10.1557/mrc.2017.2.

[193] Susanne Stemmer and S. James Allen. "Non-Fermi liquids in oxide heterostructures". In: *Reports on Progress in Physics* 81 (2018), p. 062502. ISSN: 00344885. DOI: 10.1088/1361-6633/aabdfa.

[194] Jialu Wang et al. "T-square resistivity without Umklapp scattering in dilute metallic Bi2O2Se". In: *Nature Communications* 11.1 (2020), p. 3846. ISSN: 20411723. DOI: 10.1038/s41467-020-17692-6.

[195] Xiao Lin, B. Fauqué, and Kamran Behnia. "Scalable T2 resistivity in a small single-component Fermi surface". In: *Science* 349.6251 (2015), pp. 945–948. DOI: 10.1126/science.aaa8655.

[196] Carl A Kukkonen. "T2 electrical resistivity due to electron-phonon scattering on a small cylindrical Fermi surface: Application to bismuth". In: *Physical Review B* 18.4 (1978), pp. 1849–1853. DOI: 10.1103/PhysRevB.18.1849.

[197] N. W. Ashcroft and N. D. Mermin. *Solid State Physics*. Harcourt College Publishers, 1976. ISBN: 0030839939.

[198] Nevill Francis Mott. *Metal-Insulator Transitions*. 2nd. Taylor & Francis, 1990. ISBN: 0-85066-783-6. DOI: https://doi.org/10.1201/b12795.

[199] N. F. Mott. "Metal-Insulator Transition". In: *Reviews of Modern Physics* 40.4 (1968), p. 677. ISSN: 13653075. DOI: 10.1103/RevModPhys.40.677.

[200] D. E. Shai et al. "Quasiparticle Mass Enhancement and Temperature Dependence of the Electronic Structure of Ferromagnetic SrRuO3 Thin Films". In: *Physical Review Letters* 110.8 (2013), p. 087004. ISSN: 00319007. DOI: 10.1103/PhysRevLett.110.087004.

[201] M. Brühwiler et al. "Mass enhancement, correlations, and strong-coupling superconductivity in the β-pyrochlore KOs2O6". In: *Physical Review B* 73.9 (2006), p. 094518. ISSN: 10980121. DOI: 10.1103/PhysRevB.73.094518.

[202] Lishai Shoham et al. "Scalable Synthesis of the Transparent Conductive Oxide SrVO3". In: *Advanced Electronic Materials* 6.1 (2020), p. 1900584. ISSN: 2199160X. DOI: 10.1002/aelm.201900584.

[203] Pouya Moetakef and Tyler A. Cain. "Metal-insulator transitions in epitaxial Gd1-xSrxTiO3 thin films grown using hybrid molecular beam epitaxy". In: *Thin Solid Films* 583.1 (2015), pp. 129–134. ISSN: 00406090. DOI: 10.1016/j.tsf.2015.03.065.

[204] D. Van Der Marel, J. L.M. Van Mechelen, and I. I. Mazin. "Common Fermi-liquid origin of T2 resistivity and superconductivity in n-type SrTiO3". In: *Physical Review B* 84.20 (2011), p. 205111. ISSN: 10980121. DOI: 10.1103/PhysRevB.84.205111.

[205] Tyler A. Cain, Adam P. Kajdos, and Susanne Stemmer. "La-doped SrTiO3 films with large cryogenic thermoelectric power factors". In: *Applied Physics Letters* 102.18 (2013), p. 182101. ISSN: 00036951. DOI: 10.1063/1.4804182.

[206] Evgeny Mikheev et al. "Carrier density independent scattering rate in SrTiO3-based electron liquids". In: *Scientific Reports* 6 (2016), p. 20865. DOI: 10.1038/srep20865.

[207] F. Rivadulla, J. S. Zhou, and J. B. Goodenough. "Electron scattering near an itinerant to localized electronic transition". In: *Physical Review B* 67.16 (2003), p. 165110. DOI: 10.1103/PhysRevB.67.165110.

[208] J. S. Zhou and J. B. Goodenough. "Phonon-Assisted Double Exchange in Perovskite Manganites". In: *Physical Review Letters* 80.12 (1998), pp. 2665–2668. ISSN: 10797114. DOI: 10.1103/PhysRevLett.80.2665.

[209] Guo Meng Zhao et al. "Electrical Transport in the Ferromagnetic State of Manganites: Small-Polaron Metallic Conduction at Low Temperatures". In: *Physical Review Letters* 84.26 (2000), pp. 6086–6089. ISSN: 10797114. DOI: 10.1103/PhysRevLett.84.6086.

[210] P. Graziosi et al. “Polaron framework to account for transport properties in metallic epitaxial manganite films”. In: *Physical Review B* 89.21 (2014), p. 214411. ISSN: 1550235X. DOI: 10.1103/PhysRevB.89.214411.

[211] S. Gariglio et al. “Transport properties in doped Mott insulator epitaxial La1-yTiO3+δ thin films”. In: *Physical Review B* 63.16 (2001), 161103(R). ISSN: 1550235X. DOI: 10.1103/PhysRevB.63.161103.

[212] J. Li et al. “Growth and small-polaron conduction of hole-doped LaTiO3+δ/2 and NdTiO3+δ/2 thin films”. In: *Physical Review B* 75.19 (2007), p. 195109. ISSN: 10980121. DOI: 10.1103/PhysRevB.75.195109.

[213] V. N. Bogomolov, E. K. Kudinov, and Yu A. Firsov. “Polaron nature of the current carriers in Rutile (TiO2)”. In: *Soviet Physics - Solid State* 9.11 (1968), pp. 2502–2513.

[214] Zhicheng Zhong, Qinfang Zhang, and Karsten Held. “Quantum confinement in perovskite oxide heterostructures: Tight binding instead of a nearly free electron picture”. In: *Physical Review B* 88.12 (2013), p. 125401. ISSN: 10980121. DOI: 10.1103/PhysRevB.88.125401.

[215] Nicholas P. Breznay et al. “Weak antilocalization and disorder-enhanced electron interactions in annealed films of the phase-change compound GeSb2Te4”. In: *Physical Review B* 86.20 (2012), p. 205302. ISSN: 10980121. DOI: 10.1103/PhysRevB.86.205302.

[216] J M Ziman. *Electrons and Phonons : The Theory of Transport Phenomena in Solids*. Ed. by Clarendon. Oxford University Press, 1960. ISBN: 9780198507796. DOI: 10.1093/acprof.

[217] Na Hyun Jo et al. “Extremely large magnetoresistance and Kohler’s rule in PdSn4: A complete study of thermodynamic, transport, and band-structure properties”. In: *Physical Review B* 96.16 (2017), p. 165145. ISSN: 24699969. DOI: 10.1103/PhysRevB.96.165145.

[218] S. Aizaki et al. “Self-energy on the low- to high-energy electronic structure of correlated metal SrVO 3”. In: *Physical Review Letters* 109.5 (2012), p. 056401. ISSN: 00319007. DOI: 10.1103/PhysRevLett.109.056401.

[219] W. F. Brinkman and T. M. Rice. “Application of Gutzwiller’s Variational Method to the Metal-Insulator Transition”. In: *Physical Review B* 2.10 (1970), pp. 4302–4304. DOI: 10.1103/PhysRevB.2.4302.

[220] I. A. Nekrasov et al. “Momentum-resolved spectral functions of SrVO3 calculated by LDA+DMFT”. In: *Physical Review B* 73.15 (2006), p. 155112. ISSN: 10980121. DOI: 10.1103/PhysRevB.73.155112.

[221] Hunpyo Lee et al. “Dynamical cluster approximation within an augmented plane wave framework: Spectral properties of SrVO3”. In: *Physical Review B* 85.16 (2012), p. 165103. ISSN: 10980121. DOI: 10.1103/PhysRevB.85.165103.

[222] Jan M. Tomczak et al. “Asymmetry in band widening and quasiparticle lifetimes in SrVO3: Competition between screened exchange and local correlations from combined GW and dynamical mean-field theory GW + DMFT”. In: *Physical Review B* 90.16 (2014), p. 165138. ISSN: 1550235X. DOI: 10.1103/PhysRevB.90.165138.

[223] Changan Wang et al. “Tuning the metal-insulator transition in epitaxial SrVO3 films by uniaxial strain”. In: *physical review materials* 3.11 (2019), p. 115001. DOI: 10.1103/PhysRevMaterials.3.115001.

[224] M. J. Rice. “Electron-electron scattering in transition metals”. In: *Physical Review Letters* 20.25 (1968), pp. 1439–1441. ISSN: 00319007. DOI: 10.1103/PhysRevLett.20.1439.

[225] W. E. Lawrence and John W. Wilkins. “Electron-Electron Scattering in the Transport Coefficients of Simple Metals”. In: *Physical Review B* 7.6 (1973), pp. 2317–2332. ISSN: 01631829. DOI: 10.1103/PhysRevB.19.6075.

[226] A. H. Thompson. “Electron-Electron Scattering in TiS2”. In: *Physical Review Letters* 35.26 (1975), pp. 1786–1789. ISSN: 00319007. DOI: 10.1103/PhysRevLett.35.1786.

[227] Stephen Dongmin Kang, Maxwell Dylla, and G. Jeffrey Snyder. “Thermopower-conductivity relation for distinguishing transport mechanisms: Polaron hopping in CeO2 and band conduction in SrTiO3”. In: *Physical Review B* 97.23 (2018), p. 235201. ISSN: 24699969. DOI: 10.1103/PhysRevB.97.235201.

[228] Maxwell Thomas Dylla, Stephen Dongmin Kang, and G. Jeffrey Snyder. “Effect of Two-Dimensional Crystal Orbitals on Fermi Surfaces and Electron Transport in Three-Dimensional Perovskite Oxides”. In: *Angewandte Chemie* 131.17 (2019), pp. 5557–5566. ISSN: 0044-8249. DOI: 10.1002/ange.201812230.

[229] T. Yoshida et al. “Correlated electronic states of SrVO3 revealed by angle-resolved photoemission spectroscopy”. In: *Journal of Electron Spectroscopy and Related Phenomena* 208 (2016), pp. 11–16. ISSN: 03682048. DOI: 10.1016/j.elspec.2015.11.012.

[230] T. Yoshida et al. “Direct Observation of the Mass Renormalization in SrVO3 by Angle Resolved Photoemission Spectroscopy”. In: *Physical Review Letters* 95.14 (2005), p. 146404. ISSN: 00319007. DOI: 10.1103/PhysRevLett.95.146404.

[231] Cheng Chen et al. “Electronic structures and unusually robust bandgap in an ultrahigh-mobility layered oxide semiconductor, Bi2O2Se”. In: *Science Advances* 4.9 (2018), eaat8355. ISSN: 23752548. DOI: 10.1126/sciadv.aat8355.

[232] N. Sato et al. “Effect of quasi-two-dimensional fermi surfaces on electronic properties in YbSb2”. In: *Physical Review B* 59.7 (1999), pp. 4714–4719. ISSN: 1550235X. DOI: 10.1103/PhysRevB.59.4714.

[233] Takuji Maekawa, Ken Kurosaki, and Shinsuke Yamanaka. “Physical properties of polycrystalline SrVO3-δ”. In: *Journal of Alloys and Compounds* 426.1-2 (2006), pp. 46–50. ISSN: 09258388. DOI: 10.1016/j.jallcom.2006.02.026.

[234] David Emin. *Polarons*. Cambridge University Press, 2013. ISBN: 9780521519069. DOI: 10.1017/cbo9781139023436.002.

[235] Michele Reticcioli et al. *Small Polarons in Transition Metal Oxides. In: Andreoni W., Yip S. (eds) Handbook of Materials Modeling*. Springer, Cham, 2020. ISBN: 9783319502571. DOI: 10.1007/978-3-319-50257-1.

[236] J. T. Devreese et al. “Many-body large polaron optical conductivity in SrTi1-xNbxO3”. In: *Physical Review B* 81.12 (2010), p. 125119. ISSN: 10980121. DOI: 10.1103/PhysRevB.81.125119.

[237] M. A. Husanu et al. “Electron-polaron dichotomy of charge carriers in perovskite oxides”. In: *Communications Physics* 3 (2020), p. 62. ISSN: 23993650. DOI: 10.1038/s42005-020-0330-6.

[238] Guo-meng Zhao, H. Keller, and W. Prellier. “Unusual electrical ransport mechanism in the ferromagnetic state of the magnetoresistive manganites”. In: *Journal of Physics: Condensed Matter* 12 (2000), p. L361. DOI: 10.1088/0953-8984/21/18/185502.

[239] E. S. Hellman and E. H. Jr. Hartford. “Normal-state resistivity and Hall effect in Ba1-xKxBiO3 epitaxial films”. In: *Physical Review B* 47.17 (1993), p. 11346. DOI: 10.1103/PhysRevB.47.11346.

[240] Hidetoshi Minami and Hiromoto Uwe. “Electrical Conductivity of the Oxide Superconductor Ba0.58K0.42BiO2.96”. In: *Journal of the Physical Society of Japan* 66.6 (1997), pp. 1771–1775. ISSN: 00319015. DOI: 10.1143/JPSJ.66.1771.

[241] A. Lanzara et al. “Evidence for ubiquitous strong electron-phonon coupling in high-temperature superconductors”. In: *Nature* 412 (2001), pp. 510–514. DOI: 10.1038/35087518.

[242] R. Nourafkan, F. Marsiglio, and G. Kotliar. "Model of the Electron-Phonon Interaction and Optical Conductivity of Ba1-xKxBiO3 Superconductors". In: *Physical Review Letters* 109.1 (2012), p. 017001. ISSN: 00319007. DOI: 10.1103/PhysRevLett.109.017001.

[243] R. Jaramillo et al. "Origins of bad-metal conductivity and the insulator-metal transition in the rare-earth nickelates". In: *Nature Physics* 10.4 (2014), pp. 304–307. ISSN: 17452481. DOI: 10.1038/nphys2907.

[244] James M. Rondinelli et al. "Electronic properties of bulk and thin film SrRuO3: Search for the metal-insulator transition". In: *Physical Review B* 78.15 (2008), p. 155107. ISSN: 10980121. DOI: 10.1103/PhysRevB.78.155107.

[245] E. Jakobi et al. "LDA+DMFT study of Ru-based perovskite SrRuO3 and CaRuO3". In: *Physical Review B* 83.4 (2011), 041103(R). ISSN: 10980121. DOI: 10.1103/PhysRevB.83.041103.

[246] C. Etz et al. "Indications of weak electronic correlations in SrRuO3 from first-principles calculations". In: *Physical Review B* 86.6 (2012), p. 064441. ISSN: 10980121. DOI: 10.1103/PhysRevB.86.064441.

[247] Xiaoxiang Xu et al. "A red metallic oxide photocatalyst". In: *Nature Materials* 11.7 (2012), pp. 595–598. ISSN: 14764660. DOI: 10.1038/nmat3312.

[248] Paraskevi Efstathiou et al. "An investigation of crystal structure, surface area and surface chemistry of strontium niobate and their influence on photocatalytic performance". In: *Dalton Transactions* 42.22 (2013), pp. 7880–7887. ISSN: 14779226. DOI: 10.1039/c3dt32064b.

[249] Yong Qiang Xu et al. "First-principles investigation on the structural, elastic and electronic properties and mechanism on the photocatalytic properties for SrNbO3 and Sr0.97NbO3". In: *Journal of Physics and Chemistry of Solids* 111.August (2017), pp. 403–409. ISSN: 00223697. DOI: 10.1016/j.jpcs.2017.08.030.

[250] Masanori Kaneko, Kenji Mishima, and Koichi Yamashita. "First-principles study on visible light absorption of defected SrNbO3". In: *Journal of Photochemistry & Photobiology, A: Chemistry* 375.February (2019), pp. 175–180. ISSN: 1010-6030. DOI: 10.1016/j.jphotochem.2019.02.018.

[251] Xuming Zhang et al. "Plasmonic photocatalysis". In: *Reports on Progress in Physics* 76.4 (2013), 046401 (41pp). ISSN: 00344885. DOI: 10.1088/0034-4885/76/4/046401.

[252] Teguh Citra Asmara et al. "Tunable and low-loss correlated plasmons in Mott-like insulating oxides". In: *Nature Communications* 8.May (2017), p. 15271. DOI: 10.1038/ncomms15271.

[253] Satoshi Itoh. "Electronic structure of SrVO3". In: *Solid State Communications* 88.7 (1993), pp. 525–527. DOI: 10.1016/0038-1098(93)90042-L.

[254] Andreas Herklotz et al. "Strain coupling of oxygen non-stoichiometry in perovskite thin films". In: *Journal of Physics Condensed Matter* 29.49 (2017), p. 493001. ISSN: 1361648X. DOI: 10.1088/1361-648X/aa949b.

[255] Arpita Paul and Turan Birol. "Strain tuning of plasma frequency in vanadate, niobate, and molybdate perovskite oxides". In: *Physical Review Materials* 3.8 (2019), p. 085001. ISSN: 24759953. DOI: 10.1103/PhysRevMaterials.3.085001.

[256] Stefan A Maier. *Plasmonics: Fundamentals and Applications*. NY, USA: Springer, 2007. ISBN: 9780387331508.

[257] Yuqiao Zhang and Hiromichi Ohta. "Electron Sandwich Doubles the Thermoelectric Power Factor of SrTiO3". In: *Physica Status Solidi A* 216.9 (2019), p. 1800832. ISSN: 18626319. DOI: 10.1002/pssa.201800832.

[258] Chiara Bigi et al. "Direct insight into the band structure of SrNbO3". In: *Physical Review Materials* 4.2 (2020), p. 025006. ISSN: 24759953. DOI: 10.1103/PhysRevMaterials.4.025006.

[259] C. Sönnichsen et al. "Drastic Reduction of Plasmon Damping in Gold Nanorods". In: *Physical Review Letters* 88.7 (2002), p. 077402. ISSN: 00319007. DOI: 10.1103/PhysRevLett.88.077402.

[260] Jessica L. Stoner et al. "Chemical Control of Correlated Metals as Transparent Conductors". In: *Advanced Functional Materials* 29.11 (2019), p. 1808609. ISSN: 16163028. DOI: 10.1002/adfm.201808609.

[261] F. Abelès. "Optical Properties of Metallic Films". In: *Physics of Thin Films: Advances in Research and Development, Vol. 6*. Ed. by G. Hass and Rudolf Thun. Vol. 6. New York and London: Academic Press, 1971, pp. 151–204. ISBN: 9780125330060. DOI: 10.1016/B978-0-12-533006-0.50010-4..

[262] Heinz Raether. *Excitation of Plasmons and Interband Transitions by Electrons*. Ed. by G. Köhler. Vol. 223. Springer-Verlag Berlin Heidelberg New York, 1980, p. 23. ISBN: 978-3-540-34716-3. DOI: 10.1007/BFb0045951.

[263] Richard A Ferrell. "Predicted Radiation of Plasma Oscillations in Metal Films". In: *Physical Review* 111.5 (1958), pp. 1214–1222. DOI: 10.1103/PhysRev.111.1214.

[264] A. J. McAlister and E. A. Stern. "Plasma Resonance Absorption in Thin Metal Films". In: *Physical Review* 132.4 (1963), p. 1599. DOI: 10.1103/PhysRev.132.1599.

[265] P. O. Nilsson, I. Lindau, and S. B.M. Hagström. "Optical Plasma-Resonance Absorption in Thin Films of Silver and Some Silver Alloys". In: *Physical Review B* 1.2 (1970), pp. 498–505. ISSN: 01631829. DOI: 10.1103/PhysRevB.1.498.

[266] I. Lindau and P. O. Nilsson. "Experimental Verification Of Optically Excited Longitudinal Plasmons". In: *Physica Scripta* 3.2 (1971), pp. 87–92. ISSN: 14024896. DOI: 10.1088/0031-8949/3/2/007.

[267] W. Steinmann. "Optical Plasma Resonances in Solids". In: *Physica Status Solidi (B)* 28.2 (1968), pp. 437–462. ISSN: 15213951. DOI: 10.1002/pssb.19680280202.

[268] B. Feuerbacher, R. P. Godwin, and M. Skibowski. "Plasma resonance in the reflection spectrum of thin aluminium films". In: *Physics Letters A* 26.12 (1968), pp. 595–596. DOI: 10.1016/0375-9601(68)90140-0.

[269] Richard A. Ferrell and Edward A. Stern. "Plasma Resonance in the Electrodynamics of Metal Films". In: *American Journal of Physics* 30.11 (1962), pp. 810–812. ISSN: 0002-9505. DOI: 10.1119/1.1941812.

[270] Aldin Radetinac et al. "Optical properties of single crystalline SrMoO3 thin films". In: *Journal of Applied Physics* 119.5 (2016), p. 055302. ISSN: 10897550. DOI: 10.1063/1.4940969.

[271] Hiroyuki Yamada et al. "Engineered Interface of Magnetic Oxides". In: *Science* 305.5684 (2004), pp. 646–648. DOI: 10.1126/science.1098867.

[272] Pilar Lopez-Varo et al. "Physical aspects of ferroelectric semiconductors for photovoltaic solar energy conversion". In: *Physics Reports* 653 (2016), pp. 1–40. DOI: 10.1016/j.physrep.2016.07.006.

[273] R. Nechache et al. "Bandgap tuning of multiferroic oxide solar cells". In: *Nature Photonics* 9 (2015), pp. 61–67. DOI: 10.1038/nphoton.2014.255.

[274] T. Arima and Y. Tokura. "Optical Study of Electronic Structure in Perovskite-Type RMO3 (R=La,Y; M=Sc,ti,Cr,Mn,Fe,Co,Ni,Cu)". In: *Journal of the Physical Society of Japan* 64.7 (1995), pp. 2488–2501. DOI: 10.1143/JPSJ.64.2488.

[275] Lingfei Wang et al. "Device performance of the Mott insulator LaVO3 as a photovoltaic material". In: *Physical Review Applied* 3.6 (2015), p. 064015. ISSN: 23317019. DOI: 10.1103/PhysRevApplied.3.064015.

[276] Elias Assmann et al. "Oxide Heterostructures for Efficient Solar Cells". In: *Physical Review Letters* 110.7 (2013), p. 078701. ISSN: 00319007. DOI: 10.1103/PhysRevLett.110.078701.

[277] Hai Tian Zhang et al. “High-Quality LaVO3 Films as Solar Energy Conversion Material”. In: *ACS Applied Materials and Interfaces* 9.14 (2017), pp. 12556–12562. ISSN: 19448252. DOI: 10.1021/acsami.6b16007.

[278] M. Abbate et al. “Controlled-valence properties of La1-xSrxFeO3 and La1-xSrxMnO3 studied by soft-x-ray absorption spectroscopy”. In: *Physical Review B* 46.8 (1992), pp. 4511–4519. ISSN: 0163-1829. DOI: 10.1103/PhysRevB.46.4511.

[279] T. Arima, Y. Tokura, and J. B. Torrance. “Variation of optical gaps in perovskite-type 3d transition-metal oxides”. In: *Physical Review B* 48.23 (1993), pp. 17006–17009. ISSN: 01631829. DOI: 10.1103/PhysRevB.48.17006.

[280] Kentarou Nakamura et al. “Impact of built-in potential across LaFeO3/SrTiO3 heterojunctions on photocatalytic activity”. In: *Applied Physics Letters* 108.21 (2016), p. 211605. ISSN: 00036951. DOI: 10.1063/1.4952736.

[281] M. Nakamura et al. “Spontaneous polarization and bulk photovoltaic effect driven by polar discontinuity in LaFeO3/SrTiO3 heterojunctions”. In: *Physical Review Letters* 116.15 (2016), p. 156801. ISSN: 10797114. DOI: 10.1103/PhysRevLett.116.156801.

[282] S. Y. Wang et al. “Mechanisms of asymmetric leakage current in Pt/Ba0.6Sr 0.4TiO3/Nb-SrTiO3 capacitor”. In: *Applied Physics A: Materials Science and Processing* 81.6 (2005), pp. 1265–1268. ISSN: 09478396. DOI: 10.1007/s00339-004-3001-7.

[283] Y. Hotta et al. “Growth and epitaxial structure of LaVOx films”. In: *Applied Physics Letters* 89.3 (2006), p. 031918. ISSN: 00036951. DOI: 10.1063/1.2227786.

[284] H. Rotella et al. “Octahedral tilting in strained LaVO3 thin films”. In: *Physical Review B* 85.18 (2012), p. 184101. ISSN: 10980121. DOI: 10.1103/PhysRevB.85.184101.

[285] H. Rotella et al. “Two components for one resistivity in LaVO3/SrTiO3 heterostructure”. In: *Journal of Physics: Condensed Matter* 27.9 (2015), p. 095603. ISSN: 1361648X. DOI: 10.1088/0953-8984/27/9/095603.

[286] H. Meley et al. “Structural analysis of LaVO3 thin films under epitaxial strain”. In: *APL Materials* 6.4 (2018), p. 046102. ISSN: 2166532X. DOI: 10.1063/1.5021844.

[287] Hai-tian Zhang et al. “Self-regulated growth of LaVO3 thin films by hybrid molecular beam epitaxy”. In: *Applied Physics Letters* 106.23 (2015), p. 233102. DOI: 10.1063/1.4922213.

[288] Matthew Brahlek et al. “Mapping growth windows in quaternary perovskite oxide systems by hybrid molecular beam epitaxy”. In: *Applied Physics Letters* 109.10 (2016), p. 101903. ISSN: 00036951. DOI: 10.1063/1.4962388.

[289] M. Sano et al. “Strong carrier localization in 3d transition metal oxynitride LaVO3-xNx epitaxial thin films”. In: *Journal of Materials Chemistry C* 5.7 (2017), pp. 1798–1802. ISSN: 20507526. DOI: 10.1039/c6tc04160d.

[290] Y. Hotta, T. Susaki, and H. Y. Hwang. “Polar discontinuity doping of the LaVO3/SrTiO3 interface”. In: *Physical Review Letters* 99.23 (2007), p. 236805. ISSN: 00319007. DOI: 10.1103/PhysRevLett.99.236805.

[291] C. He et al. “Metal-insulator transitions in epitaxial LaVO3 and LaTiO3 films”. In: *Physical Review B* 86.8 (2012), 081401(R). ISSN: 10980121. DOI: 10.1103/PhysRevB.86.081401.

[292] Shigeki Miyasaka, Yoichi Okimoto, and Yoshinori Tokura. “Anisotropy of Mott-Hubbard Gap Transitions due to Spin and Orbital Ordering in LaVO3 and YVO3”. In: *Journal of the Physical Society of Japan* 71.9 (2002), pp. 2086–2089. ISSN: 00319015. DOI: 10.1143/JPSJ.71.2086.

[293] N. Iwata et al. “Growth and Evaluation of [AFeOx/REFeO3] (A=Ca, Sr, RE=La, Bi) Superlattices by Pulsed Laser Deposition Method Using High Density Targets Prepared by Pechini Method”. In: *Mater. Res. Soc. Symp. Proc.* 1454 (2012), pp. 25–31. ISSN: 02729172. DOI: 10.1557/opl.2012.1235.

[294] J. E. Kleibeuker et al. “Electronic reconstruction at the isopolar LaTiO3/LaFeO3 interface: An X-ray photoemission and density-functional theory study”. In: *Physical Review Letters* 113.23 (2014), p. 237402. ISSN: 10797114. DOI: 10.1103/PhysRevLett.113.237402.

[295] Zhaoliang Liao et al. “Metal-insulator-transition engineering by modulation tilt-control in perovskite nickelates for room temperature optical switching”. In: *Proceedings of the National Academy of Sciences of the United States of America* 115.43 (2018), E10284. ISSN: 10916490. DOI: 10.1073/pnas.1816794115.

[296] Samiya Manzoor, Shahid Husain, and V. Raghavendra Reddy. “Epitaxial LaFeO3 and LaFe0.75Zn0.25O3 thin films on SrTiO3 (STO) (100) substrate: Structural studies and high energy magnon excitations”. In: *Applied Physics Letters* 113.7 (2018), p. 072901. ISSN: 00036951. DOI: 10.1063/1.5025247.

[297] M D Scafetta et al. “Optical absorption in epitaxial La1-xSrxFeO3 thin films”. In: *Applied Physics Letters* 102.8 (2013), p. 081904. ISSN: 00036951. DOI: 10.1063/1.4794145.

[298] H. Wadati et al. “Hole-doping-induced changes in the electronic structure of La1-xSrx-FeO3: Soft x-ray photoemission and absorption study of epitaxial thin films”. In: *Physical Review B* 71.3 (2005), p. 035108. ISSN: 10980121. DOI: 10.1103/PhysRevB.71.035108.

[299] Mark D. Scafetta et al. “Band structure and optical transitions in LaFeO3 : theory and experiment”. In: *Journal of Physics: Condensed Matter* 26.50 (2014), p. 505502. ISSN: 0953-8984. DOI: 10.1088/0953-8984/26/50/505502.

[300] A. E. Bocquet et al. “Electronic structure of SrFe4+O3 and related Fe perovskite oxides”. In: *Physical Review B* 45.4 (1992), pp. 1561–1570. ISSN: 01631829. DOI: 10.1103/PhysRevB.45.1561.

[301] Qing Yu et al. “A highly durable p-LaFeO3/n-Fe2O3 photocell for effective water splitting under visible light”. In: *Chemical Communications* 51.17 (2015), pp. 3630–3633. ISSN: 1364548X. DOI: 10.1039/c4cc09240f.

[302] Peipei Wang et al. “Enhanced photoelectrochemical performance of LaFeO3 photocathode with Au buffer layer”. In: *RSC Advances* 9.46 (2019), pp. 26780–26786. ISSN: 20462069. DOI: 10.1039/c9ra05521e.

[303] M. Minohara et al. “Band diagrams of spin tunneling junctions la0.6Sr0.4MnO3/Nb:SrTiO3 and SrRuO3/Nb:SrTiO3 determined by in situ photoemission spectroscopy”. In: *Applied Physics Letters* 90.13 (2007), p. 132123. ISSN: 00036951. DOI: 10.1063/1.2717517.

[304] M. Minohara et al. “Termination layer dependence of Schottky barrier height for La0.6Sr0.4MnO3/Nb:SrTiO3 heterojunctions”. In: *Physical Review B* 81.23 (2010), p. 235322. ISSN: 10980121. DOI: 10.1103/PhysRevB.81.235322.

[305] Hong Sub Lee and Hyung Ho Park. “Band structure analysis of La0.7Sr0.3MnO3 perovskite manganite using a synchrotron”. In: *Advances in Condensed Matter Physics* 746475 (2015). ISSN: 16878124. DOI: 10.1155/2015/746475.

[306] Gregory N. Derry, Megan E. Kern, and Eli H. Worth. “Recommended values of clean metal surface work functions”. In: *Journal of Vacuum Science & Technology A* 33.6 (2015), p. 060801. ISSN: 0734-2101. DOI: 10.1116/1.4934685. URL: http://dx.doi.org/10.1116/1.4934685.

[307] R. Schlaf et al. “Organic semiconductor interfaces: Discrimination between charging and band bending related shifts in frontier orbital line-up measurements with photoemission spectroscopy”. In: *Journal of Applied Physics* 86.10 (1999), pp. 5678–5686. ISSN: 00218979. DOI: 10.1063/1.371578.

[308] B. E. Nieuwenhuys, O. G. Van Aardenne, and W. M.H. Sachtler. "Adsorption of xenon on group VIII and ib metals studied by photoelectric work function measurements". In: *Chemical Physics* 5.3 (1974), pp. 418–428. ISSN: 03010104. DOI: 10.1016/0301-0104(74)85043-3.

[309] David R. Lide. *Handbook of Chemistry and Physics, 84th edition.* CRC Press LLC, 2004.

[310] Andreas Klein. "Interface Properties of Dielectric Oxides". In: *Journal of the American Ceramic Society* 99.2 (2016), pp. 369–387. ISSN: 15512916. DOI: 10.1111/jace.14074.

[311] A. Ohta et al. "Determination of energy band alignment in ultrathin Hf-based oxide/Pt system". In: *Journal of Physics: Conference Series* 417.1 (2013), p. 012012. ISSN: 17426596. DOI: 10.1088/1742-6596/417/1/012012.

[312] John D. Baniecki et al. "Strain Dependent Electronic Structure and Band Offset Tuning at Heterointerfaces of ASnO3 (A=Ca, Sr, and Ba) and SrTiO3". In: *Scientific Reports* 7.41725 (2017). ISSN: 20452322. DOI: 10.1038/srep41725.

[313] Andreas Klein et al. "Transparent conducting oxides for photovoltaics: Manipulation of fermi level, work function and energy band alignment". In: *Materials* 3.11 (2010), pp. 4892–4914. ISSN: 19961944. DOI: 10.3390/ma3114892.

[314] Karthik Krishnaswamy et al. "BaSnO3 as a channel material in perovskite oxide heterostructures". In: *Applied Physics Letters* 108.8 (2016), p. 083501. ISSN: 00036951. DOI: 10.1063/1.4942366.

[315] Woong Jhae Lee et al. "Transparent perovskite barium stannate with high electron mobility and thermal stability". In: *Annual Review of Materials Research* 47 (2017), pp. 391–423. DOI: 10.1146/annurev-matsci-070616-124109.

[316] Evgeny Y. Tsymbal and Igor Žutić. *Spintronics Handbook: Spin Transport and Magnetism, Second Edition. Semiconductor Spintronics - Volume Two.* CRC Press - Taylor & Francis Group, 2019. ISBN: 978-1-4987-6960-0.

[317] William Shockley and Hans J. Queisser. "Detailed balance limit of efficiency of p-n junction solar cells". In: *Journal of Applied Physics* 32.3 (1961), pp. 510–519. DOI: 10.1063/1.1736034.

[318] R. Brendel and H. J. Queisser. "On the thickness dependence of open circuit voltages of p-n junction solar cells". In: *Solar Energy Materials and Solar Cells* 29.4 (1993), pp. 397–401. ISSN: 09270248. DOI: 10.1016/0927-0248(93)90098-N.

[319] Woong Choi, Timothy Sands, and Kwang-Young Kim. “Epitaxial growth of semiconducting LaVO3 thin films”. In: *Journal of Materials Research* 15.1 (2000), pp. 1–3. DOI: 10.1557/JMR.2000.0001.

[320] S. Miyasaka, T. Okuda, and Y. Tokura. “Critical behavior of metal-insulator transition in La1-xSrxVO3”. In: *Physical Review Letters* 85.25 (2000), pp. 5388–5391. ISSN: 00319007. DOI: 10.1103/PhysRevLett.85.5388.

[321] Chikako Yoshida, Akira Yoshida, and Hirotaka Tamura. “Nanoscale conduction modulation in Au/Pb(Zr,Ti)O3/SrRuO3 heterostructure”. In: *Applied Physics Letters* 75.10 (1999), pp. 1449–1451. ISSN: 00036951. DOI: 10.1063/1.124721.

[322] Dongyang Wan et al. “Comparison of Typical Photocatalytic Systems with Intrinsic Plasmonic Photocatalysts Based on Strontium Niobate for Water Splitting”. In: *Energy Technology* 6.1 (2018), pp. 60–71. DOI: 10.1002/ente.201700624.

[323] H. M. Christen and G. Eres. “Recent advances in pulsed-laser deposition of complex oxides”. In: *Journal of Physics: Condensed Matter* 20.26 (2008), p. 264005. ISSN: 09538984. DOI: 10.1088/0953-8984/20/26/264005.

[324] Ho Nyung Lee et al. “Growth control of oxygen stoichiometry in homoepitaxial SrTiO 3 films by pulsed laser epitaxy in high vacuum”. In: *Scientific Reports* 6.October 2015 (2016), pp. 1–7. ISSN: 20452322. DOI: 10.1038/srep19941.

[325] Ekaterina Khestanova et al. “Untangling Electrostatic and Strain Effects on the Polarization of Ferroelectric Superlattices”. In: *Advanced Functional Materials* 26.35 (2016), pp. 6446–6453. ISSN: 16163028. DOI: 10.1002/adfm.201602084.

[326] Shishir Pandya et al. “Strain-induced growth instability and nanoscale surface patterning in perovskite thin films”. In: *Scientific Reports* 6 (2016), p. 26075. ISSN: 20452322. DOI: 10.1038/srep26075.

[327] F. Sánchez et al. “Surface roughening by anisotropic adatom kinetics in epitaxial growth of La0.67Ca0.33MnO3”. In: *Surface Science* 600.6 (2006), pp. 1231–1239. ISSN: 00396028. DOI: 10.1016/j.susc.2006.01.008.

[328] M. Kalff et al. “No coarsening in Pt(111) homoepitaxy”. In: *Surface Science* 426.3 (1999), pp. L447–L453. ISSN: 00396028. DOI: 10.1016/S0039-6028(99)00351-9.

[329] Gert Ehrlich and F. G. Hudda. “Atomic View of Surface Self-Diffusion: Tungsten on Tungsten”. In: *The Journal of Chemical Physics* 44.3 (1966), pp. 1039–1049. ISSN: 00219606. DOI: 10.1063/1.1726787.

[330] Richard L. Schwoebel and Edward J. Shipsey. “Step Motion on Crystal Surfaces”. In: *Journal of Applied Physics* 37.10 (1966), pp. 3682–3686. ISSN: 00218979. DOI: 10.1063/1.1707904.

[331] F. Tsui et al. “Strain-dependent magnetic phase diagram of epitaxial La0.67Sr0.33MnO3 thin films”. In: *Applied Physics Letters* 76.17 (2000), pp. 2421–2423. ISSN: 00036951. DOI: 10.1063/1.126363.

[332] Hangwen Guo et al. “Growth diagram of La0.7Sr0.3MnO3 thin films using pulsed laser deposition”. In: *Journal of Applied Physics* 113.23 (2013), p. 234301. DOI: 10.1063/1.4811187.

[333] D.H.A. Blank et al. “Imposed layer-by-layer growth by pulsed laser interval deposition”. In: *Applied Physics A* 69 (1999), S17–S22. ISSN: 0947-8396. DOI: 10.1007/s003399900187.

[334] Dave H.A. Blank et al. “Epitaxial growth of oxides with pulsed laser interval deposition”. In: *Journal of Crystal Growth* 211.1-4 (2000), pp. 98–105. ISSN: 00220248. DOI: 10.1016/S0022-0248(99)00880-5.

[335] G. Koster et al. “Imposed layer-by-layer growth by pulsed laser interval deposition”. In: *Applied Physics Letters* 74.24 (1999), p. 3729. ISSN: 09478396. DOI: 10.1007/s003390051348.

[336] Dave H.A. Blank, Matthijn Dekkers, and Guus Rijnders. “Pulsed laser deposition in Twente: From research tool towards industrial deposition”. In: *Journal of Physics D: Applied Physics* 47.3 (2014), 034006 (8pp). ISSN: 00223727. DOI: 10.1088/0022-3727/47/3/034006.

[337] Weiliang Liu et al. “Growth and Characterization of LaFeO3 Crystals”. In: *Key Engineering Materials* 602-603 (2014), pp. 27–31. DOI: 10.4028/www.scientific.net/KEM.602-603.27.

[338] M. Kareev et al. “Sub-monolayer nucleation and growth of complex oxides at high supersaturation and rapid flux modulation”. In: *Journal of Applied Physics* 109.11 (2011), p. 114303. ISSN: 00218979. DOI: 10.1063/1.3590146.

[339] Georg Rosenfeld et al. “Layer-by-Layer Growth of Ag on Ag(111) Induced by Enhanced Nucleation: A Model Study for Surfactant-Mediated Growth”. In: *Physical Review Letters* 71.6 (1993), p. 895. ISSN: 00319007. DOI: 10.1103/PhysRevLett.73.364.

[340] Georg Rosenfeld, Bene Poelsema, and George Comsa. “The concept of two mobilities in homoepitaxial growth”. In: *Journal of Crystal Growth* 151.1-2 (1995), pp. 230–233. ISSN: 00220248. DOI: 10.1016/0022-0248(95)00077-1.

[341] Jiameng Cui et al. “Oxygen deficiency induced strong electron localization in lanthanum doped transparent perovskite oxide BaSn O3”. In: *Physical Review B* 100.16 (2019), p. 165312. ISSN: 24699969. DOI: 10.1103/PhysRevB.100.165312.

[342] Qinzhuang Liu et al. “Effect of thickness on the electrical and optical properties of epitaxial (La0.07Ba0.93)SnO3 thin films”. In: *Superlattices and Microstructures* 96 (2016), pp. 205–211. ISSN: 10963677. DOI: 10.1016/j.spmi.2016.05.027.

[343] Zhe Wang et al. “Epitaxial integration of high-mobility La-doped BaSnO3 thin films with silicon”. In: *APL Materials* 7.2 (2019), p. 022520. ISSN: 2166532X. DOI: 10.1063/1.5054810.

[344] Timothy Nathan Nunley et al. “Optical constants, band gap, and infrared-active phonons of (LaAlO3)0.3(Sr2AlTaO6)0.35 (LSAT) from spectroscopic ellipsometry”. In: *Journal of Vacuum Science & Technology A* 34.5 (2016), p. 051507. DOI: 10.1116/1.4960356.